

Cellular interactions with protein nanofibers

DISSERTATION

zur Erlangung des Doktorgrades

der Naturwissenschaften im Fachbereich Physik

der Universität Bremen

vorgelegt von

M.Sc. Naiana Suter

Bremen, 09.07.2020



Thesis referees:

1. Prof. Dr. Dorothea Brüggemann

2. Prof. Dr. Manfred Radmacher

Abstract

The fundamental understanding of cell-material interactions plays a central role in the development of future biomaterials for tissue engineering. The current state of knowledge about cell interactions with various biomaterials has mainly been obtained from smooth 2D-cell culture systems like petri dishes. However, many of the established materials are not suitable for mimicking the nanofibrous three-dimensional (3D) topography, the biochemical and mechanical environment of the extracellular matrix (ECM). This raises the challenge of transferring cell culture results from established smooth/planar test systems into the development of novel 3D microenvironments that mimic the nanoarchitecture of the ECM.

Therefore, in this Ph.D. thesis, a new approach for the fabrication of binary protein scaffolds with spatially controlled areas of smooth and nanofibrous topography was introduced. In the first step, the ECM protein collagen was used as a model system to establish the new method. Polymer patterning was combined with pH-induced self-assembly and crosslinking of collagen to produce binary scaffolds with spatially controlled smooth nanofibrous topographies. When studying the interaction of NIH 3T3 fibroblasts with the new binary scaffolds, a direct influence of the underlying topography on cell morphology, cell size, filopodia growth and cell migration was observed. Fluorescence microscopy analysis showed that the morphology of fibroblasts changed from small spindle-like shape with long lamellipodia on collagen nanofibers to large, flat cells with many short filopodia on smooth collagen. These topography-dependent trends in fibroblast morphology were confirmed by confocal and scanning electron microscopy.

To further investigate the influence of biochemical cues on cells, the novel method of preparing binary collagen scaffolds was subsequently transferred to the fabrication of fibrinogen scaffolds with binary topography. The new fabrication process was successfully combined with the newly introduced salt-induced self-assembly of fibrinogen. When investigating the interaction of NIH 3T3 fibroblasts with binary fibrinogen scaffolds, a direct influence of the underlying topography on cell morphology was also observed. Fluorescence microscopy analysis revealed that the morphology of fibroblasts changed from small spindle-like shape with diffuse actin expression on fibrinogen nanofibers to large, flat cells with pronounced stress fibers on planar fibrinogen. Again, these topography-dependent trends in fibroblast morphology were confirmed by confocal and scanning electron microscopy. Moreover, viability studies of fibroblasts on fibrinogen showed increased proliferation rates on both, nanofibrous and planar, fibrinogen scaffolds.

Subsequently, the two protein systems and topographies were combined in one scaffold system. By spatially tailoring of the biochemical and topographical features in these protein scaffolds, it will be possible to investigate topography- and time-dependent cell recognition

processes on a single scaffold. In the future, this could make it possible to transfer *in vitro* results from cell cultures on smooth/planar surfaces directly into the development of nanofibrous protein scaffolds.

Zusammenfassung

Das grundlegende Verständnis von Zell-Material-Interaktionen spielt eine zentrale Rolle bei der Entwicklung zukünftiger Biomaterialien für das Tissue Engineering. Der aktuelle Wissensstand über Zellinteraktionen mit verschiedenen Biomaterialien wurde hauptsächlich aus glatten / flachen 2D-Zellkultursystemen gewonnen, wie z.B. Petrischalen. Viele der etablierten Substratmaterialien sind allerdings nicht dafür geeignet, die nanofaserige dreidimensionale (3D) Topographie, die biochemische und die mechanische Umgebung der extrazellulären Matrix (ECM) zu imitieren.

Daraus ergibt sich die Herausforderung, die Ergebnisse aus flachen Zellkultursystemen in die Entwicklung neuartiger 3D-Mikroumgebungen zu übertragen, die die Nanoarchitektur der ECM imitieren.

Daher wurde in dieser Dissertation zunächst eine neue Methode zur Herstellung von binären Proteingerüsten mit räumlich kontrollierten Bereichen aus glatter und nanofaseriger Topographie entwickelt. In einem ersten Schritt wurde das ECM-Protein Kollagen als Modellsystem zur Etablierung der neuen Methode genutzt. Polymerdruck wurde mit der Selbstassemblierung und Vernetzung von Kollagen kombiniert, um binäre Scaffolds mit räumlich kontrollierten Bereichen aus glatter und nanofaseriger Topographie herzustellen. Bei der Untersuchung der Interaktion von NIH 3T3-Fibroblasten mit den neuen binären Scaffolds wurde ein direkter Einfluss der Topographie auf die Zellmorphologie, die Zellgröße, das Filopodienwachstum und Zellmigration beobachtet. Fluoreszenzmikroskopische Untersuchungen haben gezeigt, dass sich die Morphologie der Fibroblasten von kleinen Spindelformen mit langen Lamellipodien auf Kollagen-Nanofasern zu großen, flachen Zellen mit vielen kurzen Filopodien auf glattem Kollagen veränderte. Diese topographieabhängigen Trends in der Morphologie der Fibroblasten wurden durch Konfokal- und Rasterelektronenmikroskopie bestätigt.

Mit dem Modellsystem Kollagen wurde eine Plattform etabliert, die es erlaubt, die Substrattopographie gezielt zu beeinflussen. Um weiter die biochemischen Einflüsse auf Zellen zu untersuchen, wurde die neue Methode zur Herstellung von binären Proteingerüsten weiter auf die salz-induzierte Selbstassemblierung von Fibrinogen übertragen. Bei der Untersuchung der Interaktion von NIH 3T3-Fibroblasten mit Fibrinogen Scaffolds mit binärer Topographie wurde ebenfalls ein direkter Einfluss der Substrattopographie auf die Zellmorphologie, Zellgröße und das Filopodienwachstum beobachtet. Fluoreszenzmikroskopische Aufnahmen haben gezeigt, dass sich die Morphologie der Fibroblasten von kleinen Spindelformen mit diffuser Aktinausprägung auf

Fibrinogen-Nanofasern zu großen, flachen Zellen mit ausgeprägten Stressfasern auf glattem Fibrinogen veränderte. Diese topographieabhängigen Trends in der Morphologie der Fibroblasten wurden wiederum durch Konfokal- und Rasterelektronenmikroskopie bestätigt. Viabilitätsuntersuchungen der Fibroblasten auf den Fibrinogen-Scaffolds zeigten zudem erhöhte Proliferationsraten sowohl auf nanofaserigen als auch auf glatten Fibrinogen-Scaffolds.

Aufbauend auf diesen Ergebnissen konnten außerdem in ersten Versuchen die beiden Proteinsysteme miteinander kombiniert werden. Mit dieser binären Scaffold-Plattform wird es in Zukunft möglich sein, topographie- und zeitabhängige Zellerkennungsprozesse in einem einzigen Substrat zu untersuchen. Damit könnten in Zukunft *in vitro*-Ergebnisse aus Zellkulturen auf glatten/planaren Oberflächen direkt in die Entwicklung von nanofaserigen Protein-Gerüsten übertragen werden.

Acknowledgment

I sincerely thank Prof. Dr. Dorothea Brüggemann for allowing me to work on this interesting topic and for the supervision during my Ph.D. thesis at the Institute of Biophysics, University of Bremen. I deeply appreciate her encouragement and timely support and I thank her for reviewing my thesis. Further, I would like to thank Prof. Dr. Manfred Radmacher for his constant encouragement, for his scientific knowledge and the reviewing of my thesis. I would also like to thank Prof. Dr. Stefan Bornholdt and Prof. Dr. Janine Kirstein for their cooperation in this committee.

Special thanks go to Dr. Carmela Rianna for introducing me to the work with the atomic force microscope, for the support during the development process of this study, for her useful comments and remarks as well as for sharing her precious time for supervising me patiently. I deeply appreciate the willingness to help of Carmela and her valuable suggestions as well as her constant motivation.

I would also like to thank the IMSAS for their cooperation and access to the scanning electron microscope (SEM), without which this work would have not been possible. Special thanks to Eva Maria Meyer for teaching me at the SEM and her advice and help with the development of protocols.

I am very grateful for the cooperation with the department of cell biology and the access to the confocal microscope. I would like to thank Dr. Anette Peter for introducing me to the confocal microscope and investing her time, giving me support, and help with challenging samples.

Special thanks to Prof. Dr. Jan-Henning Dirks for giving me scientific support and advice.

I thank all members of the Emmy Noether research group for nanoBiomaterials. Eva, thank you for supplying us with cake and cookies and for all the extra kilos we gained because of that. I want to thank Karsten Stapelfeldt (Senhor) and Dr. Jana Markhoff (Gabi) for all the scientific and non-scientific talks and endless hours we spent together in our office and the lab.

Finally, I would like to thank my family, my friends, and especially Linda Gätjen, Phillip Krieter, and Luca Schmid for supporting me, and for inspiring me to give my best at every step and for their endless patience.

DECLARATION

I hereby declare, that I am the sole author and composer of this thesis and that no other sources, other than those listed, have been used. Furthermore, I declare that I have acknowledged the work of others by providing detailed references for said work. I hereby also declare, that this thesis has not been prepared for another examination or written assignment, either wholly or excerpts thereof.

Place, date

Signature

Table of content

Motivation	1
1. Introduction	4
1.1 The extracellular matrix	4
1.1.1 Collagen	8
1.1.2 Fibrinogen.....	12
1.2 Fibroblasts and cell migration	14
1.3 Cell-substrate interactions	21
1.3 Synthetic ECM systems.....	29
1.4.1 Manufacturing methods for nanofibrous and porous scaffolds	29
1.4.2 Cell interaction with synthetic nanotopographies	41
1.5 Aim.....	45
2. Materials and methods	46
2.1 Scaffold preparation	46
2.1.1 Substrate preparation	46
2.1.2 Collagen scaffolds	46
2.1.3 Fibrinogen scaffolds.....	50
2.1.4 Protein scaffolds with nanofibrous and smooth topography	52
2.2 Characterization of scaffolds	57
2.4.1 Scanning electron microscopy	57
2.4.2 Atomic force microscopy.....	57
2.3 Cell interaction with protein scaffolds.....	59
2.6.1 Cultivation.....	59
2.6.2 Viability assays	60
2.6.3 Morphological analysis	63
2.6.4 Cell mechanics	67
2.6.4 Cell Tracking (Dil).....	68
3. Results	72
3.1 Collagen scaffolds	72
3.1.1 Self-assembly and Crosslinking	72
3.1.2 Surface coverage	75
3.1.3 Collagen nanofiber morphology	76
3.1.4 Collagen scaffold mechanics	81
3.1.5 Collagen scaffolds with binary surface topography	83
3.1.6 Cellular response to nanostructured collagen scaffolds	86

3.2 Fibrinogen scaffolds	114
3.2.1 Fibrinogen nanofiber morphology	114
3.2.2 Fibrinogen nanofiber mechanics	117
3.2.3 Fibrinogen scaffolds with binary surface topography for cell culture.....	118
3.2.4 Cellular response to nanostructured fibrinogen scaffolds.....	120
3.3 Scaffolds with binary surface topography and biochemistry for cell culture.....	131
4. Discussion	137
4.1 Collagen	137
4.1.1 Collagen scaffolds	137
4.1.2 Cell interaction with collagen scaffolds	142
4.2 Fibrinogen	150
4.2.1 Fibrinogen scaffolds	150
4.2.1 Cell interaction with fibrinogen scaffolds	152
4.3 Collagen vs Fibrinogen.....	157
4.3.1 Scaffold characteristics.....	157
4.3.2 Comparison of fibroblast interaction with collagen and fibrinogen scaffolds.....	159
4.4 Combination of biochemical cues and topographical cues.....	161
5. Conclusion and Outlook	165
Publication bibliography	168
Appendix	I
Materials.....	I
Atomic force microscopy	VII
Live Cell tracking.....	VIII
Velocity analysis of fibroblasts on collagen.....	VIII
Velocity analysis of fibroblasts on fibrinogen	XX

List of Figures

FIGURE 1. THE EXTRACELLULAR MATRIX.....	6
FIGURE 2. SCHEMATIC OF A COLLAGEN TRIPLE HELIX.....	8
FIGURE 3. THE HIERARCHICAL FEATURES OF COLLAGEN.....	10
FIGURE 4. FIBRINOGEN MOLECULE.....	13
FIGURE 5. FIBRINOGEN FIBRILLOGENESIS <i>IN VIVO</i>	14
FIGURE 6. CELL MIGRATION STEPS.....	17
FIGURE 7. THREE TYPES OF ACTIN STRESS FIBERS.....	18
FIGURE 8. CELLULAR MECHANICS IN THREE STEPS.....	20
FIGURE 9. THE CELLULAR PROCESS OF MECHANOSENSING AND RESPONSES.....	22
FIGURE 10. CELL RESPONSE CONTROL.....	24
FIGURE 11. BIOPHYSICAL CHARACTERISTICS OF HUMAN TISSUES.....	26
FIGURE 12. DIVERSE APPLICATIONS OF COLLAGEN-BASED NANOBIMATERIALS.....	31
FIGURE 13. ELECTROSPINNING PROCESS.....	35
FIGURE 14. ALDEHYDE REACTION MECHANISMS WITH PROTEINS.....	48
FIGURE 15. EDC CROSSLINKING MECHANISM.....	49
FIGURE 16. COLLAGEN SELF-ASSEMBLY PROCESS.....	50
FIGURE 17. THE SILANIZATION OF GLASS SURFACES WITH APTES.....	51
FIGURE 18. FIBRINOGEN FIBER SELF-ASSEMBLY PROCESS.....	52
FIGURE 19. OVERVIEW OF BINARY PROTEIN SCAFFOLD ASSEMBLY PROCESS.....	53
FIGURE 20. BINARY TYPE 1 (COLLAGEN FIBERS AND FIBRINOGEN FIBERS).....	54
FIGURE 21. BINARY TYPE 2 (SMOOTH FIBRINOGEN AND COLLAGEN FIBERS).....	55
FIGURE 22. BINARY TYPE 3 (SMOOTH COLLAGEN AND FIBRINOGEN FIBERS).....	56
FIGURE 23. INDENTATION OF A THIN BIOLOGICAL SAMPLE BY A TRIANGLE PROBE.....	58
FIGURE 24. TYPICAL FORCE-DISTANCE CURVES.....	59
FIGURE 25. CLEAVAGE OF TETRAZOLIUM SALTS TO FORMAZAN.....	62
FIGURE 26. CSI ANALYSIS.....	65
FIGURE 27. AFM FORCE CURVE ON A CELL.....	67
FIGURE 28. DII MOLECULAR STRUCTURE.....	68
FIGURE 29. A TYPICAL 12-WELL-PLATE FOR LIVE-CELL TRACKING.....	69
FIGURE 30. FLUORESCENCE IMAGE OF 3T3 FIBROBLASTS GROWN ON GLASS STAINED WITH DII.....	70
FIGURE 31. SEM IMAGE OF NOT CROSS-LINKED COLLAGEN.....	73
FIGURE 32. SEM IMAGES OF COLLAGEN CROSS-LINKED WITH DIFFERENT CROSSLINKING METHODS.....	74
FIGURE 33. SEM IMAGES OF COLLAGEN FIBERS ON DIFFERENT SUBSTRATES.....	75
FIGURE 34. SEM IMAGE OF COLLAGEN SURFACE COVERAGE.....	76
FIGURE 35. NANO TOPOGRAPHY OF NANOFIBROUS COLLAGEN SCAFFOLDS.....	77
FIGURE 36. NANO TOPOGRAPHY OF SMOOTH COLLAGEN SCAFFOLDS.....	78
FIGURE 37. AFM HEIGHT IMAGES OF COLLAGEN SCAFFOLDS.....	79
FIGURE 38. EXEMPLARY FORCE-DISTANCE CURVES ON NANOFIBROUS 0.5 MG ML ⁻¹ COLLAGEN.....	82
FIGURE 39. EXEMPLARY FORCE-DISTANCE CURVES ON NANOFIBROUS 2.5 MG ML ⁻¹ COLLAGEN.....	83
FIGURE 40. PHASE CONTRAST IMAGES OF DRIED BINARY COLLAGEN SCAFFOLDS.....	84

FIGURE 41. PATTERNED COLLAGEN SCAFFOLDS WITH NANOFIBER AND SMOOTH TOPOGRAPHIES	85
FIGURE 42. LIVE/DEAD 3T3 FIBROBLASTS ON DIFFERENT SUBSTRATES AFTER 72 H CULTIVATION TIME	87
FIGURE 43. PERCENTAGE OF VIABLE 3T3 FIBROBLASTS ON DIFFERENT SUBSTRATES.	89
FIGURE 44. PROLIFERATION OF 3T3 FIBROBLASTS ON COLLAGEN SCAFFOLDS	90
FIGURE 45. RELATIVE VIABILITY OF 3T3 FIBROBLASTS ON COLLAGEN SCAFFOLDS.	91
FIGURE 46. FLUORESCENCE MICROSCOPY IMAGES OF 3T3 FIBROBLASTS ON NANOFIBROUS COLLAGEN	92
FIGURE 47. SINGLE CELL AREA OF 3T3 FIBROBLASTS GROWN ON 0.5 MG ML ⁻¹ COLLAGEN	94
FIGURE 48. CELL PERIMETER OF 3T3 FIBROBLASTS GROWN ON 0.5 MG ML ⁻¹ COLLAGEN	95
FIGURE 49. CSI ANALYSIS OF 3T3 FIBROBLASTS GROWN ON 0.5 MG ML ⁻¹ COLLAGEN.	96
FIGURE 50. CELL COVERED AREA [%] 3T3 FIBROBLASTS GROWN ON 0.5 MG ML ⁻¹ COLLAGEN	97
FIGURE 51. SEM IMAGES OF 3T3 FIBROBLASTS ON NANOFIBROUS 2.5 MGML ⁻¹ COLLAGEN.	100
FIGURE 52. CONFOCAL IMAGES FROM Z-STACK OF 3T3 FIBROBLASTS ON COLLAGEN (2.5 MG ML ⁻¹)	101
FIGURE 53. YOUNG'S MODULI OF 3T3 FIBROBLASTS ON COLLAGEN SCAFFOLDS.	102
FIGURE 54. SEM IMAGES OF FIBROBLASTS ON BINARY COLLAGEN SCAFFOLDS AFTER 36 H.....	103
FIGURE 55. EXEMPLARY TRACK OF A FIBROBLAST ON GLASS.	104
FIGURE 56. MEDIAN VELOCITIES OF A SINGLE FIBROBLAST GLASS OVER TIME	105
FIGURE 57. MIGRATION VELOCITIES 3T3 FIBROBLASTS ON NANOFIBROUS 2.5 MG ML ⁻¹ COLLAGEN.....	106
FIGURE 58. MIGRATION VELOCITIES 3T3 FIBROBLASTS ON 0.5 MG ML ⁻¹ COLLAGEN.....	107
FIGURE 59. MEDIAN MIGRATION VELOCITIES OF 3T3 FIBROBLASTS ON 2.5 MG ML ⁻¹ COLLAGEN.....	109
FIGURE 60. CELL VELOCITIES OF 3T3 FIBROBLASTS ON 2.5 MG ML ⁻¹ COLLAGEN	110
FIGURE 61. ZOOM INTO NORMALIZED HISTOGRAMS OF CELL VELOCITIES.....	111
FIGURE 62. MIGRATION VELOCITIES OF 3T3 FIBROBLASTS ON DIFFERENT COLLAGEN SCAFFOLDS.	113
FIGURE 63. SEM IMAGES OF NANOFIBROUS AND PLANAR FIBRINOGEN SCAFFOLDS.....	115
FIGURE 64. AFM HEIGHT IMAGES OF FIBRINOGEN.	116
FIGURE 65. EXEMPLARY FORCE-DISTANCE CURVES ON NANOFIBROUS FIBRINOGEN SCAFFOLDS.....	118
FIGURE 66. PHASE CONTRAST IMAGE OF BINARY FIBRINOGEN SCAFFOLD.	119
FIGURE 67. SEM BINARY FIBRINOGEN SUBSTRATES.	119
FIGURE 68. PROLIFERATION RATES OF FIBROBLASTS ON FIBRINOGEN SCAFFOLDS.....	121
FIGURE 69. CELL VIABILITY OF 3T3 FIBROBLASTS ON FIBRINOGEN SCAFFOLDS.....	122
FIGURE 70. FLUORESCENCE MICROSCOPY IMAGES OF 3T3 FIBROBLASTS ON FIBRINOGEN SCAFFOLDS	124
FIGURE 71. SEM IMAGES OF 3T3 FIBROBLASTS ON NANOFIBROUS FIBRINOGEN.	125
FIGURE 72. CONFOCAL MICROSCOPY Z-STACK 3T3 FIBROBLASTS ON NANOFIBROUS FIBRINOGEN	126
FIGURE 73. SEM IMAGE OF 3T3 FIBROBLASTS ON BINARY FIBRINOGEN AFTER 36 H.	127
FIGURE 74. MEDIAN MIGRATION VELOCITIES OF 3T3 FIBROBLASTS ON FIBRINOGEN.....	129
FIGURE 75. CELL MIGRATION OF 3T3 FIBROBLASTS ON NANOFIBROUS FIBRINOGEN	130
FIGURE 76. SCHEMATIC OF A BINARY TYPE 1 SCAFFOLD.....	132
FIGURE 77. SEM IMAGES OF BINARY SCAFFOLDS TYPE 1.	133
FIGURE 78. SCHEMATIC OF A BINARY TYPE 2 SCAFFOLD.....	133
FIGURE 79. SEM IMAGES OF BINARY SCAFFOLD TYPE 2	134
FIGURE 80. SCHEMATIC OF A BINARY TYPE 3	135
FIGURE 81. SEM IMAGES OF BINARY SCAFFOLD TYPE 3	136

FIGURE 82. SCREENSHOT APPROACH AND RETRACT CURVES ON NANOFIBROUS COLLAGEN.....	VII
FIGURE 83. MIGRATION VELOCITIES OF 3T3 FIBROBLASTS ON NANOFIBROUS 0.5 MG ML ⁻¹ COLLAGEN.....	VIII
FIGURE 84. MIGRATION VELOCITIES OF 3T3 FIBROBLASTS ON SMOOTH 0.5 MG ML ⁻¹ COLLAGEN.	IX
FIGURE 85. MIGRATION VELOCITIES OF 3T3 FIBROBLASTS ON NANOFIBROUS BINARY 0.5 MG ML ⁻¹ COLLAGEN ..	X
FIGURE 86. MIGRATION VELOCITIES OF 3T3 FIBROBLASTS ON SMOOTH BINARY 0.5 MG ML ⁻¹ COLLAGEN.....	XI
FIGURE 87. MIGRATION VELOCITIES OF 3T3 FIBROBLASTS ON GLASS	XII
FIGURE 88. MIGRATION VELOCITIES OF 3T3 FIBROBLASTS ON NANOFIBROUS 2.5 MG ML ⁻¹ COLLAGEN.....	XIII
FIGURE 89. MIGRATION VELOCITIES OF 3T3 FIBROBLASTS ON SMOOTH 2.5 MG ML ⁻¹ COLLAGEN.	XIV
FIGURE 90. MIGRATION VELOCITIES OF 3T3 FIBROBLASTS ON NANOFIBROUS BINARY 2.5 MG ML ⁻¹ COLLAGEN	XV
FIGURE 91. MIGRATION VELOCITIES OF 3T3 FIBROBLASTS ON SMOOTH BINARY 2.5 MG ML ⁻¹ COLLAGEN.....	XVI
FIGURE 92. MIGRATION VELOCITIES OF 3T3 FIBROBLASTS ON GLASS.	XVII
FIGURE 93. MIGRATION VELOCITIES OF 3T3 FIBROBLASTS ON NANOFIBROUS FIBRINOGEN.....	XX
FIGURE 94. MIGRATION VELOCITIES OF 3T3 FIBROBLASTS ON PLANAR FIBRINOGEN.	XXI
FIGURE 95. MIGRATION VELOCITIES OF 3T3 FIBROBLASTS ON NANOFIBROUS BINARY FIBRINOGEN	XXII
FIGURE 96. MIGRATION VELOCITIES OF 3T3 FIBROBLASTS ON PLANAR BINARY FIBRINOGEN PREPARED	XXIII
FIGURE 97. MIGRATION VELOCITIES OF 3T3 FIBROBLASTS ON GLASS..	XXIV

List of Tables

TABLE 1. LIST OF ABBREVIATIONS	14
TABLE 2. COMPARISON OF TECHNIQUES TO PREPARE SCAFFOLDS FOR TISSUE ENGINEERING.....	40
TABLE 3. SURFACE DESCRIPTION BASED ON SURFACE ROUGHNESS IN REHYDRATED CONDITIONS.	43
TABLE 4. ROUGHNESS (RQ) OF DRIED AND REHYDRATED COLLAGEN SCAFFOLDS.....	80
TABLE 5. FIBER DIAMETERS (FD) OF DRIED AND REHYDRATED COLLAGEN FIBERS.....	81
TABLE 6. 3T3 FIBROBLASTS ON 0.5 MG ML ⁻¹ COLLAGEN FIBERS AND SMOOTH.....	99
TABLE 7. ROUGHNESS (RQ) OF FIBRINOGEN SCAFFOLDS	116
TABLE 8. FIBER DIAMETERS (FD) OF FIBRINOGEN NANOFIBERS.....	117
TABLE 9. MATERIALS.....	I
TABLE 10. DEVICES	II
TABLE 11. CHEMICALS	III
TABLE 12. SOLUTIONS	VI
TABLE 13. CELL VELOCITIES (NM MIN ⁻¹) AND COHENS'S D 0.5 MG ML ⁻¹ COLLAGEN.	XVIII
TABLE 14. CELL VELOCITIES (NM MIN ⁻¹) AND COHENS'S D 2.5 MG ML ⁻¹ COLLAGEN.	XIX
TABLE 15. CELL VELOCITIES (NM MIN ⁻¹) AND COHENS'S D 5 MG ML ⁻¹ FIBRINOGEN.	XXV

Abbreviations

Table 1. List of abbreviations

Abbreviation	Description
°C	Degree Celsius
AAO	Anodized aluminum oxide
APTES	(3-Aminopropyl)triethoxysilane
ANOVA	Analysis of variance
BSA	Bovine serum albumin
Calcein-AM	Calcein-acetoxymethylester
CSI	Cell shape index
DAPI	4',6-Diamidino-2-Phenylindole, Dihydrochloride
DDR	Discoidin domain receptors
DII	1,1'-Dioctadecyl-3,3,3',3'- Tetramethylindocarbocyanine Perchlorate (‘Dil’; DiIC18(3))
DMEM	Dulbecco’s Modified Eagle Medium
ECM	Extra cellular matrix
EthD-1	Ethidium homodimer-1
EDC	N-Ethyl-N’-(3- dimethylaminopropyl)carbodiimide
FAK	Focal adhesion kinase
FBR	Foreign body response
FBS	Fetal bovine serum
FGFs	Fibroblast growth factors
Fig.	Figure
FpA	Fibrinopeptides A
FpB	Fibrinopeptides B
GA	Glutaraldehyde
hESCs	Human embryonic stem cells
HGF	Hepatocyte growth factor
kV	Kilo Volt
LOX	Lysyl oxidase

Table 1. Continue of Table 1. Abbreviations

Abbreviation	Description
mL	Mili liter
mm	Mili meter
mM	Mili molar
ms	Miliseconds
MSD	Mean square displacement
MMPs	Matrix metalloproteinases
nm	Nano meter
NIL	Nanoimprint lithography
PDMS	Polydimethylsiloxane
PBS	Phosphate buffered saline
PFA	Paraformaldehyde
P/S	Penicillin/streptomycin
SAMs	Self-assembled monolayers
SEM	Scanning electron microscopy
Si	Silicon
SiO₂	Silica
TGFβs	Transforming growth factors
uPAs	Urokinase-type plasminogen activators
UV	Ultra violet
WST-1	Cell proliferation Reagent WST-1 (4-[3-(4-Iodophenyl)-2-(4-nitro-phenyl)-2H-5-tetrazolio]-1,3-benzene disulfonate)
μL	Micro liter
μm	Micro meter
μM	Micromolar

Motivation

Diseased tissues and organs and the related trauma potentially lead to degeneration and damage of tissues in the human body. Therefore, facilitating their replacement, regeneration, or repair is a current scientific and medical challenge (Ikada 2006; O'Brien 2011). The classical treatment typically focusses on autografts or transplants/allografts. Autografts require the transplantation of tissue from one site to another in the same patient, while an allograft is transplanted from one individual to another of the same species (O'Brien 2011). Although these treatments have been revolutionary and lifesaving, these surgical therapies have been facing several challenges (O'Brien 2011; Ikada 2006). The production of autografts is painful, expensive, constrained by anatomical limitations, and can cause infections and hematoma (O'Brien 2011). Correspondingly, allografts encounter a variety of serious constraints. A major risk is rejections by the patient's immune system along with the possibility of introducing infections or diseases from the donor to the patient (O'Brien 2011). Further problems in current organ transplantation include the shortage of donated organs and immune rejection, although immunosuppressive therapy has much advanced (Ikada 2006).

Approximately four decades ago a new alternative approach to tissue and organ reconstruction emerged (Ikada 2006). The interdisciplinary field of tissue engineering aims to regenerate damaged tissues, instead of replacing them, by developing biological substitutes that restore, maintain or improve the original tissue function (Langer 2000; Atala 2004; Ma 2004; Rice *et al.* 2005; O'Brien 2011; Ma 2008). The term 'tissue engineering' was officially introduced at a National Science Foundation workshop in 1988 and describes the following research area: "the application of principles and methods of engineering and life sciences towards the fundamental understanding of structure-function relationships in normal and pathological mammalian tissues and the development of biological substitutes to restore, maintain or improve tissue function" (O'Brien 2011). The earliest application of human cells in tissue engineering was reported around 1980 for skin repair using fibroblasts (Ikada 2006).

The field of tissue engineering is very multidisciplinary and includes disciplines like clinical medicine, mechanical engineering, materials science, genetics biophysics, and related disciplines from both engineering and the life sciences (O'Brien 2011). Fundamental understanding of physics, biology, material science, chemistry, and engineering strategies

together with the convergence of these disciplines drove the progress of tissue engineering (Khademhosseini and Langer 2016).

In the field of tissue engineering, the materials used are called biomaterials. However, over the last decades, various definitions of the term 'biomaterial' were introduced in the literature. Very recently, a concise definition of a biomaterial was derived by describing biomaterials as "any substance or combination of substances, other than drugs, synthetic or natural in origin, which can be used for any period, which augments or replaces partially or totally, any tissue, organ or function of the body, to maintain or improve the quality of life of the individual" (Bianchera, A., *et al.* 2020). Usually, three different groups of biomaterials such as ceramics, metals or metal composites, synthetic polymers, and natural polymers are used in the fabrication of scaffolds for tissue engineering (O'Brien 2011; Catledge *et al.* 2004).

A central dilemma of tissue engineering is the question of how various biomaterials influence cell behavior since these scaffolding materials carry complex information, which is intrinsically coded in their physical, chemical and topographical properties (Place *et al.* 2009). Metals, for instance, have shown to be an excellent choice for bone or dental implants due to their superior mechanical properties (Ma 2008; Catledge *et al.* 2004). The lack of degradability in a biological environment, however, is the major disadvantage of metals for scaffold applications (Ma 2008; Liu and Ma 2004).

Other inorganic/ceramic materials, e.g. hydroxyapatite (HAP) or calcium phosphates, have shown to have a good osteoconductivity and were studied for mineralized tissue engineering (Ma 2008). Yet, they are also limited due to poor processability into highly porous structures and the brittleness (Ma 2008). In contrast, polymers offer freedom in designing because the composition and structure can be tailored and thus they have been studied in different tissue engineering applications, like for example vascular replacement (Ma 2008; Rice *et al.* 2005; Liu and Ma 2004; Meinel *et al.* 2005; Huang *et al.* 2007).

Natural biomaterials, which are for instance derived from animal sources, often offer an intrinsic variety of water affinity, biocompatibility, and biological activity and can mimic natural supporting structures of the body, like the connective tissue and the extracellular matrix (Bianchera, A., *et al.* 2020). An advantage of natural biopolymers, especially if not cross-linked, is that they are generally well tolerated by the target organism (Bianchera, A., *et al.* 2020). The downside of natural polymers, however, is the difficult control of the

degradation process, which often leads to stability problems for these scaffolds under *in vivo* conditions (Bianchera, A., *et al.* 2020; Fishman *et al.* 2015).

The general strategy of tissue engineering is to develop a scaffold, a structural device that defines the geometry of the replacement tissue and provides environmental cues that promote tissue regeneration (Place *et al.* 2009). For tissue engineering approaches, to control tissue formation in three dimensions (3D), highly porous scaffolds are critical for successful cell seeding and mimicking the three dimensional ECM (O'Brien 2011; Ma 2008). The scaffolds not only define the 3D geometry but also provide the microenvironment for regenerative cells and function as synthetic temporary extracellular matrix (Ma 2008). They support cell attachment, differentiation, proliferation, and new tissue formation (Ma 2008, 2004; Liu and Ma 2004). Thus, the chemical composition and the physical structure including topographical and mechanical features are important attributes to biomaterials for tissue engineering (Ma 2008). These scaffolds act as templates for tissue formation and are usually seeded with cells and sometimes growth factors are embedded as well (O'Brien 2011). These scaffolds are used in two different ways. Either they are pre-seeded with cells and cultured *in vitro* to synthesize artificial tissues, which then are implanted into an injured site. Or they are implanted directly into the injured site, using the body's surrounding cells to induce regeneration of tissues or organs *in vivo* (O'Brien 2011). For scaffolds to serve as a temporary extracellular matrix for regenerative cell growth, it would be beneficial to mimic the three distinctive features of the natural extracellular matrix (Ma 2008). Cell behavior is modulated by the biochemical, topographical, and mechanical signals in the extracellular environment. The ECM constitutes of protein nanofibers and polysaccharides (Lukashev 1998). Collagen represents the most abundant protein in the ECM (Kadler *et al.* 2007). Therefore, the design of future biomaterials requires the engineering of new tools and substrate designs to comprehend how filopodia probe complex 3D environments and how cell motility is regulated in 3D matrices.

To further improve biomaterials for various tissue engineering applications, a better understanding of cell-cell and cell-material interaction is needed. Understanding this could improve current approaches to control cell behavior with biomaterials. To understand the individual role of the different aspects in cell-material interaction scaffold designs mimicking selected aspects of the native tissue environment is required.

1. Introduction

To study the environmental influences of materials on cell behavior a basic understanding of cell and extracellular matrix interaction is needed. In the present study, a systematic study of cellular interaction with protein nanofibers was conducted. As a model system, NIH 3T3 fibroblasts were used. Fibroblasts are the key cells of connective tissues (desJardins-Park *et al.* 2018) and deposit the protein network which embeds and provides a matrix for other cell types, the extracellular matrix (ECM) (Murray *et al.* 2009). In this chapter, a general introduction of the function and role of the extracellular matrix will be given. Moreover, fibroblasts and their characters will be introduced and cellular functions such as migration and actin expression will be presented. An overview of the state of the art of approaches to mimic the ECM will be given and the cellular interaction with synthetic ECM model systems will be presented. Lastly, the aim of this work will be defined together with a working hypothesis.

1.1 The extracellular matrix

All eukaryotic cells are embedded and make close contact with a three-dimensional nanofibrous environment called the extracellular matrix. The ECM is the non-cellular component in all tissues and organs, mainly composed of proteins and polysaccharides (Frantz *et al.* 2010; Theocharis *et al.* 2016). Cells are either in contact with these components continuously or at important phases of their lives, for example, as stem or progenitor cells or during cell migration and invasion (Hynes 2009). Structural and metabolic alterations of ECM can lead to the development or progression of diseases, therefore ECM molecules can serve as important targets for pharmacotherapy. The wide range of diseases caused by alterations in the ECM through genetic abnormalities illustrates the importance of the ECM (Järveläinen *et al.* 2009; Frantz *et al.* 2010). Recently, the focus of cancer research has also shifted towards the importance of ECM in tumorigenesis (Theocharis *et al.* 2016).

Biophysical properties and the ability to convey specific signals to cells encountering or navigating through it, both are determined by the different structural forms and biochemical compositions of the ECM (Hallmann *et al.* 2015). The ECM mediates cell growth by three different aspects such as topographical cues, biochemical and mechanical cues (Vogel 2018). The complex three-dimensional network is composed of macromolecular protein nanofibers as well as non-fibrous proteoglycans. Depending on the respective tissue, the ECM does not only vary in composition, but also physical

parameters such as elasticity and topography (Trappmann *et al.* 2012). Typical fiber diameters found in the ECM vary from 50 to 500 nm (Ma and Zhang 1999). Topographical, biochemical, and biomechanical, protective, and organizational properties of the ECM in a given tissue can vary immensely from one tissue to another (normal vs cancerous) (Frantz *et al.* 2010). The biochemical and mechanical properties of each organ, such as tensile and comprehensive strength and elasticity, are generated through the topographical and biochemical characteristics of the ECM. Moreover, it mediates protection by maintaining extracellular homeostasis and water retention (Frantz *et al.* 2010).

Essentially, the ECM is composed of water, proteins like collagens, trace cell engaging proteins like fibronectin, elastin, laminins, proteoglycans/glycosaminoglycans (GAGs) and polysaccharides and growth factors (see Fig. 1) (Theocharis *et al.* 2016; Aamodt and Grainger 2016). Polysaccharides that provide ECM structure are glycosaminoglycans and proteoglycans, which form a hydrated gel-like substance, which resists compressive forces and allows rapid diffusion. Fibrous proteins like collagens give strength and resilience to the matrix (Erler and Weaver 2009). In the ECM the fiber-forming proteins collagens and elastins serve as primary structural elements (Aamodt and Grainger 2016; Järveläinen *et al.* 2009). Collagen is the most abundant protein in the body (Kadler *et al.* 2007). Collagens provide strength and have space-filling functions (Hynes and Naba 2012) and are mainly synthesized and secreted by fibroblasts (Theocharis *et al.* 2016). Elastin fibers, provide recoil to tissues undergoing repeating stretching forces, such as among other blood vessels, lung as well as the heart (Theocharis *et al.* 2016).

Glycoproteins allow ECM assembly, promote cell adhesion, and also signaling into cells and other domains that bind growth factors (Hynes and Naba 2012). The bound growth factors can be released or be presented as solid-phase ligands by the ECM proteins (Hynes 2009). One of the best-studied glycoproteins are the fibronectins (Hynes and Naba 2012). Fibronectin interacts with various ECM components to connect the cell to the ECM (Mouw *et al.* 2014). Fibronectin also forms a fibrillar network (Schwarzbauer and DeSimone 2011). Due to its various binding sites for other ECM proteins fibronectin has been implicated in several functions, including binding sites to collagen, fibrin, and a role in collagen type 1 assembly (Walker *et al.* 2018).

Proteoglycans are amongst the most important structural and functional macromolecules in tissues (Theocharis *et al.* 2016). They interact with growth factors, cytokines and chemokines, cell surface receptors, and ECM molecules (Theocharis *et al.* 2010).

Proteoglycans are involved in cell signaling, proliferation, migration, differentiation, and adhesion (Theocharis *et al.* 2010; Iozzo and Sanderson 2011; Iozzo and Schaefer 2015). Moreover, proteoglycans like for instance hyaluronic acid provide maintenance of viscoelastic properties of liquid connective tissues, control of tissue hydration and water storage, and transport in tissues (Iozzo and Schaefer 2015).

During tissue formation and repair the ECM undergoes constant remodeling. The main group of enzymes responsible for the degradation of collagen and other ECM proteins is matrix metalloproteinases (MMPs). The MMP family constitutes of six groups: collagenases, gelatinases, stromelysins, matrilysins, membrane-type MMPs, and other not classified MMPs (Jabłońska-Trypuć *et al.* 2016).

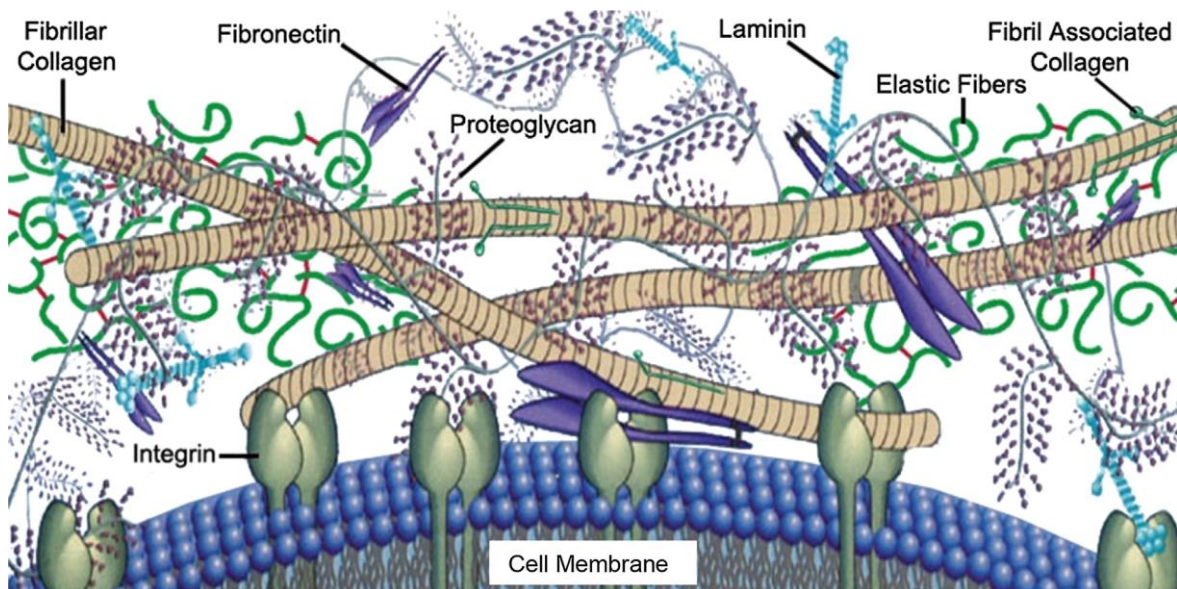


Figure 1. Schematic overview of the extracellular matrix (Aamodt and Grainger 2016). ECM Composition and Architecture ECM-specific components include collagens, elastins, trace cell-engaging proteins (fibronectin, vitronectin, osteopontin, glycosaminoglycans (GAGs), and growth factors. The ECM is anchored via integrins in the lipid membrane and the integrins build the linkage to the cytoskeleton.

The ECM initiates crucial topographical, biochemical, and biomechanical cues required for tissue morphogenesis, differentiation, and homeostasis (Frantz *et al.* 2010). Proteins and other components of the ECM have a large impact on the differentiation, determination, survival, proliferation, polarity, and migration of cells. Besides soluble signals, ECM signals are probably at least as important in governing these processes (Hynes 2009;

Hallmann *et al.* 2015; Theocharis *et al.* 2016). The ECM provides structural support for organs and tissues, for cell layers in the form of basement membranes and individual cells as substrates for migration (Hynes 2009). The ECM directs essential morphological organization by binding growth factors (GFs) and interacting with cell-surface receptors to elicit signal transduction and regulate gene transcription (Frantz *et al.* 2010).

Traditionally, the influence of tension and mechanical strength constituted by the ECM on cell migration have been investigated independently of individual ECM molecules and therefore the biochemical component was often not included in previous studies (Hallmann *et al.* 2015). Furthermore, the role of the ECM in cell adhesion and signaling to cells through adhesion receptors, such as integrins, has received major attention in the last decades (Hynes 2002; Berrier and Yamada 2007; Legate *et al.* 2009). Mechanical characteristics of the ECM, such as stiffness and deformability, have also been documented to contribute to cell behavior (Discher *et al.* 2009; Geiger *et al.* 2009; Hynes 2009). The mechanical characteristics of the ECM have a direct impact on the mechanical properties of cells. Cells bind to the ECM via transmembrane integrins and sense the mechanics of the ECM (Galbraith *et al.* 2007). Integrins are bound to the actin filaments in the cytoskeleton (Galbraith *et al.* 2007). Thereby, the ECM and cell are in constant crosstalk and the ECM has a direct influence on the actin formation inside the cell.

The actin cytoskeleton is composed of double-helical filaments (F-actin), which are assembled of globular actin (G-actin). To fulfill the diverse actin functions, the generation and disassembly of F-actin is a very dynamic process. Due to the relative instability of the actin dimer or trimer, spontaneous polymerization of G-actin into filaments is prevented (Rottner *et al.* 2017). The actin skeleton is involved in different cell functions, such as proliferation, adhesion, and migration (Rottner *et al.* 2017). The integrin-mediated cell adhesion depends on the nanotopography of the ECM. Hence, a diversity of cellular processes is influenced through changes in the actin cytoskeleton and cell shape, which are significantly influenced by the ECM (Trappmann *et al.* 2012; Storm *et al.* 2005).

The ECM is constantly in a highly dynamic state and undergoes remodeling by different matrix-degrading enzymes under normal conditions or during inflammation, wound repair, and tumor invasion (Theocharis *et al.* 2016). Cells embedded in connective tissue, especially fibroblasts, synthesize structural proteins like MMPs and urokinase-type plasminogen activators (uPAs), which are key enzymes that remodel the ECM. The basement membrane is a thin ECM found in the connective tissue of mammals, which separates the lining of the internal or external body surface. Components of the basement

membrane, as well as proteins and proteoglycans of connective tissue, are degraded by these enzymes. Moreover, they liberate latent growth factors from their storage sites in the ECM (Kierszenbaum and Tres 2012). Factors, that are activated in this manner, are for example fibroblast growth factors (FGFs), transforming growth factors (TGF β s), and hepatocyte growth factor (HGF) (Walker *et al.* 2018).

1.1.1 Collagen

Collagen is the most abundant protein within the ECM (Halper and Kjaer 2014; Theocharis *et al.* 2016; Walker *et al.* 2018). Fibroblasts synthesize and secrete collagen in the ECM where it constitutes up to 30% of the total proteins in mammals. Twenty-eight different collagens build the collagen superfamily, together with a large group of collagen-like proteins, such as acetylcholinesterase, adiponectin, macrophage receptor, and surfactant protein (Kadler *et al.* 2007).

The archetypal collagen, collagen type 1, is widespread and abundantly expressed among tissues such as bone, tendon, and dermis (Theocharis *et al.* 2016; Heino 2007). Collagen type 1 plays a major role in processes such as wound repair and organ development (Walker *et al.* 2018). Different studies have shown that, besides its function as the key tensile element of tissues, collagen scaffolds offer signals to cells affecting various cellular functions such as cell adhesion, migration, tissue development and repair (Frantz *et al.* 2010; Kadler *et al.* 2007; Theocharis *et al.* 2016).

As collagen type 1 (see Fig. 2) is the most abundant of all collagens, it was chosen as a model system in this thesis to develop protein scaffolds with nanofibrous and smooth topography to study the topography-dependent interaction with fibroblasts.

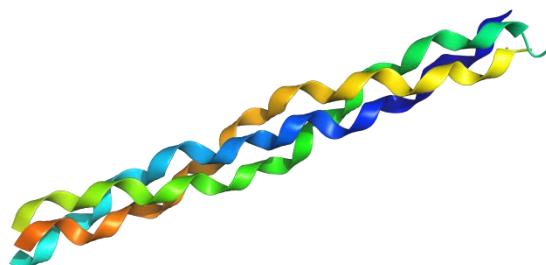


Figure 2. Schematic of a collagen triple helix. (Bella *et al.* 1994)

Collagen type 1 has a predominant structural role in many tissues and is composed of a triple helix, assembling into fibrils (see Fig. 2) (Kadler *et al.* 2007). In the endoplasmic reticulum, collagen undergoes extensive posttranslational modification before triple helix formation through glycosylation, hydroxylation, and formation of disulfide bridges (Myllyharju and Kivirikko 2004; Theocharis *et al.* 2016). Lysine and proline are hydroxylated and the molecule is glycosylated to initiate the formation of the triple helical structure (Myllyharju and Kivirikko 2004). *In vivo*, collagen typically assembles into fibrils with a 67 nm D-periodic spacing (see Fig. 3) (Kadler *et al.* 1996). Depending on the stage of development and tissue, the nanofibers are indeterminate in length while diameters range from 12 nm to >500 nm (Kadler *et al.* 2007; Huxley-Jones *et al.* 2007).

Collagen type 1 is heterotrimeric and contains two identical α chains and a third chain that differs, $[\alpha 1(I)]_2 \alpha 2(I)$ (Kadler *et al.* 2007). Three α chains display a polyproline II-type helical conformation and coil with each other with a one-residue stagger forming finally a right-handed triple helix (Shoulders and Raines 2009). In each α chain, a repeating Gly-X-Y triplet is found where X and Y positions are regularly occupied by proline and 4-hydroxyproline, respectively.

Due to the high content of proline, 4-hydroxyproline, and glycine without any formation of intrachain hydrogen bonds, α chains tend to form left-handed helices spontaneously. Lastly, α chains are held together by interchain hydrogen bonds (Shoulders and Raines 2009).

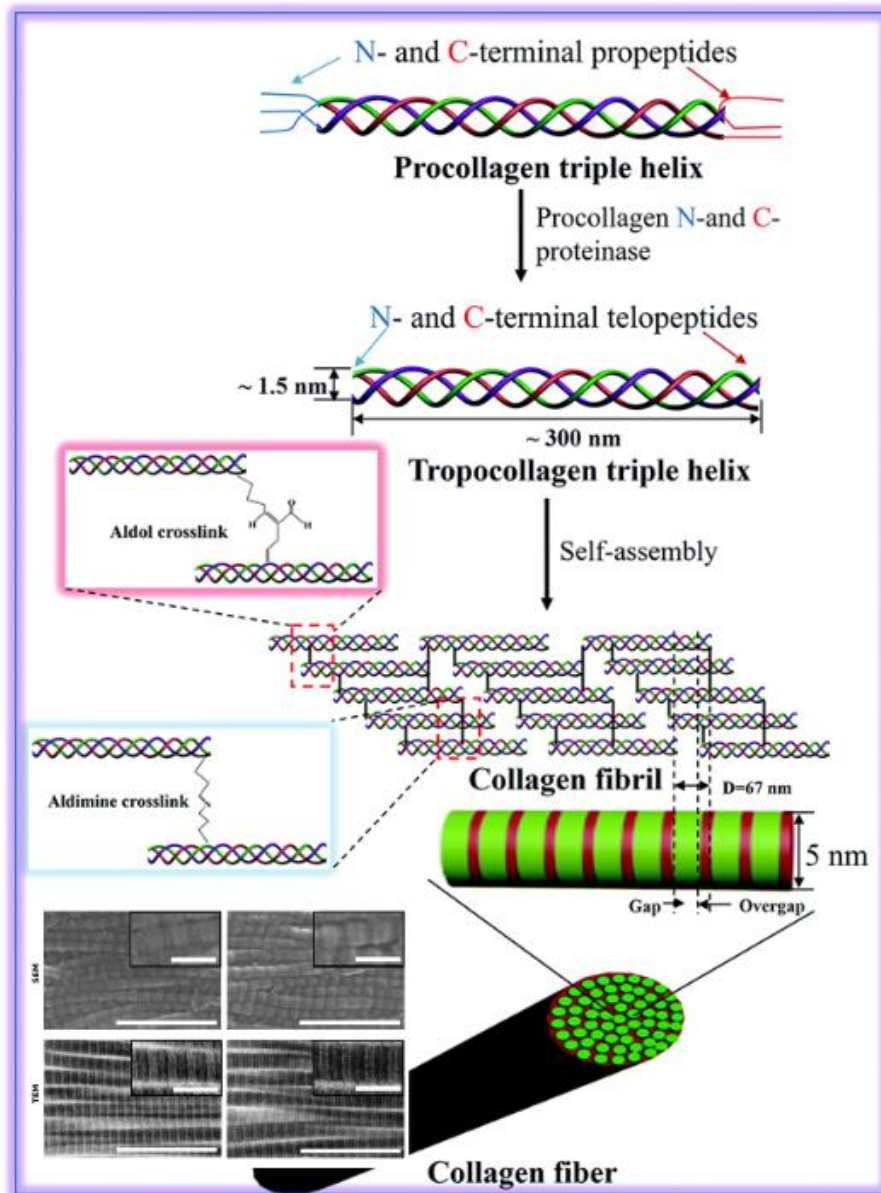


Figure 3. Schematic view of some of the hierarchical features of collagen(Zhu *et al.* 2018). The procollagen triple helix assembles to tropocollagen triple helix after cleavage of N- and C- terminal propeptides. Tropocollagens have an estimated diameter of 1.5 nm. Tropocollagens then assemble to collagen fibrils with a diameter of 5 nm via aldol cross-links creating a characteristic D-spacing ($D=67$ nm). These collagen fibrils further assemble to collagen fibers via aldimine cross-links. Length of D-periods in collagen fibrils from discoidin domain receptor 1 (DDR1) knock-out (KO) mice examined by scanning electron microscopy (SEM), and transmission electron microscopy (TEM). Representative SEM and TEM images of adventitial collagen fibrils from DDR1 KO and wild-type (WT) aortas are displayed. Higher magnification images are shown as insets. Scale bar is 225nm (inset scale bars are 100 nm). (Tonniges *et al.* 2016)

In every third residue within the α chains, there are small hydrogen atom side chains of glycine allowing tight packing of α chains in a triple helix with this residue in the interior of

the helix and the rings of the proline and 4-hydroxyproline pointing outward (Shoulders and Raines 2009). Moreover, collagens have non-collagenous (NC) non-triple helical domains at both C and N-termini that are numbered from the C-terminus (NC1, NC2, NC3, etc) (Kadler *et al.* 2007; Theocharis *et al.* 2016).

Fibril-forming collagen type 1 is synthesized as procollagen containing N- and C-propeptides at each end of the triple-helical domain. For fibrillogenesis, the cleavage of the C propeptides is required. The C-propeptides are cleaved off by procollagen C-proteinases, which are identical to the BMP-1/tolloid proteinases (Greenspan 2005; Kadler *et al.* 2007). Telopeptide sequences, that are short non-triple helical extensions of the polypeptide chains, are exposed by the cleavage of the propeptides. The fibrillar collagens are stabilized by non-reducible covalent crosslinks that evolve residues in the triple helix and telopeptides (Eyre *et al.*, 1984). The crosslinks are crucial for the mechanical properties of collagen-containing tissues. Tropocollagen (TC) triple helices have diameters of 1.5 nm and approximately 300 nm in length (see Fig. 3). They undergo self-assembly and are packaged to form collagen fibrils with diameters of 5 nm and up to several μm in length, which assemble into larger fibers (see Fig. 3) (Shoulders and Raines 2009; Theocharis *et al.* 2016)

The procollagen is then brought to the Golgi apparatus where it is prepared for cellular export. Processing of the procollagen occurs either during or after secretion in the ECM (Birk *et al.* 1989; Canty *et al.* 2004; Kalson *et al.* 2013; Starborg *et al.* 2013; Walker *et al.* 2018). The overall enhanced mechanical properties are achieved by the supramolecular assembly of collagen, which is further stabilized by lysyl oxidase (LOX). The tensile strength of collagen is largely based on the N-terminal and C-terminal ends of individual collagen molecules being covalently cross-linked by LOX both inter- and intrafibrillar (Molnar *et al.* 2003; Fratzl and Misof, Klaus and Zizak, Ivo 1998, 1998; Walker *et al.* 2018). LOX and LOX-like enzymes increase collagen crosslinking and promote signaling through collagen-binding cell surface receptors, such as integrins (Theocharis *et al.* 2016; Bonnans *et al.* 2014).

In vivo, degradation of collagen and gelatin (unfolded or denatured collagen) can be mediated by MMPs, cysteine proteinases (e.g. cathepsins B, K, and L), and serine proteinases (e.g. plasmin and plasminogen activator) (Kadler *et al.* 2007). According to Kadler *et al.* the C-terminal propeptide is cleaved off by specific matrix metalloproteinases (MMPs) and if it is not removed, it leads to high solubility of collagen that prevents it from forming fibrils (Kadler *et al.* 1996). Moreover, collagen plays a crucial role for cell adhesion

with its α A-domain containing important binding sites for the different integrins like β_1 integrins $\alpha_{10}\beta_1$, $\alpha_2\beta_1$, $\alpha_1\beta_1$, $\alpha_{II}\beta_1$ (Humphries *et al.* 2006). For *in vitro* fibrillogenesis and biomedical applications it is crucial to be aware of the degradability of collagen substrates (Davison *et al.* 2015). The collagen triple helix is resistant to proteolytic cleavage by pepsin, trypsin, and papain. *Clostridium histolyticum* produces collagenases that cleave triple helices at numerous sites. The capability of collagens to resist cleavage by pepsin and trypsin, and their sensitivity to cleavage by bacterial collagenase, are used as research tools to identify and characterize collagens (Kadler *et al.* 2007).

1.1.2 Fibrinogen

Fibrinogen is a glycoprotein that plays a significant role in wound healing (Mosesson 2005). It is found in the blood plasma in a concentration of 2 – 4 mg ml⁻¹ (Tennent *et al.* 2007). In wound healing, fibrinogen plays a key role in the coagulation cascade. It is involved in cell-cell adhesion as well as in cell-matrix-interaction (Laurens *et al.* 2006). In particular, fibrinogen plays a crucial role in cell adhesion of fibroblasts and endothelial cells with its two RGD binding sites for the blood platelet integrin $\alpha_{IIb}\beta_{III}$ and $\alpha_V\beta_{III}$ and the LDV-binding integrins $\alpha_M\beta_{II}$ and $\alpha_X\beta_{II}$ (Humphries *et al.* 2006). Additionally, fibrinogen has a high binding affinity for vascular endothelial growth factor and fibroblast growth factor (Sahni *et al.* 1998; Sahni and Francis 2000). Fibrinogen is of special importance due to its manifold biological functions such as in the field of tissue engineering (Gugutkov *et al.* 2013).

Fibrinogen is a dimer composed of two identical subunits with a length of 47.5 nm and a molecular weight of 340 kDa (Doolittle 1984). The subunits consist of three different polypeptide chains: A α , B β , and γ . Disulfide bridges connect the amino ends of those polypeptide chains and build the E-domain of the fibrinogen molecule (Mosesson 2005). The carboxyl ends of the polypeptide chains each represent an own domain. The carboxyl ends of the B β - and γ - chains are found in the D-domain in two separate smaller domains. The A α -chains are longer, and their carboxyl ends build the globular α C-domain near the E-region. The D-regions are connected with the E-region by coiled-coil structures consisting of three α -helices (Cacciafesta *et al.* 2000; Zhang *et al.* 2017). Additionally, A and B (knobs) binding sites can be found near the E-domain. The fibrinopeptides A and B (FpA and FpB) are bound to them. The complementary binding sites a and b (holes) are located at the D-domain of adjacent fibrinogen molecules (see Fig. 4).

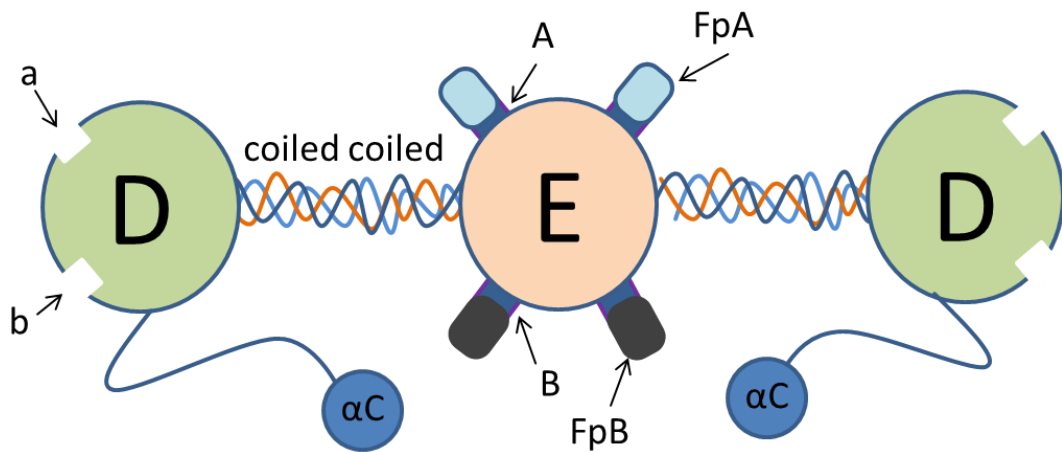


Figure 4. Schematic overview of fibrinogen molecule. Two outer D-domains (D) are connected with a central E-domain (E) with coiled-coil structures. Attached to the E-domain are the fibrinopeptides FpA (light blue) and FpB (dark blue) connected with A and B binding sites. Complementary to the binding site (A) and (B), each D-domain has pocket-like binding sites (a) and (b).

During hemostasis, the dissolved fibrinogen is transformed into insoluble fibrin by enzymatic cleavage with thrombin. Fibrin then forms stable nanofibers which function as a preliminary matrix in tissue regeneration while wound healing (Laurens *et al.* 2006). The cleavage of the FpA and FpB by thrombin and the transformation of fibrinogen to a fibrin monomer is the first step in fibrin fibrillogenesis. By cleaving FpA and FpB the binding sites A and B of the E-domain are presented. In a second step, the fibrin monomers polymerize into protofibrils (Doolittle 1984). The neighboring monomers bind via non-covalent bindings in a knob-hole-interaction binding the complementary binding sites A and a. In the last step fibrin nanofibers are formed by binding of several protofibrils at the C-domains (see Fig. 5). Finally, fibrin is assembled into a nanofibrous network to form a provisional ECM where thrombocytes aggregate (Blanco and Blanco 2017). In the resultant blood clot with fiber diameters of approximately 100 to 130 nm, which enables wound closure (Li *et al.* 2016; Siebenlist *et al.* 2005). Fibroblasts can migrate along with this temporary matrix and start replacing fibrinogen and fibrin with ECM fibers, mainly fibronectin, and collagen. They bind to fibrin and get stimulated to produce collagen, glycosaminoglycans, and proteoglycans (Laurens *et al.* 2006).

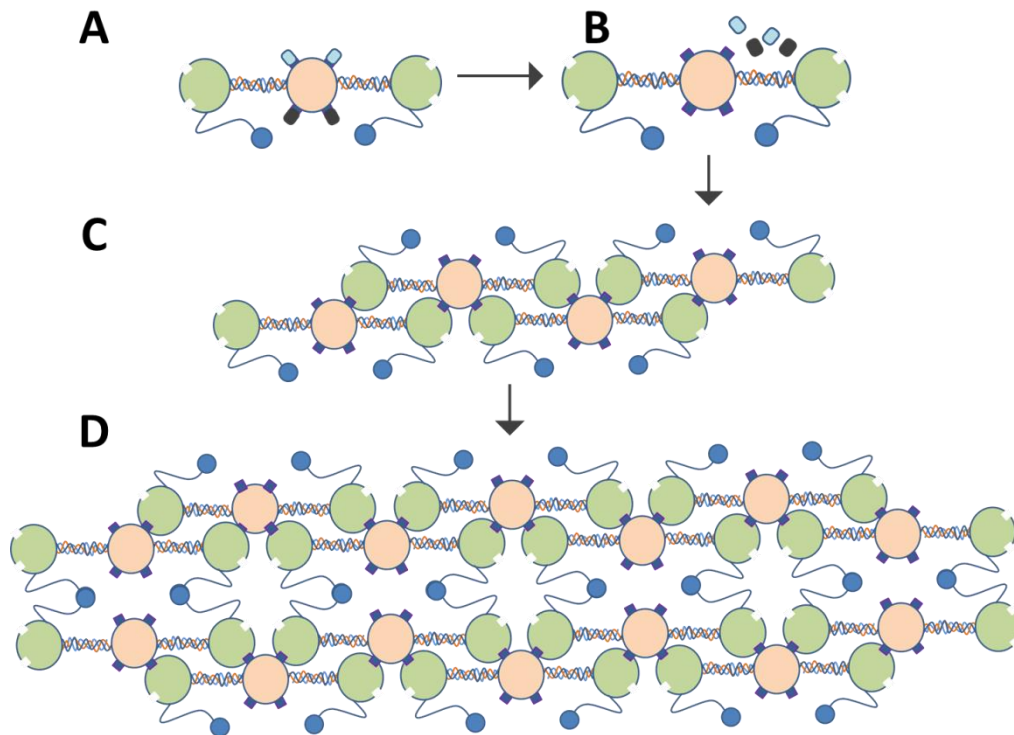


Figure 5. Fibrinogen fibrillogenesis *in vivo*. When fibrinogen polymerizes to fibrin fibrinogen molecules (A) are transformed. The fibrino-peptides FpA and FpB are cleaved off (B) exposing the binding sites A and B. The binding sites A and B of the E-domain fit the binding sites at the D-domains a and b and several molecules can polymerize to fibrin fibers (D).

1.2 Fibroblasts and cell migration

The connective tissue is composed of a variety of different cell types. Bone cells, cartilage cells, fat cells, and fibroblasts represent the family of connective tissue cells (Alberts *et al.* 2002). These cells secrete collagenous ECM and provide mechanical strength to the tissue, which is based on the supporting nanofibrous structure to the ECM itself (Alberts *et al.* 2002). In repair mechanisms, connective tissue cells play a key role. Fibroblasts are a major key player in wound healing and tissue repair and are, for instance, involved in the inflammatory response and immune-mediated diseases (Darby *et al.* 2014). (Murray *et al.* 2009)

Fibroblasts are typically found in the interstitial space of organs and are spindle-shaped cells with an oval flat nucleus (Murray *et al.* 2009). Fibroblasts are the main source for ECM protein expression, which provides a scaffold for cells and plays a major role in the determination of cell phenotype and function (Murray *et al.* 2009). Fibroblasts are

metabolically active cells. They synthesize, secrete and degrade ECM components like, collagens, laminin, proteoglycans, and fibronectin (MacKenna 2000). Additionally, they produce MMPs and their inhibitors and thereby control matrix turnover rates and the overall tissue architecture (Distler *et al.* 2005). Thus, fibroblasts are involved in injury responses as well in the initiation and the resolution phases. Furthermore, they play a vital role in normal tissue function. Fibroblast proliferation, migration, differentiation, and collagen synthesis are promoted by numerous mediators produced by different cell types and proteases of the blood coagulation cascade. (Murray *et al.* 2009)

The earliest reaction in wound healing is the formation of a fibrin clot consisting of a network of insoluble fibrin fibers. The fibrin clot functions as a provisional matrix, to which growth factors bind and which promotes cell migration into the wound, where fibroblasts start depositing ECM (Shaw and Martin 2009). During wound healing and subsequent tissue regeneration, endothelial cells, thrombocytes, fibroblasts, and macrophages migrate through tissues and the ECM. Migration of fibroblasts, for example, is a crucial step in wound healing (Velnar *et al.* 2009).

Filopodia play a key role in cell-substrate recognition and contact guidance and have typical diameters of 60 to 200 nm (Bettinger *et al.* 2009; Biggs *et al.* 2010; Albuschies and Vogel 2013). They are responsible for cell sensing, forming of focal adhesions (Jacquemet *et al.* 2015), and sensing nanostructures down to a height of 8 nm (Dalby *et al.* 2004). Thus, nanotopographic patterns are of major importance for studying the adhesion and differentiation of different cell types (Biggs *et al.* 2010; McNamara *et al.* 2010; Dalby *et al.* 2014; Kim *et al.* 2012). Dalby and co-workers showed that fibroblasts grown on polystyrene with islands of 95 nm height reduced cell spreading and the formation of confluent cell layers. They postulated that these effects were caused by the material that mediates changes in fibroblast morphology after 24 h of culture (Dalby *et al.* 2003).

The process of cell migration or locomotion can be divided into four steps: protrusion, attachment, translocation, and release (see Fig. 6). In the first step, the protrusion, cells extend actin-rich projections outward from its current location. Cells can express different types of projections (Alberts *et al.* 2002). The two most important are lamellipodia and filopodia. Lamellipodia are flat, broad, veil-like extensions containing highly branched actin networks at the leading edge of the moving cell. Filopodia are finger-like extensions containing cross-linked actin bundles. In the first step of the migration, cells use filopodia and lamellipodia to explore their environment and determine the direction of their motion.

The environmental sensing is one of the main functions of filopodia (Schäfer *et al.* 2011). The chemical composition and mechanical properties of the ECM are sensed by integrin-associated complexes called focal adhesions (FAs). In this regard, transmembrane proteins, such as integrins, cadherins, and other receptors are essential in cell-cell and cell-matrix interactions. Additionally, they are involved in the cross-talk of external and internal guiding cues (Millard and Martin 2008; Bentley and Toroian-Raymond 1986; Dent and Gertler 2003; Partridge and Marcantonio 2006). In filopodia, receptors for a variety of signaling molecules and ECM molecules are found (Mattila and Lappalainen 2008). This correlates with the role of filopodia in sensing the extracellular environment and acting as sites for signal transduction (Mattila and Lappalainen 2008). The cell adhesion molecules, integrins and cadherins, are often found in the tips of filopodia (Galbraith *et al.* 2007; Partridge and Marcantonio 2006; Steketee and Tosney 2002; Vasioukhin *et al.* 2000). The integrins in filopodia are essential to probe the matrix, creating “sticky fingers” along the leading edge that promotes cell adhesion and migration (Galbraith *et al.* 2007; Mattila and Lappalainen 2008). With that mechanism, cells can sense the density and distribution of ECM molecules by means of individual integrin proteins and integrin-containing focal adhesions complexes within the cells (Oria *et al.* 2017). Mechanosensitive ion-channels, for example, detect changes in plasma membrane tension (Anishkin *et al.* 2014; Arnadóttir and Chalfie 2010; Leckband and Rooij 2014).

In the second step, the attachment, these cellular extensions form stable adhesions with the surface, which can then be used as anchorage for the following motion of the cell. Generally, adhesions are stable; still, they are often removed after the third step, the translocation. In the third step, cells move in the direction of the attachment built afore. As this process involves a large degree of movement it necessitates substantial actin-myosin contractile activity. The fourth step, release or detachment, describes the detachment of the trailing end of the cell. This step also includes the withdrawal of adhesions formed during attachment. If the cell motion is faster than the release of the focal adhesion, parts of the cell can be pulled off and left behind. It is important to note that cells can undergo more than one of the four steps at any given time (Jacobs *et al.* 2013). In the ECM, cells can migrate through LOX-crosslinked collagen fiber networks by proteolytic and non-proteolytic mechanisms (Bonnans *et al.* 2014; Wolf and Friedl 2011). Membrane anchored MMPs are the major components in cell migration regulation through the ECM (Quaranta 2000). Most of the MMPs are secreted proteins by for example fibroblasts (Tandara and Mustoe 2011). Generally, they require activation for enzymatic activity. Some of the MMPs

show collagenolytic activity and can degrade the matrix, creating openings, through which individual cells can migrate (Quaranta 2000).

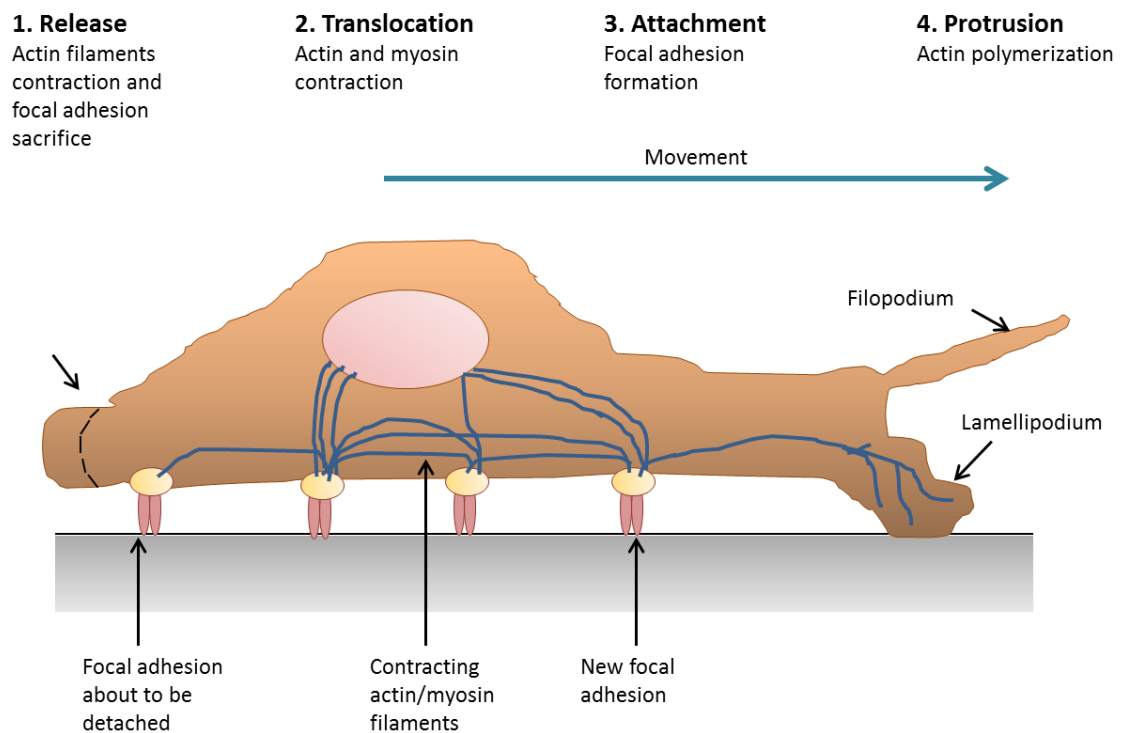


Figure 6. Cell migration steps. Schematic overview of the four steps of cell migration. The cell in this figure is migrating towards the right. In the first step, the cell releases focal adhesions. In step 2, the translocation, actin, and myosin produce contractile forces to induce movement. In step 3 new focal adhesions are expressed. In step 4 actin is polymerized and the cells explore their environment. These four steps are not static, and single cells are undergoing several steps simultaneously (modified from (Jacobs *et al.* 2013)).

Stress fibers are bundles of approximately 10-30 actin filaments. The stress fibers in fibroblasts can be classified into three types based on their subcellular location: ventral stress fibers, dorsal stress fibers and transverse arcs (see Fig. 7) (Small *et al.* 1998; Tojkander *et al.* 2012).

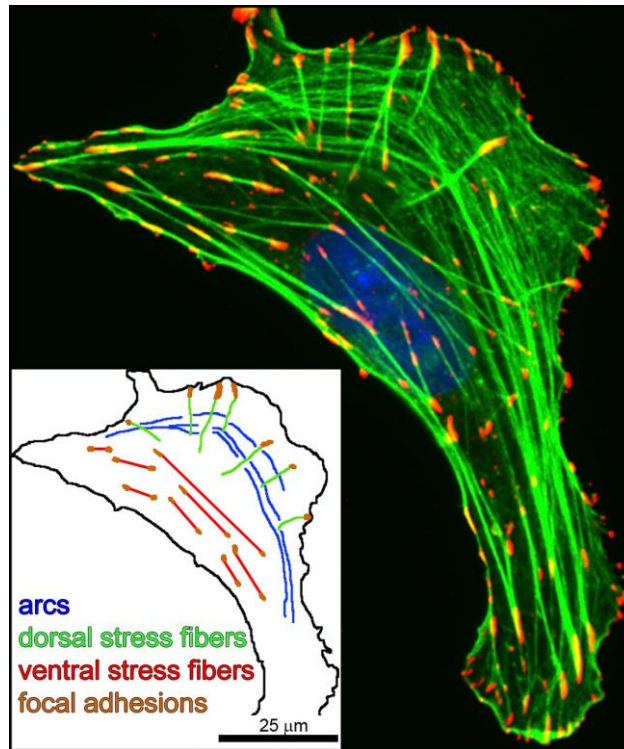


Figure 7. Three types of actin stress fibers. In the immunofluorescence image, anti-phosphotyrosine was used as a marker for focal adhesions (red), phalloidin was used for F-actin SFs (green), and the nucleus (blue) was detected by DAPI. The three main types of actin stress fibers are visible in the depicted cell: (transverse) arcs, dorsal SFs, and ventral SFs. (inset) Schematic drawing depicting the stress fiber subtypes. (taken from Burridge and Wittchen 2013).

The most commonly observed structures are ventral stress fibers. They lie along the base of the cell and are attached to integrin-rich focal adhesions. Dorsal stress fibers are tethered to the base of the cell and attached to a focal adhesion at one end only. The remaining structure reaches towards the dorsal surface and terminates in a loose matrix of actin filaments. Bundles of actin, that form beneath the dorsal surface of migrating cells behind the protrusive lamella, form the transverse arcs (Pellegrin and Mellor 2007). It has long been assumed that fibroblasts in normal connective tissue do not contain stress fibers (Ehrlich and Hembry 1984). However, it has later been reported that cells entering a wound environment experience tension, causing them to assemble stress fibers (Pellegrin and Mellor 2007). By culturing fibroblasts on rigid substrates, such as cell culture dishes, this effect can be mimicked *in vitro*, while the loss of substrate rigidity causes loss of stress fibers (Pellegrin and Mellor 2007).

It has also been shown that cells do respond to nanometric cues *in vitro* (Cerrai *et al.* 1999; Du *et al.* 1999; Curtis and Riehle 2001; Curtis and Wilkinson 2001). As mentioned above fibroblasts probe their environment with filopodia (Dalby *et al.* 2003). They detect suitable sites for adhesions and form focal adhesion and mature actin fibers (O'Connor *et al.* 1990). In respect to biomaterials, this particular behavior can be used for biomaterial development as a substrate can promote the formation of focal contacts and thereby influence the subsequent development of the cytoskeleton (Dalby *et al.* 2003). Integrins located in focal adhesion and actin filaments linked to integrins are in a constant cross-talk and are involved in signal transduction pathways (Burrige and Chrzanowska-Wodnicka 1996). These events can affect the long-term cell differentiation and migration and thus the formation of tissue (Juliano and Haskill 1993; Vuori 1998; Cary and Guan 1999).

It was hypothesized that stress fibers might provide contractile forces for migration. At the same time, other studies reported that stress fibers were more prominent in stationary cells (Pellegrin and Mellor 2007; Tojkander *et al.* 2012). Moreover, it was shown that various animal cell types display thick stress fibers on rigid and flat substrates, such as cell culture dishes or glass. However, when grown on soft substrates the same cells typically exhibited thin stress fibers or no stress fibers were detected (Tojkander *et al.* 2012). The lack of stress fibers in cells that were cultured in a three-dimensional environment (see Fig. 8) together with the aforementioned observations led to the conclusion that stress fibers are not vital for cell migration (Tojkander *et al.* 2012).

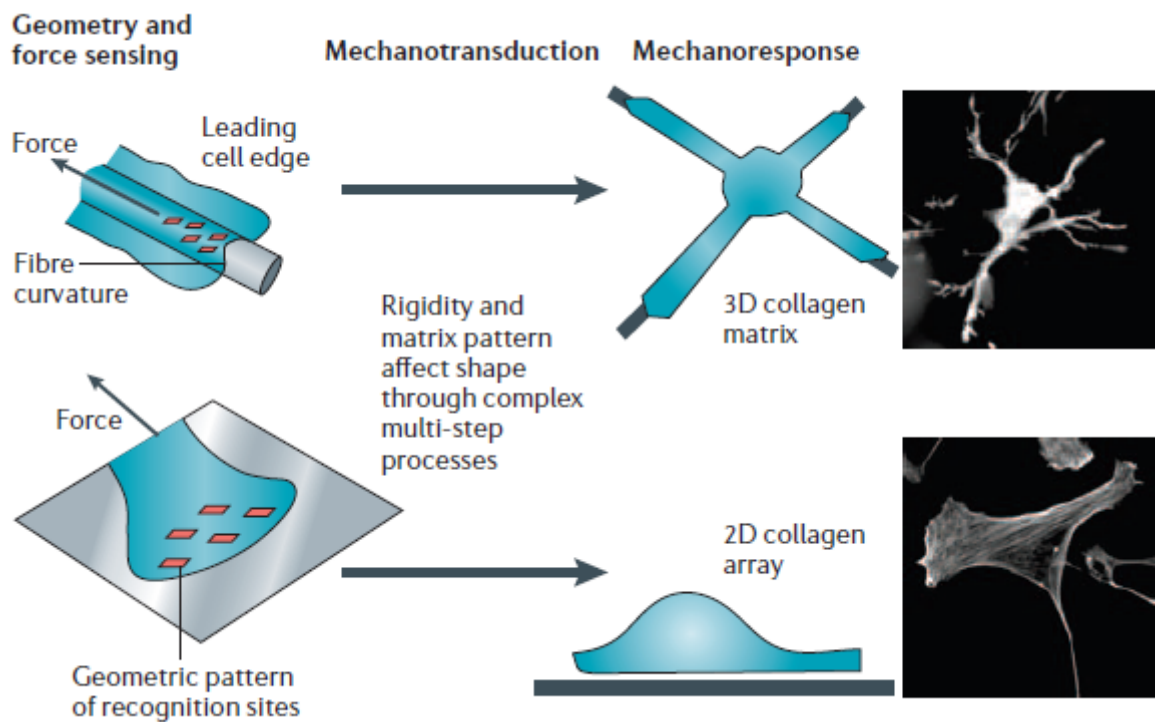


Figure 8. Cellular mechanics in three steps: mechanosensing, mechanotransduction, and mechanoresponse. As an example, the difference in morphology that the same cells will assume after only 4 h in different matrices is shown. Fibroblasts exhibited dendritic networks of extensions in 3D-collagen matrices but not on collagen-coated coverslips. Fibroblasts grown on a two-dimensional surface exhibited more distinct stress fibers as compared to cells grown on the 3-dimensional floating collagen matrix (taken from (Vogel and Sheetz 2006)).

Based on these findings, Castella and co-workers reported that the physiological significance of stress fibers in cell migration might consequently be linked to their role in contracting and deforming the substrate through the generation of tension (Castella *et al.* 2010). It was shown that fibroblasts grown on topographies with a height of 90 nm exhibited reduced cell spreading with diffuse actin and fewer stress fibers (Dalby *et al.* 2002d; Yang *et al.* 2017). Still, many aspects of stress fibers and their connection to focal adhesions remain unclear or are not in agreement with experimental results (Livne and Geiger 2016).

1.3 Cell-substrate interactions

Cells are in constant cross-talk with their environment. Not only do cells build ECM but the ECM also has an impact on the influence on cell growth. As aforementioned, the ECM regulates cellular processes like migration, differentiation, growth, survival, and morphogenesis (Theocharis *et al.* 2016). Variations in the composition and structure of the ECM affect the overall properties of the extracellular environment and thereby also induce signals that are transmitted to cells, hence modulating the cellular response (Lukashev 1998). The loss of ECM functions like mutations and modifications of ECM molecules are associated with various pathologies (Theocharis *et al.* 2016). A more profound understanding of the various biological activities and properties of ECM components will help to improve treatments for diseases. Therefore, understanding of each ECM characteristic, mainly the topographical features, biochemical and biomechanical cues, and its influence on cell growth is a key challenge. Understanding of the cross-talk between cells and their extracellular environment is important to control the interaction of cells with scaffold materials in tissue engineering (Ventre and Netti 2016). In this section it will first be described how cells sense and respond to substrates, secondly, it will be introduced how different biophysical cues affect cells (Yang *et al.* 2017).

Cell adhesion is controlled by topographical features at both nano- and microscale with nanotopographies leading to subcellular sensing mechanisms (Nguyen *et al.* 2016). At sites of cell-matrix and cell-cell contacts, several proteins form aggregates. The spacing of the extracellular ligands, to which the proteins bind, influences the size and shape of those aggregates. To form cell-adhesion sites, RGD peptide clusters are required, where the distance between the peptides is less than 73 nm (Arnold *et al.* 2004; Vogel and Sheetz 2006). Heterodimeric integrin receptors, containing one α - and one β -subunit (see Fig. 1), bind to the RGD peptide of ECM proteins with their extracellular domain and link to cytoskeletal adaptor proteins with their cytoplasmic tail, successively recruiting scaffolding proteins that connect the integrins to the actin cytoskeleton (Hynes 2002; Yang *et al.* 2017).

Throughout cell migration and cell spreading, cells frequently encounter new ligands. In a tissue, cells stabilize over time and become less dynamic. Yet, they undergo constant turnover of contact and cytoskeletal proteins on the timescale of minutes or less (see Fig. 9). (Zaidel-Bar *et al.* 2004; Machacek and Danuser 2006; Vogel and Sheetz 2006). Cellular contacts are continually renewed, whereby some contacts are also maintained for

days and possibly longer. By the frequent renewal of contacts, cells can constantly sample the rigidity of their environment. Giannone and co-workers reported that cells, while migration and spreading, generate periodic contractions of their lamellipodia on rigid substrates, but do not show this behavior on soft substrates (Giannone *et al.* 2004). Moreover, it has been shown that once cells come into contact with other cells, they lose their shape sensitivity to substrate rigidity (Yeung *et al.* 2005; Vogel and Sheetz 2006).

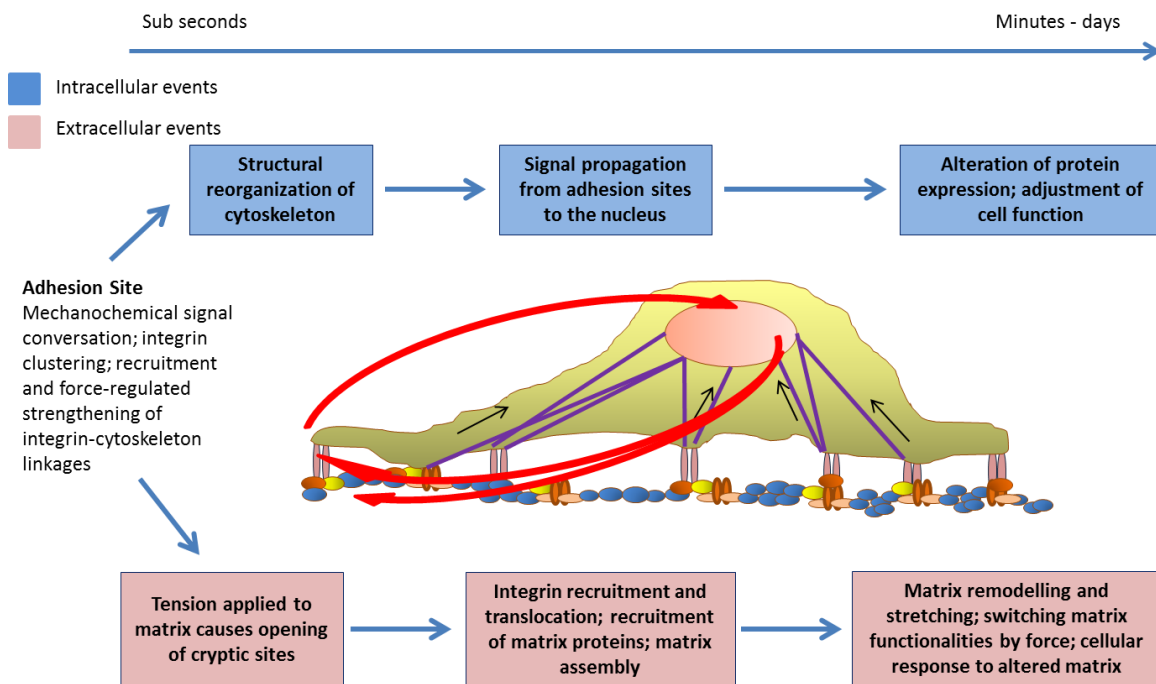


Figure 9. The cellular process of mechanosensing and responses. This schematic overview displays the steps in mechanosensing over time that involve periodic testing of the substrate, substrate modification, and changes in cellular protein content. Rapid motility and signaling responses are caused by cells sensing the mechanical features of their environment. Cells modify the ECM and create new signals, such as those originated from fibronectin unfolding. Expression patterns of cells are altered by intracellular signals. Over time, the cell shape will be changed by cellular forces, and cellularly generated matrices. Extracellular signals, such as hormones or external mechanical stimuli, can cause acute changes, that set off a further round cell and matrix modifications (adapted from Vogel and Sheetz 2006).

Cell phenotype and function can be transmitted by biophysical signals being transmitted from integrins, through focal adhesions and the actin cytoskeleton to the nucleus (Yang *et al.* 2017). In particular, substrate nanotopography and stiffness can mediate the distribution and size of focal adhesions and, consequently, cytoskeletal organization and

tension. These mechanisms can regulate cell morphology and, eventually, the overall cell function (Yang *et al.* 2017). Thereby, focal adhesion kinase (FAK) functions as a primary regulator of focal adhesion signaling, that regulates proliferation (Cary *et al.* 1996) and differentiation (Xu *et al.* 2012; Salasnyk *et al.* 2007). Upon mechanical strain its activation increases (Wang *et al.* 2001). Through FAK and non-receptor tyrosine kinases Src –mediated phosphorylation of paxillin, vinculin can be recruited to focal adhesions through myosin-dependent tension and promotes the stabilization of adhesions (Pasapera *et al.* 2010).

Therefore, together with biochemical signals, biophysical cues like mechanics and topography have previously been applied to control almost all aspects of cell behavior *in vitro* (see Fig. 10) (Yang *et al.* 2017). As shown in Fig. 10 the extracellular environment is in a constant cross-talk with cellular responses and functions. Topographical cues can be induced by porosity and roughness, the architecture of the cellular environment, and on 2 dimensional as well as on three-dimensional scales. Biochemical cues for example are induced by growth factors, cytokines, and adhesion ligands. Biomechanical cues include elasticity/stiffness of the extracellular environment or cytoskeletal forces.

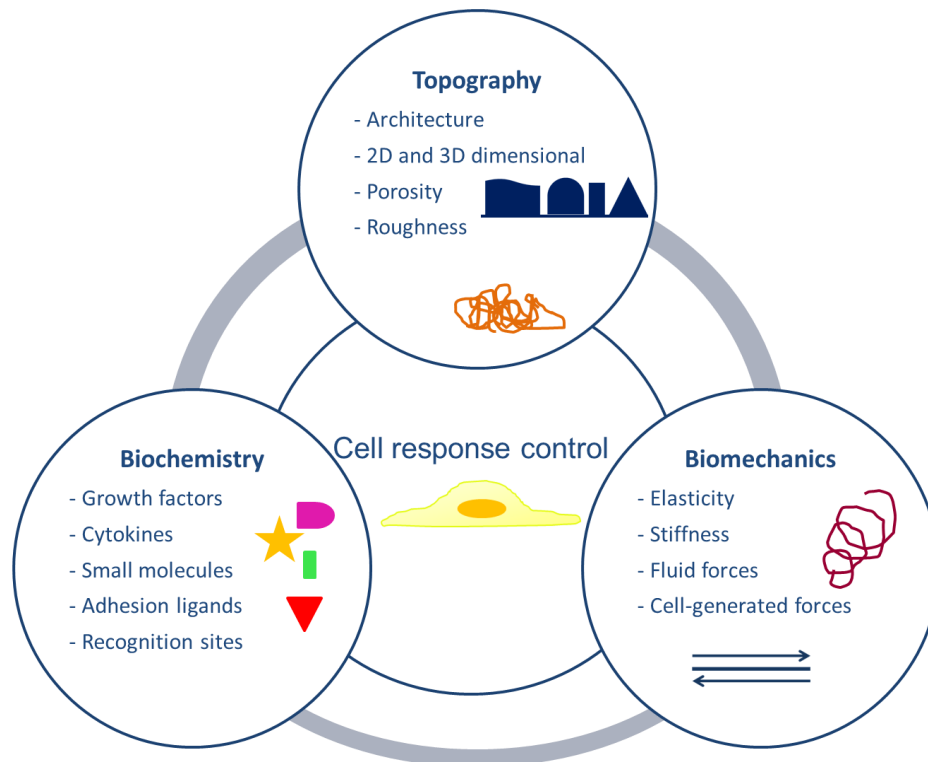


Figure 10. Cell response control. Cellular response control is a cross-talk of biochemical, biomechanical, and topographical cues. The extracellular environment is in a constant cross-talk with cellular responses and functions. Biochemical cues are induced by growth factors, cytokines, and adhesion ligands. Topographical cues can be induced by porosity and roughness. Biomechanical cues include elasticity/stiffness of the extracellular environment or cytoskeletal forces.

Since, there are variations in cell source, substrate preparation, and differentiation protocols, the ideal substrate stiffness is not the same through different studies (Yang *et al.* 2017). Current studies have stated that cells can preserve stiffness information from past culture environments and that the previous mechanical history or mechanical treatment influences future cell fate decisions (Gilbert *et al.* 2010; Balestrini *et al.* 2012; Yang *et al.* 2017, 2017; Yang *et al.* 2014a; Lee *et al.* 2014; Li *et al.* 2017). Skeletal muscle stem cells, for instance, lose their *in vivo* regenerative potential on stiff cell culture dishes. Nevertheless, they sustain their self-renewal and regenerative capacity on soft hydrogels of physiological stiffness (Gilbert *et al.* 2010).

Biochemical cues

One of the three main signaling cues between the ECM and cells are the biochemical cues. The ECM constitutes of different molecules which can be flexible and extendable (Kim *et al.* 2011b). Mechanical tension can expose their cryptic sites, allowing further interaction with growth factors or their receptors (Kim *et al.* 2011b). Collagen is the most abundant protein in the body and secreted by for example fibroblasts(Kim *et al.* 2011b). Collagens not only act as structural support but also as binding partners for other ECM proteins (Kim *et al.* 2011b). The different ECM proteins support various biological functions, through their ability to bind multiple interacting partners like other ECM proteins, growth factors, signal receptors, and adhesion molecules (Kim *et al.* 2011b). Fibronectin for instance, like other ECM proteins, is produced by fibroblasts among other cell types (Kim *et al.* 2011b). It can bind to collagens and heparin sulfate proteoglycans (Ruoslahti 1988). They thus contribute to the structural framework for many cell surface receptor systems (Kim *et al.* 2011b).

Moreover, the ECM serves as a reservoir for growth factors. ECM-bound growth factors can be released locally and bind to their receptors (Kim *et al.* 2011b). Many ECM proteins have binding sites for both growth factors and cell adhesion (Kim *et al.* 2011b). This allows the local concentration of growth factors near to cell surface receptors and cell adhesion sites (Kim *et al.* 2011b). ECM bound growth factors do not necessarily have to be released in soluble form to function (Kim *et al.* 2011b). Fibroblast growth factors for example bind to their receptors with heparin sulfate as a cofactor, while the heparan sulfate proteoglycans present these ligands during signaling (Kim *et al.* 2011b). Mediators like cytokines can influence cell behavior in distinct ways (Schönherr and Hausser 2000). A group which interacts closely with cytokines and growth factors are the proteoglycans (Schönherr and Hausser 2000). Proteoglycans interact with their core proteins. Moreover, with their glycosaminoglycan chains, they interact with cytokines (Schönherr and Hausser 2000). The binding of cytokines to their cell surface receptors can be modified by these interactions (Schönherr and Hausser 2000). Also, they can induce the storage of the soluble factors in the matrix (Schönherr and Hausser 2000).

The ECM undergoes a constant interaction of biochemical and mechanical changes. Cells respond to these changes through the crosstalk between integrins and the actin cytoskeleton (Kim *et al.* 2011b). Integrins are transmembrane receptors with receptors for different ECM molecules (Kim *et al.* 2011b; Alam *et al.* 2007). The specific integrin expression pattern of a cell dictates which ECM substrate the cell can bind to (Hemler and

Lobb 1995). The composition of integrin adhesomes on the other side, determine signaling events, thus cell behavior and fate (Kim *et al.* 2011b). The interactions of integrins with the actin cytoskeleton involve actin polymerizing and actin linking molecules (Mitra *et al.* 2005). These interactions are regulated and regulate the associated adhesion signaling molecules (Mitra *et al.* 2005). Several pathways can be activated independently by integrins (Assoian and Schwartz 2001). They also act synergistically with other growth factor receptors (Alam *et al.* 2007). An example includes the insulin receptor (Schneller 1997).

Mechanical cues

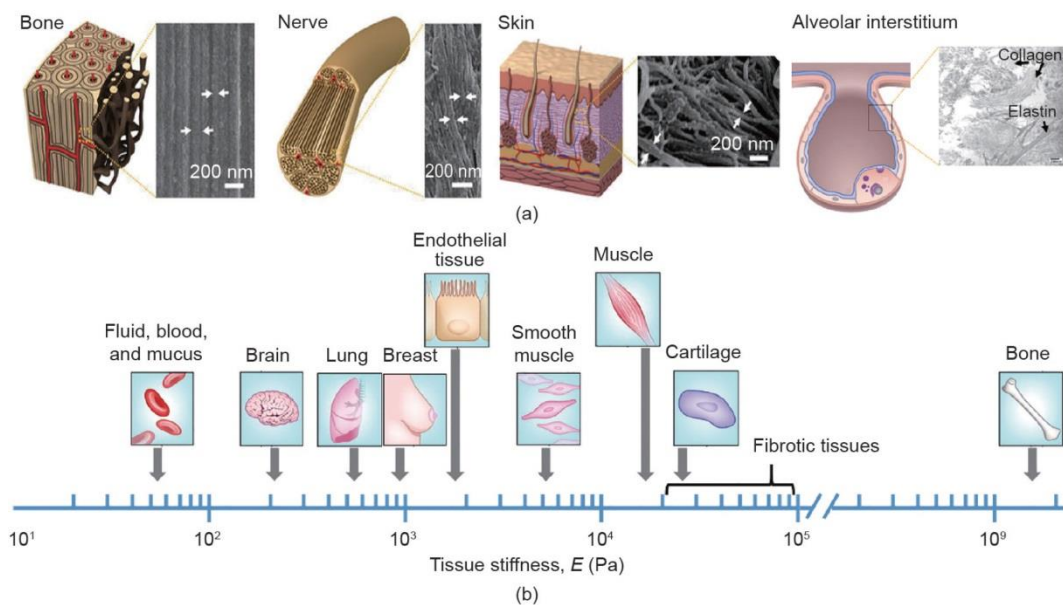


Figure 11. Biophysical characteristics of human tissues. Nanoscale structures displayed in different tissues from stiff tissues (bone) on the right and soft tissues alveolar interstitium (left) (a). A range of tissue stiffness is displayed below (b). The fibrotic tissues become stiffer than those in normal conditions. (taken from (Yang *et al.* 2017))

In general, findings on cellular responses to substrate stiffness cues are not consistent, and are sometimes even contradictory (Yang *et al.* 2017). Moreover, cells can sense the stiffness of underlying hydrogels, and even the stiffness of the supporting material, if the underlying gel is very thin (Lovett *et al.* 2013; Maloney *et al.* 2008; Merkel *et al.* 2007). Buxboim and co-workers estimated that cells can sense the underlying substrate stiffness at a depth of approximately 5 μm (Buxboim *et al.* 2010). Under certain conditions, cells can even deform a substrate to a depth of 20 μm (Franck *et al.* 2011). Hydrogels have the

advantage that they provide three-dimensional, porous structures. Simultaneously, their structures both in lateral and vertical dimensions make it challenging to dissect the influence of substrate stiffness and topography in 2D and 3D during cell regulation (Yang *et al.* 2017).

Topographical cues

Not only biochemical and mechanical cues control cell behavior but also the underlying scaffold topography on different length scales (Ventre and Netti 2016; Nguyen *et al.* 2016; Bettinger *et al.* 2009). Cell behavior can be guided physically by nanotopography and further modulated by stiffness via mechanical feedback upon cells deforming the surrounding nanostructures (Yang *et al.* 2017). Not only nanostructures but also hierarchical structures composed of microscale and nanoscale components are of interest (Tan *et al.* 2015; Zhao *et al.* 2010; Yang *et al.* 2014b). While this interaction depends on the cell type some general correlations have been established for micro- and nanotopographic patterns and their influence on cell behavior (Nguyen *et al.* 2016). Microtopographies are known to affect cell morphogenesis (Nguyen *et al.* 2016) and can specifically influence macrophage morphology, hence modulating the immune response to a biomaterial (Sridharan *et al.* 2015; McWhorter *et al.* 2015). Lately, both micro- and nanostructured biomaterials were found to control cell reprogramming (Long *et al.* 2017). While microtopographies considerably enhance the reprogramming efficiency (Downing *et al.* 2013), such as when fibroblasts or pluripotent stem cells are converted into neurons (López-Fagundo *et al.* 2013; Bruder *et al.* 2006). Fibronectin and vitronectin coated smooth and nanostructured materials had shown to have an impact on human coronary artery endothelial cells, human osteosarcoma cells and human skin fibroblasts growth. All cells in this study adapted their surface area to chemistry and topography of the surface (Sales *et al.* 2019). Moreover, they showed higher circularity on micro grooved than on smooth surfaces, independently of the coating (Sales *et al.* 2019). Also did cells seeded on smooth surfaces exhibit larger cell areas as cell on micropatterned surfaces (Sales *et al.* 2019).

Principles of cell regulation with substrate stiffness and topographical cues are often studied in 2D *in vitro* systems. These studies lack the recapitulation of the complexity found in a 3D environment. The transfer from cell studies on 2D substrates into the development of biomimetic 3D-scaffolds remains a challenge in the scaffold development in tissue engineering (Jacquemet *et al.* 2015; Tawfick *et al.* 2012; Matthews *et al.* 2002). Consequently, biophysical cues need to be translated into 3D-systems and nanofibrous

systems to provide better mimicking of the natural extracellular environment (Huebsch *et al.* 2010). In different studies, it has been shown that cells show different cell morphology (Fouchard *et al.* 2014), cell adhesion (Bryant *et al.* 2004), proliferation, and differentiation in a 3D (Huebsch *et al.* 2010; Hogrebe and Gooch 2016). Whereas, smooth substrates lead to a higher proliferation of stem cells (Gerecht *et al.* 2007; Yim *et al.* 2007). Neurite outgrowth in neuronal cell cultures was found to be stimulated by different topographical size ranges (Nguyen *et al.* 2016).

It was reported that the arrangement of nanoscale features can have a profound impact on cell phenotype and function, which makes them potent regulators of cell behavior. Fibroblast-substrate interactions can be altered by topography to strengthen or weaken cell adhesion, thus affecting cellular processes (Yang *et al.* 2017). On the other hand, shape (e.g, gratings, pits and pillars), dimensions (feature size, spacing, and height), and arrangement of nanoscale features all have distinct effects on cell behavior from cell adhesion and spreading to proliferation and differentiation, which is cell-type-specific (Yang *et al.* 2017). Likewise, nanotopography height can effectively control cell behavior (Wang *et al.* 2016). A variety of cell types exhibited more pronounced focal adhesions and actin stress fibers highly spread morphology and larger cell area on shallow (11 – 13 nm height) randomly distributed nanoislands produced by polymer demixing, in contrast to the flat control surface (Lim *et al.* 2005b; Lim *et al.* 2005a; Dalby *et al.* 2002a; Dalby *et al.* 2002c). Increasing the height to approximately 90 nm cells like human fetal osteoblastic cells (Lim *et al.* 2005b), human bone marrow cells (Frey *et al.* 2006), and human fibroblasts (Dalby *et al.* 2002d) exhibited a reduced cell spreading morphology with diffuse actin and fewer stress fibers (Yang *et al.* 2017). Different from that, human endothelial cells displayed larger lamellae and have increased numbers of stress fibers on 95 nm nanoislands (Dalby *et al.* 2002a). Cell-type-specific responses to nanotopography have been reported in various cell types (Csaderova *et al.* 2010; Chen *et al.* 2012; Stylianou *et al.* 2013). For instance, Chen and Co-workers found that human embryonic stem cells (hESCs) display long self-renewal and enhanced proliferation on smooth surfaces, nonetheless they tend to differentiate on nano rough glass surfaces. However, nano rough glass surfaces stimulated the adhesion of NIH 3T3 fibroblasts compared with smooth surfaces (Chen *et al.* 2012). Cell surface area can be limited by small spacing, whereas large spacing may reduce the increase in the apparent surface area. It is hence suggested that the aspect ratio of height to spacing of nanotopography provides a more comprehensive characterization of nanotopography than a single-dimensional parameter

(Moe *et al.* 2012; Nguyen *et al.* 2016; Crouch *et al.* 2009; Hu *et al.* 2005; Fraser *et al.* 2008; Uttayarat *et al.* 2005).

Overall, many insights into cell-topography dependence on mainly synthetic materials have been gained. The natural environment of the cell, the ECM is composed of nanofibrous proteins. To study the cell-material interaction, nanostructured protein scaffolds are needed. Furthermore, to understand topography influences independently of mechanics and biochemistry, the mechanics must be kept the same. New biophysical model systems based on protein scaffolds to be closer to the *in vivo* environment are needed, where the influence of topographies on cell growth can be studied independently from other factors like biochemical and mechanical stimuli. It would be ideal if mechanics and biochemical stimuli could later also be specifically adapted.

1.3 Synthetic ECM systems

Many of the above findings of cell interactions with their extracellular environment were obtained on synthetic hard materials. Furthermore, most of the *in vitro* systems were reduced to two dimensional properties. In order to mimic the *in vivo* cell responses to topographic, biochemical and biomechanical stimuli *in vitro*, several approaches were used to produce synthetic ECMs. The most important are presented in the following.

1.4.1 Manufacturing methods for nanofibrous and porous scaffolds

Since the ECM plays a significant role in cell adhesion, migration, and proliferation it has been widely studied to promote biomaterials design and construction, especially for the possible application in tissue engineering as cell culture scaffold and in drug delivery (Lutolf and Hubbell 2005). In tissue engineering, the strategies for tissue and organ reconstruction vary. In general, they can be classified into two categories involving either *in vitro* or *in vivo* use of so-called scaffold materials to support cell growth and tissue regeneration (Costa *et al.* 2017). Such scaffolds can be composed of synthetic materials or naturally occurring materials that are native components of the ECM, such as collagen, fibrin, and fibronectin (Costa *et al.* 2017). Biological scaffold materials composed of natural ECM components have been shown to facilitate the constructive remodeling of many different tissues in both preclinical animal studies and human clinical applications (Badylak *et al.* 2009). A large variety of polymers, biopolymers, and composites were used to create artificial ECM-mimicking biomaterials. Collagen, fibronectin, and elastin, three dominant fibrous proteins in natural ECM, received major attention because they

can form nano-scaled fibrous synthetic matrices to provide tensile strength and elasticity for tissues (Ma *et al.* 2005).

As introduced in chapter 1.1.2 another important biopolymer, which forms nanofibers *in vivo*, is the blood plasma protein fibrinogen. Fibrinogen has also been considered as an artificial substratum to mimic the temporary matrix during wound repair for cell migration (Pereira *et al.* 2002). Thus, fibrinogen nanofibers are also suitable for various biomedical applications such as tissue engineering scaffolds, wound dressings, coatings, or drug delivery vehicles (Carlisle *et al.* 2009; Shepherd *et al.* 2017). As stated above, fibrinogen and collagen have a close interaction through binding sites and fibronectin as a direct linker between collagen and fibrinogen (Balian *et al.* 1980; Makogonenko *et al.* 2002). Moreover, both proteins are involved in cellular interactions during wound repair and tissue regeneration (Shaw and Martin 2009).

As collagen represents the most abundant protein in the ECM and is a well-established model system, in the past two decades interests in collagen-based nanobiomaterials kept increasing. Over the years different approaches to create collagen-based nanobiomaterials have evolved. Collagen is considered one of the most important biomaterials in connective tissue regeneration because of the intrinsic biocompatibility, flexibility, and hydrophilicity. Due to their manifold possible application fields, extensive attention was brought to collagen nanobiomaterials (see Fig. 12). A key objective, therefore, is to recreate an *in vitro* culture system of some of the essential factors in the cellular microenvironment, which control and regulate cell function (Lia *et al.* 2005). In literature, various techniques have been reported for the fabrication of collagen nanobiomaterials. These include template-assisted synthesis, self-assembly, solvent casting, phase separation, and electrospinning techniques (Haider *et al.* 2015). Collagen can provide a biomimetic environment, which is beneficial for promoting cellular adhesion, migration, and proliferation (Lin *et al.* 2019). Thus collagen-based nanobiomaterials are becoming essential in both, basic research and clinical applications. Many different approaches were developed to create new nanobiomaterials, explicitly electrospinning, collagen-based hydrogels, freeze-dried collagen scaffolds, wet-spinning, and self-assembly (Park *et al.* 2018).

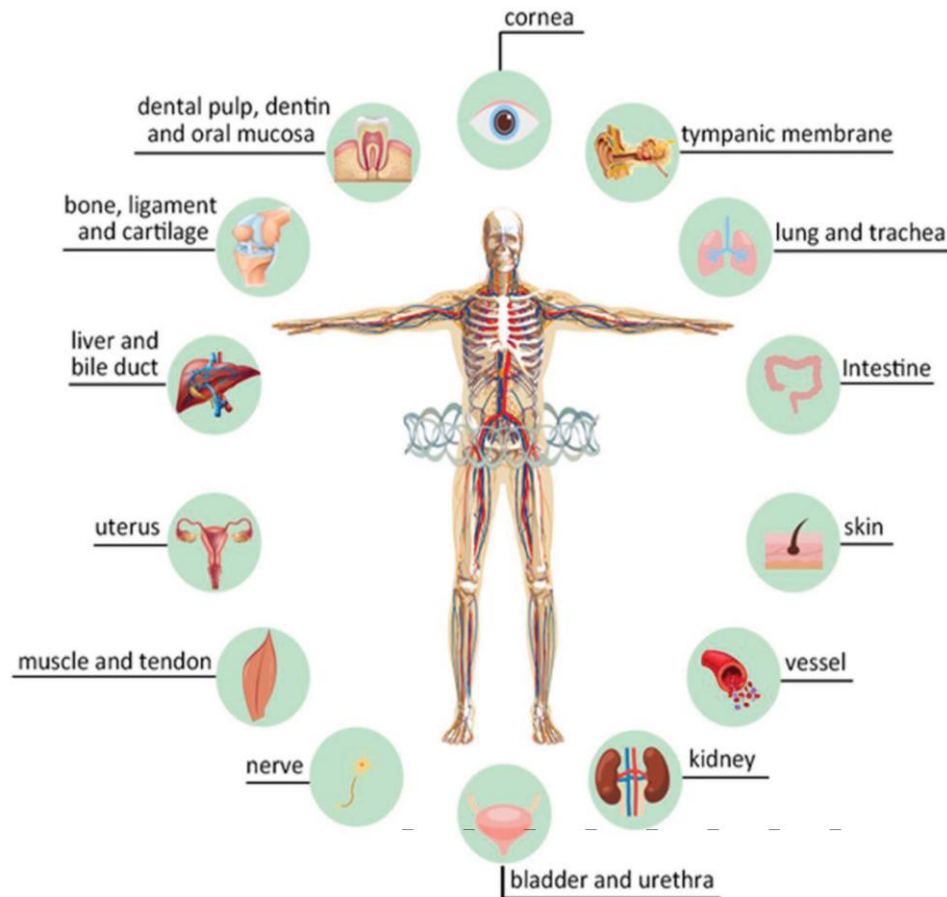


Figure 12. Diverse applications of collagen-based nanobiomaterials in the regeneration of various tissues. (Lin *et al.* 2019)

Fibrinogen-based scaffolds have previously been developed in the form of fibrin hydrogels and wet-extrusion of fibronectin–fibrinogen cables (Joo *et al.* 2015; Rajangam and An 2013). Due to its involvement in blood coagulation and wound healing fibrinogen has become increasingly attractive to develop nanofibrous scaffolds for biomedical applications. In literature, different approaches can be found to induce *in vitro* fibrillogenesis of fibrinogen and to prepare nanofibrous fibrinogen scaffolds.

The most common techniques to produce nanofibrous collagen or fibrinogen-based nanobiomaterials will be presented in the following paragraphs and advantages as well as disadvantages will briefly be discussed (also see Table 2).

Lyophilization – Freeze Drying

Porous protein scaffolds can be formed by freeze-drying. In the freezing phase, the polymer solution is frozen and the solvent is crystallized, forming a network with interpenetrating ice crystals. In the second phase, the solvent is removed under pressure. If the solvent is completely sublimed and polymeric crosslinked pores are formed (Lin *et al.* 2019). Freeze drying is regarded to be amongst the most commonly used method to fabricate collagen scaffolds. It is stated to maintain the natural structural form and biological properties of collagen (Lin *et al.* 2019). Whereas it does not lead to the fibrillary structure that collagen usually has in the natural ECM. (Shepherd *et al.* 2017) developed a composite material by freeze-drying combining collagen and fibrinogen in one scaffold (Shepherd *et al.* 2017). Vasconcelos *et al.* introduced three-dimensional fibrinogen based scaffold prepared by freeze-drying to promote bone healing and homeostasis (Vasconcelos *et al.* 2016).

Besides the positive properties of this technique, significant disadvantages are the long fabrication time and high energy consumption, limiting its expansion to the industrial scale (Lin *et al.* 2019).

Hydrogels

Zou and Co-workers defined hydrogels as 3D cross-linked networks which can absorb a large amount of water without dissolving (Zou *et al.* 2018). Another definition of (Nikolova and Chavali 2019) state hydrogels as compared to hydrophilic chains either covalently or non-covalently (hold by intermolecular attractions) bonded (Nikolova and Chavali 2019). The methods used for the fabrication of hydrogel scaffolds include solvent casting/leaching, gas foaming, photo-lithography, electrospinning, 3D printing, etc. (Nikolova and Chavali 2019). Hydrogels can be prepared by natural polymers (i.e. collagen, gelatin, fibrin, or hyaluronate) and synthetic polymers like polyacrylic acid (PAA), polyethylene oxide (PEO) and polyvinyl alcohol (PVA) after extensively swelling with water. They are not only structural like the ECM but also diffuse into hydrophilic nutrients and metabolites rapidly as well (Zou *et al.* 2018; Lin *et al.* 2019).

Physical hydrogels are formed by the transient crosslinking between polymer chains via various kinds of physical bond is exposed to aqueous conditions with water-soluble interactions. In contrast, chemical hydrogels generally possess networks formed by cross-linked covalent bonds, besides their mechanical properties can be easily tuned via controlling the crosslinking density (Zou *et al.* 2018). Crosslinking of hydrogels allows

them to retain 3D shape and to swell without dissolving. Generally, it can be stated that the higher the crosslinking extent, the lower the swelling (Nikolova and Chavali 2019).

An advantage is that hydrogel scaffolds are useful in supporting the growth of new cells and tissues due to their rubber elasticity, high water content and solute transportation (Lin *et al.* 2019; Zou *et al.* 2018). They can be derived from natural polymers and therefore exhibit high hydrophilicity, biocompatibility, flexibility, and degradability. Hydrogel scaffolds derived from natural polymers like collagen and fibrinogen, up to date have certain limitations such as limited mechanical properties, the difficulty of purification, and sometimes pathogenic transmission and immunogenicity, depending on the source (Nikolova and Chavali 2019). Collagen hydrogels have extensively been seeded with cells (Elsdale and Bard 1972; Bell *et al.* 1979; Grinnell *et al.* 2003; Busby *et al.* 2013). Collagen hydrogels have been as attempts to develop dermal substitutes (Helary *et al.* 2010), for support for bone formation (Yamamoto *et al.* 2003) or induce pre-differentiation of human mesenchymal stem cells (Fensky *et al.* 2014). Other studies for instance focused on the responses of fibroblasts to plastically compressed fibrillary collagen hydrogels (Ghezzi *et al.* 2011). Fibrinogen gels for instance are formed as modified PEG-fibrinogen hydrogels (Dikovsky *et al.* 2006).

Phase Separation

Munir and Callanan reported that increasing attention for phase separation techniques awakened due to its ability to produce scaffolds with high porosity, interconnecting networks, and desirable mechanical properties (Munir and Callanan 2018; Budyanto *et al.* 2009).

In the phase separation technique, a polymer solution is disintegrated and passes through the liquid-liquid phase separation. The polymer solution then forms two phases, a polymer-rich phase, and a polymer degraded phase. The polymer enriched phase solidifies and the phase with a smaller proportion of polymer is removed, creating a highly porous polymer network. The process is carried out at low temperatures which are beneficial for the incorporation of bioactive molecules in the construct (Ghalia and Dahman 2016). By using the phase separation technique, a nanofibrous structure is created that mimics the ECM architecture and provides a better environment for cell attachment. However, others state that this technique offers little control over the diameter and orientation of fibers, limited material selection, and an inadequate resolution (Nikolova and Chavali 2019).

Electrospinning

Electrospinning is the most common technique to prepare (bio-)polymer nanofibers to manufacture *in vitro* fibrous scaffolds for tissue engineering application with a fiber diameter ranging from less than 100 nm to a few microns (Zeugolis *et al.* 2008). Electrospun nanofibers scaffolds are, for example, already used as a drug delivery carrier and bone regeneration model (Francis *et al.* 2016).

The basic electrospinning setup is mainly comprised of four main parts: a polymer solution, a glass syringe containing a metallic needle, a power supply, and a metallic collector. The electrospinning source solution is prepared with the polymer of interest in a solvent (Palchesko *et al.* 2013b). An electric field is applied leading charges to move into the polymer solution via the metallic needle. The collector has a different charge as the needle whereby an electric field is created. The reciprocal repulsion of charges produces a force that opposes the surface tension, and ultimately the polymer solution flows in the direction of the electric field. The solvent evaporates, and polymer fibrils form (Palchesko *et al.* 2013b). Fibers emerge and are collected on the metallic collector (see Fig. 13) (Haider *et al.* 2013; Bae *et al.* 2013; Haider *et al.* 2015).

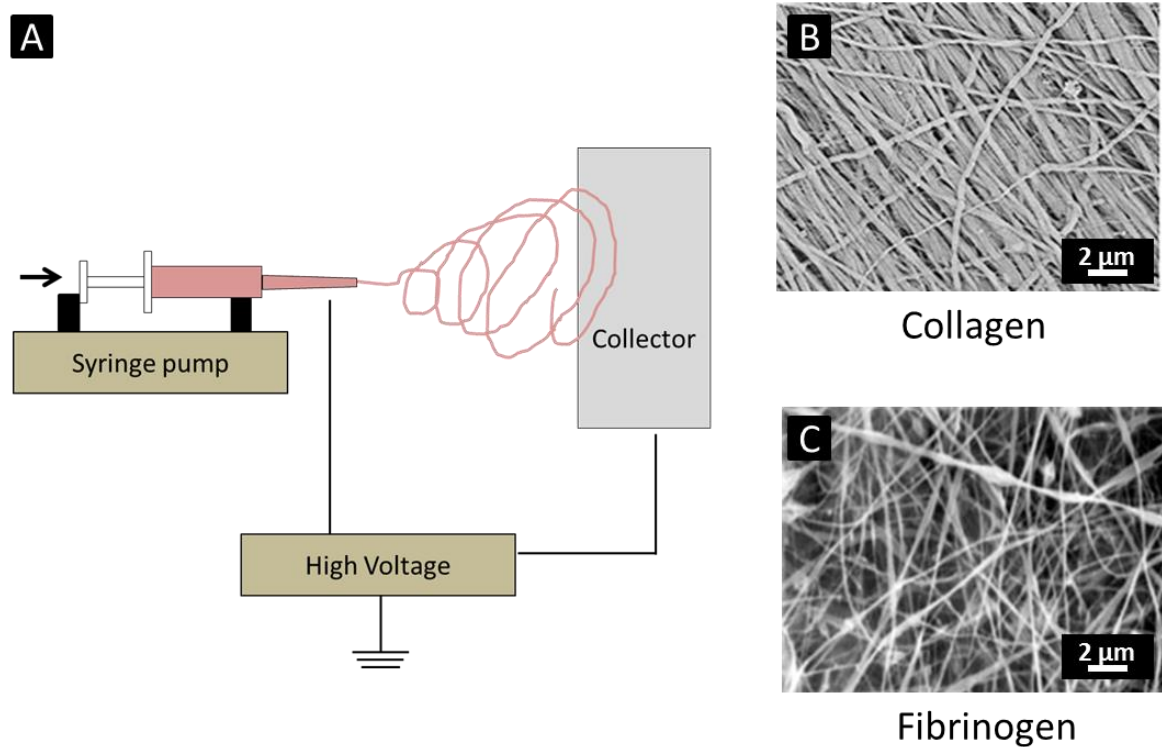


Figure 13. Electrospinning process. Schematic of a typical electrospinning system. A high voltage applied between the spinneret tip and the collector creates an electrified fluid jet, which is accelerated toward the grounded collector, forming continuous fibers (A). (adapted from Li and Bou-Akl 2016). SEM images of electrospun collagen nanofibers (B) (taken from Liu *et al.* 2012) and fibrinogen (C) (McManus *et al.* 2007b).

Electrospinning of collagen and fibrinogen has become a common procedure in the tissue engineering community. The first study reporting on the electrospinning of collagen was presented by Huang and co-workers (Huang *et al.* 2001a; Huang *et al.* 2001b). Other groups followed the electrospinning of collagen like, for instance, Matthews in 2002, Boland *et al.* in 2004, and Rho *et al.* in 2006 (Matthews *et al.* 2002; Boland *et al.* 2004; Rho *et al.* 2006). With this technique, fiber diameters in the nanometer range up to the micrometer range can be achieved (Boland *et al.* 2004). The collagen fiber mats can be produced up to a size of several cm^2 (Boland *et al.* 2004). The high porosity and high surface-area-to-volume ratio as well as features required for cell adhesion, growth, and proliferation can be achieved with electrospinning (Miguel *et al.* 2018). Different studies investigating cell behavior on electrospun collagen have been published. Shih *et al.* studied the influence of collagen fiber diameter on cell growth, proliferation, and adhesion of mesenchymal stem cells (Shih *et al.* 2006). A wide range of studies to investigate the influence of electrospun collagen on cell growth was conducted. Several studies found a

positive impact of electrospun collagen nanofibers on osteoblast adhesion, proliferation, and spreading (Casper *et al.* 2007; lafiscol *et al.* 2013; Torres-Giner *et al.* 2009). Powell *et al.* investigated the influence of electrospun collagen on wound contraction of engineered skin substitutes (Powell *et al.* 2008). They observed the positive influence of electrospun collagen on the proliferation and distribution of fibroblasts (Powell *et al.* 2008).

Fibrinogen also has been electrospun since the early 2000nds and is a protein of interest up to date. Numerous groups focused on the electrospinning of fibrinogen like Wnek *et al.* 2003, McManus *et al.* 2007, and Gugutkov *et al.* 2017 (Gugutkov *et al.* 2017; Wnek *et al.* 2003; McManus *et al.* 2007b; Sell *et al.* 2008a; Sell *et al.* 2008b). For electrospun fibrinogen nanofibers, diameters ranging from 0.5 to 1.04 μm were reported (Sell *et al.* 2008a). Dried fibrinogen scaffolds exhibited distinct pores in SEM analysis. It was observed that the same scaffolds were densely packed leaving little room for pores when being hydrated (Sell *et al.* 2008a). The average pore diameters reported in this study ranged from 0.57 to 3.7 μm , with hydrated pores being significantly smaller than their dry counterparts (Sell *et al.* 2008a). The fibrinogen fiber mats can be produced up to a size of several cm^2 (Sell *et al.* 2008a). Sell *et al.* studied the influence of different cross-linkers on cell growth on electrospun fibrinogen scaffolds (Sell *et al.* 2008b). They found that crosslinking with EDC and genipin slowed the degradation of fibrinogen by fibroblasts but at the time had negative effects on the bioactivity of the scaffolds as it slowed the cell migration (Sell *et al.* 2008b). A different study electrospun fibrinogen was found to support osteogenic differentiation of mesenchymal stem cells (Francis *et al.* 2016). McManus and Co-Workers observed that fibroblasts migrated into electrospun fibrinogen scaffolds and deposited collagen, thus indicating that electrospun fibrinogen had a big potential as a tissue engineering scaffold (McManus *et al.* 2007b).

Moreover, studies have shown that up to 45% of collagen was lost during electrospinning (Zeugolis *et al.* 2008). However, solvents for proteins used in electrospinning are often fluoro alcohols, which not only denature the native structure but also lower the denaturation temperature (Barnes *et al.* 2007). Zeugolis *et al.* 2008 report that the electrospinning of collagen out of fluoro alcohols denatures collagen to gelatin (Zeugolis *et al.* 2008).

Self-assembly

Another approach to induce fibrillogenesis of different proteins *in vitro* is the self-assembly. Self-assembly of nanofibers occurs when molecular systems spontaneously

undergo organization into nanofibers under specific conditions (Palchesko *et al.* 2013a). This process only works for specific peptides/proteins (Palchesko *et al.* 2013a). Self-assembly of ECM proteins can be induced by different approaches, such as pH driven self-assembly, surface-induced self-assembly, or temperature-induced self-assembly (Palchesko *et al.* 2013a). *In vivo* self-assembly requires cell-derived forces to unfold protein subunits and expose their cryptic self-binding domains (Palchesko *et al.* 2013a). Mimicking this process *in vitro* normally requires denaturants or reducing agents (Palchesko *et al.* 2013a). In the following, an overview of common self-assembly techniques of collagen will be presented followed by techniques for fibrinogen self-assembly.

Over more than the past four decades, the *in vitro* fibrillogenesis of collagen type I, based on pH-shift and ionic strength, has been extensively studied (Harris *et al.* 2013; Elsdale and Bard 1972). Hence, today several reproducible procedures for the production of collagen fibrils are available. The resulting fibers are to a large extent comparable to the fibers found in native biological tissues (Harris *et al.* 2013).

PH-induced self-assembly is a common method for *in vitro* fibrillogenesis. Together with ionic strength, collagen molecules can reproducibly assemble into fibers. PH of 6 to pH 8 along with the presence of chloride anions enable the formation of collagen fibers with the characteristic D-banded patterns (67 nm) (Zhu *et al.* 2018). The dimension of the fibers and the D-spacings can vary depending on the pH conditions (Harris and Reiber 2007). Depending on the pH conditions, such collagen nanofibers exhibit typical diameters between 80 and 200 nm (Li *et al.* 2009). On the other hand, pH values of 6 or pH 4.8 or the absence of chloride anions fail to induce the D-banded of native-like collagen. Instead, those fibrils tend to gather together to form sub-fibrils (Zhu *et al.* 2018). The increase rate and final pH of the solutions also affect the kinetics and fibrils morphology and collagen self-assembly (Ramírez-Rodríguez *et al.* 2014). The formation of collagen fibers increases with a gradual increase in pH and the lateral aggregation between fibrils gets promoted. A rapid increase in pH induces the formation of thin fibers (Zhu *et al.* 2018).

Yet, it often included non-physiological pH possibly affecting the biological activity of ECM proteins (Maas *et al.* 2011). Harris *et al.* 2013 stated that most research on *in vitro* self-assembly was conducted on either varying pH conditions or ionic strength. They tried to overcome this gap by bringing together these two parameters and induced collagen type I fibrillogenesis under varying pH and ionic conditions. They stated that early/sub-fibers and mature fibers formed in the presence of physiological ionic strength, namely 150 mM NaCl

and the time-dependent dynamic progression towards mature fibers occurring at neutral pH (Harris *et al.* 2013). Therefore, collagen nanofibers have already been used in cell culture studies with fibroblasts and endothelial cells, often using smooth collagen as reference substrates (Hakkinen *et al.* 2011; Jiang and Grinnell 2005; Stylianou *et al.* 2013; Huang *et al.* 2013).

Flow Processing

Lately, a flow processing technique combined with pH-shift from acidic to neutral pH was presented to produce collagen nanofiber scaffolds which could be either aligned or randomly deposited and had a diameter of approximately 20 to 45 nm (Lai *et al.* 2012a; Lai *et al.* 2011). Yet, the hierarchical fiber assembly was limited to dense fibril matrices with low porosity. Maas and Co-workers established a method to create composite fibrils made from collagen and calcium phosphate by pH-driven self-assembly through track-etched polycarbonate nanopores in a gradient of pH 3 to pH 11. The resulting fibers were tens of micrometers long and exhibited diameters between 120 and 760 nm depending on the pore geometry (Maas *et al.* 2011). Nonetheless, they used non-physiological pH-values possibly affecting the biological activity of different proteins. Raoufi and co-Workers recently presented an extrusion process using biocompatible aluminum oxide nanopores as a template to prepare nanofibers from proteins like collagen and fibrinogen (Raoufi *et al.* 2016; Raoufi *et al.* 2015). This method provides control over fiber diameter, yet does not yield high amounts of fibers, therefore not allowing creating three-dimensional scaffolds for cell culture applications.

Surface-induced self-assembly as well as pH driven self-assembly have also been used for *in vitro* fibrillogenesis of fibrinogen. In blood coagulation, fibrinogen is formed by the enzymatic cleavage of fibrinopeptides by thrombin. Surface driven assembly of fibrinogen fibers was successfully performed with hydrophobic surfaces like silica (SiO₂) (Wigren *et al.* 1991), graphite (Marchin and Berrie 2003; Reichert *et al.* 2009), different polymers (Feinberg and Parker 2010; Koo *et al.* 2012; Zhang *et al.* 2017) as well as hydrophilic gold (1,1,1) (Chen *et al.* 2010) and mica surfaces, a group of sheet silicate minerals (Wasilewska and Adamczyk 2011). When fibrinogen adsorbs to surfaces like graphite the molecule unfolds and aggregate to fibers (Dubrovin *et al.* 2019). Helbing *et al.* showed that fibrinogen molecules could align on chemically homogeneous surface topographies (polyethylene crystals) one magnitude smaller than the dimension of the protein (Helbing *et al.* 2016). Moreover, acidic pH values and the addition of ethanol were found to induce the assembly of fibrinogen molecules into fiber networks (Wei *et al.* 2008b; Wei *et al.*

2008a; Wang *et al.* 2014). The fiber formation induced by mixing fibrinogen with ethanol resulted in fiber lengths ranging from several hundred nm to few μm .

Thus far, these approaches for surface-induced fiber formation only resulted in very low fiber yields with fiber diameters of 2–20 nm (Reichert *et al.* 2009; Koo *et al.* 2012). Wei and co-workers studied self-assembly by pH-dependent procedures at a very low pH of 2, which are not physiological. Moreover, they analyzed the influence of ionic strength in their self-assembly process by introducing phosphate-buffered saline (PBS) to the self-assembly – this method leads to a very low fiber yield (Wei *et al.* 2008a). The approach was improved leading to shorter preparation time, longer fibrils, and higher fiber yield, whereas still resulting in a comparably low fiber yield (Wei *et al.* 2008b). Hämisch *et al.* induced fiber formation by a drop of ionic strength starting with a concentration of 140 mM (Hämisch *et al.* 2019). They showed a dependence of ionic strength to the fiber formation kinetics. The lower the final ionic strength was, the faster the self-assembly took place (Hämisch *et al.* 2019). Overall, no dense fibrinogen networks were previously obtained by a buffer- or surface-induced assembly. Consequently, these methods are not considered suitable for the preparation of 3D-nanofibrous fibrinogen scaffolds on a large scale.

Recently, Stapelfeldt and co-workers introduced a novel *in vitro* approach to fabricate nanofibrous fibrinogen scaffolds in the absence of cells and thrombin using tailored salt conditions (Stapelfeldt *et al.* 2019a). For the first time, fibrinogen could be assembled into dense, three-dimensional nanofibrous scaffolds without the use of high voltages, organic solvents, or enzymatic activity. This novel process could be controlled by adjusting the fibrinogen and salt concentration as well as the pH range. Remarkably, this process enabled the first time preparation of either immobilized or free-standing fibrinogen scaffolds depending on the underlying substrate material. This could be realized by tailoring the carrier substrate material and by introducing a customized fixation and washing procedure after the fiber assembly. (Stapelfeldt *et al.* 2019a) Fibrinogen fibers obtained with this novel self-assembly method showed to be soluble in water (Stapelfeldt *et al.* 2019b). Stapelfeldt *et al.* found a difference in the secondary structure after the addition of PBS. For application in cell culture, fibrinogen fibers need to be stable upon rehydration. Therefore, they introduced a crosslinking step with formaldehyde vapor (Stapelfeldt *et al.* 2019b). They found no differences in structural content between none crosslinked and crosslinked fibrinogen fibers.

A summary of the presented techniques with their key advantages and disadvantages is given in table 2.

Table 2 Comparison of techniques to prepare nanofibrous and nanoporous scaffolds for tissue engineering.

Fabrication technique	Advantages	Disadvantages
Freeze drying	Control over pore size (Lin <i>et al.</i> 2019)	<ul style="list-style-type: none"> • long fabrication time (Lin <i>et al.</i> 2019) • high energy consumption(Lin <i>et al.</i> 2019)
Hydrogels	Mimic ECM architecture (Lin <i>et al.</i> 2019; Zou <i>et al.</i> 2018)	<ul style="list-style-type: none"> • Limited mechanical properties (Nikolova and Chavali 2019) • difficulty of purification Modification of polymers are often necessary (Nikolova and Chavali 2019)
Phase separation	<ul style="list-style-type: none"> • Simple equipment (Munir and Callanan 2018) • Convenient fabrication process (Palchesko <i>et al.</i> 2013a) 	<ul style="list-style-type: none"> • Discontinuous process (Palchesko <i>et al.</i> 2013a) • Not scalable (Nikolova and Chavali 2019) • No control on fiber dimensions (Nikolova and Chavali 2019)
Electrospinning	<ul style="list-style-type: none"> • Continuous process (Mussa Farkhani and Valizadeh 2014) • Cost effective compared with other existing methods (Mussa Farkhani and Valizadeh 2014) • Scalable (Huang <i>et al.</i> 2003) • fiber diameter control (Boland <i>et al.</i> 2004) 	<ul style="list-style-type: none"> • Jet instability (Zuo <i>et al.</i> 2005) • Toxic solvents (Barnes <i>et al.</i> 2007; Zeugolis <i>et al.</i> 2008) • high electric fields(Shin <i>et al.</i> 2001)

Continuation Table 2 Comparison of techniques to prepare nanofibrous and nanoporous scaffolds for tissue engineering.

Fabrication technique	Advantages	Disadvantages
Molecular self-assembly	<ul style="list-style-type: none"> • Complex functional structures (Palchesko <i>et al.</i> 2013a) • Only smaller nanofibers of a few nanometers in diameter and few micrometers in length can be realized (Reichert <i>et al.</i> 2009) 	<ul style="list-style-type: none"> • Complex process involving intermolecular forces (Palchesko <i>et al.</i> 2013a) • Not scalable (Palchesko <i>et al.</i> 2013a) • possible weak interactions (Galeotti <i>et al.</i> 2018)
Flow processing	Control over fiber diameter (Raoufi <i>et al.</i> 2016)	<ul style="list-style-type: none"> • does not yield high amounts of fibers (Raoufi <i>et al.</i> 2016)

1.4.2 Cell interaction with synthetic nanopographies

At a sub-cellular level sensing of geometry is a key factor of the cellular sensing of two-dimensional versus three-dimensional (Vogel and Sheetz 2006). The same matrix protein can stimulate different cell responses when it is organized in filaments, as when it is displayed on a flat surface (Grinnell *et al.* 2003; Vogel and Sheetz 2006). It is known that nanopographies increase the specific surface area, thereby often enhancing the surface area accessible for cell adhesion. Nevertheless, the surface that cells can identify is determined by the particular shape and dimensions of the nanoscale features. Nanotopography can also reduce the surface that cells can identify, thereby restricting focal adhesions and weakening cell adhesion and facilitating cell migration (Frey *et al.* 2006).

Though nanotopography provides a potent control of cell growth and differentiation by modulating the cell shape (Chen *et al.* 1997; McBeath *et al.* 2004), the underlying mechanisms remain unclear. Consequently, it was suggested that a combination of nano- and microtopographies should be considered in new biomimetic strategies to control neuron behavior (López-Fagundo *et al.* 2013; Bruder *et al.* 2006). A multi-scale combination of topographical cues could offer novel insight into the immunomodulation properties of biomaterials (Sridharan *et al.* 2015).

To further study the role of microtopographies and nanotopographies novel techniques like multiple nanoimprint lithography (NIL) were developed, to fabricate defined nanotopography on micropatterns (Hu *et al.* 2005; Bao *et al.* 2002; Eliason *et al.* 2007). Still, NIL involves expertise and expensive equipment. Hence, reproducible and cost-effective techniques remain desirable (Yang *et al.* 2017). Techniques like lithography, microcontact printing, or nanoimprint lithography allow the precise preparation of nano- and microstructure biomaterials, whereby various cell functions can already be controlled (Tawfick *et al.* 2012; Ermis, M., Antmen, E., & Hasirci, V. 2018). With these techniques mostly two-dimensional topographies, often involving the use of synthetic substrate materials, are fabricated (Tawfick *et al.* 2012; Ermis, M., Antmen, E., & Hasirci, V. 2018). To more accurately mimic the ECM in the native cell environment, new strategies to control cell behavior on different length scales necessitate 3D hierarchical scaffolds (Tawfick *et al.* 2012).

Many of the presented techniques either involve non-physiological conditions or are applicable for the production of two-dimensional networks (Monroe *et al.* 2009). Still, in their native environment cells are embedded into the nanofibrous network of the ECM (Halper and Kjaer 2014). Thus, processes to regulate cell behavior on different length scales require 3D hierarchical scaffolds, which mimic the cell environment more accurately including the topography, mechanics, and biomechanics (Tawfick *et al.* 2012). Up to now, smooth collagen was also processed into micropatterns on substrate materials like glass, agarose, PDMS, or self-assembled monolayers (SAMs) (Monroe *et al.* 2009; Desai *et al.* 2011; Kwak *et al.* 2015; Kim *et al.* 2007, 2007). In 2007, Kim *et al.* used SAMs to design a complex two-dimensional pattern of co-localized cells that preferentially assume two alternative fates, paving the way for the design and construction of more complex tissue constructs with various potential biomedical applications (Kim *et al.* 2007). Their results suggest that human mesenchymal stem cells (hMSC) can respond to the varying density of nanotopographic signals by regulating their internal cytoskeletal network and using these mechanical changes to guide them to make decisions about cell fate (Kim *et al.* 2007). In a later study, fibroblasts were examined on SAMs made from collagen type 1. Using this manufacturing technique, they were able to show that collagen patterns could influence the orientation and morphology of fibroblast growth as a function of pattern spacing (Kwak *et al.* 2015). To study cellular functions, synthetic 3D-collagen matrices have been used as ECM model systems, still, no scaffolds combining 2D and 3D-topography in the same scaffold were presented (Sheehy *et al.* 2018; Parenteau-Bareil *et al.* 2010). Even though synthetic 3D-collagen matrices have been broadly used

as ECM model systems to study cellular functions, scaffolds combining 2D- and 3D-topography in the same scaffold were not presented to date (Sheehy *et al.* 2018; Parenteau-Bareil *et al.* 2010). In contrast to electrospinning, the presented self-assembly methods provide physiological buffer conditions and do not require the use of high electric fields, which can impede the biological scaffolds activity (Palchesko *et al.* 2013b; Barnes *et al.* 2007).

Up to now, there have been mainly cell studies on electrospun fibrinogen fibers. In one study, for example, the biocompatibility of fibroblasts on fibrinogen fibers was assessed using a WST-1 cell proliferation test. Post culture scaffolds were examined by scanning electron microscopy and histology. Cell culture showed that fibroblasts easily migrate into electrospun fibrinogen scaffolds and remodel them under the deposition of native collagen (McManus *et al.* 2007b). Furthermore, fibrinogen was used as a model for early-stage bone regeneration. In this model, the ability of electrospun fibrinogen (Fg) nanofibers to regulate osteoblastogenesis between different mesenchymal stem cell populations was investigated (Francis *et al.* 2016). Fibrinogen has been further proposed in tissue engineering applications for smooth muscle remodeling (McManus *et al.* 2007b; Gugutkov *et al.* 2013).

Different surface topographies have been introduced in a variety of studies. To date, the most common cell culture topography is a smooth or planar surface, which does not resemble the natural environment of cells. To further understand the distinct influence of surface topography on cellular growth three different categories of surface roughness were introduced and the respective cell responses of fibroblasts were studied in this Ph.D. thesis. To produce nanofibrous scaffolds, established self-assembly procedures were used for the ECM protein collagen and the blood plasma protein fibrinogen. The categories of the three different surface topographies are presented in table 3.

Table 3. Surface description based on surface roughness in rehydrated conditions. This table gives an overview of different surface roughness in liquid, resembling cell culture condition and the nomenclature throughout this Ph.D. thesis.

Surface description	Roughness (rq)
Nanofibrous	≥ 30 nm
Smooth	20 to 30 nm
Planar	≤ 10 nm

Throughout this study, the surface classification presented in table 3 will be used. All scaffolds with a roughness above 30 nm will be classified as nanofibrous topographies. This applies to both, collagen and fibrinogen, nanofibers. Collagen surfaces with a surface roughness between 20 and 30 nm were categorized as smooth topographies. Non-fibrous fibrinogen surfaces with roughness below 10 nm were classified as planar.

Previously, very thin collagen patterns combining fibrillar and smooth regions in a single scaffold, have been prepared by introducing a pre-patterning with hydrophilic and hydrophobic self-assembled monolayers (SAMs) on the carrier substrate (Elliott *et al.* 2007). Nevertheless, this SAM-assisted patterning process only led to film thickness in the range of 2 to 47 nm. Therefore, these thin films were not suited to be used as three-dimensional cell scaffolds, into which cells could migrate.

1.5 Aim

This work aims to establish a biophysical platform, which combines smooth and nanofibrous topographies in a single protein scaffold to study the influence of topographical cues on cell growth independent of biochemical and mechanical signals. To disentangle these factors from the influence of topographical cues, a protein scaffold will be developed, which offers different topographies while maintaining the same mechanical and biochemical properties.

Collagen and fibrinogen scaffolds were used as model proteins since collagen is the most abundant protein in the ECM and fibrinogen is a key protein in wound healing, thus contributing to the assembly of ECM during tissue repair *in vivo*. Fibroblasts were used as a model cell line to study cell interaction with protein scaffolds with different topographies since it is a well-established model system for wound healing and tissue repair. Therefore, in this Ph.D. thesis study of fibroblast growth on topographically patterned collagen and fibrinogen scaffolds provided a representative model system to study fundamental principles of cell response to topographical cues.

The key question of this study consequently is:

How do cells respond to different topographies when biochemical and biomechanical cues remain the same?

Based on this question and the state-of-the-art in cell-material interactions **three hypotheses** were developed, which will be investigated in this work.

1. Nanofibrous protein scaffolds lead to morphological changes of cells: It is expected that cells grown on nanofibers exhibit smaller cell areas than on smooth scaffolds due to different topographical cues.
2. Cell proliferation is reduced on nanofibrous protein scaffolds due to a higher surface area and fewer cell-cell-contacts as compared to smooth substrates.
3. An increase in migration velocity is expected on nanofibrous protein scaffolds due to higher surface roughness in comparison to smooth scaffolds.

2. Materials and methods

In the following chapter, the preparation of protein scaffolds will be introduced, and cell culture procedures like viability assays, cell mechanical analysis, and live-cell tracking will be presented. Moreover, microscopy techniques including fluorescence microscopy, confocal fluorescence microscopy, scanning electron microscopy, and atomic force microscopy will be introduced.

2.1 Scaffold preparation

Surface modification was an essential tool to assemble collagen and fibrinogen scaffolds on the respective carrier substrates. The different surface modifications used in this work are presented in the following chapter.

2.1.1 Substrate preparation

Glass cover slides (VWR, Darmstadt, Germany) with a diameter of 15 mm were used to assemble nanofibrous protein scaffolds. To activate the surface and to remove all organic residues all glass slides were treated with piranha acid. Piranha acid was prepared in a ratio of 3:1 with 95% sulfuric acid (VWR) and 30% hydrogen peroxide (Sigma-Aldrich, Steinheim, Germany). The glass slides were immersed with the acidic solution for 5 min and subsequently washed with deionized water three times. The cover slides were stored in deionized water at 4 °C until further usage. Before protein assembly, all glass slides were dried with a nitrogen flow.

2.1.2 Collagen scaffolds

Collagen stock solutions with 5 mg ml⁻¹ and 1 mg ml⁻¹ were prepared by dissolving collagen type 1 from calfskin (Sigma-Aldrich) in a 5% acetic acid (VWR) solution.

For the preparation of smooth collagen scaffolds, 100 µl of 0.5% acetic acid solution was placed on piranha-cleaned glasses before 100 µl collagen stock solution was added. Collagen nanofibers were obtained by self-assembly induced by a pH shift (see Fig. 16). First, 10x PBS (pH 7.4) was added to the glass, followed by a 100 µl collagen solution in acetic acid (pH 3). During fiber assembly, the samples were placed in an ultrasound bath at room temperature and with a power of 42 kHz (Branson, USA) for 20 min to increase the surface coverage (Jiang *et al.* 2016).

To preserve fiber morphology and to stabilize the smooth collagen scaffold for subsequent cell culture studies the protein layers needed to be cross-linked. Crosslinking should preserve the substrate morphology but also not negatively influence the substrate biocompatibility. Different crosslinking methods were tested to establish a standard procedure for all substrates in this work.

Aldehydes

Aldehydes can be created wherever oxidizable sugar groups (also called reducing sugars) exist, (McIntosh 2018). However, they do not naturally occur in proteins or other macromolecules in typical biological samples. Reducing sugars are common monomer constituents of polysaccharides or carbohydrates in the post-translational glycosylation of many proteins. Furthermore, the ribose of RNA is a reducing sugar. A well-known mild agent for effectively oxidizing vicinal diols in carbohydrate sugars is periodic acid (HIO_4) from dissolved sodium periodate (NaIO_4), which yields reactive aldehyde groups. The carbon-carbon bonds are cleaved between adjacent hydroxyl groups (Customer Service Thermo Scientific).

Aldehydes are well known crosslinking agents that can inactivate, stabilize, or immobilize proteins (Metz *et al.* 2004). Formaldehyde, for example, is used for isotope labeling of proteins (Gold *et al.* 1996) or for studying protein-protein interactions and for fixations of cells and tissues (Metz *et al.* 2004). Likewise, glutaraldehyde is utilized for the fixation of cells and tissues (Tian *et al.* 2016). It was shown that aldehydes react first with the amino and thiol groups of amino acids and form methylol derivatives (see Fig. 14). The methylol groups partially undergo condensation to an imine, also called a Schiff-base. Successively, the imine can cross-link with asparagine, glutamine, tryptophan, arginine, histidine, cysteine, and tyrosine residues, leading to a methylene bridge (Metz *et al.* 2004).

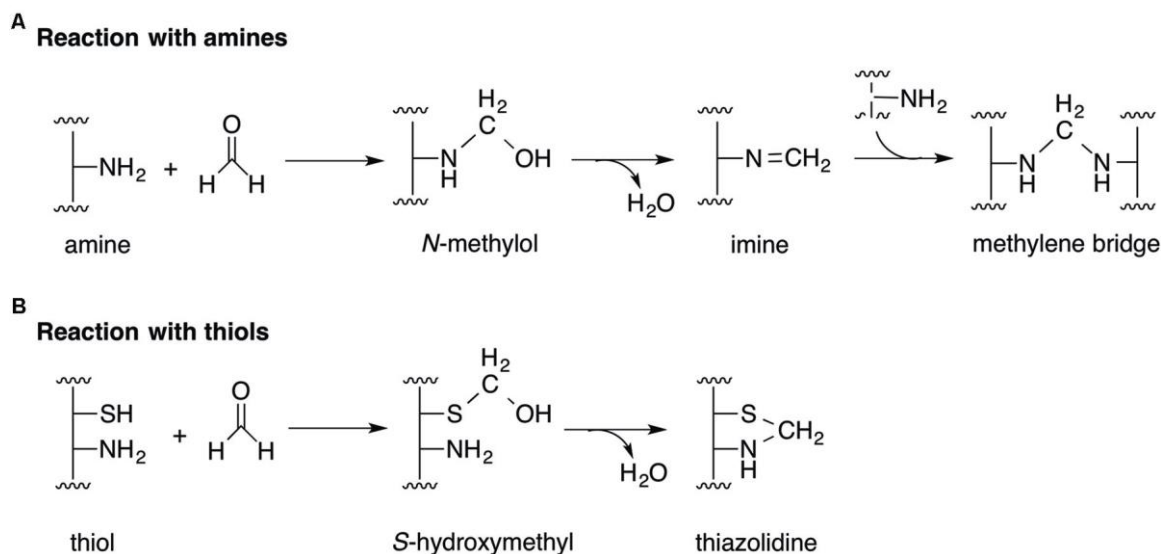


Figure 14. Aldehyde reaction mechanisms with proteins. The reaction of aldehydes with amines (A) result in methylene bridges. The reaction of aldehydes with thiols leading to thiazolidine (B) (Chen *et al.* 2016).

Glutaraldehyde crosslinking

Glutaraldehyde is a well-established cross-linker for proteins and cells (Peng *et al.* 2017). For crosslinking of collagen fibers and smooth collagen films the substrates were immersed with 400 μL of 2 % (v/v) glutaraldehyde in 1x PBS for 30 min. Substrates were washed with deionized water to remove excessive glutaraldehyde.

EDC

As aldehydes have shown to have cytotoxic potential, 1-ethyl-3-(3-dimethyl aminopropyl) carbodiimide hydrochloride (EDC) was explored as an alternative cross-linker for proteins (Powell and Boyce 2006; Gough *et al.* 2002). Firstly, EDC reacts with a carboxyl group and forms an amine-reactive O-acyl isourea intermediate that reacts with an amino group to form an amide bond and release of an isourea by-product. Carboxyl-to-amine crosslinking with the carbodiimide, EDC Molecules (1), and (2) can be peptides, proteins, or any chemicals that have respective carboxylate and primary amine groups (see Fig. 15) (URL 1).

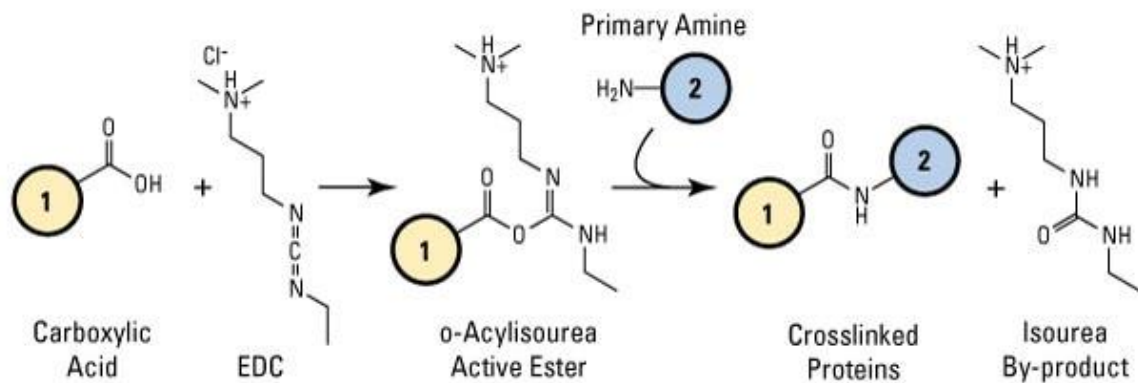


Figure 15. EDC crosslinking mechanism. One step EDC reaction with carboxyl and amine-containing molecules. Carboxylic acid reacts with EDC to o-acylisourea active ester. This reaction leaves the cross-linked proteins with primary amines and Isourea as a product. (URL 1)

For the crosslinking of collagen nanofibers, the scaffolds were incubated with a 50 mM EDC (Sigma-Aldrich) (Lai *et al.* 2018) in ethanol solution for 30 min and washed with 200 mM NH_4HCO_3 for 10 minutes. This procedure was carried out three times before the protein scaffolds were dried overnight.

Ultraviolet radiation crosslinking

Physical crosslinking methods for proteins result in non-covalent bonds (Reddy *et al.* 2015). For ultraviolet radiation crosslinking substrates were exposed to UV light of a laminar flow cabinet (ESI Flufrance, France) for 30 minutes. All samples were washed with 200 mM NH_4HCO_3 for 10 min three times and subsequently dried overnight.

Methanol crosslinking

Methanol is a coagulant fixative. Examples of coagulant fixatives are acetone and alcohol such as ethanol and methanol (MeOH). Alcohols fixate through coagulation without forming additive compounds, thus, they permit good antibody penetration while they do not block immunoreactive determinants (Yamanushi *et al.* 2015).

For methanol crosslinking collagen nanofibers were incubated with methanol in a sealed container at 4 °C for 30 min and subsequently washed with 200 mM NH_4HCO_3 for 10 min three times and subsequently dried overnight. After studying the influence of these different crosslinking methods on the nanofibrous topography glutaraldehyde crosslinking was chosen as the standard preparation procedure for collagen nanofibers. Collagen

samples were dried overnight under ambient conditions and were then crosslinked for 30 minutes using 2 % glutaraldehyde (GA) (AppliChem GmbH, Germany) in 1x PBS. Aldehyde residues were removed by three successive washing steps with 200 mM NH_4HCO_3 (Carl Roth GmbH, Germany). Before further analysis collagen scaffolds were dried under ambient conditions. A schematic overview of the established standard procedure for collagen nanofiber assembly is shown in Fig. 16.

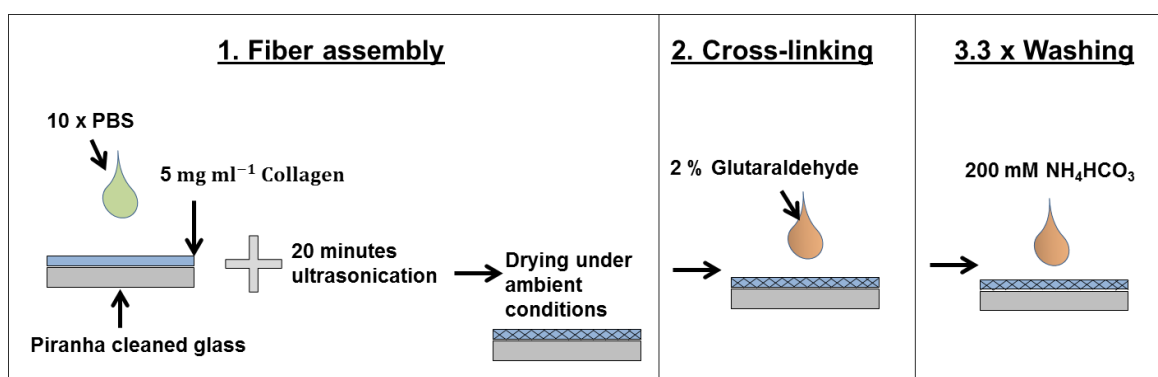


Figure 16. Collagen self-assembly process. The collagen fiber assembly is a four-step procedure. First, fiber assembly is initiated by a mixture of 10 x PBS with the collagen solution on an activated glass surface. To achieve high surface coverage the samples are exposed to ultra-sonication and subsequently dried under ambient conditions. The scaffolds are cross-linked with a 2% glutaraldehyde solution for 30 min and finally washed with 200 mM NH_4HCO_3 three times.

To determine, if the nanofiber assembly was independent of the carrier substrate, different substrates commonly used in cell culture were used as carrier substrates, such as polycarbonate, Lumox® Foil (Sarstedt, Nümbrecht, Germany) and glass, which was used in the standard protocol. Additionally, the biocompatible anodized aluminum oxide (AAO) membranes (Whatman, Sigma Aldrich, Taufkirchen, Germany) were tested as carrier substrates.

2.1.3 Fibrinogen scaffolds

Fibrinogen scaffolds were also assembled on transparent glass slides to facilitate subsequent microscopy analysis during cell culture studies. Nevertheless, to immobilize the fibrinogen scaffolds on the underlying glass a surface functionalization with amino groups was necessary, which was obtained by silanization with (3-Aminopropyl) triethoxysilane (APTES) (Seed 2001). The silanization process is displayed in Figure 17.

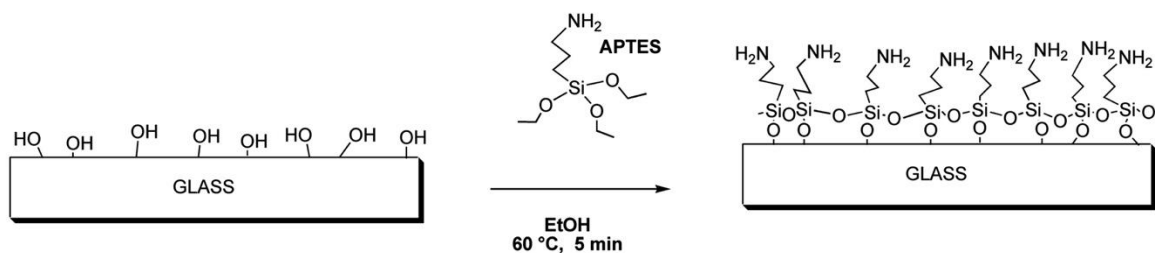


Figure 17. Scheme representing the silanization of glass surfaces with APTES (Taglietti *et al.* 2014)

To assemble and immobilize fibrinogen scaffolds on the underlying substrate piranha-cleaned glass slides were functionalized via silanization using APTES (Sigma Aldrich) (Butruk-Raszeja *et al.* 2016; Stapelfeldt *et al.* 2019a). First, a solution in a ratio of 5:95 of APTES with 100% ethanol was prepared. The glass slides were incubated in the APTES-ethanol solution for 16 h. Next, the glass slides were washed three times with 100% ethanol. The APTES coated glass slides were stored in dry ambient conditions.

Fibrinogen stock solutions were prepared by dissolving 10 mg ml⁻¹ fibrinogen (Merck, Darmstadt, Germany) in a 10 mM ammonium carbonate (Carl Roth GmbH) solution. The fibrinogen stock solution was dialyzed against 10 mM ammonium carbonate solution overnight using cellulose membrane dialysis tubing with 14 kDa cut-off (Sigma) to remove low molecular weight compounds (Stapelfeldt *et al.* 2019a).

Nanofibrous fibrinogen scaffolds were fabricated by the recently introduced salt-induced self-assembly process (Stapelfeldt *et al.* 2019a). Smooth fibrinogen layers were prepared by incubation in an aqueous fibrinogen solution. All solutions were prepared with deionized water from a TKA water purification system (Thermo Fisher Scientific, Schwerte, Germany). Planar fibrinogen (Merck) layers were prepared by drying a final concentration of 5 mg ml⁻¹ fibrinogen in 5 mM NH₄HCO₃ for 12 h using a self-built climate chamber at a relative humidity of 30 %. Fibrinogen nanofiber scaffolds were prepared in the presence of 2.5x PBS (pH 7.4) during the 12 h drying process (see Fig. 18).

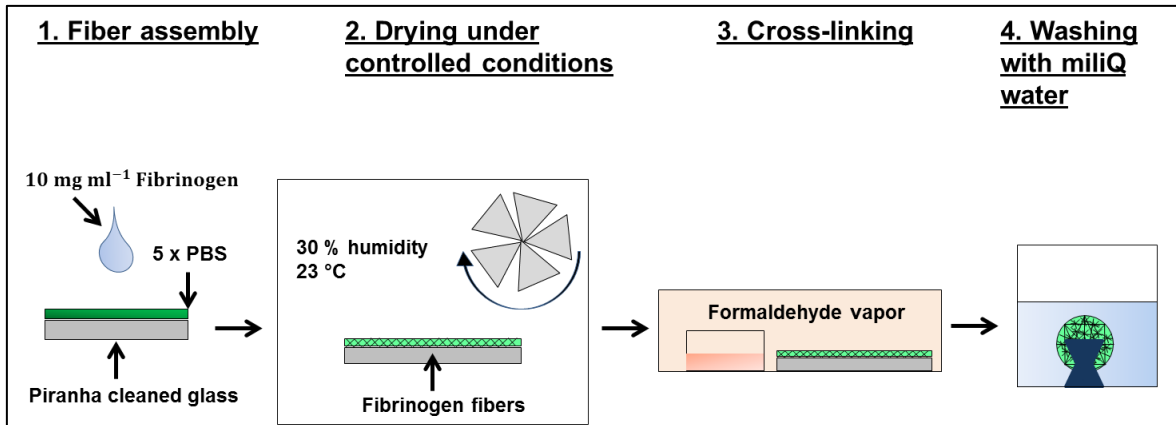


Figure 18. Fibrinogen fiber self-assembly process. The fibrinogen fiber assembly is a four-step procedure. First, the fiber assembly is initiated by the mixture of 5X PBS with the fibrinogen solution on an activated and silanized glass surface, followed by drying under controlled temperature and humidity. The scaffolds are then cross-linked with 37% formaldehyde vapor for 2 h and subsequently washed with deionized water four times for 15 min.

Formaldehyde is a well-established cross-linker for proteins and cells (Gold *et al.* 1996). Fibrinogen scaffolds were cross-linked in formaldehyde vapor, as they are soluble in an aqueous environment (Stapelfeldt *et al.* 2019a). For this procedure the samples were placed in a sealed beaker for 2 h. $1 \mu\text{l}$ of a 37% formaldehyde solution per cm^3 was added into the beaker and allowed to evaporate. After crosslinking the samples were washed with deionized water (Stapelfeldt *et al.* 2019b).

2.1.4 Protein scaffolds with nanofibrous and smooth topography

To prepare collagen and fibrinogen patterns with nanofibrous and smooth topographies in the same scaffold, one-half of the glass slides was initially covered with a polymer mask consisting of Fixogum (Marabu GmbH + Co. KG, Germany) (see Fig. 19).

Collagen nanofibers were assembled with PBS on the accessible glass surface and dried overnight. Subsequently, the protein fibers were crosslinked, washed, according to their respective standard protocol described before, and the mask was removed. Next, the other half of the glass surface was manually coated with collagen in acetic acid to prepare a smooth collagen film and dried overnight.

Fibrinogen nanofibers were assembled as described in chapter “2.3.3 Fibrinogen”. Subsequently, the protein fibers were crosslinked, washed, according to their respective standard protocol described before, and the mask was removed. Smooth fibrinogen areas

were assembled by mixing fibrinogen and water and dried under controlled conditions. Another fixation and washing step were carried out until the patterned samples were finally dried overnight (see Fig. 19).

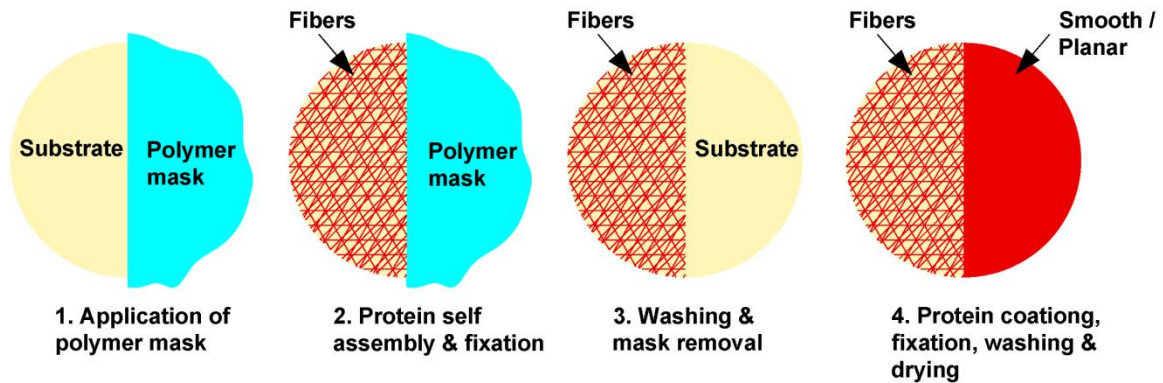


Figure 19. Schematic overview of binary protein scaffold assembly process. The shown scheme shows the standard procedure used throughout this study. In a first step, a polymer mask was added on the substrate covering half of the carrier substrate. In the second step, protein fibers were assembled and cross-linked. In the third step, the polymer mask was removed and the samples were washed. In the fourth step, a smooth protein layer was assembled, fixated, washed, and finally dried.

In the further development of topographically patterned protein scaffolds, different variations of the above-mentioned protocol were exemplarily explored with collagen to improve the reproducibility.

- a) The Fixogum mask was replaced with a Polydimethylsiloxane (PDMS) mask (Distrelec, Bremen, Germany).
- b) In a second approach, nanofibers were assembled as described above, then cross-linked and washed before the PDMS mask was transferred onto the fibrous region while the smooth protein layer was prepared. The smooth collagen film was prepared, and after drying and crosslinking of the smooth region the PDMS mask was removed from the nanofibers.
- c) The smooth protein film was prepared in a first step on the accessible side of the glass, dried and subsequently crosslinked and washed. Subsequently, a PDMS mask was used to cover the smooth collagen film. Collagen nanofibers were then assembled on the accessible side of the glass and dried overnight, crosslinked washed and dried overnight.

The binary patterned scaffolds allow control over topographical cues in selected scaffold regions. The tailoring of biochemical cues with different ECM proteins during topographical patterning would provide an important addition in the introduced model system. To establish such binary patterned scaffolds, which are composed of two different proteins and exhibit different topographical cues, three different approaches were conducted to combine smooth and fibrous topographies. Exemplarily, collagen, and fibrinogen were used in these experiments. To assure the immobilization of fibrinogen scaffolds, both proteins were assembled on APTES-coated glass cover slides.

- I) In the first approach samples combining nanofibrous collagen and nanofibrous fibrinogen were prepared (see Fig. 20). In the first step, one half of the cover slide was covered with a PDMS mask and nanofibrous collagen prepared with 2.5 mg ml^{-1} collagen was assembled according to the standard protocol described above. After a drying step the collagen fibers were cross-linked with glutaraldehyde and washed according to the standard protocol. In a second step, the PDMS mask was removed and fibrinogen nanofibers were assembled with 5 mg ml^{-1} , cross-linked with formaldehyde vapor, and washed according to the standard procedure. The collagen nanofibers were not covered during this process.

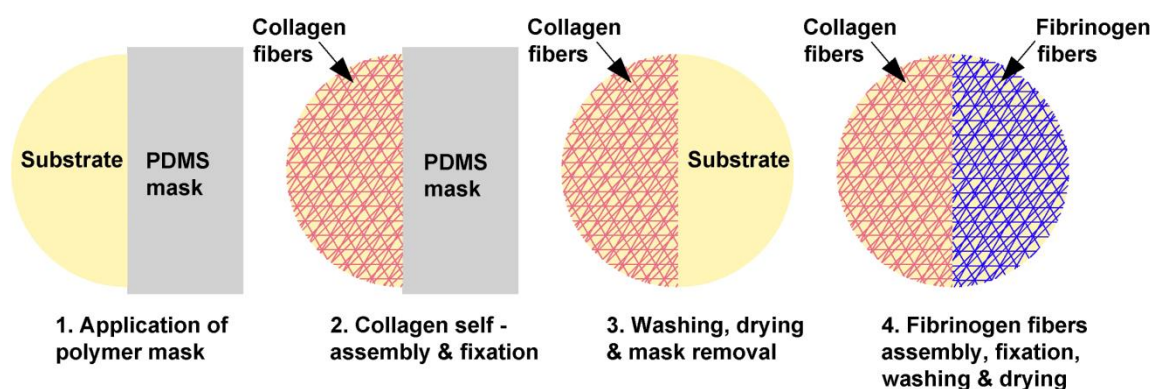


Figure 20. Schematic overview of binary type 1 (collagen fibers and fibrinogen fibers) protein scaffold assembly process. In the first step, the glass substrate was half-covered with a PDMS mask. In the second step, collagen nanofibers were assembled according to the standard protocol on the free-standing substrate and subsequently cross-linked with 2% GA. In the third step, the collagen fibers were washed and the PDMS mask was removed after a drying step. In a third step, fibrinogen nanofibers were assembled on the other half of the substrate according to the standard protocol, fixated with FA vapor, washed, and lastly dried under ambient conditions.

II) The second scaffold type combined collagen nanofibers prepared with 2.5 mg ml^{-1} and smooth fibrinogen prepared with 5 mg ml^{-1} (see Fig. 21). In the first step, one half of the cover slide was covered with a PDMS mask and smooth fibrinogen prepared with 5 mg ml^{-1} fibrinogen was assembled, cross-linked, and washed according to the standard protocol described above. In a second step, the PDMS mask was removed and the smooth fibrinogen layer was covered with a PDMS mask. Collagen nanofibers prepared with 2.5 mg ml^{-1} were assembled, cross-linked, and washed according to the standard procedure. After a drying step the polymer mask was removed.

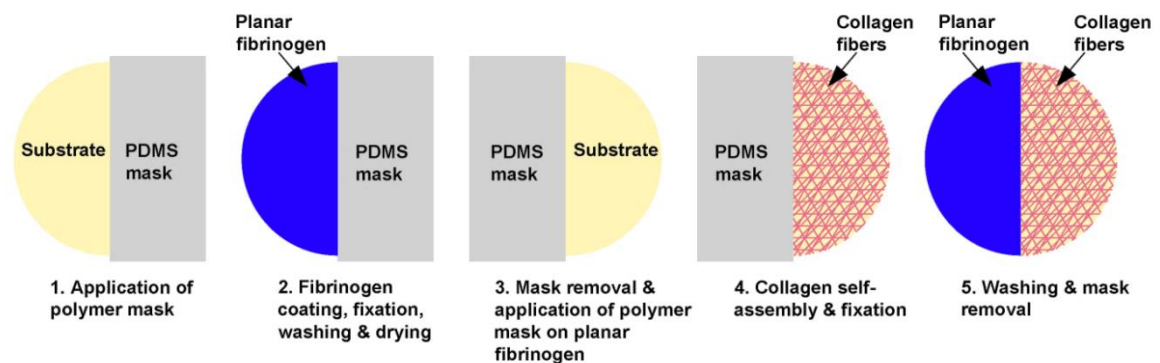


Figure 21. Schematic overview of binary type 2 (smooth fibrinogen and collagen fibers) protein scaffold assembly process. In the first step, the glass substrate was half-covered with a PDMS mask. In the second step, the free-standing substrate was coated with smooth fibrinogen and subsequently cross-linked FA vapor. In the third step, the smooth fibrinogen was washed and dried. In a third step, the PDMS mask was removed and the smooth fibrinogen was covered with a PDMS mask. Collagen nanofibers were assembled on the now free-standing substrate area according to the standard protocol, fixated with 2% GA, washed and lastly dried under ambient conditions after removing the PDMS mask.

III) The third sample type combined fibrinogen nanofibers prepared with 5 mg ml^{-1} and smooth collagen prepared with 2.5 mg ml^{-1} in a single scaffold (see Fig. 22). In the first step, one half of the cover slide was covered with a PDMS mask and smooth collagen prepared with 2.5 mg ml^{-1} collagen was assembled, cross-linked, and washed according to the standard protocol described above. In a second step, the PDMS mask was removed and the smooth collagen layer was covered with a PDMS mask. Fibrinogen nanofibers prepared with 5 mg ml^{-1} were assembled, cross-linked, and washed according to the standard procedure. After a drying step, the PDMS mask was removed.

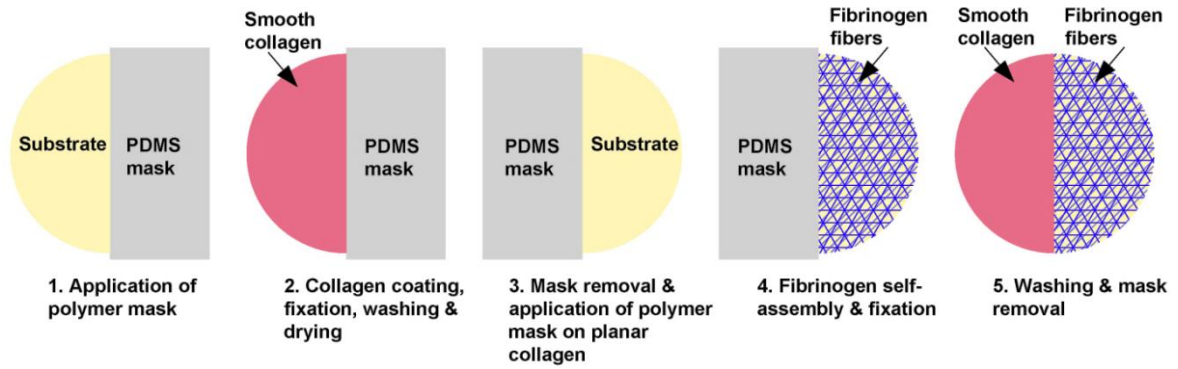


Figure 22. Schematic overview of binary type 3 (smooth collagen and fibrinogen fibers) protein scaffold assembly process. In the first step, the glass substrate was half-covered with a PDMS mask. In the second step, the free-standing substrate was coated with smooth collagen and subsequently cross-linked with 2% GA. In the third step, the smooth collagen was washed and the PDMS mask was removed after a drying step. In a third step, the smooth collagen was covered with a PDMS mask. Fibrinogen nanofibers were assembled on the now free-standing substrate area according to the standard protocol, fixated with FA vapor, washed, and lastly dried under ambient conditions after removing the PDMS mask.

2.2 Characterization of scaffolds

All microscopy techniques used for the characterization of protein scaffolds with a focus on the substrate topography and subsequent cell culture studies are presented in the following subchapters.

2.4.1 Scanning electron microscopy

To analyze collagen and fibrinogen scaffold topography on a nanometer length scale scanning electron microscopy (SEM) was performed.

SEM analysis of collagen substrates, fibrinogen scaffolds was conducted with a Zeiss Auriga field emission device (Zeiss, Oberkochen, Germany). Dried collagen or fibrinogen samples were sputter-coated with 7 nm of gold in a Bal-tec SCD 005 sputter system (Leica Microsystems GmbH, Wetzlar, Germany). All SEM measurements were performed with an operating voltage of 3 kV.

Fiber diameters of collagen and fibrinogen fibers obtained from SEM images were analyzed with the BoneJ plugin for the open-source software ImageJ provided by the NIH (Rueden *et al.* 2017). Three different samples were analyzed (n=3). Five images for each respective sample were analyzed. Results are shown means \pm standard deviation.

2.4.2 Atomic force microscopy

To analyze the topography of collagen and fibrinogen scaffolds in dry and wet conditions an MFP3D atomic force microscope (AFM, Asylum Research, Santa Barbara, CA, USA) was used. An optical light microscope was combined with the AFM to control the scanning process. Surface topography analysis of dried collagen and fibrinogen scaffolds was conducted in ambient air. Topographical analysis in the wet environment was carried out after rehydration in Dulbecco's Modified Eagle's Medium (DMEM) (Merck). Silicon nitride cantilevers (MLCT Bio, Bruker, Wissembourg, France) with average nominal resonant frequencies of 38 kHz and a nominal spring constant of 0.1 N m^{-1} were used. Height profiles were measured in contact mode with a scan rate of 1 Hz and 256 scanning lines. For roughness analysis height profiles of $5 \mu\text{m} \times 5 \mu\text{m}$ were analyzed with an ROI of $1 \mu\text{m}$ scanning the complete image (25 measurements). Three independent samples were analyzed; three height profiles for each sample and 25 measurements on each height profile image were conducted. The given values represent the average roughness with standard deviations.

The analysis of the mechanical properties of fibrous and smooth collagen or fibrinogen was carried out with the same device. First, the spring constant of the cantilever was calibrated by using a thermal tune method (Hutter and Bechhoefer 1993). Successively, force curves were recorded in random positions of the substrates. Typically, a scan rate of 1 Hz was used, which corresponds to a maximum loading rate of 1 nN s^{-1} and a maximum force of 1 nN. The used indentation depth was 100 nm. At least 3 independent samples were measured for each substrate type with an indentation depth of 100 nm. A minimum of 100 force curves was acquired over an area of $5 \times 5 \mu\text{m}$ in the form of grids, called force maps or volumes.

A schematic of an indentation of a cantilever in a biological sample is given in Figure 23.

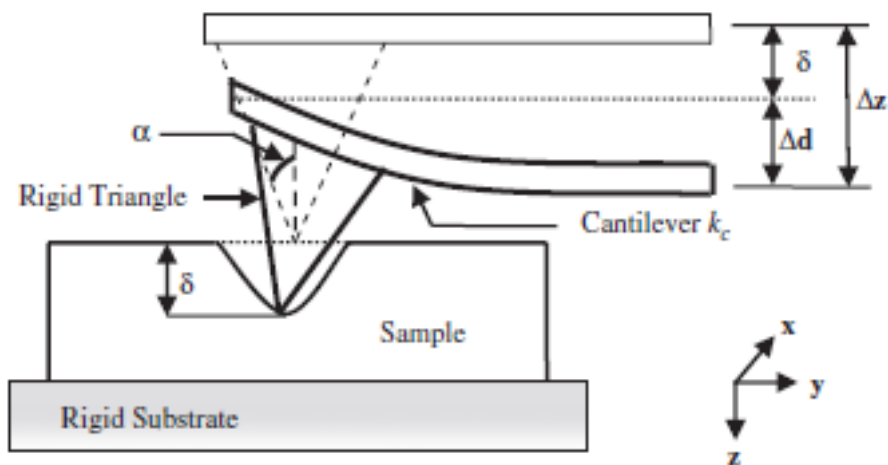


Figure 23. Schematic of indentation: indentation of a thin biological sample by a triangle probe (Zhu *et al.* 2011).

Typical force curves for hard and soft substrates are depicted in Figure 24. Hard substrates result in force-distance curves with a slope of approximately 1, whereas, force-distance curves on soft substrates are flat and show a slope smaller than 1 (Fig. 24 A). The retract curve in Figure 24 B shows an adhesion on a stiff substrate. This could happen on sticky substrates such as protein layers. Molecule–molecule and cell–surface detachment process with three unbinding events are visible in the retract curve in Figure 24 C.

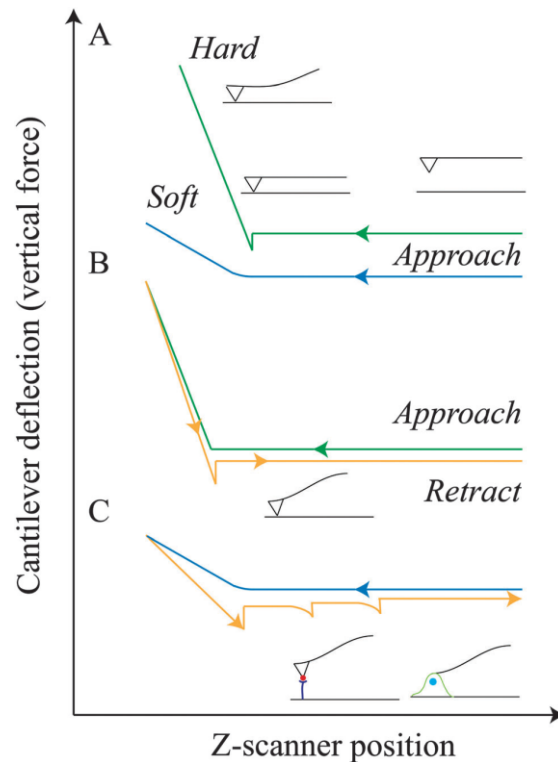


Figure 24. Typical force-distance curves for hard (green) and soft (blue) materials (A). Adhesion on a hard surface (B). Molecule–molecule and cell–surface detachment process with three unbinding events (C). (Variola 2015)

The statistical analysis of AFM experiments was conducted with the data analysis package IGOR (Wavemetrics, Lake Oswego, OR, USA).

2.3 Cell interaction with protein scaffolds

To study the response of cells to protein scaffolds with different topographies viability assays, morphology analysis, cell mechanical characterization, and live-cell tracking were conducted.

2.6.1 Cultivation

Adherent NIH 3T3 mouse fibroblasts (ATCC CRL1658, a kind gift from Louis Lim, Institute of Molecular and Cell Biology ASTAR Singapore) were used as a model system to study the interaction with topographically patterned collagen scaffolds. Fibroblasts were cultivated using DMEM cell culture medium (Biochrom GmbH, Germany) with an additional 1 % (v/v) penicillin and streptomycin and 5 % (v/v) fetal bovine serum (FBS) (Sigma-Aldrich).

Adherent NIH 3T3 mouse fibroblasts (CLS Cell Lines Service, Eppelheim, Germany) were used as a model system to study the interaction with topographically patterned fibrinogen scaffolds. Fibroblasts were cultivated using DMEM cell culture medium (Merck) with an additional 2 % (v/v) penicillin and streptomycin and 10 % (v/v) fetal bovine serum (FBS) (Sigma-Aldrich). The cells were subcultured at a confluence of approximately 80 % and transferred into a fresh 25 cm² cell culture flask (Sarstedt) for further cultivation under physiological conditions. For splitting, the cell medium was aspirated, and the cell layer was washed carefully with phosphate-buffered saline (PBS) followed by incubation with 1 mL trypsin/EDTA solution (1 % (v/v), diluted in PBS) for 3 minutes at 37 °C. The enzymatic reaction was stopped through dilution with DMEM medium, followed by centrifugation at 1300 rpm min⁻¹ for 3 min. For further cultivation, approximately 1.2 x 10⁵ cells were seeded in cell culture flasks with 25 cm².

Before cell seeding, collagen and fibrinogen scaffolds were sterilized in the UV light of a laminar flow cabinet (ESI Flufrance) for 30 minutes.

For proliferation and morphology studies, collagen and fibrinogen scaffolds were paced in 12-well-plates (Greiner-Bio-One, Germany) and fibroblasts were seeded with a density of 7500 cells cm⁻². Fibroblasts were incubated on the different scaffolds for 24 h, 48 h, and 72 h, respectively, at 37 °C with 5 % CO₂. For AFM analysis of cell mechanics on collagen, cell migration tracking, and morphological analysis with SEM after 36 h on collagen and fibrinogen scaffolds a density of 12,500 cells cm⁻² was used. Cell mechanics were measured between 24 h and 33 h incubation time. Cell migration analysis was carried out between 24 h and 40 h.

2.6.2 Viability assays

To study the cell viability on different protein scaffolds two different methods were used. A LIVE/DEAD® staining was conducted on collagen scaffolds with different topographies. The metabolic WST-1 viability assay was performed to study the metabolic activity of fibroblasts on collagen and fibrinogen scaffolds. The experimental details will be described in the following paragraphs.

LIVE/DEAD® staining

To determine the cell viability a calcein assay was initially conducted. Living cells can be distinguished by the presence of ubiquitous intracellular esterase activity, which can be determined by the enzymatic conversion of the nonfluorescent cell-permeant calcein AM

(Affymetrix, Thermo Fisher Scientific, Germany) to the strongly fluorescent calcein emitting green fluorescence (ex/em ~495 nm/~515 nm) (Bratosin *et al.* 2005). Ethidium Homodimer-1 (EthD-1, Promokine, PromoCell GmbH, Heidelberg, Germany) only enters cells with disrupted membranes and undergoes a 40-fold enhancement of fluorescence when binding to nucleic acids, thus emitting a red fluorescence in dead cells (ex/em ~495 nm/~635 nm). The intact plasma membrane of viable cells excludes EdthD-1 (Kummrow *et al.* 2013).

Dead cells were used as a positive control (PC), which were killed by incubating them with 1 % 100 X Triton (v/v) (Carl Roth GmbH) in 1 x PBS for 30 min at 37 °C. All samples were washed with pre-heated 1 x PBS once, before immersing them with 2 µM calcein-AM and 4 µM EthD-1 in 1x PBS (Siriwardane *et al.* 2014). After 1 h incubation at 37 °C, cells on collagen scaffolds were imaged with 20 x magnification.

A Nikon Eclipse Ti-E –V5.30 inverted fluorescence microscope (Nikon, Tokyo, Japan) was used for phase contrast and fluorescence imaging of substrates and cell samples. For LIVE/DEAD® staining ten images with 20x magnification were taken. Dead cells were imaged at an emission wavelength of 617 nm and living cells were imaged at an emission wavelength of 395 nm.

WST-1 assay

(2-(4-Iodophenyl)-3-(4-nitrophenyl)-5-(2,4-disulfophenyl)-2H-tetrazolium sodium salt (WST-1) is a colorant, which is used in common proliferation assays to determine cell viability. The WST-1 is cleaved to a soluble formazan by a complex cellular mechanism that occurs primarily at the cell surface (Berridge *et al.* 2005). This bioreduction is largely dependent on the glycolytic production of NAD(P)H in viable cells. Hence, the amount of formazan dye formed directly correlates to the number of metabolically active cells in culture. Cell proliferation and viability assays are of particular importance for routine applications in cell biology. Tetrazolium salts (e.g. WST-1) are predominantly useful for this type of analysis. Tetrazolium salts are cleaved to formazan by the succinate-tetrazolium reductase system (EC 1.3.99.1), which belongs to the respiratory chain of the mitochondria, and is only active in metabolically intact cells (see Figure 25).

In this study, tetrazolium salt (WST-1) (Roche Diagnostics, Germany) was diluted in incubation buffer at a ratio of 1:50 to measure the cell proliferation on collagen and fibrinogen scaffolds after 24 h, 48 h, and 72 h. After removing the cell culture medium

cells were incubated with 1 mL WST-1 solution for 2 h. The absorption of the supernatant was photometrically measured in a Cecil CE 1021 device (Cecil, Cambridge, UK) at 450 nm. All shown results represent three independent experiments (n=3) for collagen substrates and four independent experiments (n=4) for fibrinogen scaffolds with triplicates for each substrate type.

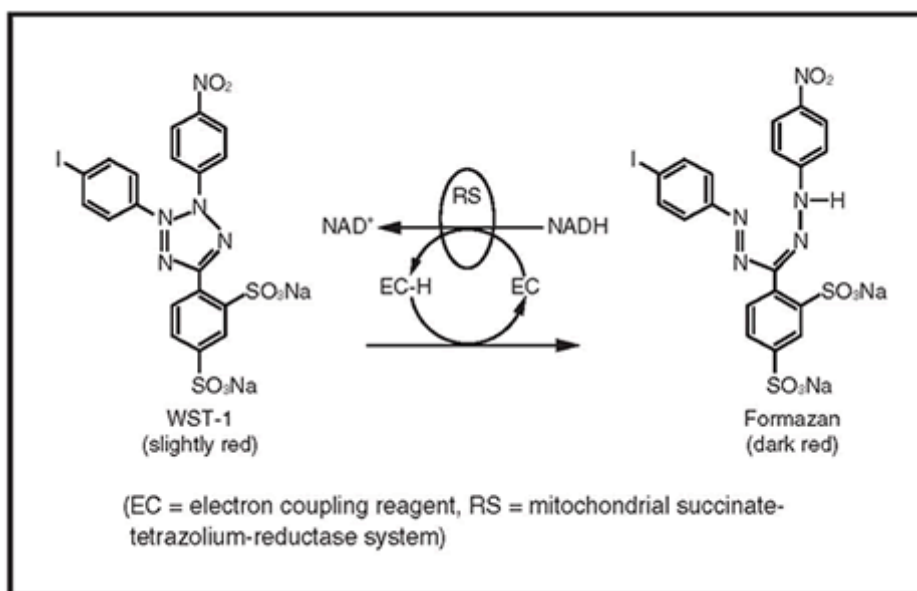


Figure 25. Cleavage of tetrazolium salts to formazan. The WST-1 is cleaved to a soluble formazan by a complex cellular mechanism that occurs primarily at the cell surface (EC = electron coupling reagent; RS = mitochondrial succinate-tetrazolium reductase system) (URL 2)

For the quantification of cell viability, the negative control was assigned to 100 % viability (Khalilpour *et al.* 2010). The data analysis was performed according to DIN EN ISO 10993-5 which suggested that the cytotoxic potential of a sample is given at viability values below 70 % of the negative control (EN ISO 10993-5:2009). Consequently, the lower the viability of the cells, the higher the cytotoxic effect of the test sample. For the calculation of the cell viability of sample extracts in comparison to the negative control the following equation was used (Equation 1):

$$Viability (\%) = \frac{100 * OD_{450\ sample}}{OD_{450\ nc}}$$

Equation 1: Equation for the calculation of the cell viability. The cell viability of the negative control (nc) was assigned to represent 100 % viability. OD_{450nc} describes the optical density of the mean value of the negative control, while the optical density of the mean value of the sample is defined by the $OD_{450sample}$.

The results of cell viability data were analyzed using one-way ANOVA and *t*-test analysis for simple linear regression. P-values less than or equal to 0.05 were considered statistically significant. Statistical analyses were done with Graphpad Prism software. The data of these experiments are presented as mean \pm standard deviation. Statistical parameters including the standard deviation, linearity, and normal distribution were determined.

2.6.3 Morphological analysis

As mentioned above the cell morphology can differ dependent on the extracellular environment. To analyze the influence of collagen and fibrinogen scaffold topography on cell growth the fibroblast morphology was analyzed using different methods like fluorescence microscopy, confocal microscopy, and scanning electron microscopy. Each method will be described in more detail in the following subchapters.

2.6.5 Fluorescence microscopy

To analyze the cell morphology and to examine the cell area on collagen and fibrinogen scaffolds double fluorescence staining of actin (phalloidin) and nuclei (DAPI) was performed. The fluorescence staining was used for different purposes in this study. The fluorescence staining in combination with the fluorescence microscopy allows visualizing the cells on most surfaces, other than the light microscopy.

4',6-Diamidin-2-phenylindol (DAPI) is a nuclear counterstain for fixed cells that emits blue fluorescence when bound to DNA (Wilson *et al.* 1990). Actin was stained with Actin Red™ (Actin Red™ 555 ReadyProbes® Reagent). Actin Red™ is a selective, high-affinity F-actin probe conjugated to, photostable, red-orange-fluorescent Alexa Fluor® 555 dye (URL 3). Phalloidin is a bicyclic peptide that belongs to a family of toxins isolated from the deadly *Amanita phalloides* “death cap” mushroom (Lengsfeld *et al.* 1974). It is commonly used in imaging applications to selectively label F-actin in fixed cells, permeabilized cells, and cell-free experiments. Labeled phalloidin conjugates have a similar affinity for both large and small filaments and bind in a stoichiometric ratio of about one phalloidin per actin subunit

in both muscle and non-muscle cells; they reportedly do not bind to monomeric G-actin, unlike some antibodies against actin (DesMarais *et al.* 2019).

In the present study, cells were fixed in 2 % (v/v) glutaraldehyde (GA) in PBS for 30 minutes and washed in PBS one time for 10 min. Subsequently, actin was stained with Actin Red™ (Actin Red™™ ReadyProbes® Reagent) (Life Technologies Europe BV, Netherlands) for 30 min, followed by nuclei staining with DAPI (NucBlue® Live ReadyProbes™ Reagent (R37605)) (Life Technologies Europe BV) for 30 min. After washing in PBS the stained samples were mounted to glass slides with Prolong™ Gold antifade mounting medium (Thermo Fisher Scientific). Subsequently, fibroblasts were imaged at 40x and 60x magnification using an inverted fluorescence microscope (Ti-E–V5.30, Nikon) and appropriate filter settings ($\lambda_{\text{ex}} = 549 \text{ nm}$; $\lambda_{\text{em}} = 565 \text{ nm}$ for Actin Red and $\lambda_{\text{ex}} = 330\text{-}380 \text{ nm}$; $\lambda_{\text{em}} = 435\text{-}485\text{nm}$ for DAPI). Phase-contrast images and fluorescence images in the red and blue channels were then analyzed using the open-source software ImageJ.

A Nikon Eclipse Ti inverted fluorescence microscope was used for phase contrast and fluorescence imaging of substrates and cell samples. For cell shape index (CSI) analysis 10 to 15 images with 40x magnification were taken per sample. Actin was imaged at an emission wavelength of 565 nm and Dapi labeled nuclei were imaged at an emission wavelength of 461 nm.

2.6.5.1 Cell shape

Fluorescence images of 3T3 fibroblasts on scaffolds prepared with 0.5 mg ml^{-1} collagen were analyzed with the ImageJ function “analyze particles” by setting a threshold in the images taken with the 40 x objective. Particles – in this case, each particle represents a single cell – were analyzed to obtain information about the fibroblast morphology. Area (A) and perimeter (P) of 20 single cells per sample were measured. Only fibroblasts cultured on samples prepared with 0.5 mg ml^{-1} collagen were used for quantitative cell analysis to minimize the autofluorescence of collagen crosslinked with glutaraldehyde (Lee *et al.* 2013). Furthermore, the cell shape index (CSI) was obtained by analyzing fluorescence images with ImageJ, using the following equation as previously described by Muthusubramaniam *et al.* (Muthusubramaniam *et al.*, 2012):

$$CSI = \frac{4 * \pi * A}{P^2}$$

Equation 2: Equation for the calculation of the CSI. The CSI was represented as the circularity of the cells. The area (A) and perimeter (P) were determined with image J. A CSI value of 1 stands for a perfect circle and a CSI of 0 would represent a line.

Equation 2 describes the calculation of the CSI with A being the area and P is the perimeter of the cell. With this equation, a value between 0 and 1 is calculated in reference to the circularity of the cell. The closer the value to 0, the more elongated the cell. If the CSI reaches 1, the cell is completely circular (Gruschwitz *et al.*, 2010). Furthermore, the total area of cells was measured by ImageJ and used to calculate the coverage of the samples in percent. An exemplary CSI analysis is shown in Fig. 26.

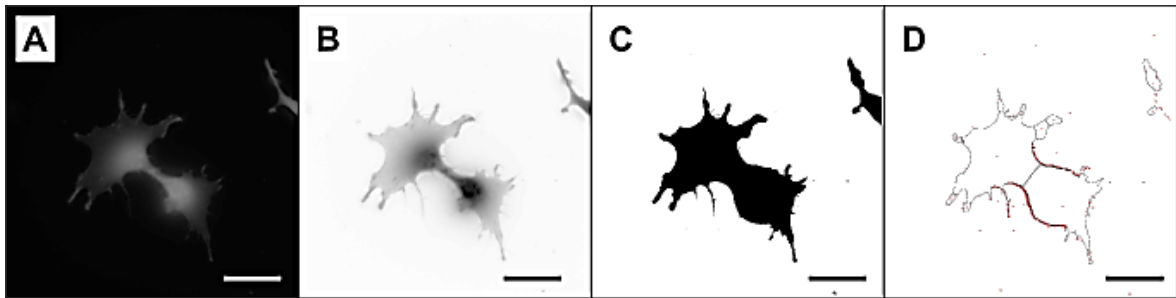


Figure 26. Exemplary steps of CSI analysis. Original fluorescence image of the fibroblast actin channel Alexa 555 (A), inverse image converted to 8-Bit image (B), the same image with adjusted grey values (C), and the edges of the actin cytoskeleton recognized by ImageJ (D). Scale bars represent 40 μm .

The area covered by cells was analyzed by only considering the actin channel (red). After adjusting the threshold settings it was possible to determine the covered area with the “particle analyze” function. The distribution of cell size, perimeter, CSI, and cell covered area was displayed using the software GraphPad Prism (GraphPad, San Diego, CA). The results of cell area, perimeter, CSI, and cell-covered scaffold area analysis were analyzed using one-way ANOVA and *t*-test analysis for simple linear regression. P-values less than or equal to 0.05 were considered statistically significant. Statistical analyses were done with Graphpad Prism software. Four independent experiments (n=4) with triplicates were conducted. For each sample, 20 cells were analyzed. The data of these experiments are

presented as mean \pm standard deviation. Statistical parameters including the standard deviation, linearity, and normal distribution were determined.

2.4.4 Confocal microscopy

To study the cell morphology on collagen and fibrinogen scaffolds with a higher resolution confocal microscopy was performed using an LSM880 system with Airyscan (Carl Zeiss). All shown images were taken with a 40 x magnification. Actin was imaged at an emission wavelength of 565 nm and Dapi labeled nuclei were imaged at an emission wavelength of 461 nm. All samples were bleached for 10 min at a wavelength of 565 nm before imaging with confocal microscopy to reduce the autofluorescence of collagen and fibrinogen scaffolds.

2.6.3.1 Scanning electron microscopy

To analyze cells cultivated on collagen and fibrinogen scaffolds in the SEM, samples were cross-linked and dried using an ethanol exchange approach, whereby the samples were dried in small steps and preserved their shape. After 24 h, 36 h, 48 h, and 72 h, respectively, the samples were crosslinked with 2 % (v/v) GA in 1x PBS for 2 h, followed by three rinsing steps with 200 mM NH_4HCO_3 for 5 min to remove remaining salt crystals. The samples were kept in a volume of 2 mL 200 mM NH_4HCO_3 . For rehydration, 50 % of the volume was replaced by ethanol absolute (VWR International) to reach an ethanol concentration of 50 % in the first step. The samples were incubated with 50 % ethanol for 2.5 h. The step was repeated and the samples were incubated at an ethanol concentration of 75 % and 4 °C overnight. The ethanol concentration was increased successively with 4 more exchange steps with incubation times of 15 min resulting in a final ethanol concentration of 98.4 % (Brüggemann, 2010). Finally, the remaining liquid was removed and the samples were dried at room temperature. Cell samples were fixated with 2 % glutaraldehyde (GA) solution and cells grown on fibrinogen scaffolds were fixated with 4 % formaldehyde (FA) vapor. Subsequently, all samples were dried by ethanol exchange before they were sputter-coated with gold.

The cell morphology and cell interaction with the respective substrates were analyzed with SEM. SEM analysis of fixated cells was conducted with a Zeiss Auriga field emission device (Carl Zeiss). The samples were sputter-coated with 7 nm of gold in a Bal-tec SCD 005 sputter system (Leica Microsystems GmbH). All SEM measurements were performed with an operating voltage of 3 kV.

2.6.4 Cell mechanics

To analyze the mechanical characteristics of 3T3 fibroblasts on collagen scaffolds an MFP3D atomic force microscope (AFM, Asylum Research) was used. An optical light microscope was combined with the AFM to control the scanning process. Following, the fibroblast stiffness on different collagen scaffolds was measured with MLCT-BIO cantilevers. To average the stiffness over a large contact area, the indentation depths were always between 200 nm and 500 nm giving values that do not depend on local variations of the cytoskeleton structure (Pogoda *et al.* 2012). After 24 h growth time on the respective substrate types cell samples were transferred to the AFM and constantly supplied with CO₂. The AFM tip was approached to each fibroblast in an area close to the cell nucleus (see Fig. 27), where the cell reaches its maximum height. This process can be seen in the approach and retract curves showing the deflection of the cantilever (see Fig. 27 B). A minimum of 17 cells per substrate type was analyzed. A minimum of 100 force curves was acquired over an area of 5 × 5 μm in the form of grids, called force maps or volumes.

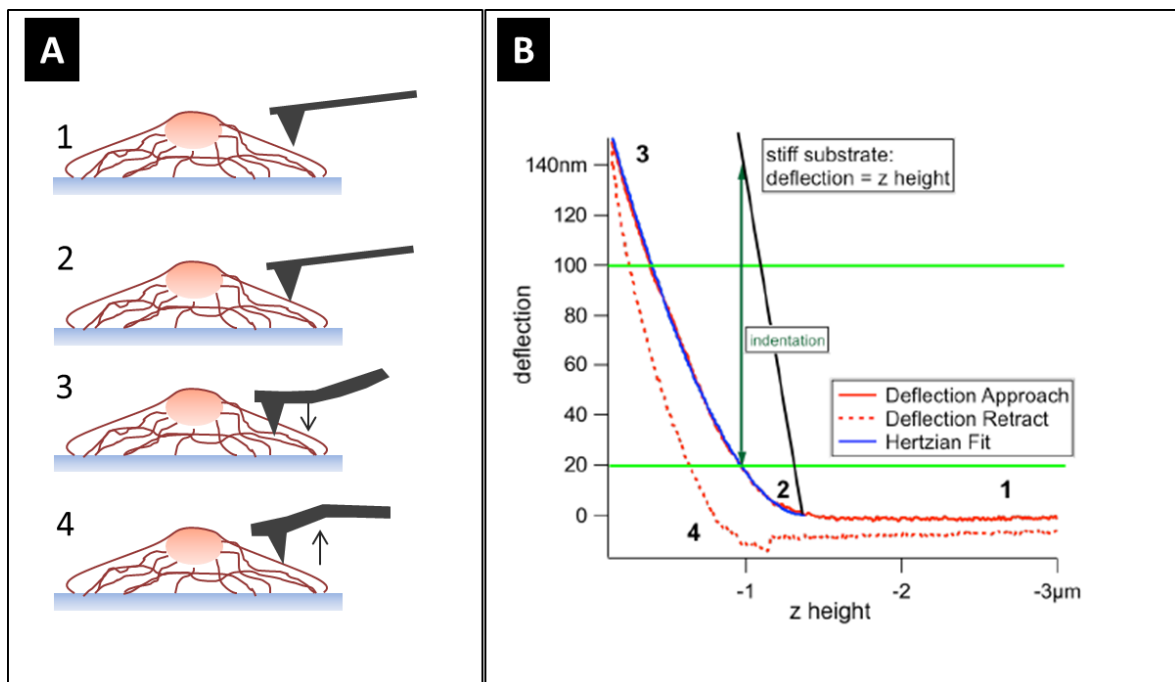


Figure 27. AFM force curve on a cell. Schematic representation of cantilever and cell (A); the cantilever is first free in air (1), then in contact with the cell (2), indenting the sample (3), and finally retracted (4). AFM approach and retract force curves (B). Numbers 1 to 4 correspond to those of the sketch in (A), the blue curve represents the Hertz fit. (adapted from Rianna and Radmacher 2016).

Dil Vybrant™ cell-labeling solutions (Fisher Scientific) were used to stain the lipid membrane of 3T3 fibroblasts on different substrates during live-cell tracking. Dil was prepared in DMEM medium with 5 μ l Dil of 1 mM in ethanol Dil solution in 9995 μ l DMEM. 3T3 fibroblasts on different substrates were cultivated for 24 h before adding 1 ml Dil solution to each sample and incubated for 30 minutes at 37 °C. Cells were tracked over 20 h in the fluorescence microscope with 20x magnification using the Quadband filter.

A Nikon Eclipse Ti inverted fluorescence microscope was used for phase contrast and fluorescence imaging of cell samples during live-cell tracking. The membrane lipids in live imaging were imaged at an emission wavelength of 565nm. For live-cell imaging cells were kept under a humidified atmosphere, 37 °C and 5 % CO₂. Cells were seeded on each substrate type in 12-well-plates using triplicates for each sample type. Columns were used for one substrate type and the replicates were organized in rows (see Fig. 29). The imaging scheme was kept the same in all experiments. Each row was imaged after the other as shown in Fig. 29 highlighted with red arrows. Fibroblasts on collagen scaffolds were imaged every 2 min. Cells grown on fibrinogen were imaged every 5 min.

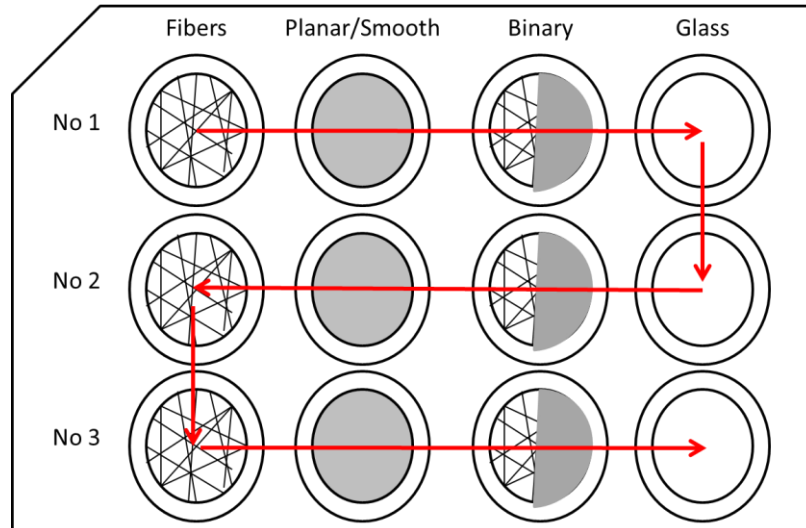


Figure 29. Schematic overview of a typical 12-well-plate for live-cell tracking. Triplicates of each substrate type like fibers, smooth and binary patterned protein scaffolds, and glass as control were seeded in columns. No 1, No 2, and No3 show the number of each triplicate in rows. The red arrows highlight the imaging way while live-cell tracking. All collagen and fibrinogen cell tracking experiments were set-ups as depicted in this figure.

Cell migration velocity and distance were determined with the Nikon NIS-Elements AR tracking module. All shown results represent four independent experiments (n=4) with triplicates for each substrate type. An exemplary image of Dil-stained fibroblasts is shown in Figure 30 A. The Nikon tracking tool recognizes the characteristic shape and automatically tracks every cell over the defined time. The dislocation of each cell is recognized by the software and displayed as individual paths (see Fig. 30B).

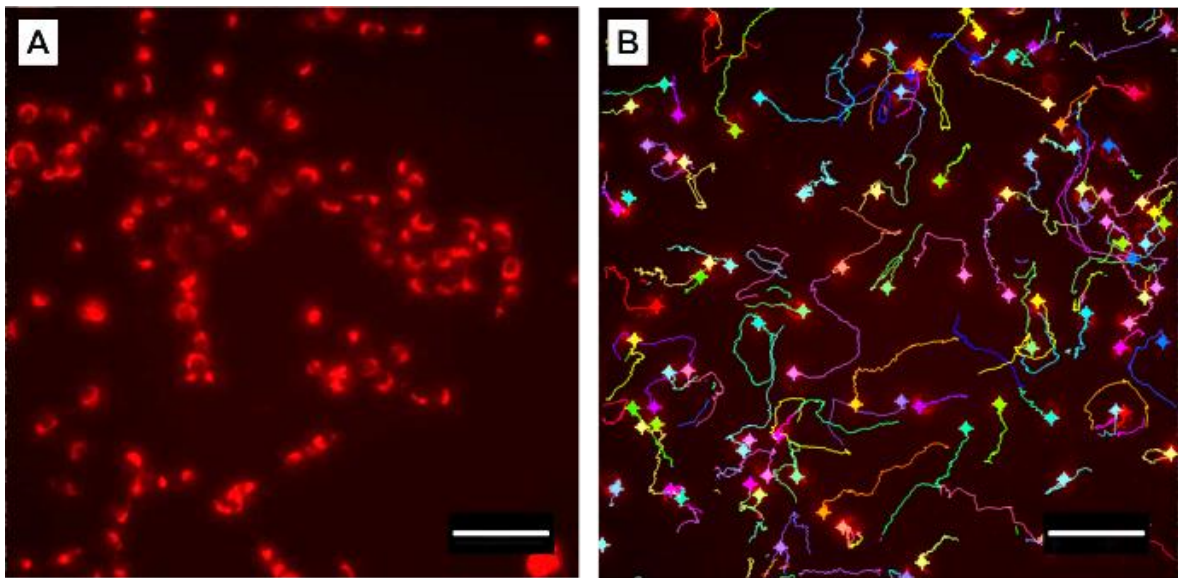


Figure 30. Fluorescence image of 3T3 fibroblasts grown on glass stained with Dil. Cells were grown on different substrates. (A) The dye accumulates around the nucleus forming fluorescent sickle-shapes, which can be recognized by the tracking software. (B) The tracking software tool recognizes each cell and tracks the movement of each cell. Scale bar represents 100 μm .

Over 20 h, images were collected with a pco.edge 4.2 LT CMOS camera (PCO, Kelheim, Germany) at 2 min intervals using the Nikon NIS-Elements AR tracking module. Live cell tracking was conducted in four independent experiments (n = 4) with triplicates for each substrate type. To ensure statistical relevance, videos with less than 20 tracks were excluded from the velocity analysis. Tracking data (position data) were imported in the data analysis package IGOR (Wavemetrics) for further analysis. Velocities were calculated in a 20 min window (i.e. from 10 or 4 position data depending on the frame rate of the video), where the window is sliding over the entire video sequence by shifting it by 10 minutes. These velocity data (typically 10.000 to 50.000 data points per sample type) were investigated for differences between the different collagen topographies. Since

velocity data showed a log-normal distribution, the logarithm of the velocity was considered here, which showed a normal (Gaussian) distribution. Since case numbers were very high, even the tiniest differences would show up as statistically significant. Thus, a measure for the size of differences by using Cohen's *d* was calculated first. Cohen's *d* was the difference between two statistical samples (here two different topography types) normalized by the combined standard deviation, i.e. by the geometrical mean of the two standard deviations. Since the velocity histograms showed a main peak at around 50...100 nm min⁻¹ and a secondary peak at very low velocities (at around 1...10 nm min⁻¹), which corresponds to non-mobile cells and reflects the accuracy of our position data, the mean and standard deviations values used for calculating Cohen's *d* were obtained from a Gaussian fit to the main peak of the histogram. Only Cohen's *d* > 0.2 was considered as a significant or large effect (Cohen 2013). In these cases, significance values obtained from a Student's *t*-test (on the log *v* data) were always considered as highly significant (i.e. < 10⁻⁶). All velocity data were plotted as peak values of log (*v*) (from the Gaussian fit to the histograms) and subsequently displayed as *v* ± standard deviation using the software Graphpad Prism (GraphPad).

3. Results

This work aimed to establish a biophysical platform, which combines smooth and nanofibrous topographies in a single protein scaffold to study the influence of topographical cues on cell growth. The results of this study will be presented in the following subchapters. To establish a new scaffold type, which provides a combination of nanofibrous and smooth topographies, collagen was initially used as a model system before this concept was transferred to the plasma protein fibrinogen. First, results of collagen scaffold development will be presented, including characterization, and improvement including the stability of nanofibers for cell culture and substrate thickness of the nanofibrous scaffold. Subsequently, the results of cellular interaction with nanofibrous and smooth collagen scaffolds will be presented. In the second part of this chapter, the morphological analysis of a novel class of nanofibrous fibrinogen scaffolds will be introduced, and the results of the cellular interaction with this new scaffold type will be presented. Finally, a new binary biomaterial will be introduced, which combines smooth and nanofibrous topographies of different proteins in a single scaffold.

3.1 Collagen scaffolds

In the following chapter, the development and improvement of collagen scaffolds prepared by self-assembly will be described. The results from morphological scaffold analysis with SEM, AFM, and phase-contrast microscopy will be presented.

3.1.1 Self-assembly and Crosslinking

The addition of salt to collagen resulted in nanofiber formation. For the application of the collagen scaffolds in cell culture the smooth collagen needed to be cross-linked to prevent fiber formation. Due to the ionic strength in the cell culture medium, non-cross-linked collagen would form fibers. To assure, that the biochemistry for both smooth and nanofibrous collagen would remain the same, the collagen nanofibers were also cross-linked with 2% GA. An image of non-cross-linked collagen nanofibers is shown in Figure 31. A suitable cross-linker should preserve the fiber morphology. Planar collagen did not show any fibrous structures (see Fig. 31B).

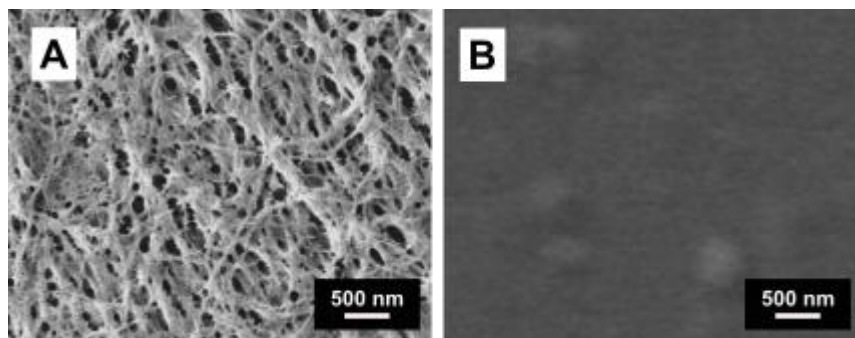


Figure 31. SEM image of not cross-linked collagen nanofibers (A) and planar collagen (B) prepared with 0.5 mg ml^{-1} . A dense network of collagen fibers with different diameters and fiber bundles was found.

To provide a reproducible protein scaffold for subsequent cell culture experiments, different crosslinking techniques were explored. The high ionic strength in the cell culture medium may lead to fiber formation on smooth collagen samples under cell culture conditions. Therefore, to reproducibly compare collagen scaffolds with different topographies, i.e. nanofibers versus smooth surfaces, the scaffolds needed to be cross-linked. To preserve the respective morphology, different crosslinking methods were studied. Chemical cross-linkers, like EDC, methanol, glutaraldehyde, and formaldehyde, were used, as well as a physical crosslinking method with ultraviolet irradiation. Comparative SEM images of collagen nanofibers and smooth collagen samples cross-linked with these different approaches are shown in Figure 32. Crosslinking with EDC led to blurred fiber morphology (A) and an uneven surface for the smooth scaffold (B). UV-radiation exhibited a more distinct fiber morphology (C) but a rough appearing smooth surface (D).

Nanofibers cross-linked with liquid formaldehyde (E) and methanol (G) did not preserve the fibrous topography prepared by self-assembly so that the topography of smooth and fibrous samples did not vary significantly from each other (see smooth formaldehyde sample in (F) and smooth methanol sample in (H)). For collagen nanofibers cross-linked with liquid glutaraldehyde, the distinct fiber morphology was well preserved (I), while smooth collagen cross-linked with glutaraldehyde depicted a smooth surface. In summary, both collagen topographies were best preserved by the glutaraldehyde crosslinking procedure. Thus, it was used as a standard operating procedure during subsequent cell culture studies.

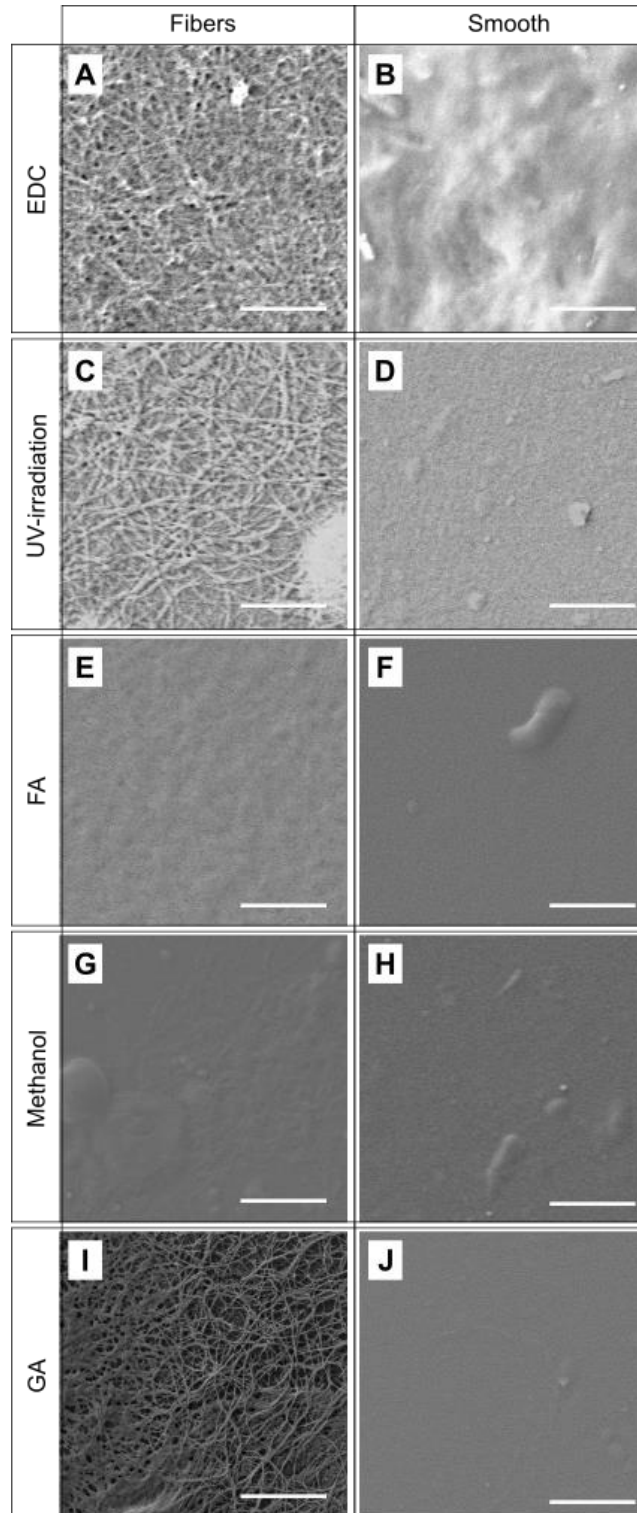


Figure 32. SEM images of dried collagen scaffolds prepared with 0.5 mg ml^{-1} were cross-linked with different crosslinking methods. Collagen nanofibers (A) and smooth collagen (B) cross-linked with EDC. Collagen nanofibers (C) and smooth collagen (D) cross-linked with 30 min UV-radiation. Collagen nanofibers (E) and smooth collagen (F) cross-linked with 4% FA. Collagen nanofibers (G) and smooth collagen (H) cross-linked with methanol. Collagen nanofibers (I) and smooth collagen (J) cross-linked with 2% GA. Scale bars represent $2 \mu\text{m}$.

In preparation for later cell culture studies, it was also analyzed on which different substrate materials collagen could be assembled into nanofibers. Therefore, collagen nanofiber assembly was carried out on polycarbonate (see Fig. 33A), Lumox® Foil (see Fig. 33B), anodized aluminum oxide (see Fig. 33C) and piranha-cleaned glass slides (see Fig. 33D). It can be seen that nanofibers prepared with 0.5 mg ml^{-1} exhibited well-defined fiber morphologies on all these surfaces. Self-assembly of collagen nanofibers on AAO yielded the lowest surface coverage. Overall, the collagen fiber assembly was found to be independent of the underlying substrate material. In the following cell, culture studies all experiments were conducted on the glass to facilitate reproducible settings for microscopic analysis of cell cultures on collagen scaffolds.

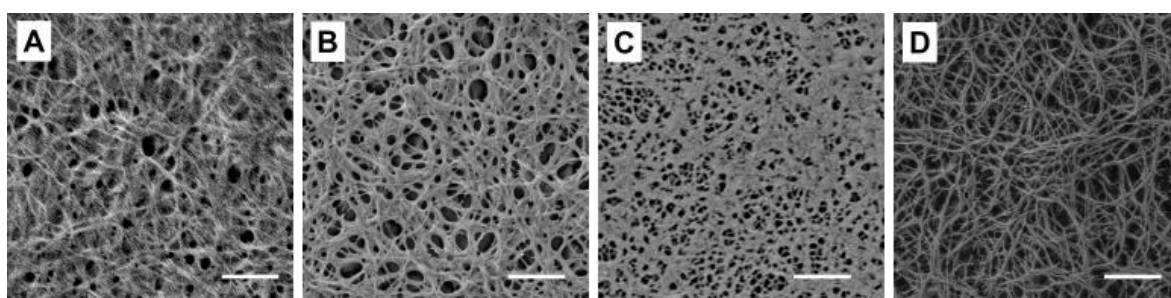


Figure 33. SEM images of Collagen fibers prepared with 0.5 mg ml^{-1} collagen. Fiber assembly was successful on different surfaces like polycarbonate (A), Lumox® Foil (B), anodized aluminum oxide (C), and piranha-cleaned glass (D). Scale bars represent $1 \mu\text{m}$.

3.1.2 Surface coverage

A homogeneous and complete coverage with the protein scaffold was required to carry out cell culture studies on protein scaffolds with different topographies. Self-assembly of collagen by simple drying overnight led to an irregular surface coverage where only approximately 50% of the carrier substrate was covered with collagen nanofibers (see Figure 34 (A)). In particular, for low collagen concentrations in the self-assembly solution, a full surface coverage on glass cover slides could not be achieved. To assure good overall coverage independent of the protein concentration we studied how the surface coverage could be increased, using 0.5 mg ml^{-1} as exemplary collagen concentration. For this purpose, an ultrasonication step was added to the preparation procedure. While assembling collagen nanofibers, the samples were exposed to ultrasonication for 30 min (Spurlin *et al.* 2010). Introducing this step allowed us to reproducibly achieve a surface coverage of approximately 100% in comparison to 50% without using self-assembly (Figure 34B).

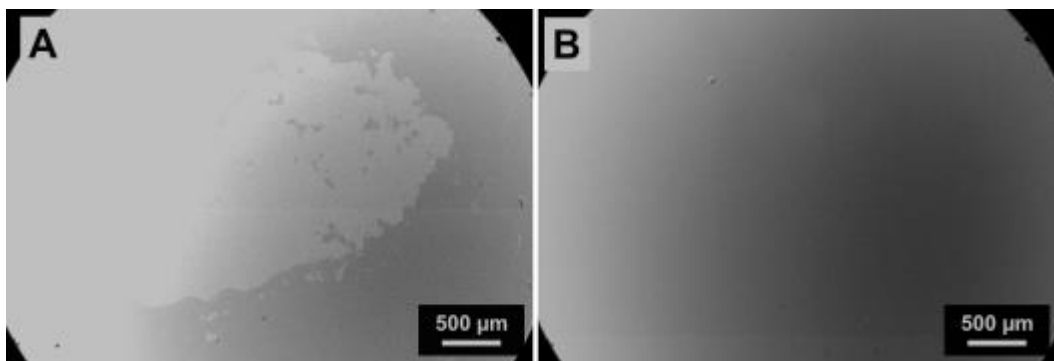


Figure 34. SEM image of collagen nanofibers prepared with 0.5 mg ml^{-1} . Self-assembly without ultrasonication (A) and surface coverage after introducing 30 min of ultrasonication (B). Dark grey areas represent confluent protein layers and lighter grey areas represent the glass where no fibers could be assembled.

3.1.3 Collagen nanofiber morphology

With the preparation of self-assembled collagen scaffolds using a simultaneous ultrasonication step, porous networks of nanofibrous collagen were reproducibly obtained (see Fig. 35). Collagen nanofibers prepared with 0.5 mg ml^{-1} displayed distinct fiber morphology with fiber diameters of $136 \pm 5 \text{ nm}$ (see Fig. 35A). Higher collagen concentrations of 2.5 mg ml^{-1} yielded less porous nanofiber networks with fiber diameters of $149 \pm 12 \text{ nm}$ and single nanofibers assembling into fiber bundles (see Fig. 35D). Using cross-sectional SEM analysis scaffold thicknesses between 200 and 600 nm were found for collagen scaffolds prepared with 0.5 mg ml^{-1} (see Fig 35 B), and scaffolds prepared with 2.5 mg ml^{-1} displayed thicknesses between 4 and 7 μm (see Fig. 35E).

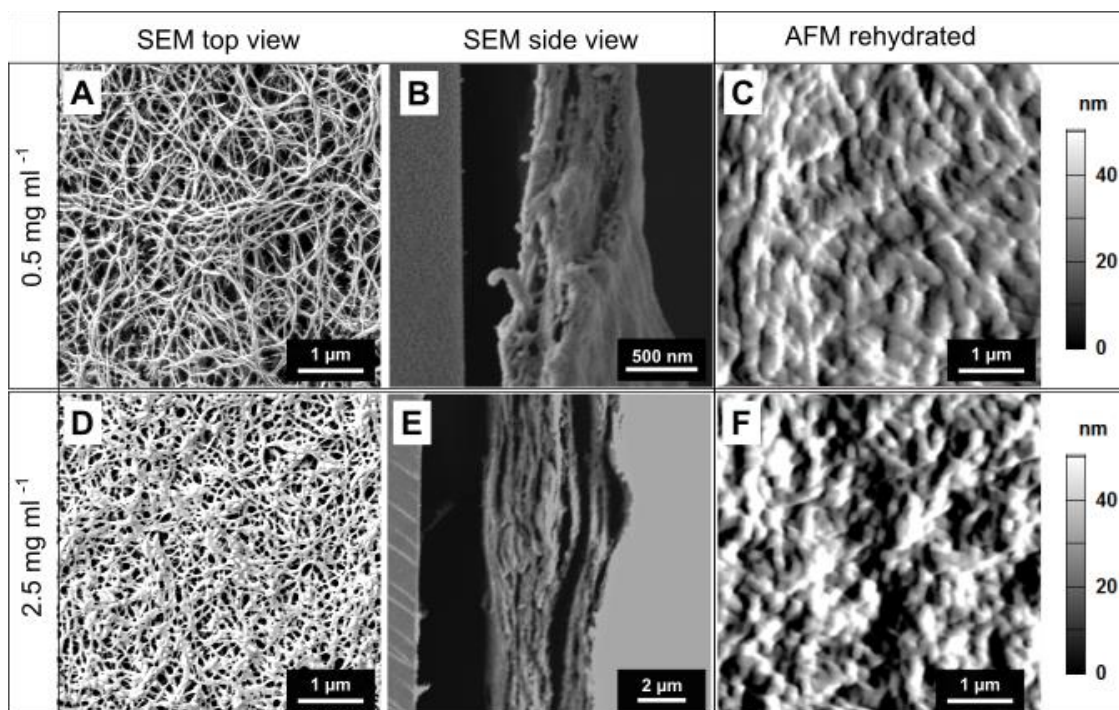


Figure 35. Nanotopography of nanofibrous collagen scaffolds prepared with 0.5 mg ml^{-1} collagen (A to C) and prepared with 2.5 mg ml^{-1} collagen (D to F). (A) and (D) show SEM images of dried scaffolds. (B) and (E) show AFM scans (deflection error) of dried scaffolds. (C) and (F) show AFM images of collagen scaffolds rehydrated in DMEM.

To evaluate the influence of aqueous cell culture environment on the nanotopographical features collagen scaffolds were rehydrated in DMEM cell culture medium. AFM analysis showed that the fiber morphology was preserved for both protein concentrations in DMEM (see Fig. 35C and 35F).

Smooth collagen scaffolds exhibited a very smooth surface in the dried state for both concentrations of 0.5 mg ml^{-1} and 2.5 mg ml^{-1} (see Figure 36A and 36B). Scaffolds prepared with 0.5 mg ml^{-1} were approximately 400 nm thick, whereas smooth samples prepared with 2.5 mg ml^{-1} ranged approximately from 8 to 10 μm (see Fig 36B and 36E). Smooth scaffolds prepared with 0.5 mg ml^{-1} rehydrated with DMEM exhibited more pronounced topographical features than scaffolds prepared with 2.5 mg ml^{-1} (see Fig. 36C and 36F).

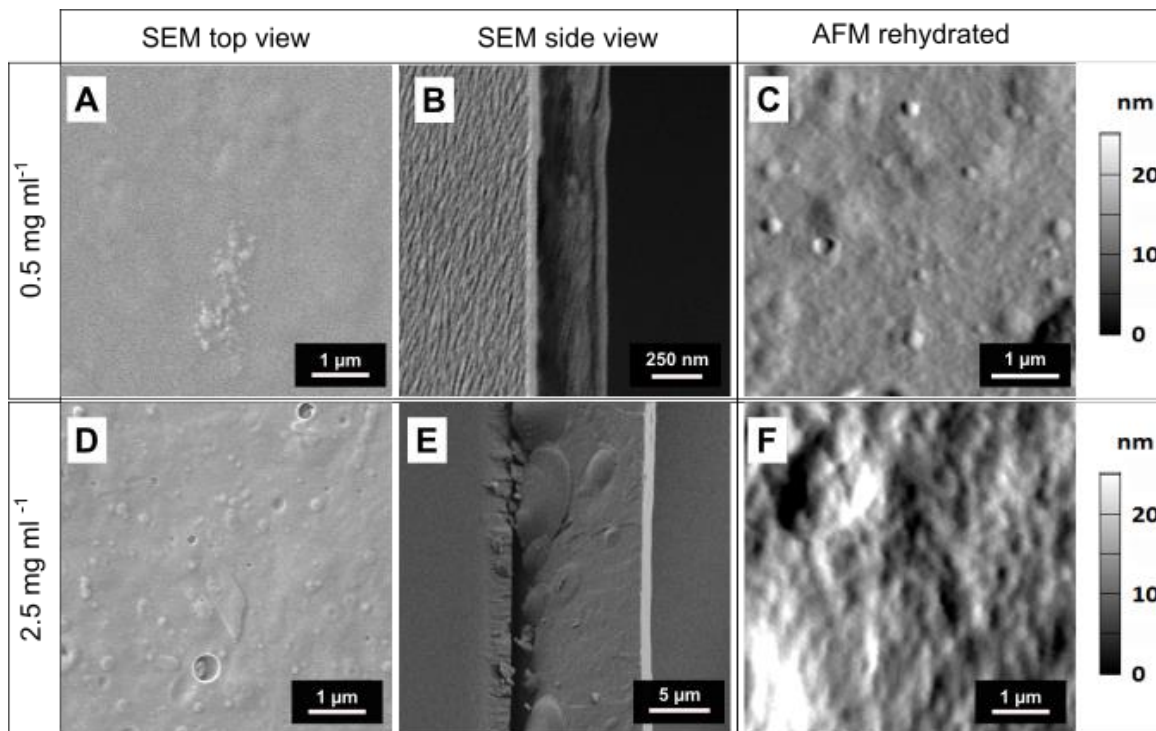


Figure 36. Nanotopography of smooth collagen scaffolds prepared with 0.5 mg ml^{-1} collagen (A to C) and prepared with 2.5 mg ml^{-1} collagen (D to F). (A) and (D) show SEM images of dried scaffolds. (B) and (E) show AFM scans of dried scaffolds. (C) and (F) show AFM images of collagen scaffolds rehydrated in DMEM.

To characterize the surface roughness of collagen scaffolds AFM height images were analyzed and height profiles were obtained (see Fig. 37). Exemplary height variations in the profiles are shown in Figure 37 for collagen scaffolds prepared with 0.5 mg ml^{-1} . These profiles were in the range of several nanometers for both, fibrous and smooth, scaffolds rehydrated in DMEM (see Fig 37 A, B, and C, D). The difference between smooth and fibrous collagen scaffolds was more evident for collagen scaffolds prepared with 2.5 mg ml^{-1} (see Fig. 37 E to H). Height profiles of fibrous scaffolds showed variations around 100 nanometers while the height profiles of smooth collagen scaffolds were in the lower nanometer range.

For both concentrations, fibrous scaffolds exhibited stronger variations of height profiles than smooth scaffolds. To analyze the roughness of the height images an ROI of $1 \mu\text{m}$ was chosen and moved over the entire image.

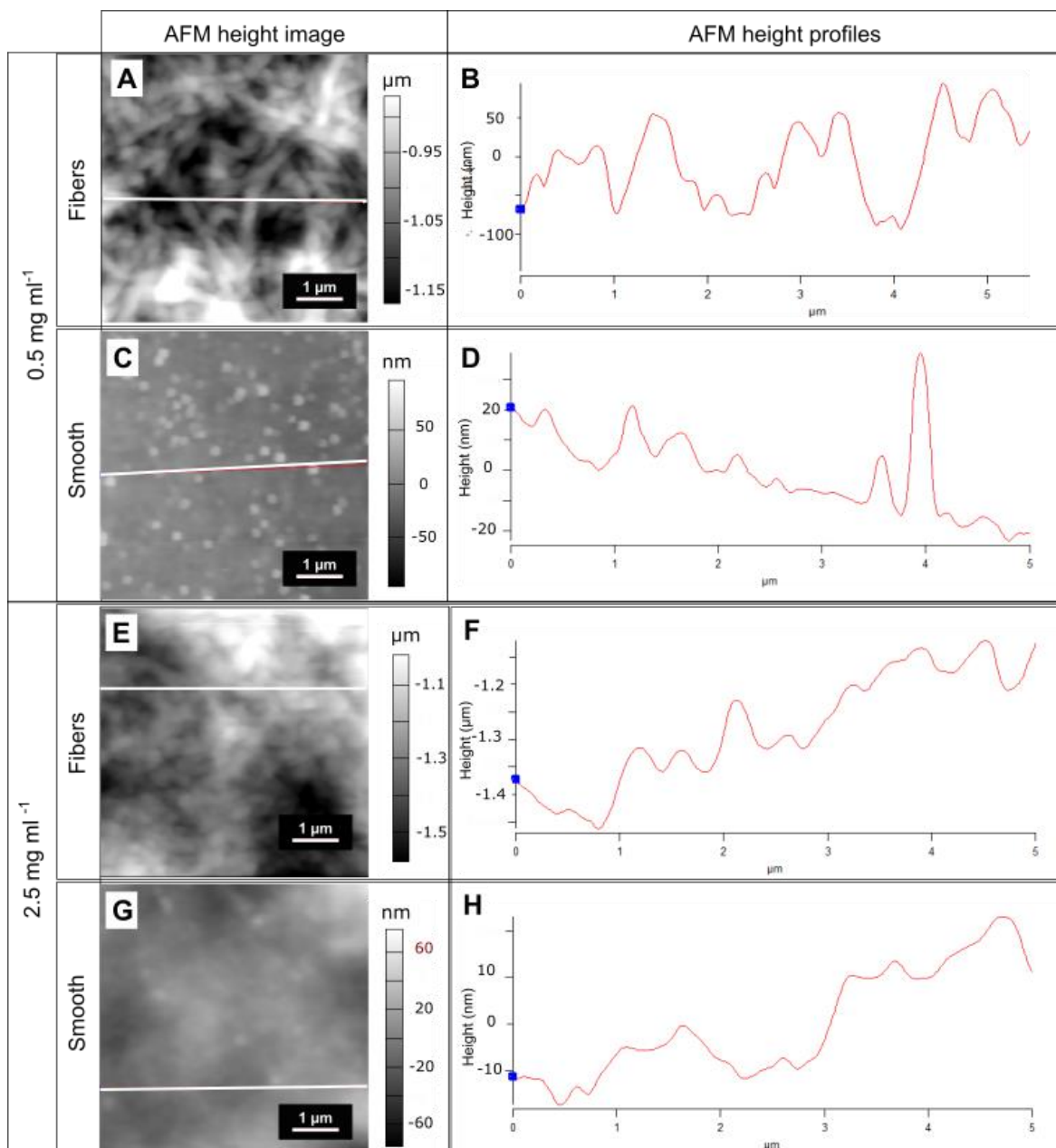


Figure 37. AFM height images of collagen scaffolds prepared with 0.5 mg ml^{-1} (A and B) and 2.5 mg ml^{-1} (E and G) and height profiles of fibrous collagen scaffolds (B) and smooth collagen (D) prepared with 0.5 mg ml^{-1} and fibrous collagen scaffolds (F) and smooth collagen (H) prepared with 0.5 mg ml^{-1} . AFM scans display height images of the respective collagen scaffolds. The offset was subtracted from the height images. White lines show the location of the height profiles displayed in (B), (D), (F), and (H). All collagen scaffolds were rehydrated with DMEM cell culture medium.

AFM analysis showed that overall, dry and rehydrated nanofibers prepared with 0.5 mg ml^{-1} collagen displayed a lower roughness than the respective scaffolds fabricated with 2.5 mg ml^{-1} (see Table 4). Scaffolds rehydrated in DMEM in comparison to dried

scaffolds showed increased roughness values for both collagen concentrations. Interestingly, the roughness values for smooth collagen scaffolds prepared with 2.5 mg ml^{-1} were found to be lower after rehydration. Smooth collagen scaffolds prepared with 0.5 mg ml^{-1} exhibited the lowest roughness value. After rehydration, the roughness of smooth collagen prepared with 0.5 mg ml^{-1} was comparable to smooth collagen scaffolds prepared with 2.5 mg ml^{-1} .

Table 4. Root mean square roughness (Rq) of dried and rehydrated collagen scaffolds. For roughness analysis, three independent samples were analyzed. Three images of $5 \times 5 \mu\text{m}$ were scanned with an ROI of $1 \mu\text{m}$ (25 ROIs). The values given in the table represent mean Rq-values with standard deviation.

	0.5 mg ml^{-1}		2.5 mg ml^{-1}	
	Rq _{dried} (nm)	Rq _{rehydrated} (nm)	Rq _{dried} (nm)	Rq _{rehydrated} (nm)
Collagen fibers	39.9 ± 1.2	43.2 ± 3.8	46 ± 5.7	114.8 ± 87.5
Smooth collagen	8.8 ± 4.3	29 ± 5.4	27.3 ± 3.2	22.6 ± 6.6

To analyze the swelling behavior of collagen nanofibers prepared with 0.5 mg ml^{-1} and 2.5 mg ml^{-1} after incubation in the cell culture medium, additional fiber diameter analysis was carried out with SEM for dry samples and with AFM for dry and rehydrated scaffolds (see Table 5).

SEM analysis of dried collagen nanofibers resulted in comparable diameters of approximately 140 nm independently of the collagen concentration. With diameters of approximately 230 nm AFM analysis of dried collagen fibers resulted in higher fiber diameters than the previous SEM analysis. After rehydration in DMEM cell culture, medium AFM analysis yielded fiber diameters of approximately 400 nm, independently of the collagen concentration. This result shows that collagen scaffolds prepared with 0.5 mg ml^{-1} collagen have a swelling factor of approximately 1.9 and scaffolds prepared with 2.5 mg ml^{-1} had a swelling factor of approximately 1.67.

Table 5. Fiber diameters (FD) of dried and rehydrated collagen fibers. Diameters of dried collagen fibers were measured with SEM and AFM. Diameters of collagen fibers rehydrated in DMEM were measured with AFM.

	SEM	AFM	
	FD _{dried} (nm)	FD _{dried} (nm)	FD _{rehydrated} (nm)
0.5 mg ml⁻¹ Collagen	137 ± 5	228 ± 21	435 ± 34
2.5 mg ml⁻¹ Collagen	149 ± 12	232 ± 5	388 ± 22

3.1.4 Collagen scaffold mechanics

To characterize the stiffness of nanofibrous and smooth collagen scaffolds, AFM measurements were performed. Thereby, force curves were obtained, which appeared infinitely stiff for both, nanofibrous and smooth collagen scaffolds independent of the collagen concentration. Exemplary force curves for nanofibrous and smooth collagen scaffolds prepared with 0.5 mg ml⁻¹ collagen are shown in Figure 38. The slope of approximately 1 in these diagrams is typical for stiff substrates. Stiff hydrogels have been reported with values of 30–40 kPa (Rianna and Radmacher 2017). In other studies, glass controls were reported to be nearly infinitely stiff (Bhana *et al.* 2010). While glass has young's moduli of 40 – 90 kPa (Kuchling 2011). Since only such steep force curves were obtained the Young's moduli of nanofibrous or smooth collagen scaffolds could not be calculated, as they appear infinitely stiff for the MLCT Bio cantilevers used in this study.

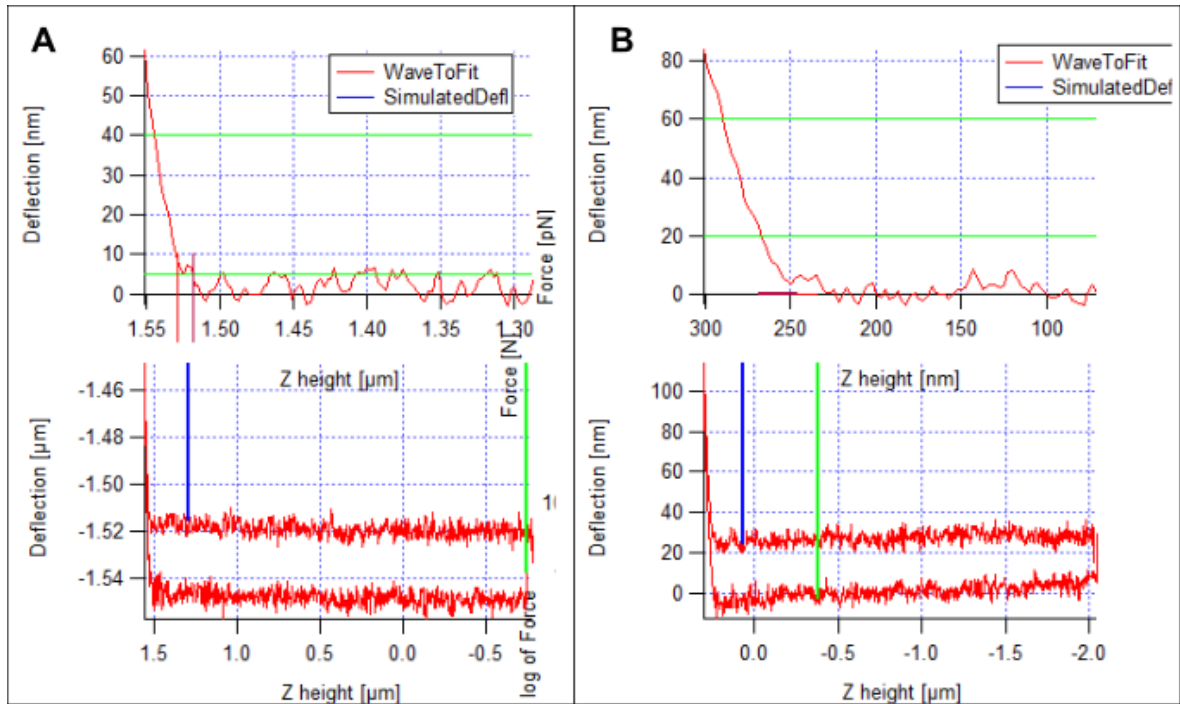


Figure 38. Exemplary force-distance curves on nanofibrous collagen scaffolds (A) and smooth collagen scaffolds (B) prepared with 0.5 mg ml^{-1} collagen. Force-distance curves with a slope of approximately 1 are typical for very stiff substrates

Representative force curves for nanofibrous and smooth collagen scaffolds prepared with 2.5 mg ml^{-1} collagen are shown in Figure 39. Again, the slope of approximately 1 is typical for stiff substrates. Despite the higher collagen scaffold thickness, these force curves were not suited either to obtain the Young's modulus, since these thicker scaffolds also appeared infinitely stiff.

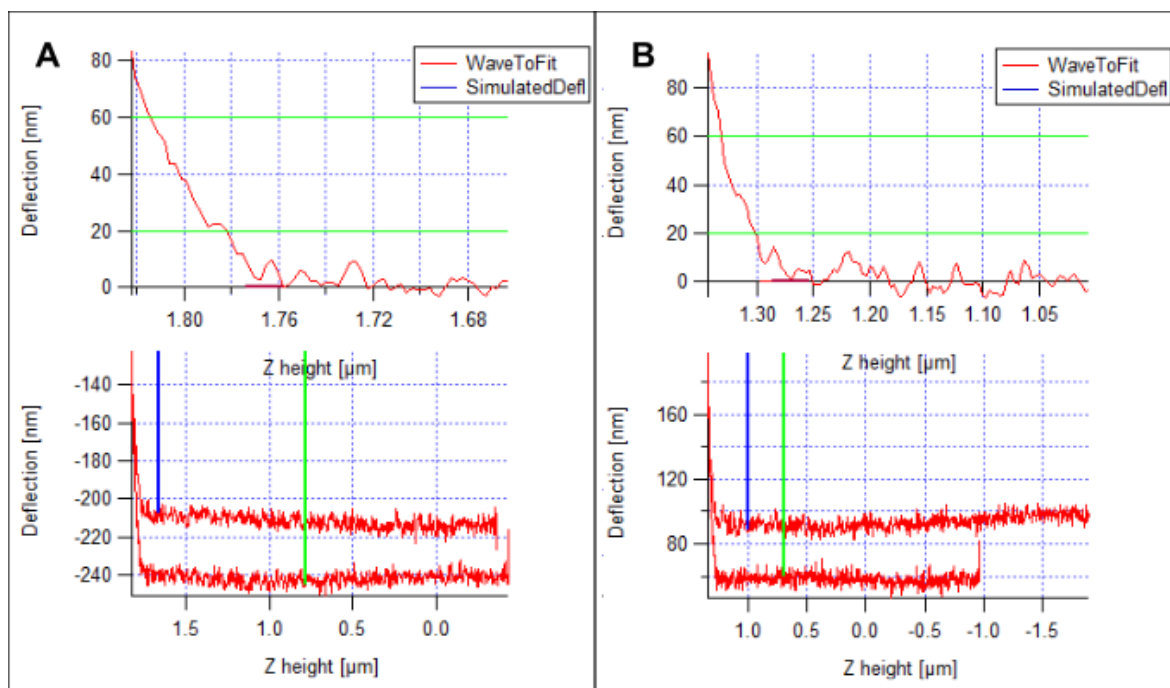


Figure 39. Exemplary force-distance curves on nanofibrous collagen scaffolds (A) and smooth collagen scaffolds (B) prepared with 2.5 mg ml^{-1} collagen. Force-distance curves resemble typical curves for stiff substrates like glass.

3.1.5 Collagen scaffolds with binary surface topography

To study the influence of surface topography on cellular interactions without altering biochemical or mechanical cues a new protein scaffold platform was established based on the results presented in sections 3.1.1 to 3.1.4. A new process was developed, which facilitated the preparation of protein scaffolds with nanofibrous and smooth topographies in the same scaffold. The workflow to prepare these topographically patterned scaffolds is based on the self-assembly of collagen into nanofibers, and the technical details were described in chapter 2.3.4 Binary Substrates.

For cell culture applications a visible boundary between smooth and nanofibrous areas is important to facilitate time-critical cell culture studies in dependence of the underlying scaffold topography. When the patterning process, shown in Fig. 19, was carried out phase-contrast microscopy of dried collagen scaffolds revealed a defined boundary between the different topographies for both collagen concentrations (see Fig. 40). Smooth and nanofibrous areas were distinguishable via phase-contrast microscopy, thus enabling further cell culture studies.

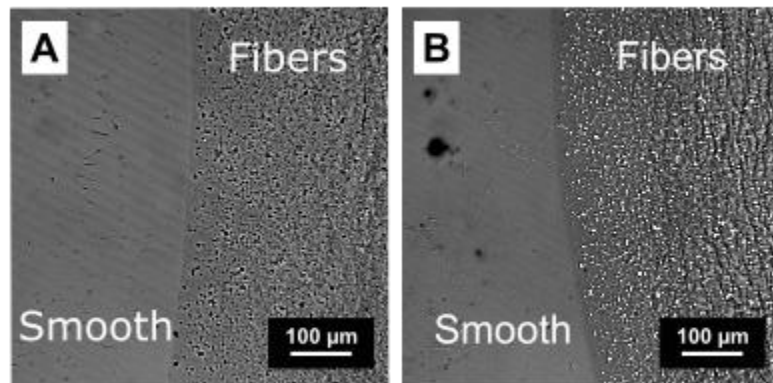


Figure 40. Phase-contrast images of dried collagen scaffolds prepared with 0.5 mg ml^{-1} collagen (A) and 2.5 mg ml^{-1} collagen (B) with binary topography patterns. The boundary between smooth and fibrous areas is visible in phase-contrast images.

Subsequent SEM analysis showed that the different topographies were successfully established in the different scaffold regions (see Fig. 41B and C). For the first time, a scaffold made from one protein with two different topographies was introduced with this process (see Fig. 41A). First, the novel patterning routine was established with thin binary collagen scaffolds prepared from 0.5 mg ml^{-1} (see Fig. 41B) and subsequently with thick scaffolds fabricated with 2.5 mg ml^{-1} collagen (see Fig. 41C). SEM analysis showed that the differences in surface topography were more pronounced for thick than for thin collagen patterns. Moreover, SEM analysis confirmed that the border between both topographies was clearly defined for both concentrations. With this new procedure, the first-time preparation of binary collagen scaffolds with spatially controlled variations of the nanotopography in the same scaffold was achieved. Overall, this novel preparation method was highly reproducible, thus facilitating subsequent cell culture experiments, which will be presented in the following chapters.

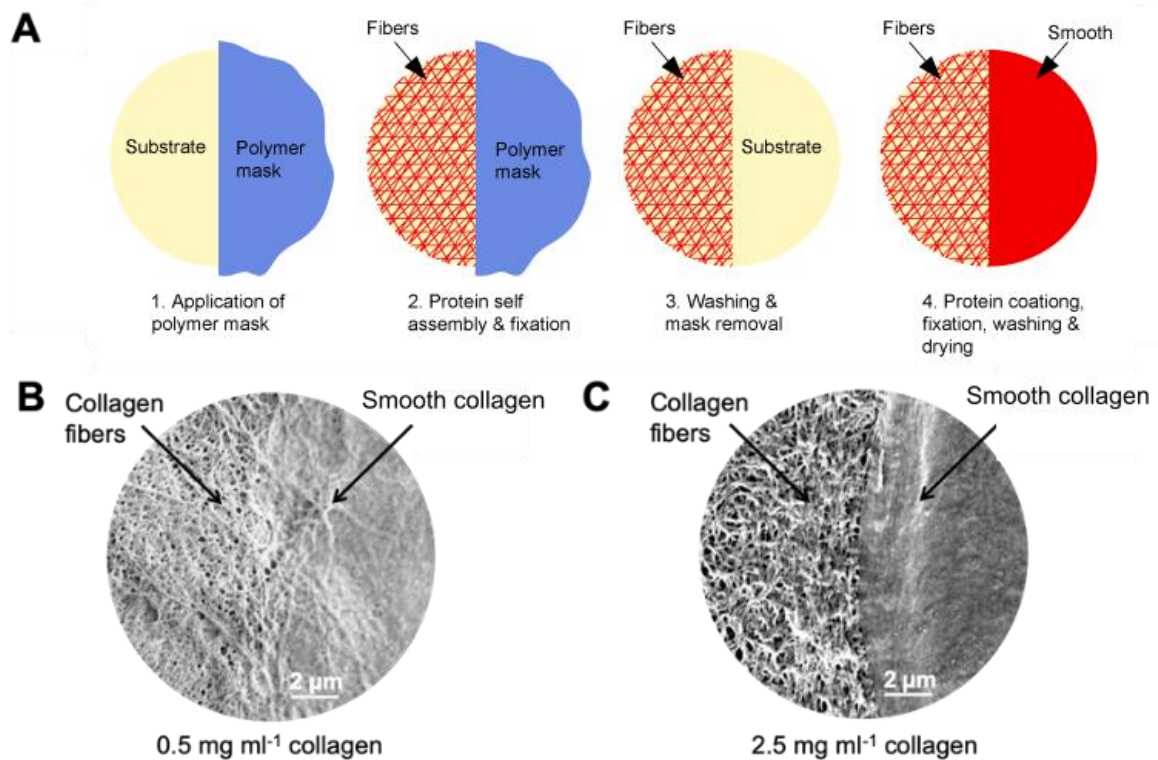


Figure 41. Preparation of collagen scaffolds with patterned nanofiber and smooth topographies. Schematic of the preparation process by combining collagen self-assembly with polymer mask patterning (A). The shown scheme shows the standard procedure used throughout this study. In a first step, a polymer mask was added on the substrate covering half of the carrier substrate. In the second step, protein fibers were assembled and cross-linked. In the third step, the polymer mask was removed and the samples were washed. In the fourth step, a smooth protein layer was assembled, fixated, washed, and finally dried. SEM images of topographically patterned protein scaffolds prepared with 0.5 mg ml⁻¹ (B) and with 2.5 mg ml⁻¹ collagen(C).

3.1.6 Cellular response to nanostructured collagen scaffolds

In this subchapter, the results on the cellular response to self-assembled collagen scaffolds will be presented. First, results on the cell viability obtained with a LIVE/DEAD® staining and the metabolic WST-1 assay will be shown. Later, the results of cell morphology analysis by fluorescence and confocal microscopy as well as SEM results and the analysis by live-cell tracking will be presented.

3.1.6.1 Cell viability

To measure the viability of 3T3 fibroblasts on collagen scaffolds Calcein-EthD-1 staining was performed in initial experiments. Living cells were stained in green and dead cells were stained in red. Phase-contrast images were used to visualize the cell shape. An exemplary selection of cell images on different collagen substrates prepared with 0.5 mg ml^{-1} and control substrates after a growth time of 72 h is shown in Fig. 42. Fluorescence microscopy analysis revealed that almost all cells on the different substrates were alive after this time. Except for the dead cell control, only a few dead cells were detected on collagen nanofibers, smooth collagen, and glass. In phase-contrast mode, it could be shown that dead cells were much smaller and rounder while live cells exhibited a spindle-like shape, which is typical for fibroblasts.

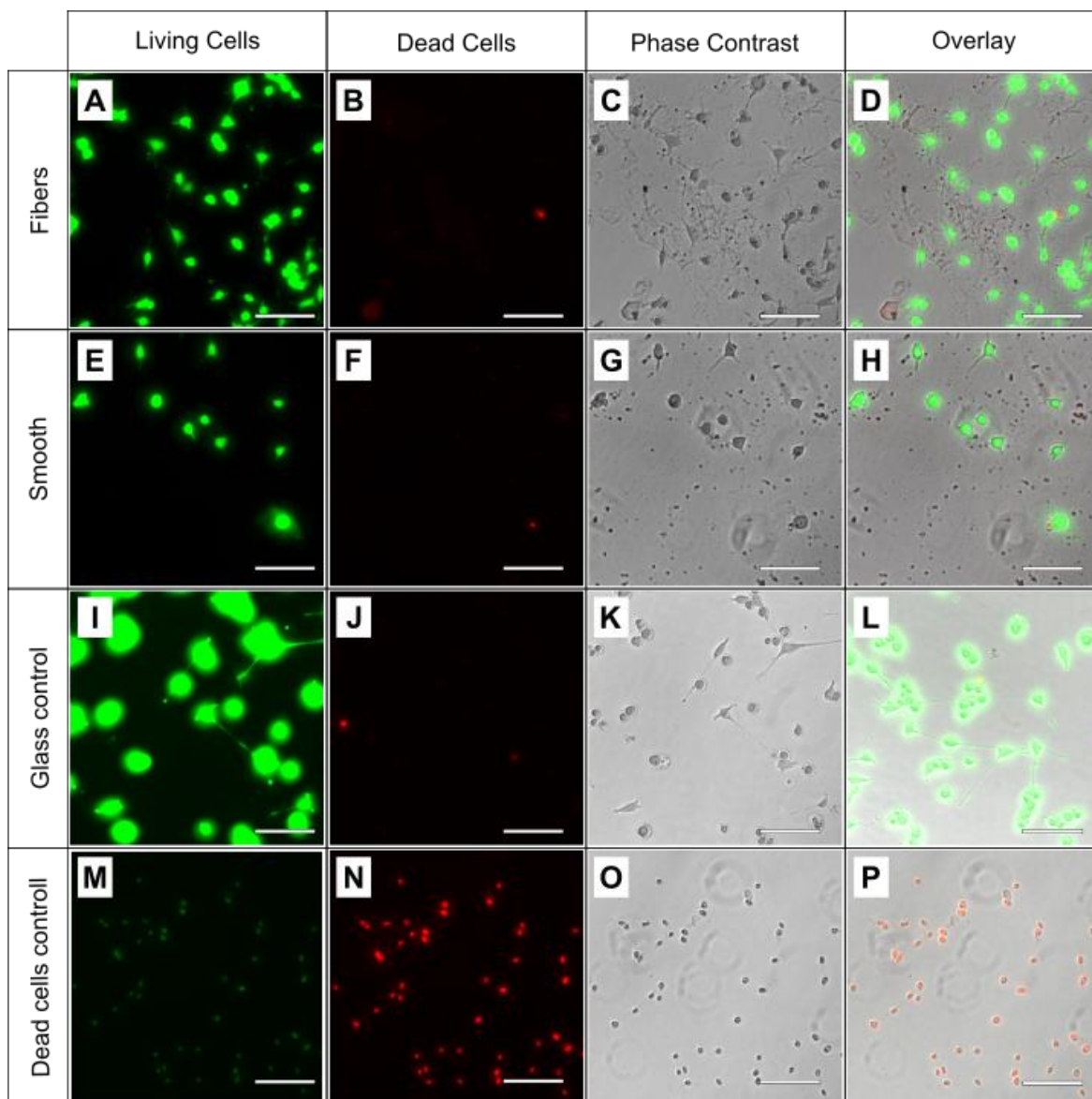


Figure 42. Fluorescence images of 3T3 fibroblasts on different substrates after 72 h cultivation time. Living cells were stained with Calcein (green) on collagen fibers prepared with 0.5 mg ml^{-1} (A), smooth collagen prepared with 0.5 mg ml^{-1} (E), glass control (I), and dead cells (M). Dead cells on collagen fibers (B), smooth collagen (F), glass control (J) and dead cells (N) were stained with EthD-1 (red). Phase-contrast images of 3T3 fibroblasts on collagen fibers (C), smooth collagen (G), glass control (K), and dead cells on glass (O). An overlay of all channels is shown for 3T3 fibroblasts on collagen fibers (D), smooth collagen (H), glass control (L), and dead cells on glass (P). Scale bars represent $100 \mu\text{m}$

As a reference substrate, glass substrates were used. One positive control (PC) on glass was included per experiment, where all cells were killed incubation in Triton. The percentage of live cells per sample was calculated using the following equation:

$$\text{Live cells [\%]} = \frac{\text{number of live cells}}{(\text{number of live} + \text{dead cells})} * 100$$

Equation 4: Percentage of the viability of the CalceinAM assay.

As shown in Fig. 43, the average percentage of viable cells was over 80 % for all substrates. On smooth collagen after 24 h of growth time, 84 ± 7 % viable cells were found, which was significantly lower than 89 ± 5 % viable cells on collagen nanofibers ($p \leq 0.01$). On glass 91 ± 4 % viable cells were found, which was significantly more than on smooth collagen ($p \leq 0.01$).

From 24 h to 48 h the percentage of viable cells on collagen nanofibers increased significantly from 89.5 ± 5 % to 94 ± 3 % ($p \leq 0.01$) and to 98 ± 1 after 72 h ($p \leq 0.0001$). The same trend was observed for cells grown on smooth collagen, where the percentage of viable cells increased from 84 ± 7 % after 24 h to 93 ± 4 % after 48 h and to 72 h of growth time ($p \leq 0.0001$). After 72 h growth time 98 ± 1 % viable cells were found on collagen nanofibers, which was significantly more than on smooth collagen displaying 93 ± 4 % viable cells ($p \leq 0.01$). All positive controls showed 100 % of dead cells.

The assay was performed on collagen scaffolds prepared with 0.5 mg ml^{-1} collagen because scaffolds prepared with 2.5 mg ml^{-1} collagen exhibited a strong autofluorescence signal, which impeded the analysis of the assay. Since the LIVE/DEAD staining was limited to analyzing only scaffolds prepared with 0.5 mg ml^{-1} collagen WST-1 assay was introduced as an alternative viability assay. The WST-1 assay allowed the analysis of cell viability independent of the substrate since the readout was not conducted by fluorescence microscopy. Instead, the supernatant containing the formazan was measured photometrically.

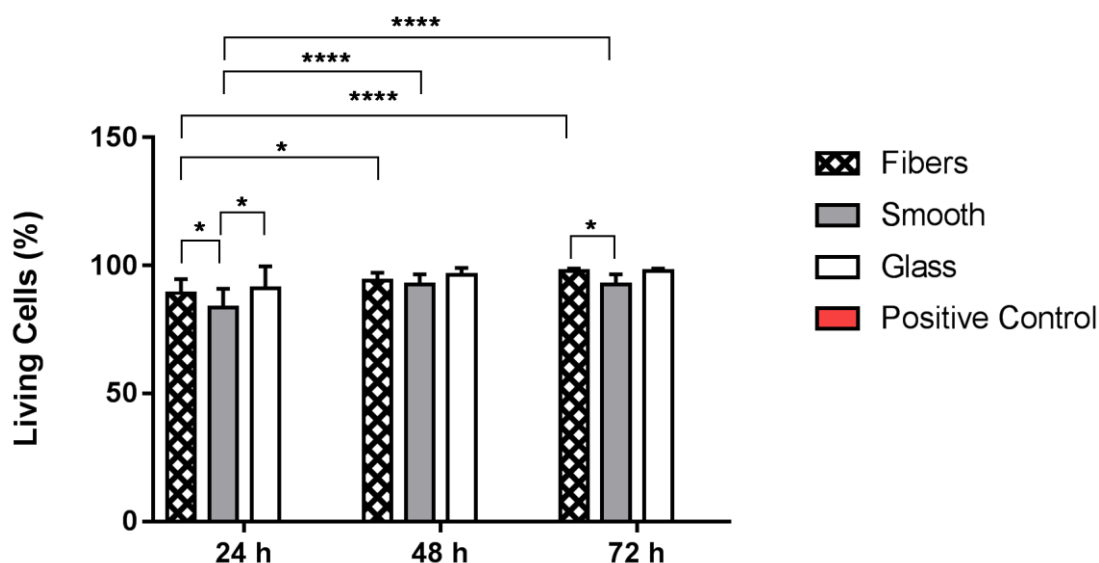


Figure 43. Percentage of viable 3T3 fibroblasts on different substrates (LIVE/DEAD® staining). Percentage of viable fibroblasts grown on 0.5 mg mL^{-1} smooth collagen, 0.5 mg mL^{-1} collagen nanofibers, and glass for 24 h, 48 h, and 72 h. Positive control represents dead cells on glass. As all cells died on this sample the percentage of living cells was too small to be displayed. $n = 4$ experiments were conducted. Data are presented with average \pm standard deviation of replicates. PC is excluded from ANOVA-test. Significant differences indicated by * $p \leq 0.05$, ** $p \leq 0.01$, *** $p \leq 0.001$, **** $p \leq 0.0001$ (data for 24 h were collected by Sophie Stebel as part of her BSc thesis (Stebel 2018)).

Using the WST-1 proliferation assay, comparable results for the proliferation of 3T3 fibroblasts on nanofibrous and smooth collagen scaffolds were obtained over a time period of 72 h in culture. These observations were independent of the collagen concentration (see Fig. 44). The proliferation rate of fibroblasts grown on smooth collagen prepared with 2.5 mg mL^{-1} was significantly lower than on glass ($p \leq 0.05$) after 48 h growth time. For both collagen concentrations, the cell proliferation rate was highest on glass controls after 72 h cultivation. After 72 h in culture the proliferation rate of fibroblasts on fibrous and smooth collagen scaffolds prepared with 0.5 mg mL^{-1} was significantly lower than on glass ($p \leq 0.0001$) (see Fig. 44A). The proliferation rate of fibroblasts on smooth collagen scaffolds prepared with 2.5 mg mL^{-1} and 0.5 mg mL^{-1} collagen was significantly lower than the proliferation rate on glass controls ($p \leq 0.0001$). After 72 h, proliferation rates on fibrous and smooth collagen scaffolds were significantly lower than on glass ($p \leq 0.0001$) (see Fig. 44B).

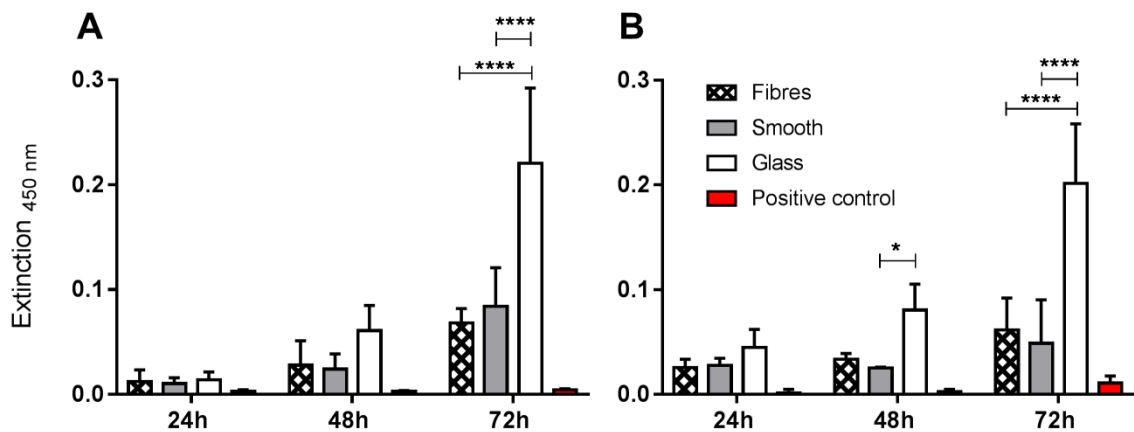


Figure 44. The proliferation of 3T3 fibroblasts on collagen scaffolds prepared from 0.5 mg^{-1} (A) and 2.5 mg ml^{-1} (B) obtained with WST-1. Cell proliferation was plotted for time points of 24, 48, and 72 h. $n = 4$ experiments were conducted. Data are presented with average \pm standard deviation of replicates. PC excluded from ANOVA-test. Significant differences indicated by * $p \leq 0.05$, ** $p \leq 0.01$, *** $p \leq 0.001$, **** $p \leq 0.0001$.

Using the WST-1 proliferation assay comparable viabilities were obtained for 3T3 fibroblasts on nanofibrous and smooth collagen scaffolds until 72 h in culture. These observations were independent of the protein concentration (see Fig. 45). The dashed lines between 100 % and 70 % define the “biocompatible viability range” for biomaterials according to the norm (EN ISO 10993-5:2009). The viability was plotted in relation to the metabolic activity of 3T3 fibroblasts on the glass control. After 24 h the viability of cells on all substrate types prepared with 2.5 mg ml^{-1} collagen decreased below 70 %. The decrease of cell viability did not result in a significant difference between different substrates prepared from 0.5 mg ml^{-1} .

For cells grown on fibrous collagen scaffolds prepared with 2.5 mg ml^{-1} the viability decreased significantly after 72 h ($p \leq 0.05$). Cell viability on smooth collagen scaffolds decreased after 48 h ($p \leq 0.05$) and 72 h ($p \leq 0.01$).

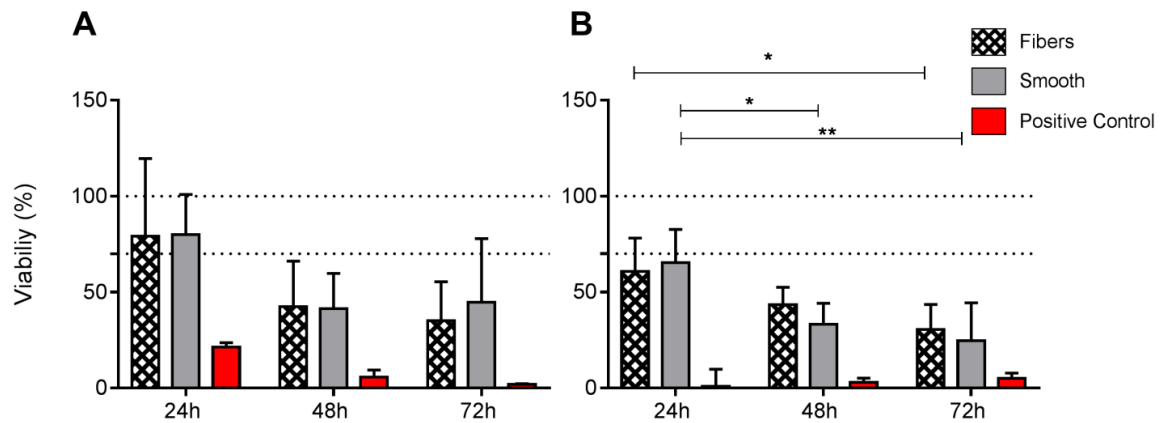


Figure 45. Relative viability of 3T3 fibroblasts on collagen scaffolds prepared with 0.5 mg ml⁻¹ (A) and 2.5 mg ml⁻¹ (B) obtained from WST-1. Dashed lines represent 100 % and 70 % of the glass control. Cell viability was plotted for time points of 24, 48, and 72 h. n = 4 experiments were conducted. Data are presented with average \pm standard deviation of replicates. PC is excluded from ANOVA-test. Significant differences indicated by * p \leq 0.05, ** p \leq 0.01, *** p \leq 0.001, **** p \leq 0.0001.

3.1.6.2 Cell morphology

NIH 3T3 fibroblasts were cultivated on collagen scaffolds prepared with two different concentrations, consisting of either nanofibrous or smooth topography. To analyze the cell morphology over a time of 72 h the cytoskeletal actin filaments were stained with phalloidin and imaged with fluorescence microscopy (see Fig. 46). 3T3 fibroblasts showed a trend towards a spindle-like and more elongated morphology with long filopodia, on collagen nanofibers independent of the protein concentration (Fig. 46A to 46F). In contrast, fibroblasts, which were cultivated on smooth collagen, displayed a more flat morphology and larger cell areas than cells on collagen nanofibers (Fig. 46G to 46L). Morphological differences were found to be most pronounced after 48 h in culture.

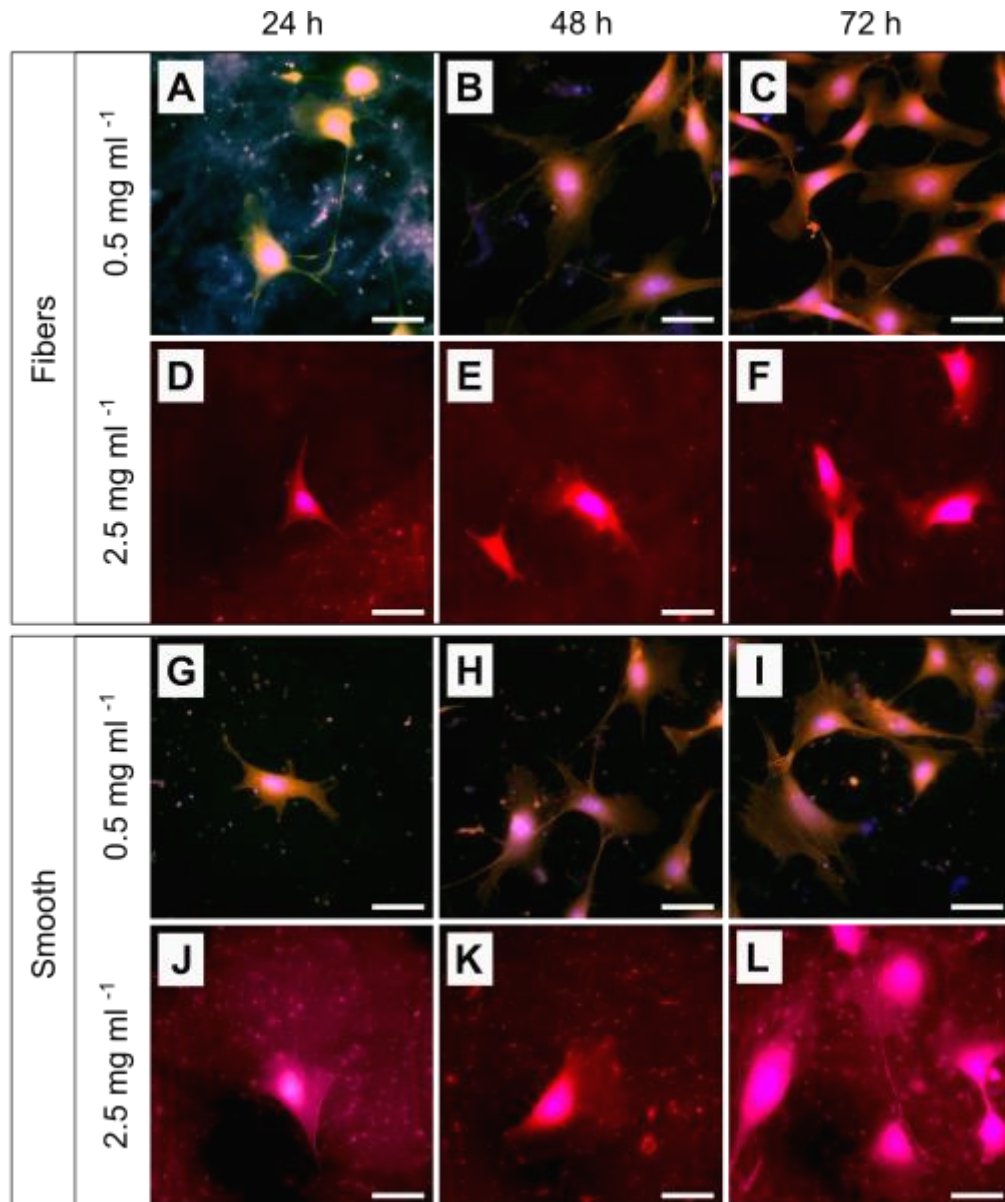


Figure 46. Fluorescence microscopy images of 3T3 fibroblasts on nanofibrous collagen prepared with 0.5 mg ml⁻¹ (A to C) and with 2.5 mg ml⁻¹ concentration (D to F) and on smooth collagen substrates prepared with 0.5 mg ml⁻¹ (G to I) and with 2.5 mg ml⁻¹ concentration (J to L). Nuclei were stained with Dapi (blue) and actin filaments with phalloidin (red). Scaffolds prepared with 2.5 mg ml⁻¹ express higher autofluorescence due to higher protein concentration. Scale bars represent 20 μm.

Using fluorescence microscopy images, the average single-cell area and single-cell perimeter were analyzed to characterize the morphological differences in more detail. Due to the strong autofluorescence of collagen, this analysis could only be performed on thin collagen scaffolds prepared with 0.5 mg ml⁻¹. Moreover, the circularity of the cells and the total substrate coverage were calculated. The area of the respective microscope images

was defined as A_{image} . The total area covered with actin was determined with ImageJ as described in section 3.1.6.2 Cell morphology and defined as total cell area $A_{(total\ cell\ area)}$ was determined with ImageJ. The relative cell-covered area $A_{covered}$ was determined by the following equation:

$$A_{covered} [\%] = \frac{A_{total\ cell\ area}}{A_{image}} * 100$$

Equation 5: Percentage of the total area covered with cells. *The relative cell covered area was determined by calculating the percentage of actin covered area for each image.*

As presented in Figure 47 and summarized in Table 6, the average area of fibroblasts on different substrates after a growth time of 24 h was the largest on smooth collagen films with $1796 \pm 6 \mu\text{m}^2$, differing significantly from collagen nanofibers ($p \leq 0.001$) and glass ($p \leq 0.0001$). Cells on collagen nanofibers had an average cell area of $1233 \pm 3 \mu\text{m}^2$; however, cells on glass had an area of $901 \pm 3 \mu\text{m}^2$. These trends remain after 48 h growth time, while the significance levels decrease. The cell area decreased to $926 \pm 2 \mu\text{m}^2$ on collagen nanofibers in contrast to an average cell area of $1378 \pm 3 \mu\text{m}^2$ on smooth collagen, still being significantly different ($p \leq 0.01$). In comparison to smooth collagen films, cells on glass displayed an increased average cell area of $1033 \pm 3 \mu\text{m}^2$ ($p \leq 0.05$). After 72 h the differences in cell area were less pronounced. Cells on nanofibrous collagen exhibited a cell area of $959 \pm 214 \mu\text{m}^2$ in contrast to cells on smooth collagen films with an area of $1497 \pm 3 \mu\text{m}^2$ ($p \leq 0.01$).

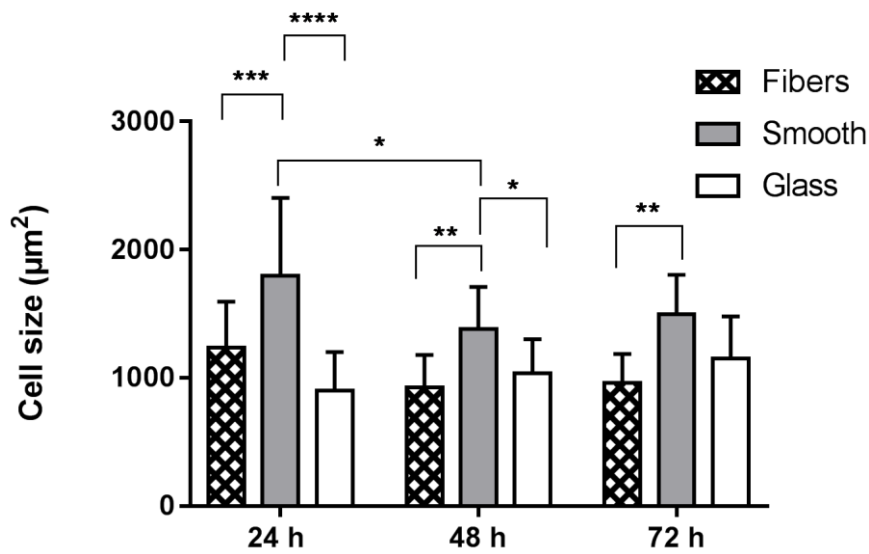


Figure 47. Single-cell area of 3T3 fibroblasts grown on fibrous collagen, nanofibrous collagen prepared with 0.5 mg ml^{-1} collagen and glass for 24 h, 48 h, and 72 h. $n = 4$ experiments were conducted. Data are presented with average \pm standard deviation of replicates. Significant differences indicated by * $p \leq 0.05$, ** $p \leq 0.01$, *** $p \leq 0.001$, **** $p \leq 0.0001$. (data for 24 h acquired by (Stebel 2018))

As an additional parameter for differences in cell shape the perimeter of fibroblasts on the different substrates was analyzed. As shown in Figure 48 the cell perimeter was largest on smooth collagen after 24 h growth time, with an average perimeter of $543 \pm 1 \text{ } \mu\text{m}$, a significantly higher value ($p \leq 0.01$) than for fibroblasts on collagen nanofibers with a perimeter of $433 \pm 9 \text{ } \mu\text{m}$. With a perimeter of $282 \pm 6 \text{ } \mu\text{m}$ fibroblasts on glass had a significantly smaller perimeter than cells on nanofibrous collagen ($p \leq 0.0001$) and smooth collagen ($p \leq 0.001$). Overall, the perimeter of cells grown on collagen nanofibers, and smooth collagen decreased significantly between 24 h and 48 h growth time. Over the growth time of 72 h, this trend was stable. Fibroblasts grown on smooth collagen showed the largest perimeter, while cells on glass exhibited the smallest perimeter, and fibroblasts on collagen nanofibers showed an intermediate perimeter between smooth collagen and glass for all examined time points. With increasing growth time, the significance decreased.

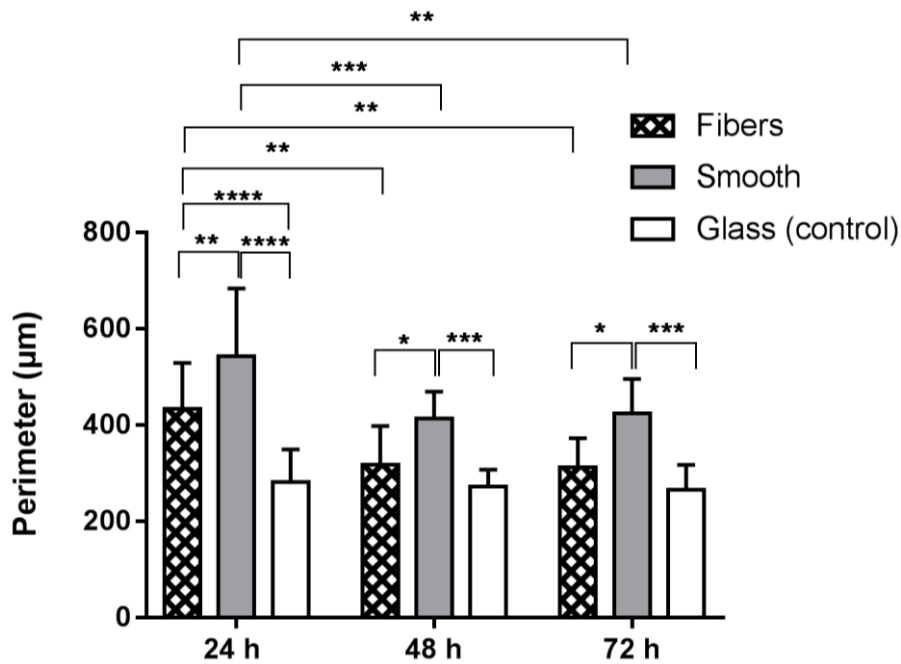


Figure 48. Cell perimeter of 3T3 fibroblasts grown on smooth collagen and fibrous collagen prepared with 0.5 mg ml^{-1} collagen for 24 h, 48 h, and 72 h. $n = 4$ experiments were conducted. Data are presented with average \pm standard deviation of replicates. PC excluded from ANOVA-test. Significant differences indicated by * $p \leq 0.05$, ** $p \leq 0.01$, *** $p \leq 0.001$, **** $p \leq 0.0001$. (data for 24 h acquired by (Stebel 2018))

To calculate the cell shape index the data of the cell area and perimeter were used in Equation 6. The CSI was calculated with the results for cell area A and perimeter P obtained from Figure 47 and Figure 48.

$$\text{CSI} = \frac{4 * \pi * A}{P^2}$$

Equation 6: Equation for the calculation of the CSI. The CSI was represented as the circularity of the cells. The area (A) and perimeter (P) were determined with image J. A CSI value of 1 stands for a perfect circle and a CSI of 0 would represent a line.

As shown in Figure 49 the CSI was largest on glass after 24 h growth time, with an average CSI of 0.204 ± 0.1 , a significantly higher value ($p \leq 0.001$) than for fibroblasts on smooth collagen with a CSI of 0.142 ± 0.1 and on collagen nanofibers ($p \leq 0.0001$) with an

average CSI of 0.131 ± 0.03 . The CSI remained largest on glass after 48 h growth time, with an average CSI of 0.226 ± 0.03 , a significantly higher value ($p \leq 0.0001$) than for fibroblasts on smooth collagen with a CSI of 0.137 ± 0.02 and collagen nanofibers ($p \leq 0.01$) with an average CSI of 0.1730 ± 0.05 . After 72 h growth time, the CSI on glass with a CSI of 0.25 ± 0.051 was still significantly higher than the smallest CSI found for fibroblasts on smooth collagen ($p \leq 0.0001$) with a CSI of 0.142 ± 0.27 in comparison to fibroblasts on collagen nanofibers ($p \leq 0.001$), which exhibited an intermediate CSI of 0.177 ± 0.04 .

CSI analysis revealed that for all time points cells on nanofibrous collagen and smooth collagen were significantly more elongated than cells on glass, which exhibited a higher circularity (see Fig. 49). While average cell areas and perimeters were comparable for fibroblasts on collagen nanofibers and glass, the CSI did not differ significantly for fibroblasts on nanofibrous and smooth collagen. In contrast to the aforementioned trends for cell area and perimeter, the CSI of cells did not converge over time.

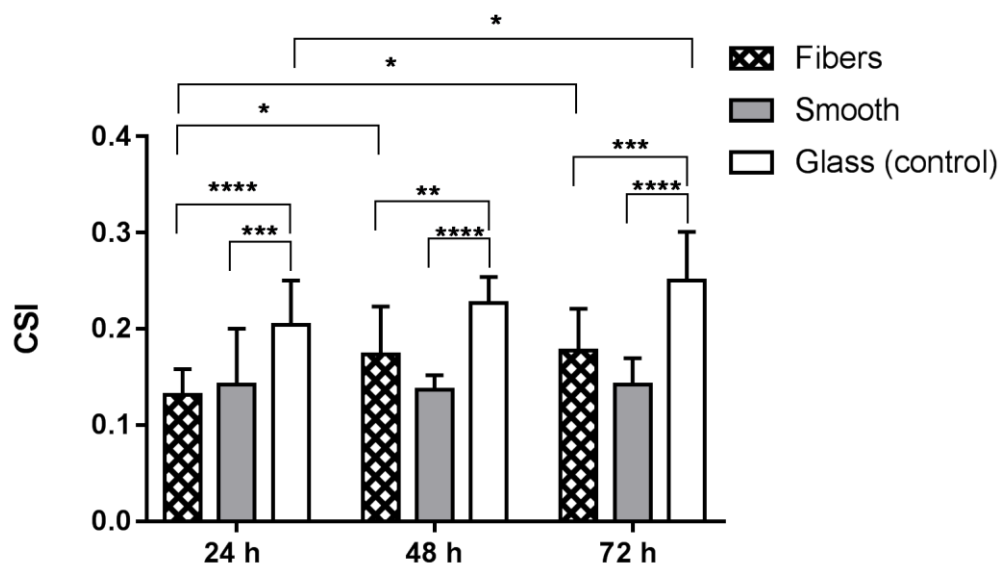


Figure 49. CSI analysis of 3T3 fibroblasts grown on smooth collagen and fibrous collagen prepared with 0.5 mg ml^{-1} collagen for 24 h, 48 h, and 72 h. $n = 4$ experiments were conducted. Data are presented with average \pm standard deviation of replicates. PC excluded from ANOVA-test. Significant differences indicated by * $p \leq 0.05$, ** $p \leq 0.01$, *** $p \leq 0.001$, **** $p \leq 0.0001$ (data for 24 h collected by (Stebel 2018)).

To elucidate the differences in cell growth on the different substrates even further the total substrate area covered with fibroblasts was analyzed (see Fig. 50). Interestingly, the percentage area covered by cells was not significantly different between the respective substrates. This observation was independent of the growth time (see Fig. 50). Over the cultivation time of 72 h, the percentage of the substrate area covered by cells increased significantly and was found to be independent of the substrate type ($p \leq 0.0001$).

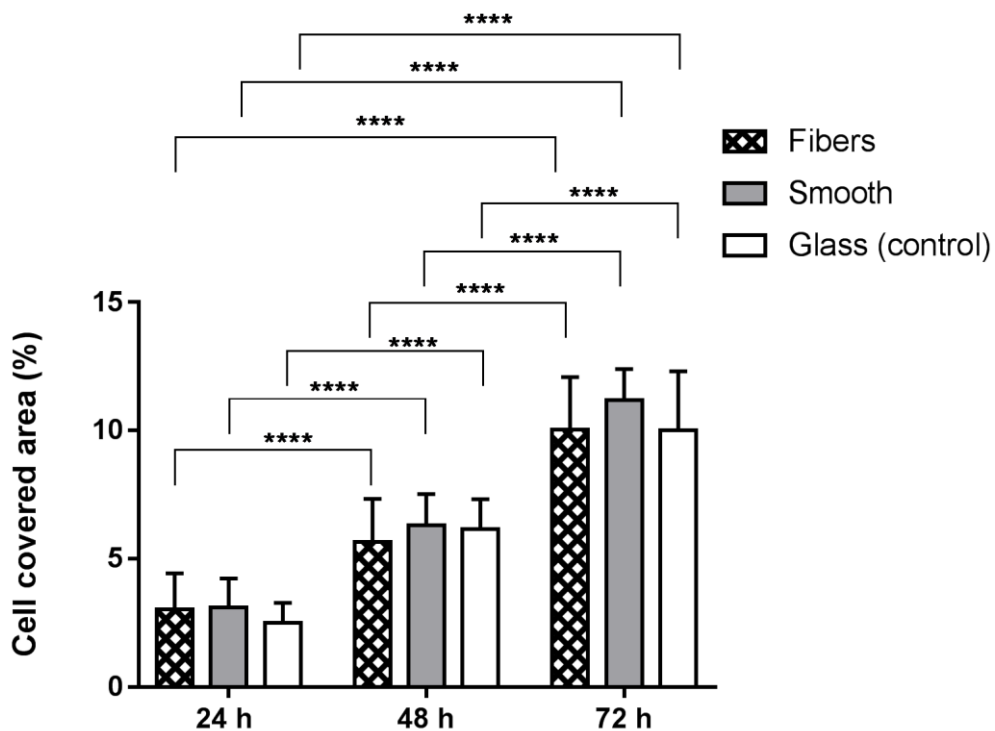


Figure 50. Cell covered area [%] of 3T3 fibroblasts grown on smooth collagen and fibrous collagen prepared with 0.5 mg ml^{-1} collagen for 24 h, 48 h, and 72 h. $n = 4$ experiments were conducted. Data are presented with average \pm standard deviation of replicates. PC excluded from ANOVA-test. Significant differences indicated by * $p \leq 0.05$, ** $p \leq 0.01$, *** $p \leq 0.001$, **** $p \leq 0.0001$. (data for 24 h collected by (Stebel 2018))

The results of the cell studies on collagen substrates prepared with 0.5 mg ml^{-1} can be summarized as follows:

Between 84% and 98% living cells were found on all substrates over all time points. The largest cells and perimeter were found on smooth collagen. The relative viability was between 41% and 79% on collagen prepared with 0.5 mg ml^{-1} and between 25% and 61% on collagen prepared with 2.5 mg ml^{-1} . The CSI of cells was highest on glass, while the CSI of cells on nanofibrous and smooth collagen were comparable. The cell covered area on the substrates was comparable independent of the substrate and increased with cultivation time. The quantitative results of the morphological analysis of 3T3 fibroblasts on thin collagen scaffolds are summarized in table 6.

Table 6. 3T3 fibroblasts on collagen fibers and smooth collagen prepared with 0.5 mg ml⁻¹ collagen. Relative viability for collagen prepared with 0.5 mg ml⁻¹ and 2.5 mg ml⁻¹.

	Fibers			Smooth			Glass		
	24 h	48 h	72 h	24 h	48 h	72 h	24 h	48 h	72 h
% living cells	89 ± 5	94 ± 3	98 ± 1	84 ± 7	93 ± 4	93 ± 4	91 ± 4 7	96 ± 2	98 ± 1
Relative viability 0.5 mg ml⁻¹ collagen	79%	43%	35%	80%	41%	45%	100%	100%	100%
Relative viability 2.5 mg ml⁻¹ collagen	61%	43%	30%	65%	33%	25%	100%	100%	100%
Cell size [μm]	1233 ± 344	926 ± 241	959 ± 214	1796 ± 581	1378 ± 317	1497 ± 288	901 ± 288	1033 ± 257	1151 ± 309
Cell perimeter [μm]	433 ± 92	318 ± 77	312 ± 57	543 ± 135	413 ± 53	424 ± 67	282 ± 65	272 ± 34	265 ± 49
Cell shape index	0.131 ± 0.03	0.173 ± 0.04	0.177 ± 0.04	0.142 ± 0.06	0.137 ± 0.01	0.142 ± 0.03	0.204 ± 0.04	0.226 ± 0.03	0.249 ± 0.05
Covered area [%]	3.03 ± 1.3	5.65 ± 1.6	10.01 ± 1.9	3.09 ± 1.0	6.31 ± 1.2	11.18 ± 1.1	2.49 ± 0.8	6.16 ± 1.1	10.00 ± 2.2

To study the observed trends in fibroblast morphology in dependence of the underlying topography in more detail, additional confocal microscopy and SEM analysis were conducted (see Fig. 51). Nanofibrous and smooth collagen scaffolds prepared with 2.5 mg ml⁻¹ with several micrometers in thickness were also used for this analysis since the collagen autofluorescence did not interfere with these experimental procedures (see Fig. 51). Thereby, thick collagen scaffolds prepared with 2.5 mg ml⁻¹ collagen were of particular interest to study whether fibroblasts protruded into the nanofibrous collagen scaffolds. The trends regarding fibroblast size and morphology, which were previously

found for 3T3 fibroblasts using fluorescence microscopy (see Fig. 46), were confirmed in confocal microscopy and SEM analysis (see Fig. 51). In addition to the aforementioned trends, it was observed that fibroblasts grown on collagen nanofibers displayed only a few long filopodia, while fibroblasts on smooth collagen exhibited more but shorter filopodia.

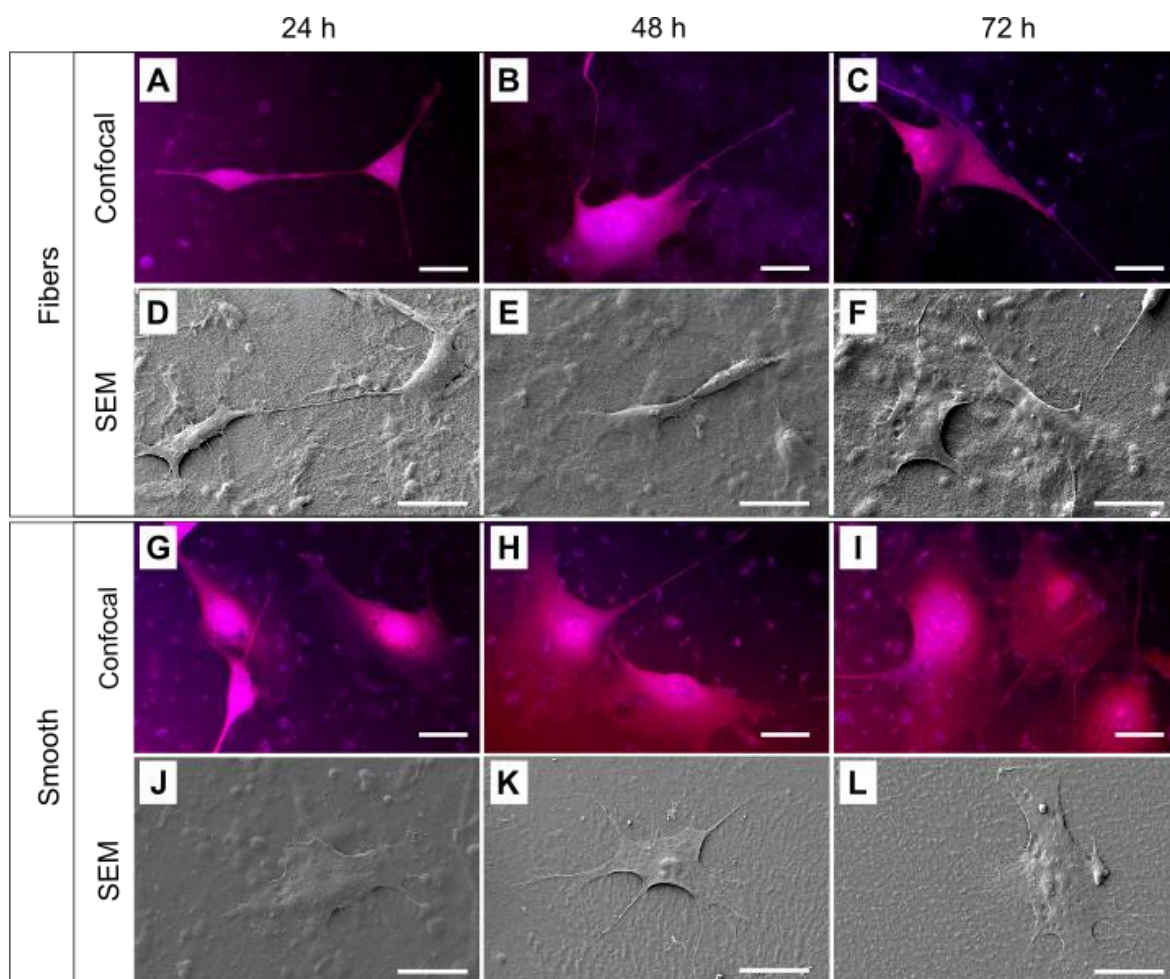


Figure 51. SEM images of 3T3 fibroblasts on nanofibrous collagen prepared with 2.5 mg ml^{-1} (A to C) and confocal microscopy images (D to F) and SEM images of 3T3 fibroblasts on smooth collagen substrates (G to I) and confocal microscopy images (J to L). Scale bars represent $20 \text{ }\mu\text{m}$.

To study whether fibroblasts protruded into the porous network of nanofibrous collagen scaffolds additional z-stack images of 3T3 fibroblasts grown on collagen scaffolds prepared with 2.5 mg ml^{-1} collagen were recorded *via* confocal microscopy (see Fig. 52). The z-stack was conducted over a z-height of 1734 nm with a step size of 289 nm . It can be seen that 3T3 fibroblasts on collagen nanofibers did not grow into the porous scaffolds.

No ingrowth of filopodia into the collagen scaffolds was observed, while most of the actin skeleton remained in one focal plane.

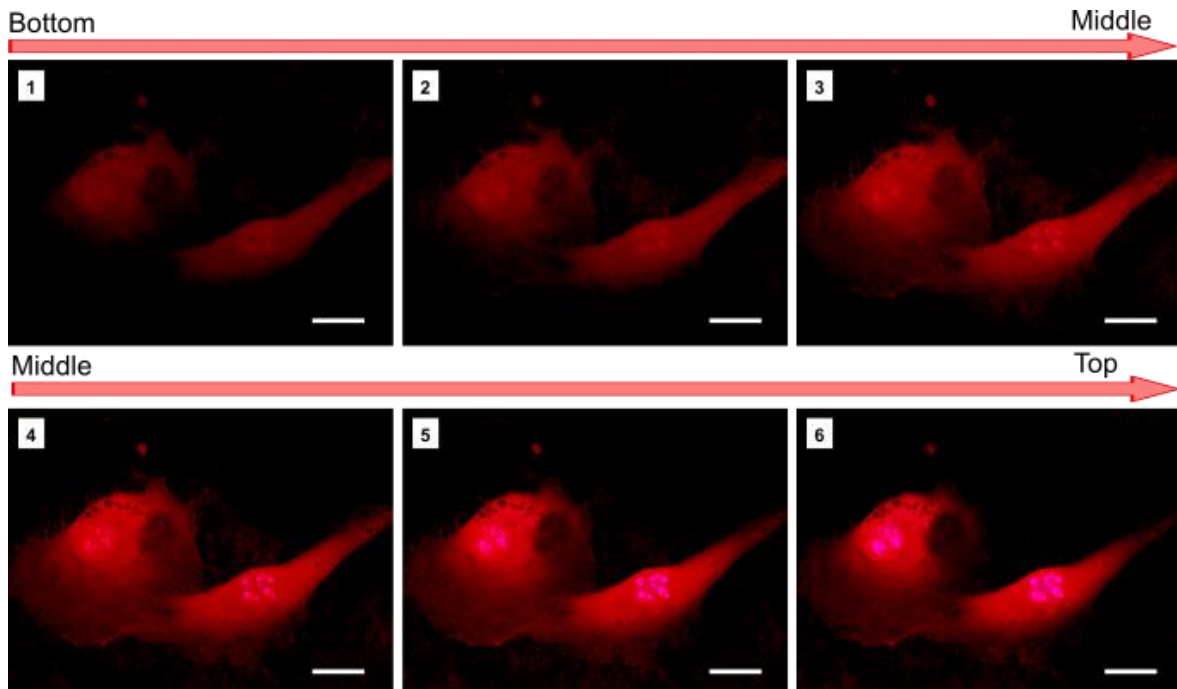


Figure 52. Confocal images from z-stack of 3T3 fibroblasts on collagen (2.5 mg ml^{-1}) with a step size of 289 nm and a total z-height of 1734 nm. Actin stained with phalloidin in red imaged at a wavelength of 555 and nuclei stained with DAPI in blue. Image 1 starting point in the substrate and every image 289 nm higher. The z-stack was taken after a growth time of 72 h. Scale bars represent $20 \mu\text{m}$.

3.1.6.3 Cell mechanics

The morphological differences were most pronounced until 48 h cultivation time. To study, if the observed differences in fibroblast morphology may result in differences of the cell stiffness atomic force microscopy analysis of the cell mechanics was carried out after 24 h growth time. In these experiments, 3T3 fibroblasts on scaffolds prepared with 0.5 mg ml^{-1} and 2.5 mg ml^{-1} collagen were compared to study whether the substrate thickness affected the cell stiffness (see Fig. 53). Three independent experiments were conducted and 17 individual cells per sample were measured. The Young's modulus for cells grown on collagen nanofibers, smooth collagen was measured (see Fig. 53) and ranged from 1.5 kPa to approximately 2.5 kPa. It can be seen in Fig. 53 that the standard deviations were larger than the median values. Overall, no significant differences in the Young's

moduli of fibroblasts were observed for the different substrate types or scaffold thicknesses.

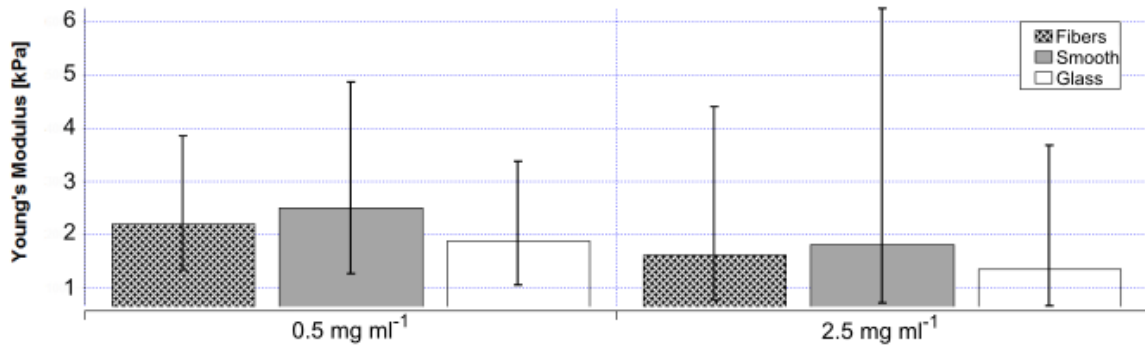


Figure 53. Young's moduli of 3T3 fibroblasts on nanofibrous and smooth collagen scaffolds. Young's moduli of fibroblasts grown on collagen nanofibers (checked) and smooth collagen (grey) prepared with 0.5 mg ml⁻¹ and 2.5 mg ml⁻¹ were measured. Young's moduli of fibroblasts grown on glass (white) were measured as a control. Fibroblasts grown on glass were measured as a control group. n=3 experiments were conducted. Data are presented with median and standard deviation of replicates.

3.1.6.4 Cellular response to binary patterned collagen scaffolds

Fixation of fibroblasts on binary collagen scaffolds was analyzed by SEM after 36 h, it was shown that the previously observed differences in cell morphology also occurred when the fibroblasts migrated from one topography region to the other (see Fig. 54(A) and 54(B)). For both scaffold thicknesses fibroblasts, which grew directly on the boundary between nanofibrous and smooth collagen, were analyzed. It can be seen clearly that cells on the boundary grew short but many filopodia on the smooth scaffold part while few and long filopodia protruded from the cell on the nanofibrous region. These observations show that fibroblasts dynamically react to spatial changes in the underlying topography while they migrate over the binary scaffolds.

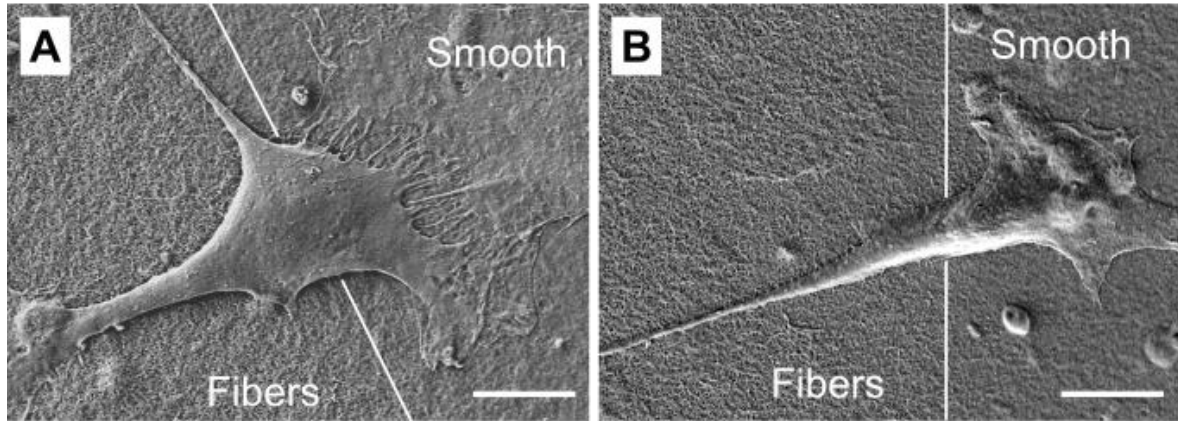


Figure 54. SEM images of fibroblasts on binary collagen scaffolds after 36 h in culture. (A) Thin binary scaffolds were prepared with 0.5 mg ml⁻¹ collagen. (B) Thick scaffolds were assembled with 2.5 mg ml⁻¹ collagen. For both concentrations, fibroblasts growing on the border between nanofibrous and smooth collagen exhibited many short filopodia on the smooth area while longer filopodia were observed on the nanofibrous scaffold region. Scale bars represent 10 μ m.

To analyze how the migration of 3T3 fibroblasts is influenced by the underlying topography, live-cell tracking was performed. The cells adhered to the scaffolds for 24 h. The velocity of individual cells on collagen nanofibers, smooth collagen, and patterned substrates prepared with 0.5 mg ml⁻¹ and 2.5 mg ml⁻¹ collagen was tracked for 20 h, respectively. An exemplary track with x- and y coordinates for a single cell on glass is plotted in Fig. 55. A typical cell trace followed a certain direction but a random movement was visible (see Fig. 55). The cell velocity was calculated over the displacement of the cell over time. The fast random movement is probably a random walk, whether it is an error in the algorithm or a (random) trembling movement of the cell. This is diffusive behavior, i.e. mean square displacement $\sim t$ (MSD). The drift is linear transport, i.e. distance (= $\sqrt{\text{MSD}}$) $\sim t$. The migration with x- and y-coordinates was tracked with imaging frames of every 2 min. An imaging window of 2 min was on the lower resolution limit for cell movement. To calculate the velocities over a larger time, windows over 10, 20 and 50 frames or 20 min, 40 min and 100 min were calculated.

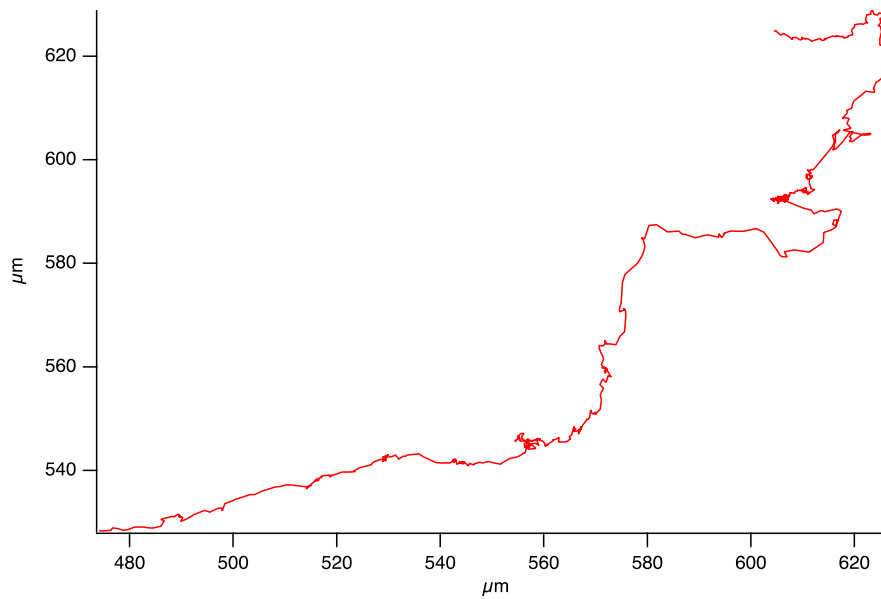


Figure 55. Exemplary track of a fibroblast migrating on glass. The track is plotted over the entire migration time of the cell. X- and y-axes represent x- and y coordinates.

The distance (d) was calculated as $\sqrt{\text{MSD}(t)}$ and a straight line fit following the equation

$f(x) = a + b * x$ with $a = 0$ was applied. To exclude possible random walk and algorithm artifacts from the Nikon tracking tool the cell velocities for single cells were calculated with a rolling average. The median velocity over 10, 20, and 50 individual time frames was calculated as described above. The frames were then shifted by half the frame size and the median value was calculated again. The trends of the median velocity of a single cell over time showed the same trend for all frame sizes (see Fig. 56). A frame size of 10 frames showed many peaks (green line). The frame size of 20 frames followed the trend but was less sensitive to random movements (yellow line) while the frame size of 50 frames showed the same trend (blue line). However, the setting of 50 frames was less sensitive to fluctuations in cell migration velocities. Therefore, for further cell migration velocity analysis, a frame size of 20 frames was used, which corresponds to 40 min intervals.

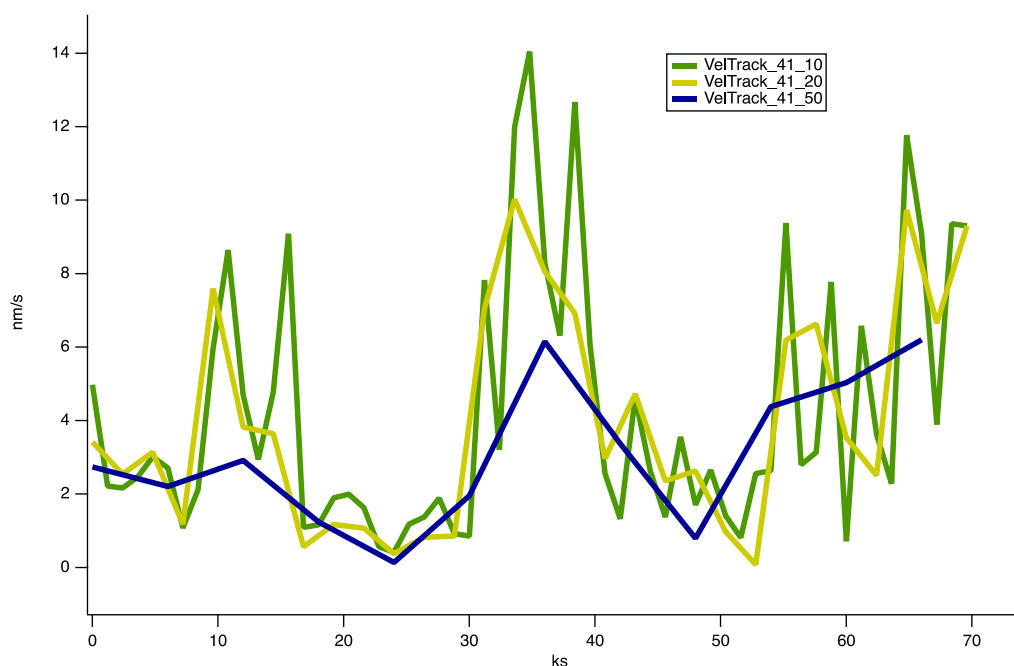


Figure 56. Median velocities of a single fibroblast migrating on glass over time displayed with different frame sizes. Median velocities were calculated with different frame sizes of 10 (green), 20 (yellow), and 50 (blue). A frame size of 10 frames showed many peaks (green line). The frame size of 20 frames followed the trend but was less sensitive to random movements (yellow line) while the frame size of 50 frames showed the same trend (blue line).

To show that the migration behavior of fibroblasts was reproducible, pooled median velocities of each triplicate were plotted in an organized manner to compare the velocity trends between independent experiments. Overall, the triplicates and independent experiments showed comparable migration velocities. After analyzing the velocities of single cells over time, the median velocities of all cells on one sample were summarized in histograms. An exemplary graph for cell migration velocities on nanofibrous collagen prepared with 2.5 mg ml^{-1} collagen is shown in Fig. 57. Deviations between the histogram groups from independent experiments were smaller than between triplicates. Thus, allowing pooling the median velocities of all experiments, displayed as a black histogram (see Fig. 57).

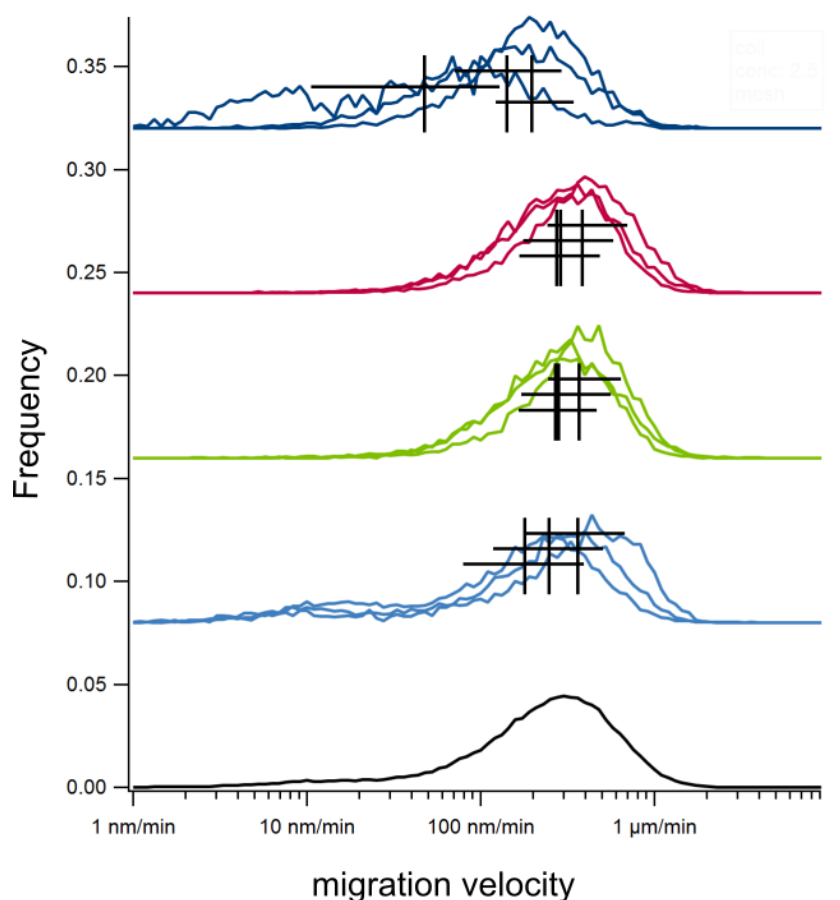


Figure 57. Normalized pooled histograms of migration velocities of 3T3 fibroblasts on nanofibrous collagen prepared with 2.5 mg ml^{-1} collagen. This graph displays the median velocities of cells on single samples. For better visualization, the velocities are plotted on a logarithmic axis. Median velocities of cells on the same dependent triplicates are shown in the same color. Different independent experiments are shown in different colors: n=1 (light blue), n=2 (green), n=3 (purple) and n=4 (dark blue). Vertical black lines in the histograms represent the corresponding median velocity. Horizontal black lines in the histograms represent the standard deviations. The black histogram represents the pooled median migration velocity of cells on glass (all experiments pooled). Overall, all histograms are very similar indicating reproducible results for the four independent experiments.

Migration velocities of 3T3 fibroblasts on nanofibrous and smooth collagen prepared with 0.5 mg ml^{-1} collagen were comparable. Velocities fibroblasts on nanofibrous and smooth collagen were approximately 600 nm min^{-1} being faster than cells on glass with a median peak of approximately 300 nm min^{-1} (see Fig. 58). On binary scaffolds, significantly fewer tracks were analyzed than on scaffolds with a single topography. Overall, migration velocities on binary substrates showed lower values than on scaffolds with a single topography. Remarkably, when fibroblast velocities on patterned scaffolds were analyzed both topographical areas showed a second shoulder at very low migration velocities

(dashed black and red line), which was not observed on scaffolds exhibiting a single topography (full black and red line). On binary scaffolds, significantly fewer tracks were analyzed than on scaffolds with a single topography. Thus, single lower values have stronger effects on the distribution. Migration velocities on binary substrates have lower values as on scaffolds with a single topography. Both topographical areas show a second shoulder at very low migration velocities.

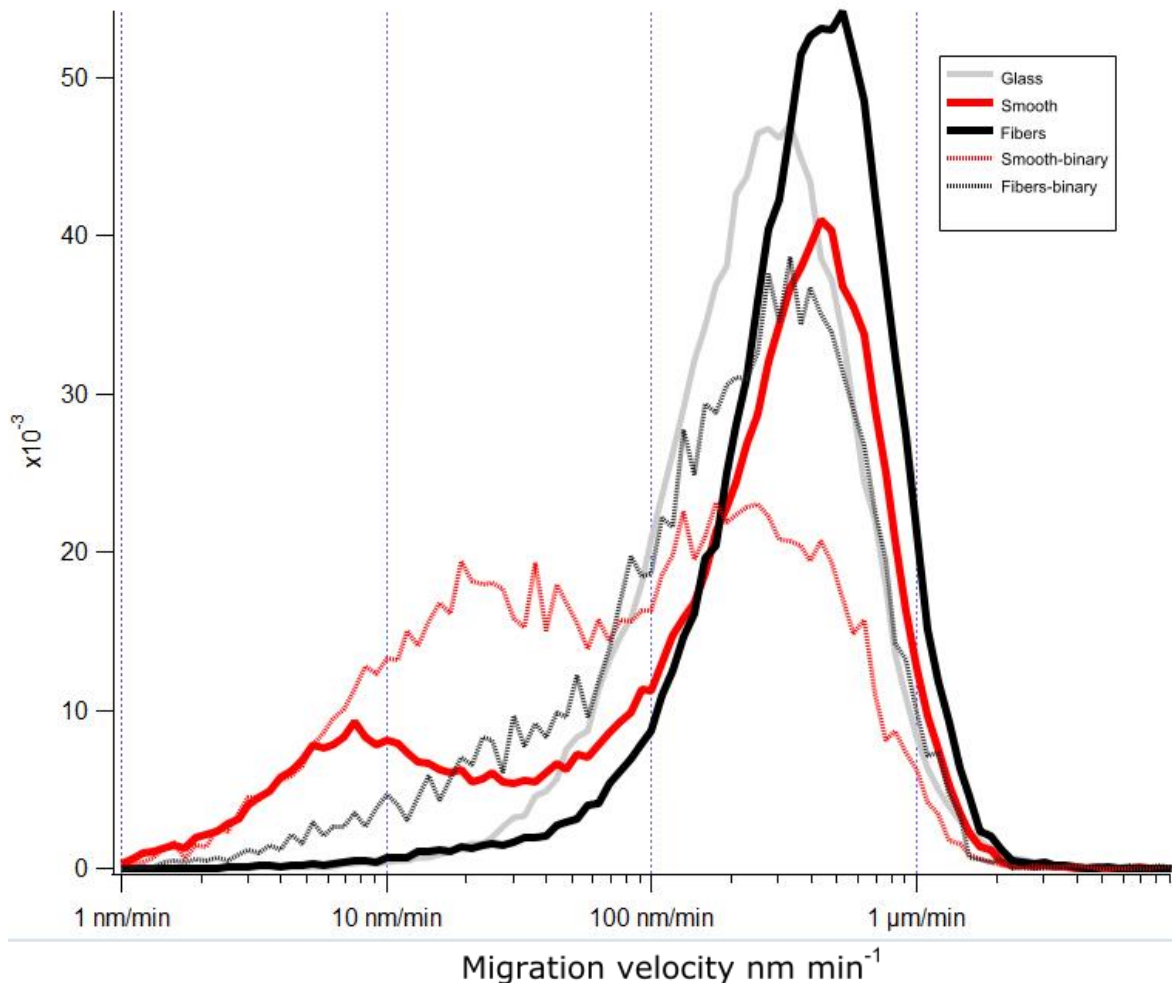


Figure 58. Histograms of median migration velocities of 3T3 fibroblasts on collagen scaffolds prepared with 0.5 mg ml^{-1} collagen. Histograms are plotted for cell velocity on nanofibrous collagen, smooth collagen, nanofibrous areas on binary patterned, and smooth areas on binary patterned scaffolds. Cell migration velocities on the glass are shown as a control. Velocities are plotted on a logarithmic scale. Cells grown on nanofibrous and smooth collagen scaffolds have a comparable peak showing a similar median velocity. Median velocities of cells on nanofibrous and smooth collagen are higher than on glass. On binary scaffolds, significantly fewer tracks were analyzed than on scaffolds with a single topography. Migration velocities on binary substrates have lower values than on scaffolds with a single topography. Both topographical areas show a second shoulder at very low migration velocities.

Migration velocities of 3T3 fibroblasts on nanofibrous and smooth collagen prepared with 2.5 mg ml⁻¹ collagen were comparable. Velocities of cells on nanofibrous and smooth collagen were approximately 500 nm min⁻¹ and faster than cells on glass with a median peak at approximately 300 nm min⁻¹ (see Fig. 59). On binary scaffolds, significantly fewer tracks were analyzed than on scaffolds with a single topography. Again, migration velocities of fibroblasts on binary substrates exhibited lower values than on scaffolds with a single topography. Both topographical areas showed a second shoulder at very low migration velocities.

In comparison, the migration velocities of cells grown on collagen scaffolds prepared with 2.5 mg ml⁻¹ collagen were lower than on scaffolds prepared with 0.5 mg ml⁻¹. The distribution of cell velocities on collagen scaffolds with a single topography was comparable to the distribution of cells grown on glass independent of the protein concentration.

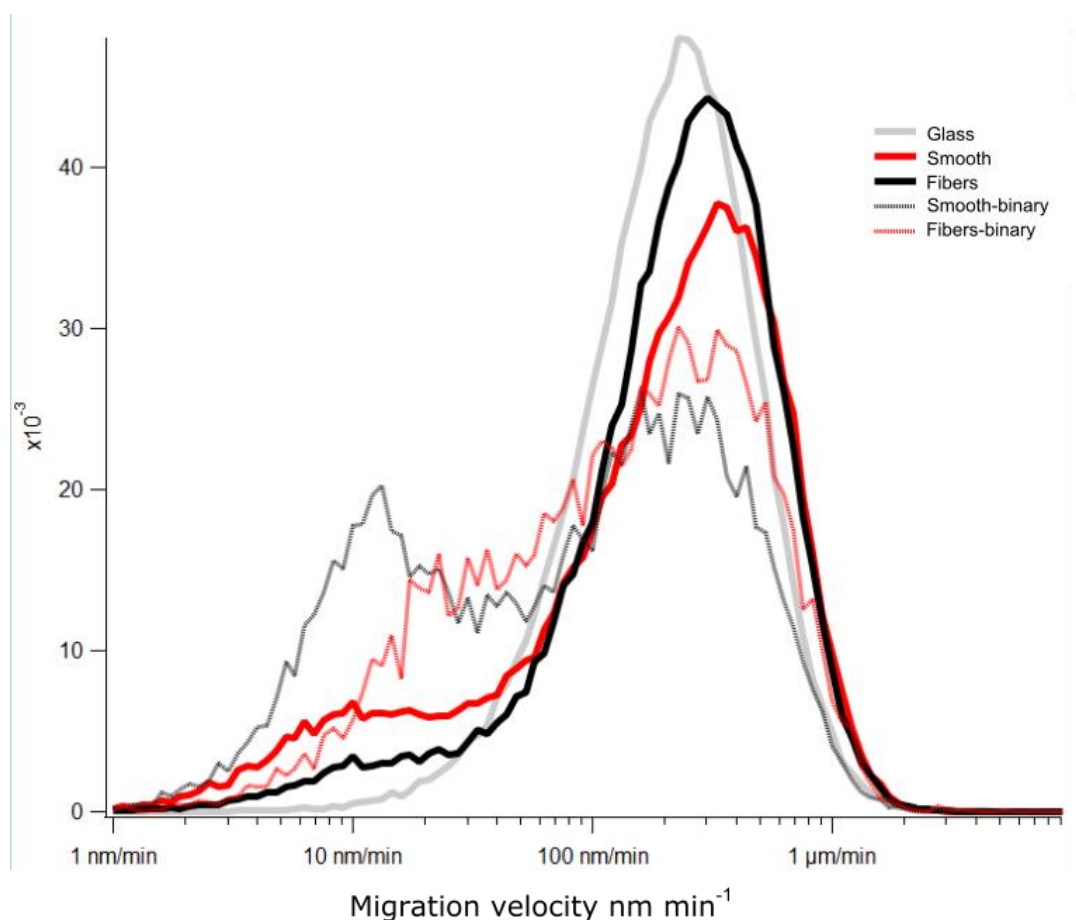


Figure 59. Histograms of median migration velocities of 3T3 fibroblasts on collagen scaffolds prepared with 2.5 mg ml^{-1} collagen. Histograms are plotted for cell velocity on nanofibrous collagen, smooth collagen, nanofibrous areas on binary patterned, and smooth areas on binary patterned scaffolds. Cell migration velocities on glass are shown as a control. Velocities are plotted on a logarithmic scale. Cells grown on nanofibrous and smooth collagen scaffolds have a comparable peak showing a similar median velocity. Median velocities of cells on nanofibrous and smooth collagen are higher than on glass. On binary scaffolds, significantly fewer tracks were analyzed than on scaffolds with a single topography. Migration velocities on binary substrates have lower values than on scaffolds with a single topography. Both topographical areas show a second shoulder at very low migration velocities.

For both concentrations, shoulders were observed at low migration velocities. Those are almost stationary tracks or cells. Further analysis focused on migrating cells. Therefore for further analysis, the (linear) histogram of $\log(v)$ was used (see Fig. 60). The procedure is shown exemplarily for scaffolds prepared with 2.5 mg ml^{-1} collagen and later applied to all migration data. As the binary patterned only had few tracks the analyzing procedure was established with data from 3T3 cells on nanofibers and smooth collagen and glass as a control. A gauss fit conducted for the migration velocities of nanofibrous and smooth

collagen as well as for glass (see Fig 60). This position of the maximum is different from the mean value of the entire histogram, because of the shoulders at low speeds.

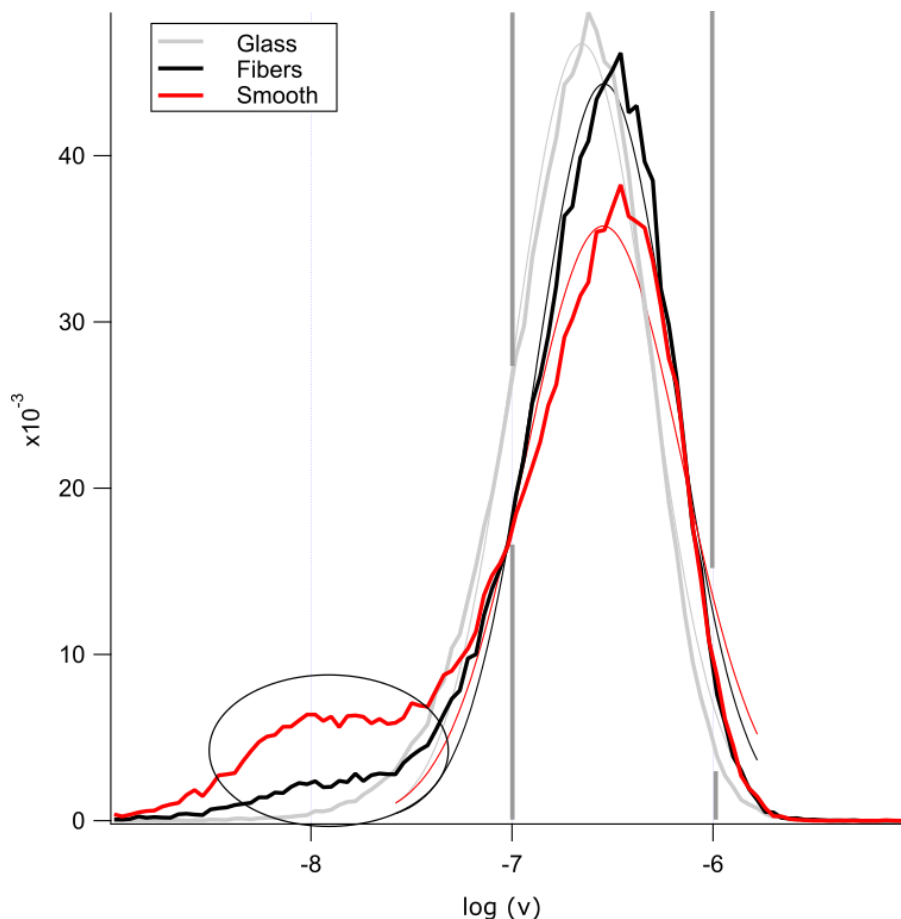


Figure 60. Normalized Histograms of cell velocities of 3T3 fibroblasts on nanofibrous collagen (red) and smooth collagen (blue) prepared with 2.5 mg ml^{-1} collagen and glass as control (black). The logarithm of migration velocities plotted on a linear axis. The black circle highlights the shoulders of the histograms at low migration velocities. The thinner lines are shown gauss fit near the maximum to determine the height and width of the Gauss peak. The maxima of the fitted curves are shifted compared to the original histograms.

The graph in Fig. 61 shows the mean values of the entire data set (vertical lines) versus the positions of the maximum obtained by local gauss-fit (dashed lines). Not only the values shift, but also the order of the samples. So Cohen's d should be calculated based on the gauss-fit. This takes into account only the data in the main peak, i.e. values from 100 nm min^{-1} to $10 \text{ } \mu\text{m min}^{-1}$.

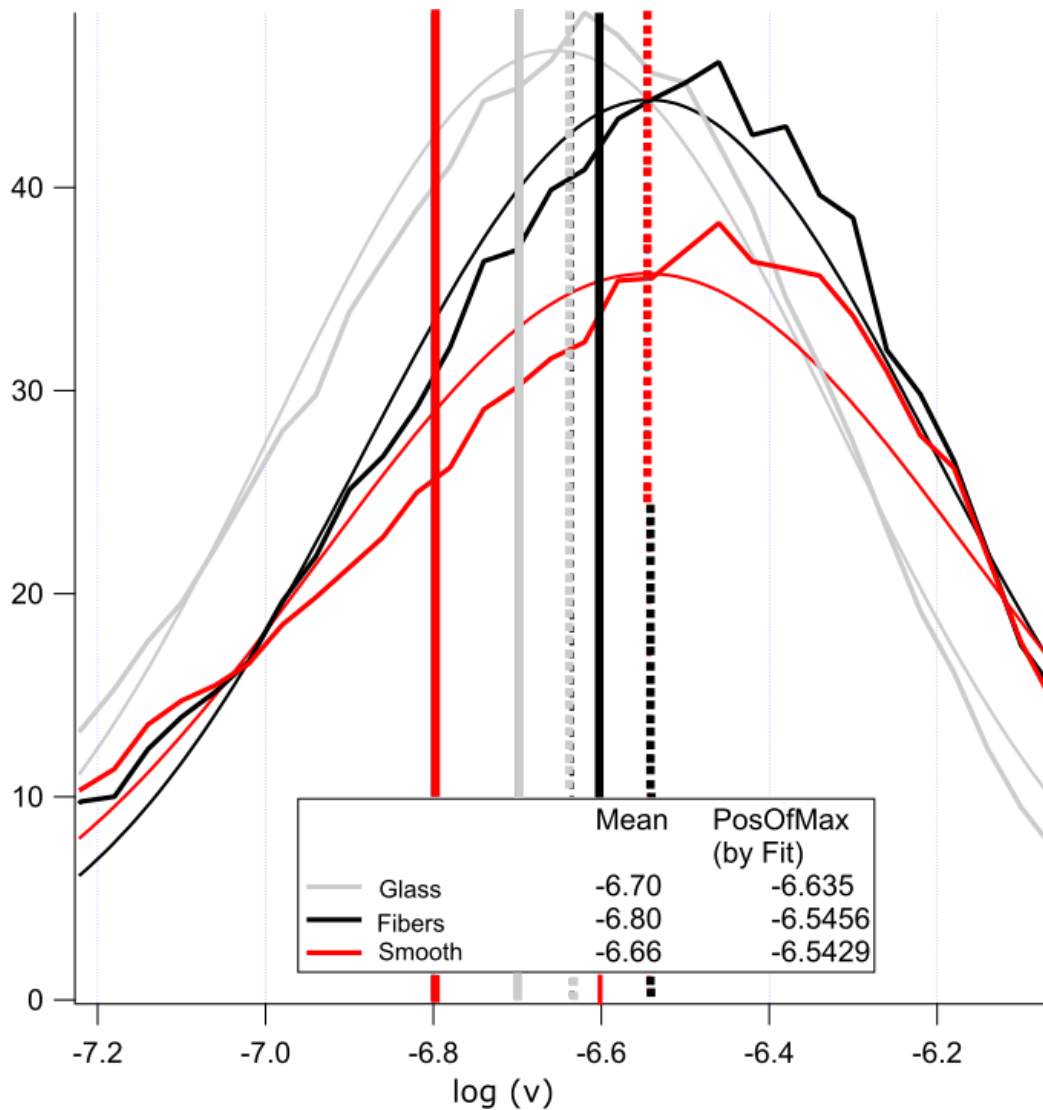


Figure 61. Zoom in to normalized Histograms of cell velocities of 3T3 fibroblasts on nanofibrous collagen (red) and smooth collagen (blue) prepared with 2.5 mg ml^{-1} collagen and glass as control (black). The logarithm of migration velocities plotted on a linear axis. The thinner lines are shown gauss fit near the maximum to determine the height and width of the Gauss peak. The maxima of the fitted curves are shifted compared to the original histograms. The mean values of the entire data set (vertical lines) versus the positions of the maximum obtained by local gauss-fit (dashed lines). Not only the values shift, but also the order of the samples.

Overall, migration velocities between 180 nm min^{-1} and 430 nm min^{-1} were found (see Fig. 62A). Cells on nanofibrous scaffolds prepared with 0.5 mg ml^{-1} collagen migrated with a velocity of approximately $430 \pm 28 \text{ nm min}^{-1}$ showing a small effect size (* Cohens $d \geq 0.2$) compared to cell migration velocity of approximately $342 \pm 29 \text{ nm min}^{-1}$ on smooth

collagen prepared with 0.5 mg ml^{-1} collagen and $267 \pm 20 \text{ nm min}^{-1}$ on glass and medium effect size (** Cohens $d \geq 0.5$) compared to the migration speed of $181 \pm 21 \text{ nm min}^{-1}$ on smooth areas of binary patterned scaffolds with the same collagen concentration. Migration velocities on smooth collagen prepared with 0.5 mg ml^{-1} collagen showed small effects sizes (* Cohens $d \geq 0.2$) compared to velocities of $267 \pm 20 \text{ nm min}^{-1}$ on glass and smooth areas of binary patterned scaffolds.

Cells on nanofibrous scaffolds prepared with 2.5 mg ml^{-1} collagen migrated with a velocity of approximately $286 \pm 21.1 \text{ nm min}^{-1}$ showing a small effect size (* Cohens $d \geq 0.2$) compared to cell migration velocity of approximately $285 \pm 24 \text{ nm min}^{-1}$ on smooth collagen prepared with 2.5 mg ml^{-1} collagen, $222 \pm 16 \text{ nm min}^{-1}$ on glass and $189 \pm 21 \text{ nm min}^{-1}$ on smooth areas of binary patterned scaffolds with the same collagen concentration. Migration velocities on smooth collagen prepared with 2.5 mg ml^{-1} collagen showed small effects sizes (* Cohens $d \geq 0.2$) compared to velocities of $222 \pm 16 \text{ nm min}^{-1}$ on glass, nanofibrous areas of binary scaffolds with migration velocities of $200 \pm 23 \text{ nm min}^{-1}$ and $189 \pm 21 \text{ nm min}^{-1}$ on smooth areas of binary patterned scaffolds.

However, fibroblasts displayed a trend towards faster migration on nanofibrous collagen than on smooth scaffolds. Compared to collagen scaffolds exhibiting only one topography, the migration velocity on binary patterns was marginally lower. Cell migration velocities of fibroblasts on patterned collagen scaffolds did not vary significantly between the two topographies, either. (For an overview of all mean velocities and Cohens d see Table 14 and 15 in Appendix).

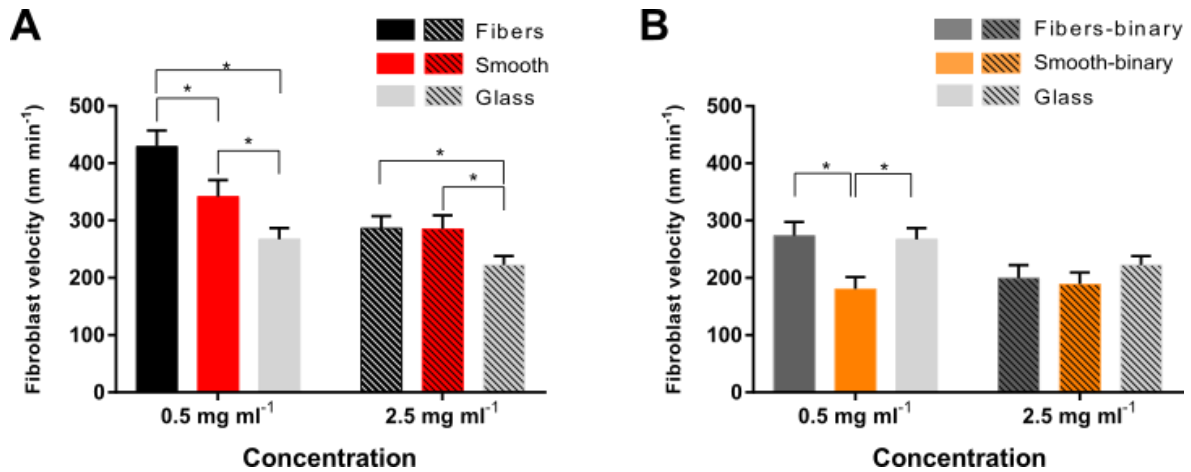


Figure 62. Migration velocities of 3T3 fibroblasts on different collagen scaffolds. (A) Median velocities of fibroblasts on nanofibrous and smooth collagen scaffolds, which exhibited the respective topography on the whole surface, in comparison to glass references. Migration analysis was performed on thin and thick collagen scaffolds prepared with 0.5 mg ml⁻¹ or 2.5 mg ml⁻¹ collagen, respectively. (B) Median velocities of fibroblasts on binary collagen scaffolds with nanofibrous and smooth topography in comparison to bare glass references. All velocity data are presented with an average \pm standard deviation of $n=4$ independent experiments. Small effect sizes are indicated by * Cohen's $d \geq 0.2$.

3.2 Fibrinogen scaffolds

In this chapter, the results on our novel scaffolds composed of self-assembled fibrinogen nanofibers will be summarized. To analyze the substrate characteristics, like surface roughness and thickness, SEM analysis of cross-linked fibrinogen scaffolds was carried out. Additionally, AFM analysis was performed to determine the swelling properties of fibrinogen scaffolds under cell culture conditions.

3.2.1 Fibrinogen nanofiber morphology

After establishing a new class of collagen scaffolds with binary topography the aim was to apply the new patterning process to other proteins. By broadening the biochemical range of patterned protein scaffolds it could then become possible to study the response of different cell types to topographical differences. Therefore, it was investigated whether the patterning process could be combined with the preparation of self-assembled fibrinogen scaffolds as it was recently introduced by Stapelfeldt *et al.* (Stapelfeldt *et al.* 2019a).

First, the individual topographies were prepared from fibrinogen and characterized with regard to their morphology using SEM and AFM analysis (see Fig. 63). Dried fibrinogen nanofibers prepared with 5 mg ml⁻¹ fibrinogen and 2.5x PBS displayed a distinct fiber morphology with fiber diameters in the range of 100 nm to 300 nm (see Fig. 63A). Planar fibrinogen scaffolds prepared with the same protein concentration and 5 nM NH₄HCO₃ exhibited a very planar surface. Using cross-sectional SEM analysis, scaffold thicknesses between 1.7 ± 0.4 μm were found for these planar fibrinogen scaffolds while nanofibrous scaffolds displayed thicknesses of 2.8 ± 0.4 μm (see Fig. 63B and 63E).

Crosslinking of the scaffolds in FA vapor was found to preserve the respective topography. It has been shown before that fibrinogen fibers dissolve upon rehydration (Stapelfeldt *et al.* 2019a). Consequently, all results shown here represent crosslinked scaffolds.

To evaluate the influence of aqueous cell culture environment on the nanotopographical features in preparation for subsequent cell culture studies the FA vapor cross-linked fibrinogen scaffolds were rehydrated in DMEM cell culture medium. AFM analysis showed that the fiber morphology was preserved in DMEM (see Fig. 63C). Planar fibrinogen scaffolds displayed a very planar surface even after rehydration with DMEM.

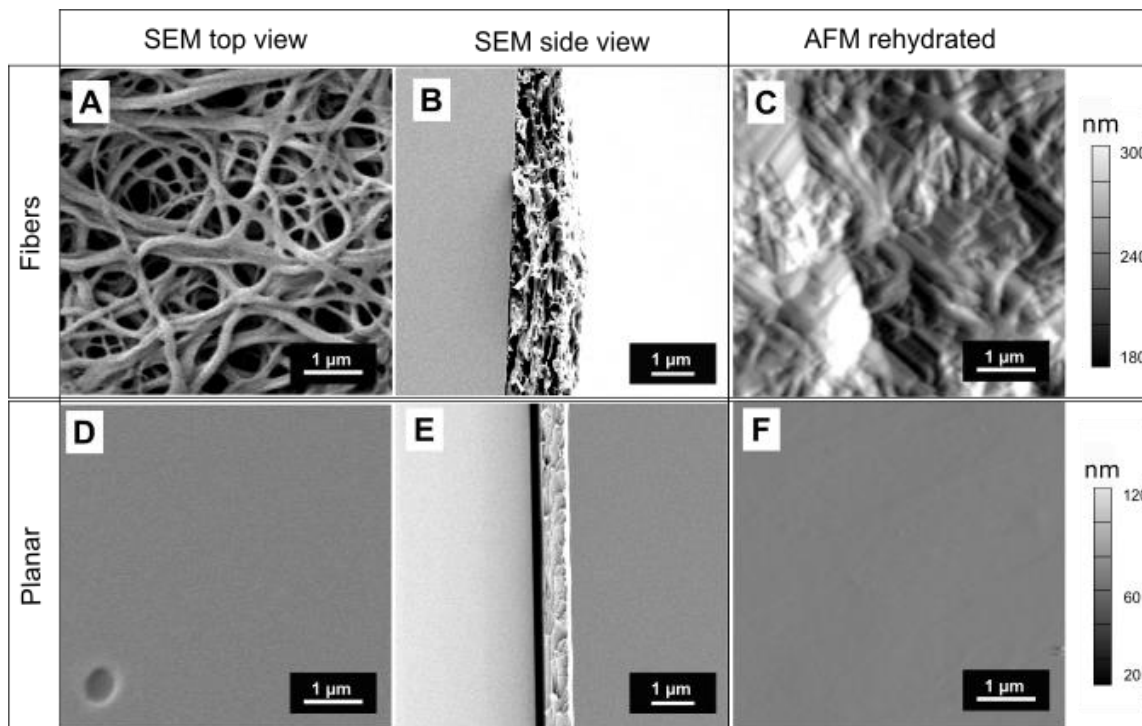


Figure 63. SEM images of crosslinked nanofibrous and planar fibrinogen scaffolds prepared with 5 mg ml^{-1} fibrinogen and AFM images of rehydrated scaffolds. SEM images of nanofibrous fibrinogen (A) and planar fibrinogen (D) and cross-sections of fibrinogen nanofibers (B) and planar fibrinogen scaffolds (E). AFM images of fibrinogen nanofibers (C) and planar fibrinogen (F) rehydrated in cell culture medium DMEM.

To analyze the roughness of nanofibrous and planar fibrinogen scaffolds, height images were taken with an AFM. Height profiles were derived from these height images. Fibrous fibrinogen scaffolds displayed more height changes over a shorter distance than planar scaffolds as can be seen in Fig. 64A to D. The height of fibrous scaffolds differed over the entire sample surface, whereas the height of planar scaffolds decreased. The height profile of the planar scaffolds did not show any peaks as they were observed for nanofibrous fibrinogen.

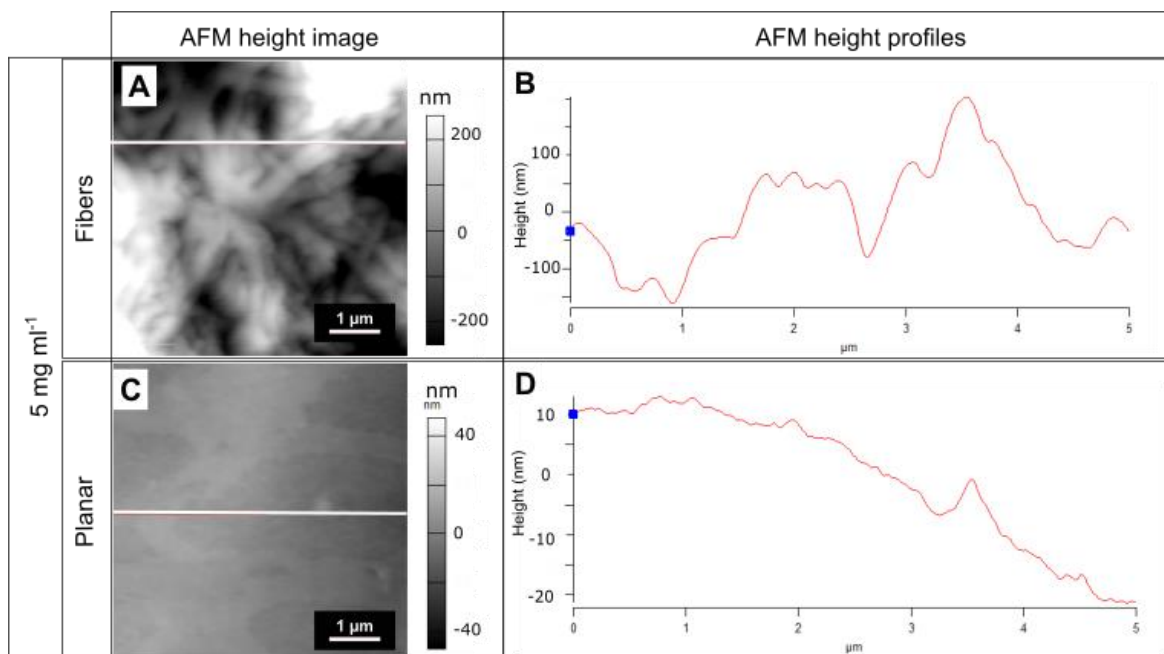


Figure 64. AFM height images of fibrinogen scaffolds prepared with 5 mg ml^{-1} (A and C) and height profiles of fibrous fibrinogen scaffolds (B) and planar fibrinogen (D). AFM scans display height images of the respective scaffold. The offset was subtracted from the height images. White lines show the location of the displayed height profiles (B), (D). All images display fibrinogen scaffolds rehydrated with DMEM.

Subsequent AFM roughness analysis showed a roughness of $118 \pm 16 \text{ nm}$ for dried fibrinogen fibers and distinct lower roughness of only $7.2 \pm 1.7 \text{ nm}$ for dried planar fibrinogen scaffolds. After rehydration, the fibrinogen nanofiber roughness showed a roughness of $121.3 \pm 29.37 \text{ nm}$ and $9.2 \pm 5.2 \text{ nm}$ for planar fibrinogen scaffolds. AFM analysis revealed that cross-linked fibrous fibrinogen scaffolds rehydrated in DMEM did not increase in roughness (see Table 7). Overall, planar scaffolds exhibited a considerably lower surface roughness than nanofibrous fibrinogen scaffolds.

Table 7. Roughness R_q values of fibrinogen scaffolds obtained by AFM analysis. Roughness was measured for nanofibrous and planar fibrinogen scaffolds prepared with 5 mg ml^{-1} fibrinogen. Values are given for dried scaffolds and rehydrated scaffolds in cell culture medium DMEM.

	5 mg ml^{-1}	
	R_q dried (nm)	R_q rehydrated (nm)
Fibrinogen fibers	118 ± 16	121.3 ± 29.37
Planar Fibrinogen	7.12 ± 1.7	9.2 ± 5.2

To analyze the swelling behavior of fibrinogen nanofibers prepared with 5 mg ml^{-1} after exposure to the cell culture medium, the fiber diameters were also analyzed with AFM (see Table 8). AFM analysis of dried, cross-linked fibrinogen nanofibers resulted in diameters of approximately 230 nm. After rehydration in cell culture medium DMEM, the diameter of fibrinogen nanofibers increased to an average value of 337 nm.

Table 8. Fiber diameters (FD) of fibrinogen nanofibers prepared with 5 mg ml^{-1} . Diameters of dried, crosslinked fibers and diameters of rehydrated fibers in cell culture medium DMEM.

	AFM	
	FD _{dried} (nm)	FD _{rehydrated} (nm)
5 mg ml^{-1} Fibrinogen	230 ± 7.7	337 ± 21

3.2.2 Fibrinogen nanofiber mechanics

To determine the mechanical properties of nanofibrous and planar fibrinogen scaffolds exemplary AFM measurements were performed. In this analysis, force curves, which appeared infinitely stiff for both, nanofibrous and planar fibrinogen scaffolds, were obtained. Representative force curves are shown in Figure 65. The data shown below display force curves for nanofibrous and planar fibrinogen scaffolds prepared with 5 mg ml^{-1} fibrinogen. The steep slope of approximately 1 of the approach curve is typical for stiff substrates. With these curves, Young's moduli could not be calculated, as they appear infinitely stiff.

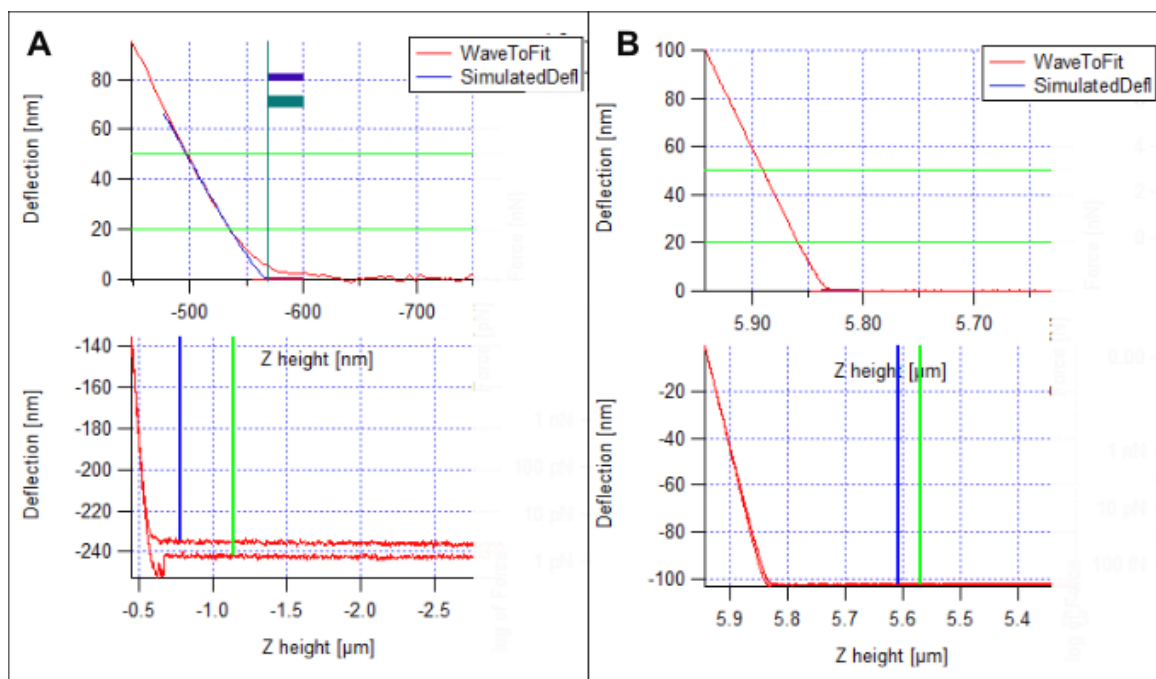


Figure 65. Exemplary force-distance curves of nanofibrous fibrinogen scaffolds (A) and planar collagen scaffolds (B) prepared with 5 mg ml^{-1} fibrinogen. Force-distance curves with a slope of approximately 1 are typical for very stiff substrates.

3.2.3 Fibrinogen scaffolds with binary surface topography for cell culture

Building up on the patterning process to prepare protein scaffolds with selected areas of nanofibrous and planar topography, which we established with collagen as a model system (see section 3.2), this routine was now adapted for the blood plasma protein fibrinogen. Analogous to the process established for collagen, for fibrinogen the ability of this protein to self-assemble into nanofibrous scaffolds was exploited to prepare topographically patterned scaffolds. The technical details of this procedure were described in 2.1.4 before.

To achieve a stable fibrinogen scaffold with a binary topography for subsequent cell culture studies the fibrinogen scaffolds were prepared on APTES-modified glass slides. By combining the method of salt-induced self-assembly with the new patterning process introduced in chapter 2.1.4 fibrinogen scaffolds with nanofibrous and planar topographies could be prepared for the first time. Phase-contrast microscopy images showed that a distinct boundary between planar and nanofibrous area could be achieved (see Fig. 66). This allows good visual control in cell culture applications of this novel scaffold type.

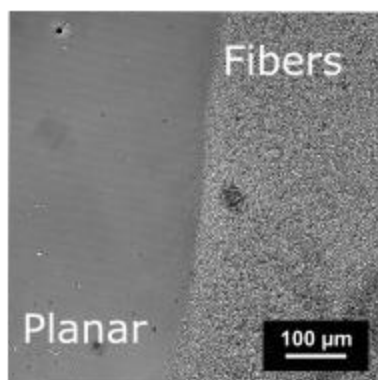


Figure 66. Phase-contrast image of a fibrinogen scaffold prepared with 5 mg ml^{-1} fibrinogen with binary topographical features. The boundary between planar and nanofibrous areas is clearly defined.

To gain further insight into the nanoscale topographical features of binary fibrinogen scaffolds SEM analysis of dried scaffolds was carried out. SEM analysis of these scaffolds showed that a clearly defined border between the highly porous fibrinogen nanofibers and the planar fibrinogen was obtained in the patterning process (see Fig. 67).

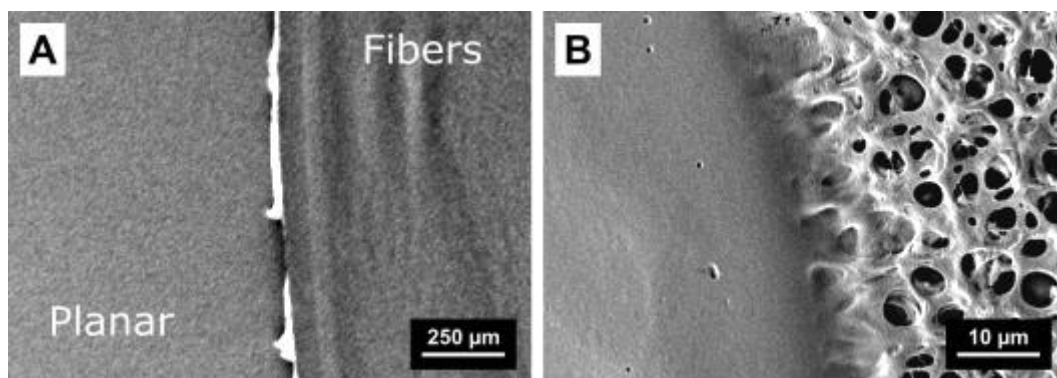


Figure 67. Patterned fibrinogen substrates prepared with 5 mg ml^{-1} planar and nanofibrous fibrinogen on APTES coated glass slides. An overview of a binary fibrinogen scaffold is given in (A), and subfigure (B) shows a clearly defined border between planar and nanofibrous areas with a higher magnification. The planar area shows few surface topography, while the fibrinogen fibers are well defined (B).

3.2.4 Cellular response to nanostructured fibrinogen scaffolds

Since the self-assembly process of fibrinogen into nanofibers has only recently been established (Stapelfeldt *et al.* 2019a; Stapelfeldt *et al.* 2019b), nothing is known about the interaction of cells with this novel scaffold type. Therefore, to analyze the interaction of cells with this new biomaterial class of nanofibrous and planar fibrinogen scaffolds 3T3 fibroblasts were used as a model system in analogy to the previous studies with different collagen topographies. The results of the cell interaction studies are presented in the following subsections starting with the results of cell viability assays, which are followed by the analysis of fibroblast morphology and live cell tracking.

3.2.4.1 Cell viability

To measure the metabolic activity of 3T3 fibroblasts a WST-1 assay was conducted. The supernatant was measured photometrically at a wavelength of 450 nm. The viability was measured for the time points of 24 h, 48 h, and 72 h. Four independent experiments with triplicates were performed with glass as control substrates. Moreover, APTES was introduced as a second control, because all fibrinogen scaffolds were assembled on APTES-modified glass.

Using the WST-1 proliferation assay, comparable proliferation rates were obtained for 3T3 fibroblasts on nanofibrous fibrinogen, on planar fibrinogen scaffolds, and APTES until 72 h in culture (see Fig. 68). No significant differences in fibroblast proliferation were found between the respective substrates at all time points. Nanofibrous and planar fibrinogen scaffolds as well as APTES yielded proliferation rates, which were comparable to fibroblasts cultivated on glass throughout all cultivation times. Furthermore, a trend towards higher proliferation rates with increasing cultivation time was observed for nanofibrous fibrinogen, planar fibrinogen, and APTES.

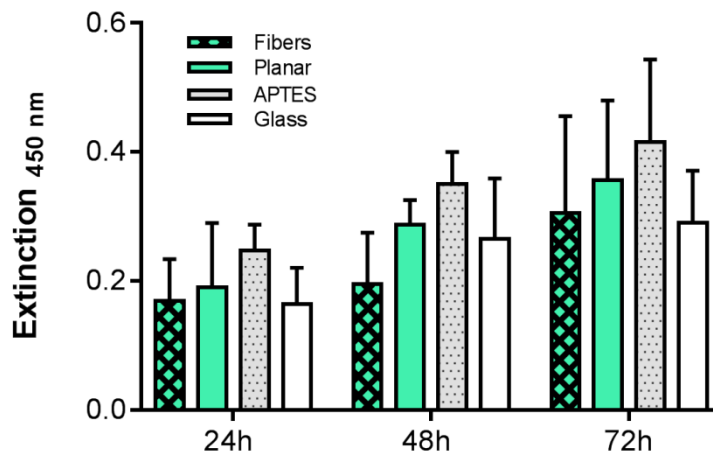


Figure 68. Proliferation rates of fibroblasts on fibrinogen scaffolds. Measurements were taken after 24 h, 48 h, and 72 h. Cells proliferated in a comparable range over 72 h. n = 4 experiments with triplicates were conducted. Data are presented with average \pm standard deviation of replicates.

Subsequently, the viability of 3T3 fibroblasts was analyzed in relation to the metabolic activity of 3T3 fibroblasts on the glass control (see Fig.69). The dashed lines between 100 % and 70 % define the “biocompatible viability range” for biomaterials according to the norm (EN ISO 10993-5:2009). Overall, the viability of fibroblasts on different substrates can be classified as biocompatible throughout all time points of the cultivation, i.e. the viability was above 70 % of the glass control at all time points. After 24 h cultivation time cells on APTES exhibited significantly higher viability (164%) in comparison to cells on nanofibrous (106%) and planar fibrinogen (116%) ($p \leq 0.05$). After 48 h the viability of cells decreased to approximately 73% on nanofibrous fibrinogen and 145% on APTES while the viability on planar fibrinogen was around 112%. At 48 h significantly lower cell viability on nanofibrous fibrinogen in comparison to APTES substrates ($p \leq 0.01$) was observed. At 72 h cultivation time, fibroblast viability on nanofibrous fibrinogen and APTES increased again to 102% and 142%, respectively, while fibroblast viability on planar fibrinogen was around 126%. Overall, after 72 h the cell viability on all substrate types was 100 % or higher and no significant differences in cell viability on the different substrate types were found anymore.

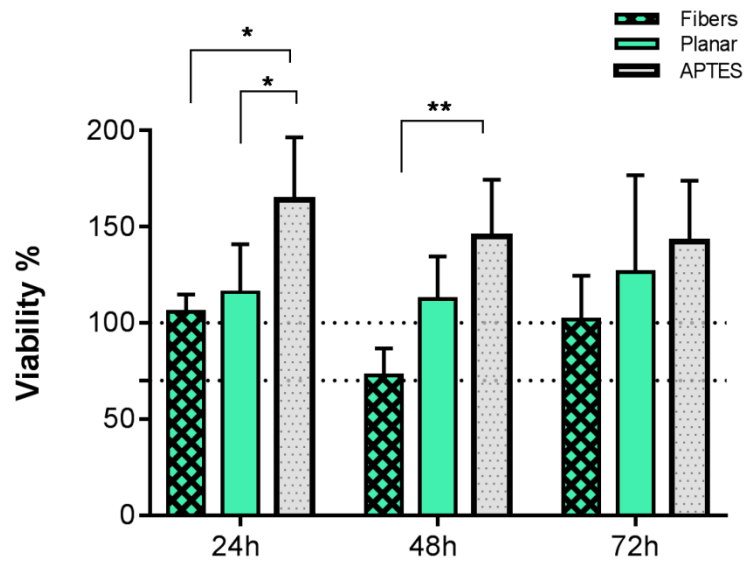


Figure 69. Cell viability of 3T3 fibroblasts on fibrinogen scaffolds. Dashed lines represent the biocompatibility range defined as 70 % to 100% of cells grown on glass. Viability was measured after 24 h, 48 h, and 72 h. n = 4 experiments with triplicates for each substrate type were conducted. Data are presented with average \pm standard deviation of replicates. PC excluded from ANOVA-test. Significant differences indicated by * $p \leq 0.05$, ** $p \leq 0.01$

3.2.4.2 Cell morphology

For the morphological analysis, NIH 3T3 fibroblasts were cultivated on nanofibrous and planar fibrinogen scaffolds prepared with 5 mg ml^{-1} , respectively. The cell morphology was analyzed with fluorescence microscopy over 72 h cultivation time by staining cytoskeletal actin filaments with phalloidin, and nuclei were stained with DAPI (see Fig. 70). Nanofibrous fibrinogen scaffolds exhibited a strong autofluorescence, which was caused by the crosslinking in formaldehyde vapor (see Fig. 70A to 70C) in comparison to planar fibrinogen scaffolds (see 70D to F). The autofluorescence of nanofibrous fibrinogen was probably stronger than for planar fibrinogen because of the topographical features in the nanofibrous scaffolds. Moreover, the scaffolds were thicker. More protein led to more autofluorescence. The nanofibers increase the surface topography and therefore the accessible area for aldehyde groups. Due to the higher porosity aldehyde groups can bind deeper in the scaffolds, thus increasing the autofluorescence. Despite the strong autofluorescence, it can be seen that 3T3 fibroblasts proliferated well on nanofibrous fibrinogen scaffolds at all time points. The fibroblast morphology on nanofibrous fibrinogen could only be investigated to a limited extent with the help of fluorescence microscopy. On nanofibrous fibrinogen (Fig. 70A to 70C) more nuclei were visible. The nuclei closer to each other than on planar fibrinogen, indicating smaller cell sizes on these respective samples. The morphology of fibroblasts on planar fibrinogen could be analyzed without any significant autofluorescence of the underlying scaffold. In Fig. 70D to 70F it can be seen that the actin filaments in 3T3 fibroblasts on planar fibrinogen were spread out through individual cells and that fibroblasts exhibited large cell areas (see Fig. 70D to 70F).

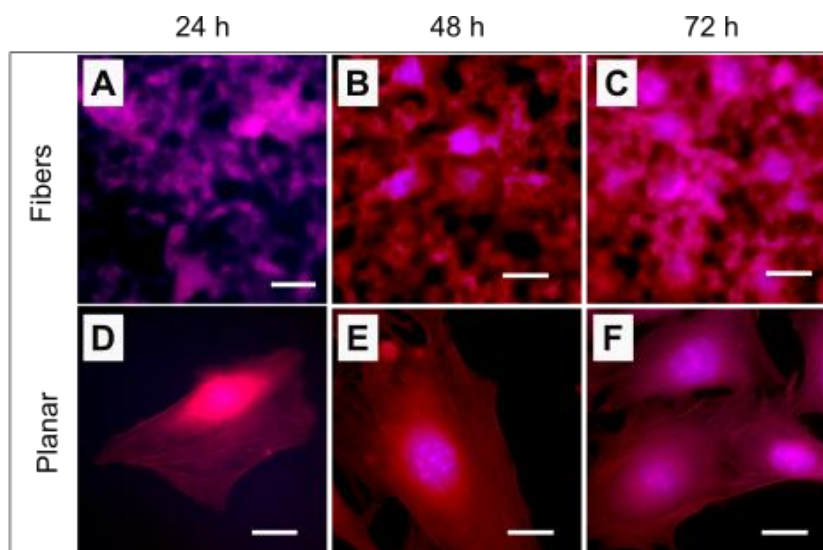


Figure 70. Fluorescence microscopy images of 3T3 fibroblasts on fibrinogen scaffolds. 3T3 fibroblasts grown on nanofibrous fibrinogen prepared with 5 mg ml^{-1} (A) to (C) and planar fibrinogen (D) to (F). Nuclei were stained with Dapi (blue) and actin filaments with phalloidin (red). Scale bars represent $20 \mu\text{m}$.

To further study the observed trends in fibroblast morphology in dependence of the underlying fibrinogen topography, confocal microscopy, and SEM analysis were conducted (see Fig. 71). In particular, these techniques could overcome the previous limitations of fluorescence microscopy, thus allowing us to analyze the cell morphology on nanofibrous fibrinogen scaffolds without any or with reduced autofluorescence.

It can be seen in Fig. 71 that 3T3 fibroblasts on planar fibrinogen exhibited larger cell areas than on planar fibrinogen. Confocal microscopy and SEM analysis both confirmed this observation.

Moreover, it can be seen in the confocal images (see Fig. 71A-C), that fibroblasts on nanofibrous fibrinogen expressed much fewer stress fibers than fibroblasts on planar fibrinogen. On planar fibrinogen, distinct stress fibers were found in most cells, which were most pronounced at 48 and 72 h in culture (see Fig. 71G to 71L). The observed stress fibers are mostly dorsal and ventral. The confocal images of fibroblasts on planar fibrinogen (see Fig. 71 G-I) revealed a flatter and more spread morphology than on nanofibrous fibrinogen (see Fig. 71 A-C).

SEM analysis revealed that cells on nanofibrous fibrinogen were smaller but grew flat (see Fig. 71D-F) than on planar fibrinogen (see Fig. 71J-L). In contrast to that, some spindle-

like cells along with well spread and large morphology grown on planar fibrinogen (see Fig. 71J-L) could be found in the SEM images. Overall, it can be seen that cells on planar fibrinogen were larger and seem to express more actin filaments than on nanofibrous fibrinogen.

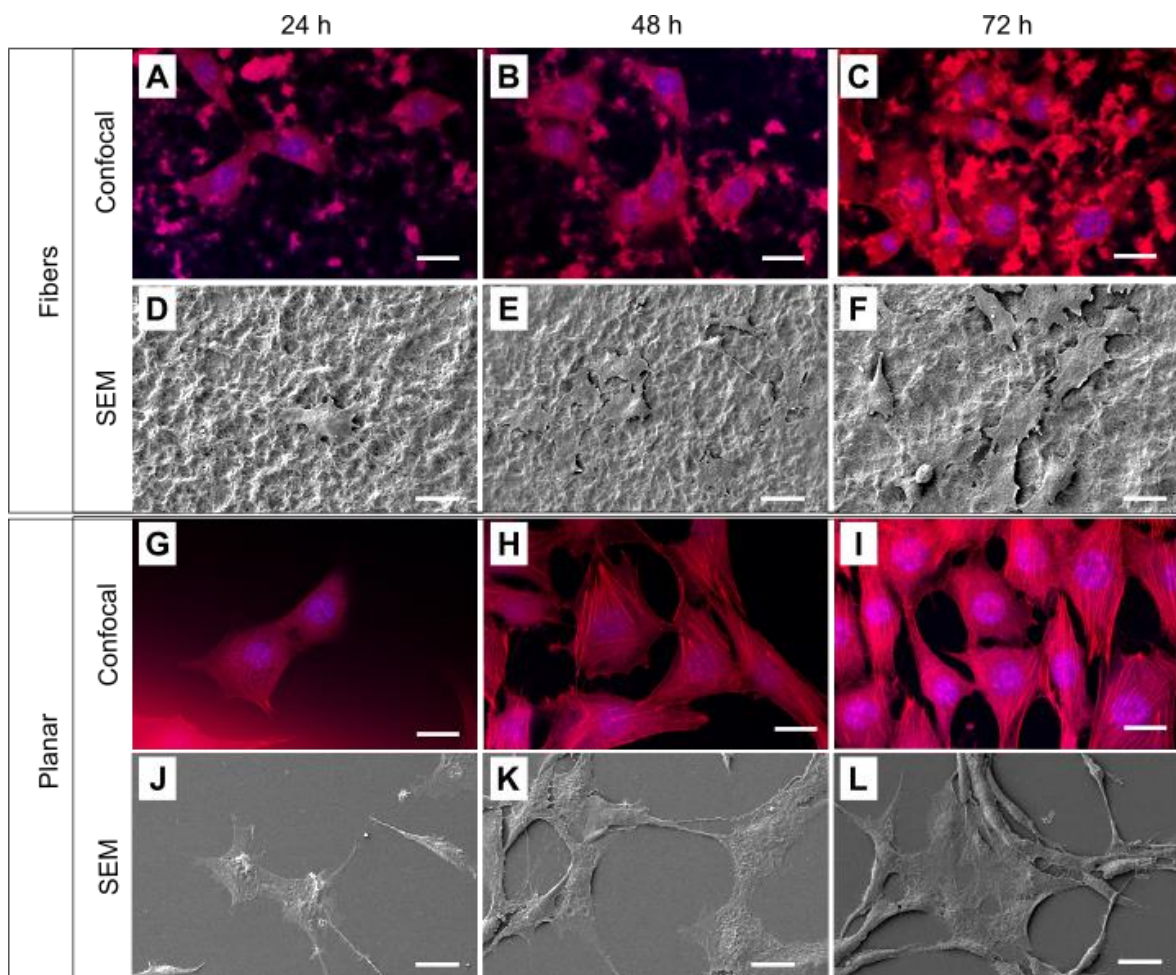


Figure 71. SEM images of 3T3 fibroblasts on nanofibrous fibrinogen prepared with 5 mg ml^{-1} fibrinogen (A) to (C) and confocal microscopy images (D) to (F) and SEM images of 3T3 fibroblasts on planar fibrinogen substrates (G) to (I) and confocal microscopy images (J) to (L). Actin filaments were stained with phalloidin (red) and nuclei stained with DAPI (blue). All samples were bleached for 10 min at a wavelength of 565 nm to reduce the autofluorescence of the fibrinogen scaffolds. Scale bars represent $20 \mu\text{m}$.

To study whether 3T3 fibroblasts protrude into fibrinogen nanofibers, z-stack images with a total thickness of 1650 nm and step size of 275 nm were obtained with confocal microscopy (see Fig. 72). In this z-stack, it can be seen that the cells were in close contact with the underlying nanofibers. Single filopodia grew into the scaffold. Overall, it is difficult

3. Results

to distinguish between the fluorescent signals of actin filaments and the surrounding autofluorescent fibrinogen nanofibers. The surface was sufficiently bleached by the bleaching procedure, but focusing deeper into the fibrinogen scaffolds was challenging because of the autofluorescence.

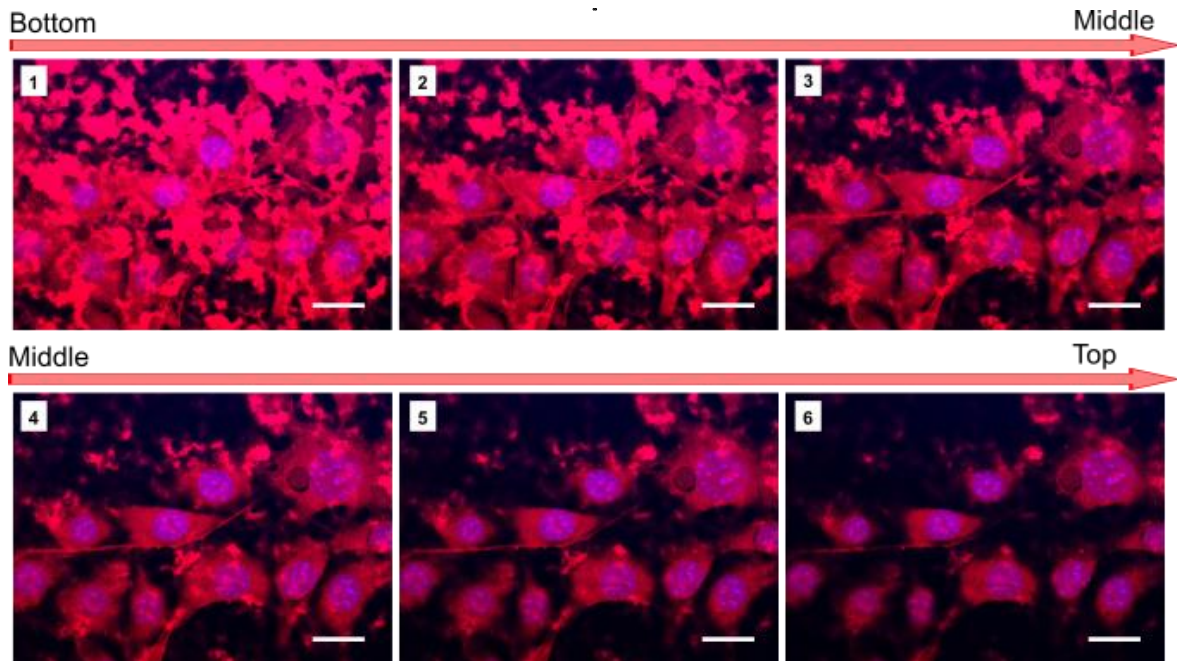


Figure 72. Confocal microscopy z-stack images of 3T3 fibroblasts on nanofibrous fibrinogen (5 mg ml^{-1}) after 72 h cultivation with a step size of 275 nm and a total thickness of 1650 nm. Actin stained with phalloidin in red imaged at a wavelength of 565 and nuclei stained with DAPI in blue at a wavelength of 461 nm. Image 1 starting point in the scaffold and subsequent images were recorded with a step size of 275 nm. Patches with red fluorescence represent autofluorescence of the nanofibrous fibrinogen scaffold. Scale bars represent 20 μm .

3.2.4.3 Cellular response to binary patterned fibrinogen patterns

To analyze whether fibroblasts would dynamically adapt their morphology on binary substrates SEM analyzes were carried out. Fibroblasts were fixated on binary collagen scaffolds were analyzed by SEM after 36 h. Fibroblasts, which grew directly on the boundary between nanofibrous and planar fibrinogen, were analyzed with regard to their morphology. Thus, it could be shown that the observed differences in cell morphology occurred when the fibroblasts migrated from one topography region to the other (see Fig. 73). Fibroblasts on the boundary grew well spread and with pronounced stress fibers on the planar scaffold part while the cell bodies were less flat on the nanofibrous region without visible actin fibers. The white lines outline the spread cell on the planar area of the binary patterned scaffold. Cells on the planar part exhibited stronger pronounced stress fibers whereas cell parts grown on fibers were less spread.

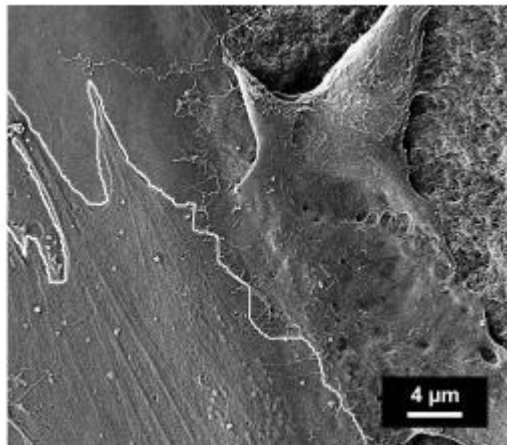


Figure 73. SEM image of 3T3 fibroblasts grown on the boundary between two topographies left planar and right side nanofibrous. SEM analysis of fibroblasts grown on the border between fibrous and planar areas revealed that cells adapt their actin skeleton to their underlying surface topography. The white lines outline the spread cell on the planar area of the binary patterned scaffold. Cells on the planar part exhibited stronger pronounced stress fibers whereas cell parts grown on fibers were less spread.

To analyze how the migration velocity of 3T3 fibroblasts was influenced by the underlying topography a live cell tracking was performed. The velocity of individual cells on fibrinogen nanofibers, planar fibrinogen, and patterned substrates prepared with 5 mg ml⁻¹ fibrinogen was tracked for 20 hours. Overall, migration velocities between 33 nm min⁻¹ and 91 nm min⁻¹ were found (see Fig. 74). Migration velocities of 3T3 fibroblasts on

nanofibrous fibrinogen prepared with 5 mg ml^{-1} were approximately 80 nm min^{-1} . Mean velocities found on planar fibrinogen were approximately 56 nm min^{-1} . Mean velocities of fibroblasts on glass were approximately 91 nm min^{-1} . Cells on nanofibrous areas of binary fibrinogen scaffolds showed velocities of approximately 42 nm min^{-1} , while cells on planar areas migrated with a velocity of approximately 33 nm min^{-1} .

The velocity distribution of cell migration on nanofibrous fibrinogen was comparable to the velocity distribution of cells on glass samples (see Fig. 74). The distribution of cell velocities on planar fibrinogen was comparable while the mean velocity on planar scaffolds was lower than on nanofibrous scaffolds and glass. Median velocities for fibroblasts on nanofibrous areas of fibrinogen scaffolds with binary topography lower than on nanofibrous fibrinogen scaffolds with a single topography. Cells on nanofibrous areas on binary patterned scaffolds were slower than on planar areas. The same trend was observed for cells on planar areas on binary patterned scaffolds. Cells on nanofibrous areas on binary patterned scaffolds were faster than on planar areas on binary patterned scaffolds, confirming the trend observed on scaffolds with a single topography. Overall all migration velocities have a similar distribution.

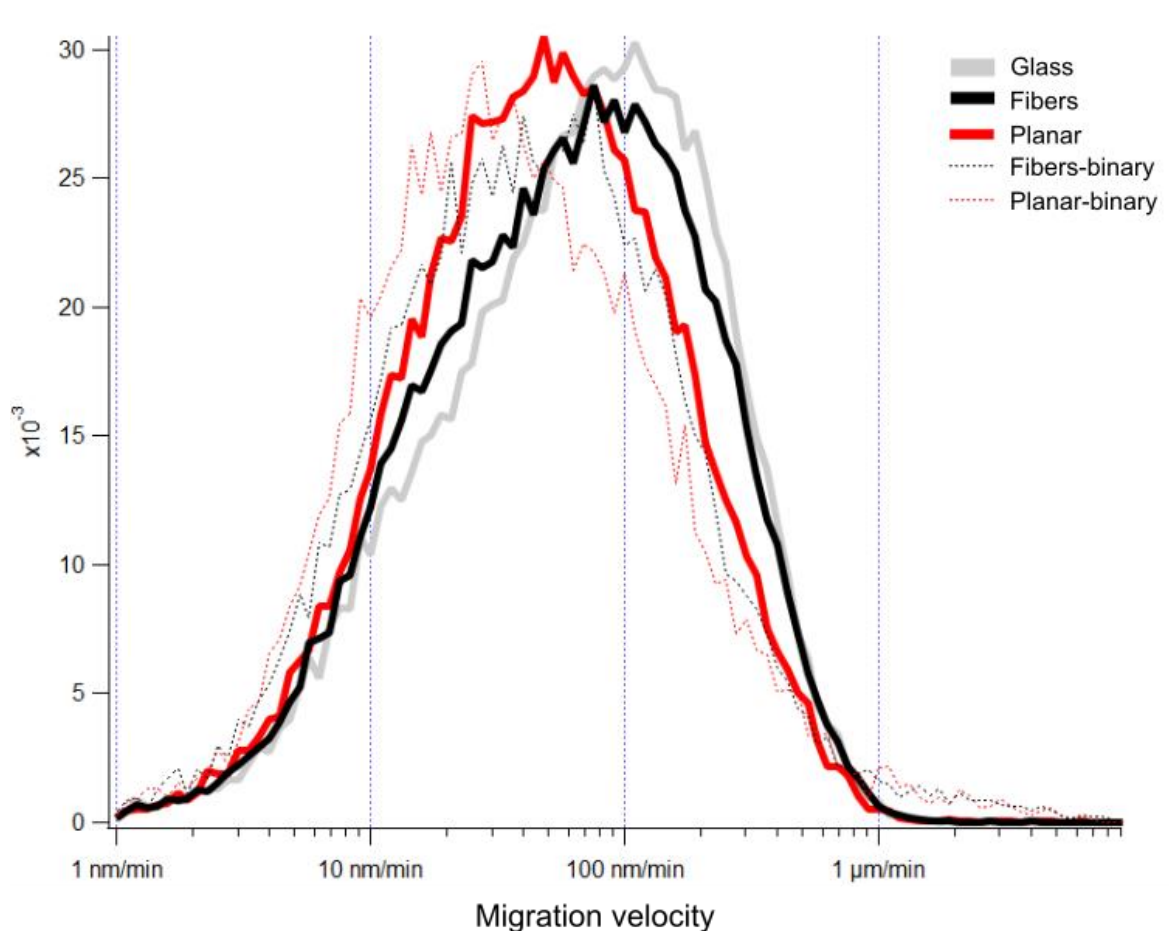


Figure 74. Histograms of median migration velocities of 3T3 fibroblasts on fibrinogen scaffolds prepared with 5 mg ml⁻¹ fibrinogen. Histograms are plotted for cell velocity on nanofibrous fibrinogen, planar fibrinogen, nanofibrous areas on binary patterned, and planar areas on binary patterned scaffolds. Cell migration velocities on glass are shown as a control. Velocities are plotted on a logarithmic scale. Cells grown on nanofibrous scaffolds and glass have a comparable peak showing a similar median velocity. Median velocities of cells on nanofibrous and planar collagen are higher than on glass. Cells on planar fibrinogen were slower than on nanofibrous fibrinogen and glass. On binary scaffolds, significantly fewer tracks were analyzed than on scaffolds with a single topography. Migration velocities on binary substrates have lower values than on scaffolds with a single topography. On binary patterned substrates, the same trends as on substrates with a single topography were observed.

Cells on nanofibrous scaffolds prepared with 5 mg ml⁻¹ fibrinogen migrated with a velocity of approximately $80 \pm 8 \text{ nm min}^{-1}$ which was significantly slower than the median cell migration velocity of $56 \pm 6 \text{ nm min}^{-1}$ for fibroblasts on planar fibrinogen (* Cohens $d \geq 0.2$) (see Fig. 75). Fibroblasts on glass migrated with a velocity of approximately $91 \pm 8 \text{ nm min}^{-1}$, which is significantly faster than on planar fibrinogen (* Cohens $d \geq 0.2$).

On nanofibrous areas of binary fibrinogen scaffolds, cells migrated with a velocity of $42 \pm 5 \text{ nm min}^{-1}$. On planar areas, cells migrated with a mean velocity of $33 \pm 4 \text{ nm min}^{-1}$. Cells on glass migrated with velocities of $91 \pm 8 \text{ nm min}^{-1}$ being significantly faster than on nanofibrous areas (* Cohen's $d \geq 0.2$) and on planar areas (** Cohen's $d \geq 0.5$)(for an overview of all mean velocities and Cohens d see Table. 16 in Appendix).

However, fibroblasts displayed a trend towards faster migration on nanofibrous fibrinogen than on planar scaffolds. Altogether, fibroblasts on binary protein scaffolds showed a tendency towards lower migration speeds than on untreated glass and substrates with only one topography. Compared to fibrinogen scaffolds exhibiting only one topography, migration velocities on binary patterns were marginally lower. Cell migration velocities of fibroblasts on patterned fibrinogen scaffolds did not vary significantly between the topographies, either. Yet, on the planar regions of binary fibrinogen scaffolds, cell velocities were observed, which were significantly lower than on scaffolds, which consisted only of fibrinogen nanofibers (* Cohens $d \geq 0.2$).

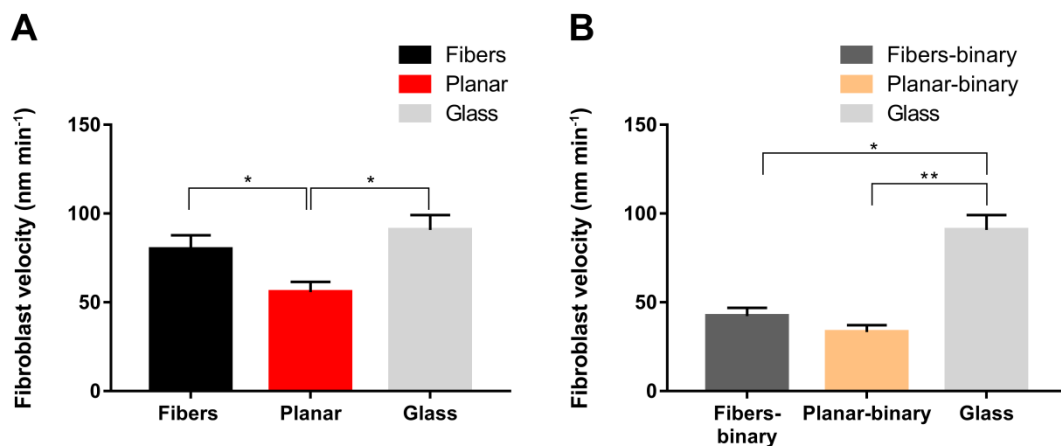


Figure 75. Cell migration of 3T3 fibroblasts on nanofibrous fibrinogen (A) and planar fibrinogen (B). $n = 4$ experiments were conducted. Data are presented with average \pm standard deviation of replicates. Cohens effect size d indicated by * $d \geq 0.2$, ** $d \geq 0.5$.

3.3 Scaffolds with binary surface topography and biochemistry for cell culture

The results presented in section 3.1 and 3.2 show that the combination of different surface topographies in a single protein scaffold could be successfully established. With this scaffold platform, it was possible to control one of the cues, which is known to influence cell response during cell-biomaterial interactions besides mechanical cues and biochemical signals. Since binary topographical scaffolds could be established with collagen and fibrinogen, the next aim was to combine these topography variations with different biochemical stimuli to provide a multiparametric biophysical scaffold platform to study individual aspects in cell-scaffold interactions in a controlled model system. Therefore, it was studied how the new patterning process could be applied to binary topography scaffolds, which contained two different proteins. The presented results were a proof of concept, thus all results represent n=1 experiments with triplicates.

Three different experimental designs were investigated to combine different topographical cues in scaffolds comprising two different proteins by choosing the two proteins collagen and fibrinogen:

- Binary scaffold type 1 consisted of the combination of collagen nanofibers and fibrinogen nanofibers.
- Binary scaffold type 2 consisted of the combination of collagen fibers and planar fibrinogen.
- Binary scaffold type 3 consisted of a combination of fibrinogen nanofibers and smooth collagen.

The first sample type binary type 1 included the combination of the techniques to prepare fibrous collagen and nanofibrous fibrinogen in selected scaffold areas (see Fig. 76).

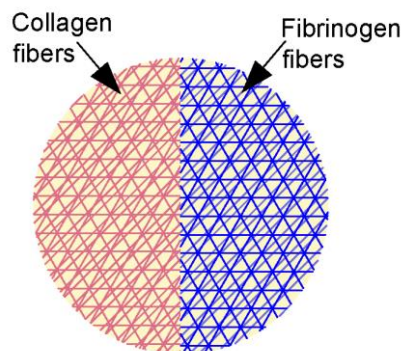


Figure 76. Schematic of a binary type 1 scaffold. In the patterning process, the routines to prepare nanofibrous collagen regions and nanofibrous fibrinogen were combined.

SEM analysis of sample type 1 revealed the border between both proteins was not clearly defined, a smooth boundary region between the two fibrous areas was observed (see Fig. 77A). On both protein boundaries a well-defined line separated protein fibers and the boundary region (see Fig. 77A). Fibrinogen fibers were well defined. The distribution of fibrinogen fibers followed a pattern with round areas between fibers bundles (see Fig. 77B). A distinct boundary to the boundary area was observed. Fibrinogen fibers exhibited typical morphology as it has been previously reported for scaffolds with one topography only. Collagen fibers exhibited distinct fiber morphology (see Fig. 77C). A dense uniform collagen network was assembled. The boundary to the boundary region was well defined on a smaller length scale (see Fig. 77C). Collagen fibers exhibit light grey or white regions, which can be due to charging effects of organic substrates in SEM analysis. Therefore, it can be summarized that the fiber assembly of both proteins could be transferred to this scaffold designed with combined biochemical cues. However, it remains unclear why a smooth region between the two protein nanofiber regions was obtained and which protein this smooth part was composed of.

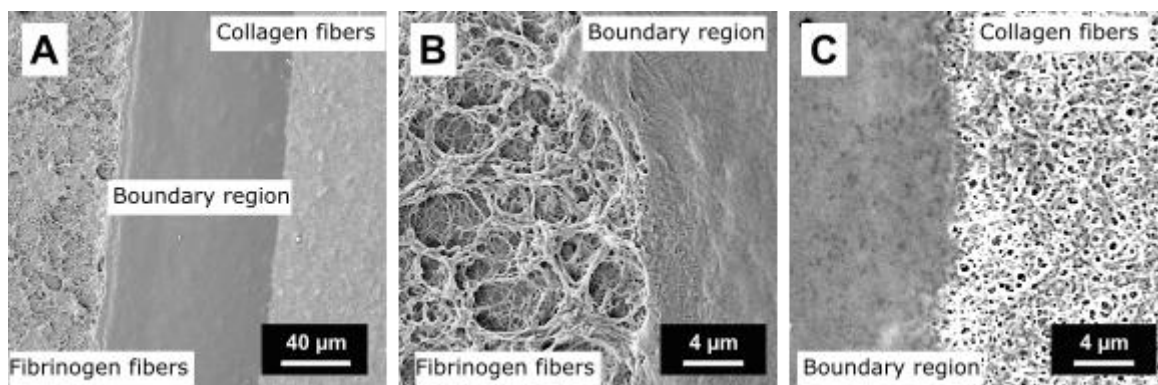


Figure 77. SEM images of binary scaffolds type 1 prepared with nanofibrous fibrinogen (5 mg ml^{-1}) fibrinogen and nanofibrous collagen (2.5 mg ml^{-1}). Fibrinogen on the left and collagen on the right. This figure shows a first explanatory experiment to combine topographical features and biochemical cues in the same protein scaffold. The different nanofibrous areas did not form a defined border. Fibrinogen fiber assembly was successful with a defined border (A). Collagen nanofiber assembly was successful and also depicted a defined border (B). A layer of planar protein defined the border between the two different proteins (C). The white line represents where the border between fibrinogen and collagen fibers should have been.

For binary scaffold type 2, the process for planar fibrinogen was combined with the approach to prepare nanofibrous collagen in selected scaffold regions (see Fig. 78). First, the planar fibrinogen area was coated fixated and washed. After that, the collagen nanofibers were assembled while the planar fibrinogen area was covered with a PDMS mask (see Fig. 22).

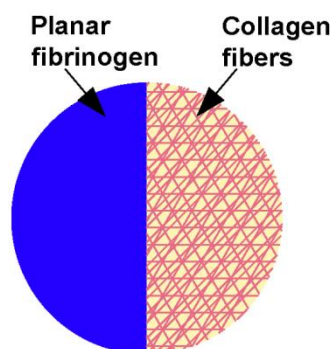


Figure 78. Schematic of a binary type 2 scaffold. The patterning approach was designed to combine planar fibrinogen with nanofibrous collagen areas.

The morphology of the different topographical regions in scaffold type 2 was analyzed by SEM (see Fig. 79). The border between the different topographies was not found to be clearly defined (highlighted as a white dashed line in the SEM image in Fig. 79A). The SEM image shows an intensity gradient of the greyscale from the upper left to the lower right of the image, indicating charging effects. On the very left a darker area was visible. In the middle, a lighter area was observed. On the right of the dashed white line, a lighter area was observed (see Fig. 79A). The lighter area showed a different surface structure compared to the darker area (planar fibrinogen). However, the nanofibrous collagen regions did not show the typical nanofiber morphology (see Fig. 79A) and were found to be partly removed from the underlying glass substrate. SEM analysis with higher magnification showed that the assembly of collagen nanofibers was not successful in this combined patterning procedure (see Fig. 79B and 79C). Whereas, the planar fibrinogen region exhibited few light spots (see Fig. 79B). No collagen fibers were found on any of the triplicates prepared with the procedure shown in Fig. 78. The area coated with collagen exhibited crystalline structures (see Fig. 79C). Nevertheless, planar fibrinogen regions exhibited the typically flat surface topography (see Fig. 79).

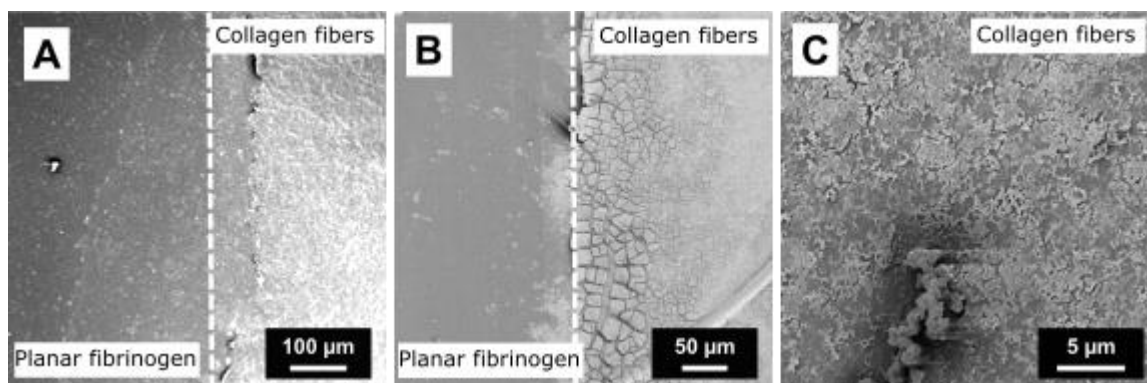


Figure 79. SEM images of binary scaffold type 2 prepared with planar fibrinogen (A left side) prepared with 5 mg ml^{-1} and nanofibrous collagen (A right side) prepared with 2.5 mg ml^{-1} . This figure shows the attempt to assemble planar fibrinogen with nanofibrous collagen (A). (B) shows only collagen but no fibers could be found. The assembly of planar fibrinogen was successful (C left), while the assembly of collagen nanofiber was not (B).

The third binary scaffold type no. 3 was prepared to combine nanofibrous fibrinogen with smooth collagen areas (see Fig. 80). The results represent $n=1$ experiment with triplicates.

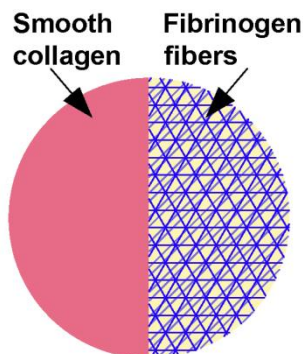


Figure 80. Schematic of a binary type 3 scaffold. The patterning process was adapted to combine smooth collagen regions with nanofibrous fibrinogen areas.

Sample type 3 combined smooth collagen with nanofibrous fibrinogen by first assembling smooth collagen, crosslinking it, and subsequently covering it with a PDMS mask. With the smooth collagen being covered the fibrinogen nanofibers were assembled, cross-linked, and washed (as described in section 2.1.4) (see Fig. 22). Finally, the PDMS mask was removed from the smooth collagen.

With this set-up, the nanofibrous fibrinogen scaffold attached to the PDMS mask and parts of the scaffold were detached (see Fig. 80A). Thus, the boundary between the areas coated with two different proteins was not clearly defined (see Fig. 80A). The region coated with planar collagen is darker than the area coated with fibrinogen fibers. On the planar collagen area, white spots were observed (see Fig. 80A and Fig. 80B). SEM analysis of scaffolds prepared with this routine revealed that the assembly of smooth collagen and fibrous fibrinogen areas in a single scaffold was successful (see Fig. 81B). The fibrinogen fibers were well defined (see Fig. 81 B and Fig. 81C). The fibrinogen fibers formed a dense network (see Fig. 81C). Despite the technical problems, the fibrinogen fibers showed the typical fiber morphology in those areas where the fibers were not detached by the PDMS mask. The planar collagen areas were very flat (see Fig. 81B). In Fig. 81 white spots can be seen.

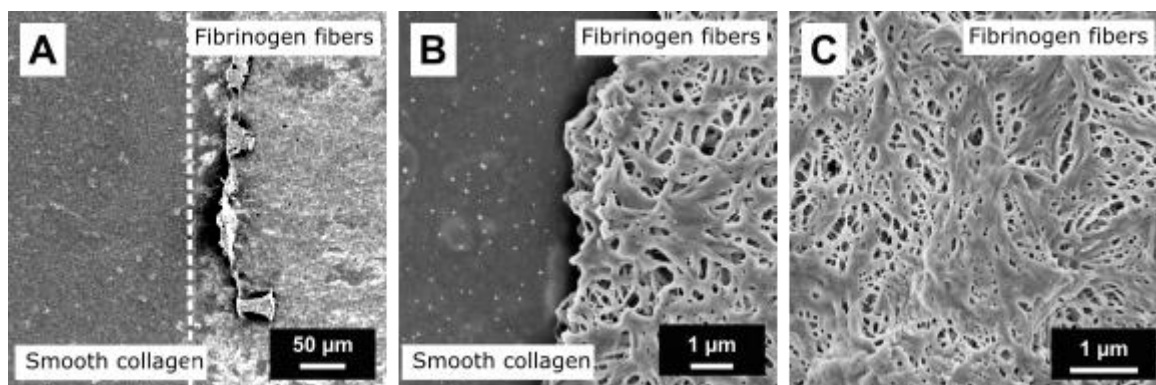


Figure 81. SEM images of binary scaffold type 3 prepared with smooth collagen (A, left) prepared with 2.5 mg ml^{-1} and nanofibrous fibrinogen (A, right) prepared with 5 mg ml^{-1} . The border was well defined, yet parts of the fibrinogen scaffold were detached by the removal of the polymer mask (A). The assembly of a smooth collagen layer was successful (B, left) and the assembly of fibrinogen scaffold exhibited well-defined nanofibers (B, C).

4. Discussion

To create a biophysical platform combining smooth/planar and nanofibrous topographies in a single protein scaffold, collagen was used as a model protein. First, the results for substrate characterization are discussed, followed by cellular interaction with collagen scaffolds. In the following subchapters, the transfer of the established method from collagen to the model platform fibrinogen is discussed and the cellular interaction with this novel biomaterial will be discussed. Subsequently, the results for both protein platforms are discussed in direct comparison. Finally, the preliminary results of combining biochemical and topographic cues in a single protein scaffold are discussed.

4.1 Collagen

In this thesis, a novel biophysical model system was presented to study the interaction of cells with different topographies in a single scaffold. A pH shift can induce the self-assembly of collagen into fibers (Harris *et al.* 2013). Therefore, collagen was presented as a model system to manufacture protein scaffolds with nanofibrous and smooth topographies in selected scaffolding regions. To develop this new biophysical platform, nanofibrous and smooth scaffolds were first produced and characterized. These were also used as a reference for the later developed scaffolds with binary topography properties.

4.1.1 Collagen scaffolds

In the present study, it was shown that collagen nanofibers can be self-assembled on surfaces such as polycarbonate, Lumox® film, and aluminum oxide membranes (see Fig. 33). In comparison, collagen fibers have already been assembled in previous studies on various substrates such as titanium, hydroxyapatite (He *et al.* 2014), magnesium (Zhao and Zhu 2014), phlogopite and muscovite mica (Fang *et al.* 2013). Smooth collagen has so far been processed on substrate materials such as glass, agarose, polydimethylsiloxane (PDMS) or self-assembled monolayers (SAMs) to form micropatterns (Kim *et al.* 2007; Kwak *et al.* 2015; Desai *et al.* 2011; Monroe *et al.* 2009). These earlier findings together with the here presented results show the wide variety of possible substrates for collagen scaffold assembly. With regard to possible future applications of binary collagen scaffolds in tissue engineering, the structuring process could also be carried out on other material surfaces so that there is the freedom to tailor binary collagen scaffolds independently of the carrier substrate. For handling reasons, like piranha cleaning and sterilization for cell culture, all further protein scaffolds in this work were assembled on glass.

The introduction of ultra-sonication during fiber assembly reproducibly improved the surface coverage to approximately 100% (see Fig. 34), which was much higher than reported fiber coverages of 45 % on PDMS surfaces, where collagen self-assembly was carried out in a microfluidic device (Spurlin *et al.* 2010).

To achieve optimal preservation of the fiber morphology for future cell culture application, different chemical and physical crosslinking methods were investigated. The crosslinking method that best preserved the morphology of the collagen nanofibers was crosslinking with liquid GA (see Figs. 31 and 32). Crosslinking with UV irradiation, EDC, methanol, and FA did not preserve the fiber morphology as well as glutaraldehyde. In the future, a combination of crosslinking with EDC and *N*-hydroxysuccinimide (NHS) could improve the crosslinking of collagen (Yang 2012). EDC forms amine-reactive *O*-acylisourea intermediates, which then react with primary amines to form an amine bond and an isourea by-product (Hermanson 2013). The *O*-acylisourea intermediates are unstable in aqueous solutions which can lead to failure for further reaction steps (Hermanson 2013). NHS is coupled by EDC to carboxyls, which form an NHS ester that is more stable than the *O*-acylisourea intermediate, allowing more effective conjugation to primary amines at physiological pH (Staros *et al.* 1986). It remains unclear why FA crosslinking has not preserved the morphology of collagen fibers. It has been shown that FA crosslinking has worked earlier in collagen (Côté and Doillon 1992; Levy *et al.* 1986). Methanol is a more common method for cell fixation and has been suggested to be a good fixative for nucleic acid components of cells (Hobro and Smith 2017). However, the fixation with methanol may not be suitable for pure protein samples, because it can denature proteins (Fernández and Sinanoğlu 1985). So far, UV crosslinking for corneal collagen has been combined with riboflavin, which could improve the crosslinking approach with UV (Mazzotta *et al.* 2012). Crosslinking with FA vapor instead of liquid FA could possibly also improve fiber conservation. It has been shown to work well with electrospun collagen nanofibers (Yang *et al.* 2008). Since the developed scaffolds were used in cell culture with cell culture medium with high salt concentration, non-fixed collagen scaffolds would form fibers, which has been shown in the literature before (Gobeaux *et al.* 2008). It was therefore important to preserve the smooth regions. Glutaraldehyde is a common crosslinker for collagen in biomedical applications and was therefore used for all further experiments in the present work (Reddy *et al.* 2015).

The analysis of dry collagen scaffolds with the SEM revealed fiber diameters of about 140 nm. In contrast, measurements of the same samples with the AFM yielded fiber

diameters of about 230 nm (see Table 5). This discrepancy between the two measuring methods could be due to the limitations of the respective method. SEM analysis only allows 2D analysis of gray values, while AFM analysis contains 3D information. For SEM analysis, collagen frameworks had to be sputtered with gold, which artificially increased the fiber diameter. However, when measuring fiber diameters with AFM images, tip artifacts can occur, which can be influenced by the aperture angle of the AFM tip and the geometry of the imaged substrate (Schwarz *et al.* 1994). Overall, AFM analyses showed a comparable swelling behavior of collagen nanofibers after rehydration with DMEM cell culture medium, independent of protein concentration. The AFM results of dried and rehydrated scaffolds could be compared since tip artifacts would occur in both measurements. After rehydration, collagen nanofibers had diameters of about 400 nm, which is in good agreement with literature values describing native collagen fibers (Huxley-Jones *et al.* 2007; Kadler *et al.* 2007). In other studies where collagen nanofibers were prepared by electrospinning, fiber diameters of 100-730 nm were reported for dry fibers (Matthews *et al.* 2002). After rehydration, these fibers would have larger diameters than the fibers presented in this study. In another study, fiber diameters of 150-450 nm were reported for electrospun dry GA-crosslinked collagen. After immersion with PBS diameters of 210-425 nm were measured for these fibers (Yang *et al.* 2008), which is much closer to the results presented in this study.

By adjusting the protein concentration, the scaffold thickness of the collagen nanofibers could be adjusted between 200 nm and 7 μm and between 400 nm and 10 μm for smooth collagen (see Fig. 34 and Fig. 35). In contrast, collagen patterns combining fibrillar and smooth regions in a single scaffold have so far been produced by introducing a pre-patterning with hydrophilic and hydrophobic self-assembled monolayers (SAMs) on the carrier substrate (Elliott *et al.* 2007). However, the introduction of tailored surface chemistry with SAMs only resulted in collagen thickness in the range of 2 to 47 nm (Elliott *et al.* 2007). The scaffolds prepared in the present work exceed this range by far and have the potential to be further tailored towards three-dimensional scaffolds (Walters and Stegemann 2014).

The analysis of the nanofibrous collagen scaffold roughness using AFM revealed roughness values of approx. 40 to 115 nm after rehydration and approx. 9 to 30 nm for smooth scaffolds (see Table 4), which is in good agreement with collagen scaffold roughness values from previous studies (Johanes *et al.* 2011; Stylianou *et al.* 2013). For

collagen-coated PDMS, for example, roughness values of about 90 nm have previously been reported for non-crosslinked collagen (Razafiarison *et al.* 2016).

In the present study it was found that nanofibrous and smooth collagen scaffolds appeared to have an unlimited stiffness independent of the respective topography (see Figs. 38 and 39). Therefore, the mechanical properties of collagen scaffolds were considered comparable to glass for subsequent cell culture studies. To determine the real elastic modulus of the respective substrates, the elastic moduli of the scaffolds would have to be measured with stiffer cantilevers (Suriano *et al.* 2014). It has been reported earlier that crosslinking of cell culture collagen gels leads to increased stiffness with Young's moduli between 20 and 100 kPa (Spurlin *et al.* 2010). Others reported a 20-fold increase in collagen film stiffness after crosslinking (Bigi *et al.* 2001). It can, therefore, be assumed that the mechanics of the nanofibrous and smooth collagen scaffolds used in the present studies are probably mainly influenced by the crosslinking process. In previous studies, it was shown that the mechanical properties of the collagen scaffolds can be controlled by the degree of crosslinking. The degree of crosslinking can be adjusted by the glutaraldehyde concentration and the crosslinking time (Bigi *et al.* 2001). A further possibility for adjusting the elastic modulus of collagen gels was presented by Tirella *et al.* They successfully adjusted the elasticity modules of collagen gels by crosslinking with riboflavin and UV irradiation (Tirella *et al.* 2012).

Combining two topographies in one scaffold:

To produce scaffolds with spatially controlled topographies, *in vitro* self-assembly was combined with polymer printing. Using glass substrates, smooth and fibrous topographies with high reproducibility were achieved in the respective scaffold areas. This method allows the fabrication of protein scaffolds with different topography regions (nanofiber vs. smooth). For the first time, a new biophysical model system was introduced for the simultaneous investigation of cell cultures on nanofibrous and smooth collagen topographies in a single scaffold (see Fig. 40 and 41). The results of collagen scaffolds with a single topography were used to establish the model platform on which two topographies were combined into a single protein scaffold. In the scaffold design presented, the topography was the only feature of the collagen substrates that was modified in the different scaffold regions, while the mechanical and biochemical cues remained the same in both regions. This scaffold design opens the possibility to disentangle the influence of mechanical cues and nanotopography in the cell environment

to understand the independent role of topographic cues during cell growth (Yang *et al.* 2017).

In the past, different substrate materials were used to obtain structured samples, while the combination of fibrous and smooth collagen regions in a single substrate was only performed by one group (Elliott *et al.* 2007). The results in the present study are in contrast to this previous study in which nanofibrous and smooth collagen regions were combined in a single surface due to interaction with hydrophobic and hydrophilic SAMs (Elliott *et al.* 2007). Contrary to the results presented here, their patterned collagen substrates only had a substrate thickness in the lower nanometer range (Elliott *et al.* 2007). The structuring of collagen on the nano- and microscale was performed in different studies using different techniques. For example, silanized Si wafers pre-patterned with hydrophilic and hydrophobic SAMs were used to subsequently prepare topographic patterns of collagen on the SAM films. Due to this substrate modification, the structuring of the collagen is more time and cost-intensive than the structuring process established in this thesis. Furthermore, the different collagen patterns could only be achieved if a layer of self-assembled monolayers (SAMs) was applied underneath the binary collagen pattern. Therefore, it has not been possible so far to modify other biomaterial surfaces such as glass, polymers, or metals with nanofibrous and smooth collagen patterns. The procedure presented in the present work can be performed independently of the underlying substrate, which is a major advantage over the studies just mentioned. Such thin collagen layers would not be suitable for the future preparation of binary 2D/3D scaffolds into which cells can migrate. To increase the scaffold thickness in future experiments, an increase in protein concentration would be necessary, as demonstrated in this work.

With other techniques for the production of protein nanofibers, such as electrospinning or extrusion through nanoporous ceramics, the combination with polymer structuring would not be feasible as presented here, since in these processes the fiber deposition takes place successively on a substrate. Furthermore, in contrast to electrospinning, which uses high electric fields and organic solvents (Barnes *et al.* 2007), self-assembly offers the important advantage of physiological process parameters to prepare structured protein scaffolds for subsequent cell culture studies (Matthews *et al.* 2002; Barnes *et al.* 2007).

Furthermore, to achieve a higher spatial resolution of the binary pattern, the proof-of-concept patterning method presented in this work was combined with the use of established PDMS masks for future application in cell cultures (Bernard *et al.* 2000; Shen *et al.* 2008; Filippini *et al.* 2016). This combination of processes facilitated the production

of micro-patterns with nanofibrous and smooth areas with higher throughput and potentially allows for a variety of geometries.

4.1.2 Cell interaction with collagen scaffolds

A new method to produce protein scaffolds, which allow studies of the cell response to different topographical cues, was successfully established and characterized. In the next step the cellular response to collagen scaffolds with spatially different topographies was studied using fibroblasts as model system.

LIVE/DEAD® staining of NIH 3T3 fibroblasts on collagen scaffolds prepared with 0.5 mg ml^{-1} showed predominantly vital cells (see Fig. 42). This assay was only performed on scaffolds with one topography. The analysis of living cells showed between approx. 84% and 98% living cells independent of growth time and underlying substrate (see Fig. 43). A disadvantage of this assay is that it is only sensitive to cytotoxic effects that affect membrane integrity (Crocini *et al.* 2019). Furthermore, the autofluorescence of the collagen scaffolds made the evaluation of the assay difficult. Therefore, the analyses for this assay were only performed on substrates prepared with 0.5 mg ml^{-1} collagen and only one topography, which is why the metabolic WST-1 assay was performed as an alternative method. This assay also allowed the analysis of cell viability of fibroblasts on thick collagen scaffolds prepared with 2.5 mg ml^{-1} . Extinction of 3T3 fibroblasts grown on collagen showed that the cells proliferated over time. Fibroblasts grown on glass showed the highest proliferation rate (see Figure 44). Further repetition of these experiments would be necessary to ensure this trend and reduce the standard deviation.

Overall, the relative viability of fibroblasts grown on nanofibrous and smooth collagen scaffolds obtained by the WST assay showed relative viabilities below 70%, which is not considered biocompatible according to DIN EN ISO 10993-5 (see Fig. 45) (EN ISO 10993-5:2009). This viability was different from the results obtained with the LIVE/DEAD® staining. A possible reason for this discrepancy could be the high proliferation on glass. Besides, initial variations in cell density during seeding could influence the results of WST-1 assays. A possible reason for different extinction values could be randomly different initial seeding densities. These would lead to inconsistent cell densities and thus to more or fewer mitochondria, which could have been caused by handling errors. More mitochondria would convert more WST-1 to formazan and finally to a higher optical density. Poor resuspension or pipetting could lead to this effect. Also, glutaraldehyde fixation leads to residues of aldehyde groups which could reduce the viability of the cells on these scaffolds. It has been shown that aldehyde residues have cytotoxic effects *in*

vitro (Naahidi *et al.* 2017). In addition, it has been reported that the number of free amino groups of cross-linked collagen decreased largely from 100% to 32.76% (Tian *et al.* 2014). It has been shown that amino groups increase cell adhesion and consequently cell viability (Okada *et al.* 2006). These effects could influence cell adhesion and thus reduce cell proliferation. An adaptation of the crosslinking process could improve cell viability on collagen scaffolds in future studies. In some cases, the collagen scaffolds detached from the carrier substrate when the WST-1 assay was performed. This could have significantly influenced the results of the assay. Cells may have been detached by this effect or may not have been in contact with the reagent when floating on the liquid.

The WST-1 assay was performed with relatively low cell counts to compare the results with those obtained in morphology studies. The low cell densities used in WST-1 assays, together with the increased surface area on nanofibrous collagen scaffolds, could result in few cell-cell contacts and thus reduce proliferation. Nevertheless, the LIVE/DEAD staining showed good overall fibroblast viability on nanofibrous and smooth collagen scaffolds. Therefore, an additional viability assay could help to gain a better insight into fibroblast viability on collagen scaffolds. Dead cells with a lost membrane integrity can be detected by measuring markers leaking from the cytoplasm into the cell culture medium (Riss *et al.* 2019). The most common marker is lactate dehydrogenase (LDH) (Korzeniewski and Callewaert 1983; Decker and Lohmann-Matthes 1988). In order to gain a better insight into cell viability on collagen substrates, an LDH assay could be a suitable complement to cell viability studies in future.

4.1.2.3 Cell morphology

Collagen scaffolds with one topography:

In this study, the quantitative analysis of fluorescence microscopic images of fibroblasts on nanofibrous and smooth collagen scaffolds prepared with 0.5 mg ml^{-1} revealed cell sizes (see Fig. 47) between 901 and $1796 \mu\text{m}^2$. The largest cells were found on smooth collagen substrates and smaller cells on collagen fibers and bare glass. Together with the cell size, the perimeter was largest on smooth collagen and comparatively smaller on nanofibrous collagen and glass (see Fig. 48). Cell area and cell perimeter showed the same trends on all corresponding substrates. Cells on nanofibrous collagen surfaces had a spindle-like morphology with long filopodia, while cells grown on smooth scaffolds had large contact areas (see Fig. 46). This is in contrast to the results of previous studies where randomly organized nanofibers did not seem to have any influence on the cell morphology. Numerous studies have found that aligned collagen nanofibers influence cell

morphology and induce differences in cell alignment and migration (Gruschwitz *et al.* 2010; Lai *et al.* 2011; Lai *et al.* 2012b, 2012a; Huang *et al.* 2013; Stylianou *et al.* 2013; Zhong *et al.* 2006; Bao *et al.* 2002; Muthusubramaniam *et al.* 2012). To determine the cell-covered area, the area covered by actin was quantified (see Fig. 50). In contrast to the observation from the WST-1 assay, the cell-covered area increased over time independently of the underlying substrate. This indicates a similar proliferation of 3T3 fibroblasts on all substrates. Further cell viability studies are required to ensure good cell viability on all substrates.

In other studies it was reported that fibroblasts and endothelial cells grown on collagen fibers exhibited an elongated morphology in the alignment direction of aligned fibers, whereas no cell orientation was found on randomly oriented fibers (Gruschwitz *et al.* 2010). In contrast, the CSI in the present study differed from the trends observed for perimeter and cell size (see Figure 49). The lowest circularity was observed in collagen fibers prepared with 0.5 mg ml^{-1} with a CSI of about 0.131, and the highest circularity was observed in glass with a CSI of 0.249. Cells on collagen substrates regardless of topography were more elongated than cells on glass. In contrast to the size and perimeter of the cells, these differences were independent of the cultivation time. The differences between cell area and cell perimeter on different substrates became less pronounced during the course of the cultivation time. On both collagen topographies the cell size and cell perimeter decreased between 24 and 72 h, while the fibroblast area on glass increased slightly. NIH 3T3 fibroblasts typically assemble their own ECM *in vitro* up to 72 h in culture (Franco-Barraza *et al.* 2016; Kubow *et al.* 2009). It can therefore be assumed that fibroblasts on untreated glass initially deposited their own ECM during the first cell culture period, which probably led to smaller cell sizes than fibroblasts on both collagen scaffolds. Overall, the analysis of CSI only allows an analysis of possible trends, since the resolution limit of the inverted fluorescence microscope in combination with the autofluorescence of the collagen scaffolds in this study did not facilitate the detailed recognition of smaller cell parts such as thin filopodia. Another cross-linking method that causes less autofluorescence could improve fluorescence imaging, since glutaraldehyde is known to induce autofluorescence (Baschong *et al.* 2016; Davis *et al.* 2014). Furthermore, 2D images only consider one focal plane. Cells projecting into a 3D substrate would appear smaller with this method. Together with another crosslinking agent, the use of a high-resolution imaging technique of cell morphology on nanofiber scaffolds could penetrate further into the interior and overcome the limitations of the

methods used here, e.g. by improving confocal microscopy protocols or using Stimulated Emission Depletion Microscopy (Vicidomini *et al.* 2018).

The observed differences in fibroblast morphology were most pronounced in culture up to 48 h. It can be assumed that the influence of the underlying collagen topographies is compensated by the deposition of own fibroblast ECM. It has already been shown that *in vitro* cultivated fibroblasts deposit their own ECM up to 72 h cultivation time (Beacham *et al.* 2007; Kubow *et al.* 2009). This time window could explain why cells cultivated on glass showed larger areas after 48 h and 72 h. It suggests that cell attachment increases over time along with ECM deposition. Additionally, this could explain that the morphological differences in nanofibrous and smooth collagen scaffolds are less pronounced throughout the cultivation period.

Since the detailed morphological analysis with fluorescence microscopy could only be performed with collagen scaffolds prepared with 0.5 mg ml^{-1} , further analyses were performed with SEM and confocal microscopy, and including thick collagen scaffolds (see Fig. 51). The trends observed for fibroblasts on collagen scaffolds prepared with 0.5 mg ml^{-1} were confirmed for collagen scaffolds prepared with SEM and confocal microscopy independent of protein concentration. In addition to the trends mentioned above, it was observed that fibroblasts grown on collagen nanofibers had few long filopodia, while fibroblasts grown on smooth collagen had more but shorter filopodia. This could be an indicator that cells grown on nanofibers explore their environment by filopodial scanning (Schäfer *et al.* 2011). It was shown that the different collagen topographies had the strongest influence on fibroblast morphology and filopodia formation. Cells on smooth scaffold regions had large contact areas, many short filopodia, and pronounced actin filaments. In contrast, nanofibrous collagen induced a spindle-like fibroblast morphology with smaller cell sizes, few long cell extensions, and significantly reduced actin stress fibers. These results are in good agreement with previous reports on fibroblast growth on randomly oriented collagen nanofibers (Hakkinen *et al.* 2011; Jiang and Grinnell 2005; Stylianou *et al.* 2013). In previous studies, it was found that the amount of focal adhesion proteins differs between 2D and 3D scaffolds (Cukierman *et al.* 2002). The limited available surface area of nanotopographies has been associated with the reduction of the formation of focal adhesion proteins (Frey *et al.* 2006). These correlations were confirmed in this work by the observation of reduced actin fiber formation on nanofibrous collagen surfaces. Since it is not yet fully understood which mechanisms are responsible for their multiple functions during filopodia scanning (Gupton and Gertler 2007; Jacquemet *et al.*

2015), it will be highly interesting to further develop the current scaffolds with binary topography towards thicker 3D matrices to allow studies of topography-dependent cell adhesion and migration processes in real-time.

Z-stack images (see Fig. 52) showed no protrusion into nanofibrous collagen scaffolds and consequently no fibroblast growth into the deeper regions of the nanofibrous collagen scaffolds. In the native ECM, cells can migrate through LOX-crosslinked collagen fiber networks via proteolytic and non-proteolytic mechanisms (Bonnans *et al.* 2014; Wolf and Friedl 2011). Since the collagen scaffolds used in this study were chemically crosslinked with glutaraldehyde, the fibroblasts were probably not able to migrate into the network via their native migration mechanisms. Therefore, it will be important to adapt the crosslinking procedure in the patterning process to investigate whether cells can migrate into fibrous scaffold regions. Other crosslinking strategies could include riboflavin UV treatment, 1-ethyl-3-(3-dimethylaminopropyl)-carbodiimide or transglutaminase, which are known to maintain the topography of collagen nanofibers in cell culture studies (Gruschwitz *et al.* 2010; Lai *et al.* 2011; Spurlin *et al.* 2010; Spurlin *et al.* 2009).

AFM analysis of fibroblasts on nanofibrous and smooth collagen scaffolds yielded Young's moduli that ranged from approximately 1.5 kPa to approximately 2.5 kPa (see Fig. 53). Overall, no significant differences for Young's moduli of fibroblasts were observed independent of the collagen topography or the scaffold thickness. The standard deviations were larger than the median values. A possible explanation for this observation might be that the fibroblast stiffness was mainly influenced by the crosslinking routine and independent of the collagen topography. It is known in the literature that cells on topographies, on rigid substrates, which cells cannot deform, react only to topographic signals. While cells were grown on soft substrates, they can also deform, perceive, and respond to both stiffness and topographic signals (Yang *et al.* 2017). This phenomenon was also observed in the present study. It is known that fibroblasts adapt their mechanical properties when they are seeded on substrates with different rigidity (Rianna and Radmacher 2016). The measured Young's moduli in the present study are in good agreement with values measured for NIH 3T3 fibroblasts on stiff polyacrylamide gels (Rianna and Radmacher 2016). It was found that the stiffer the gels were the higher the Young's moduli of the fibroblasts were (Rianna and Radmacher 2016).

Collagen scaffolds with binary topography:

The most significant morphological differences on scaffolds with on topography were observed between 24 h and 48h. Therefore, fibroblasts were fixed on samples with binary topographies after 36 h and examined for their morphology by SEM. Fibroblasts that migrated from one topography to another dynamically adapted their morphology (see Fig. 62). Cells growing directly on the border between nanofibers and smooth collagen topography showed short but many filopodia on the smooth scaffold area, while few and long filopodia protruded from the cell bodies on the nanofiber scaffold region. These observations show that fibroblasts reacted dynamically to the topographic differences in their environment while migrating on the binary collagen scaffolds. The morphological trends found on scaffolds with only one topography were also confirmed on scaffolds with binary topographies. Cells grown at the borders of two topographies showed spread morphology on smooth areas and spindle-shaped forms on nanofibrous areas, indicating that the cells dynamically adapted their morphology. There is consensus in the literature that topography can influence cell morphology (Yang *et al.* 2017). It has been shown that fibroblasts growing on polystyrene with nanotopographic features reduce their spread (Dalby *et al.* 2003). This trend was confirmed in the present study when fibroblasts migrated across the border from smooth to nanofibrous collagen regions.

With the new model system presented in this thesis, it will be possible in the future to directly investigate the participation of different focal adhesion proteins in the formation of adhesion sites as a function of the underlying topography. Topographic preferences in cell growth are controlled by filopodia (Albuschies and Vogel 2013). The novel topographic scaffold design developed in this work could, therefore, allow the analysis of topography-dependent processes during filopodial scanning in real-time. This is an advantage over current systems where cell culture results had to be transferred from conventional 2D substrates, such as Petri dishes, to soft protein scaffolds with nanofiber topography. Also, the new structuring technique introduced in this study revealed nanofibrous and smooth collagen regions in the same scaffold that exhibited the same stiffness. This scaffold design will allow future studies of cell adhesion and contact guidance independent of variations in mechanical or biochemical signals (Yang *et al.* 2017; Cukierman *et al.* 2002; Frey *et al.* 2006).

Migration on binary patterned collagen scaffolds:

Since it is known that the topographic properties of the ECM can also influence the migration behavior of cells (Frey *et al.* 2006), a live cell tracking was used to investigate whether the different collagen topographies also influence the migration behavior of 3T3 fibroblasts. For this purpose, cells were tracked over a total time of 20 h and imaged in time windows of two minutes each. The analysis of the cell migration traces showed that the distance the cells migrated during 2 min was at the lower limit of the microscopic resolution. Therefore, larger time windows should be used for future experiments.

Logarithmically plotted histograms of the mean velocities of 3T3 fibroblasts per sample type showed a second peak for smooth and nanofibrous regions of binary patterned collagen scaffolds prepared with 0.5 mg ml^{-1} collagen at low migration rates (see Fig. 57). These second peaks indicate populations of almost stationary cells that were visible in the videos and tracks. The same trends were observed in scaffolds prepared with 2.5 mg ml^{-1} collagen. In these scaffolds, the histogram for cells on fibers also showed a second peak. On a linear axis, these effects would not be visible. The corresponding adjustments, in which the mean velocities with and without the second peaks were compared, showed that the second peaks influence the mean values for the velocities (see Figs. 56 and 61). Therefore, a cut-off was set at velocities below $0.1 \text{ } \mu\text{m min}^{-1}$, since the focus of this assay was on the mean velocities of the migrating cells. The cut-off was possible because they represented only a minority of the data population and therefore did not represent the overall behavior of the cells.

Overall, fibroblasts on collagen scaffolds showed migration velocities of 180 nm min^{-1} to 430 nm min^{-1} , which is in good agreement with the literature (Yang *et al.* 2017). In a different study mean cell migration velocities of 416 nm min^{-1} were reported for 3T3 fibroblasts on 3D collagen nanofiber matrices (Hakkinen *et al.* 2011). Other studies have shown that, when primary adult human dermal fibroblasts were grown on poly(ethylene glycol) (PEG) hydrogels, the average cell migration velocity decreased from 810 nm min^{-1} on soft gels (95 Pa) to 380 nm min^{-1} on stiff gels (4.3 kPa) (Ghosh *et al.* 2007; Yang *et al.* 2017). The rather stiff collagen scaffolds used in this study yielded average velocities, which resemble the values previously found for stiff PEG gels so that the migration velocity might primarily have been influenced by the collagen stiffness. In summary, fibroblasts displayed a trend towards faster migration on nanofibrous collagen than on smooth scaffolds.

Compared to collagen scaffolds with only one topography, the migration rate on binary patterns was lower. Cell migration on binary scaffolds prepared with 0.5 mg ml^{-1} collagen was significantly faster on nanofibrous areas than on smooth areas. The observations are in good agreement with the literature, showing that cells migrated faster on nanotopographies than on smooth topographies (Hakkinen *et al.* 2011). For fibroblasts on scaffolds prepared with 2.5 mg ml^{-1} collagen, no significant difference in cell migration speed was observed. The thicker collagen scaffolds also showed higher roughness values than the thin scaffolds. Nanotopographies may also reduce the surface area that can be identified by the cells, thereby limiting focal adhesions and weakening cell adhesion and facilitating cell migration (Frey *et al.* 2006). This observation of fibroblasts on nanofibrous collagen scaffolds could be the reason for the similar migration rates found in the present work. In the first step of the migration, cells use filopodia and lamellipodia to explore their environment and control cell migration (Schäfer *et al.* 2011; Alberts *et al.* 2002). In the morphology studies presented here, a stronger expression of lamellipodia on nanofibrous areas was observed. This is a further indication that cells on nanofibers migrated more frequently.

In general, cells on scaffolds with binary topographies showed slower migration rates than on scaffolds with only one topography. Overall, the results of binary scaffolds had fewer traces because the boundary was recorded during tracking and therefore only half the image area per topography was evaluated compared to samples with only one topography. For methodological reasons, this led to a lower number of evaluated cell tracks on the binary samples. For a better comparison of cell behavior on samples with binary and a single topography, proliferation assays on binary scaffolds would be required in future studies. Also, the imaging routine could be adapted to track cell migration in similar areas as on scaffolds with a single topography. Recent studies have shown that NIH 3T3 fibroblasts migrate preferentially towards the topographically denser areas and away from the sparser ones (Kim *et al.* 2009). These findings may indicate that cells may migrate preferentially towards the denser fibrous scaffold areas on the binary substrates presented here. To further investigate whether the results of Kim *et al.* can be reproduced on our binary substrates, a single cell tracking could be performed. To further investigate the correlation of fibroblast migration rates with the underlying topography and roughness (see Table 8); thicker protein scaffolds would be required. This could be achieved by scaffold preparation with higher collagen concentrations in future studies.

The results of cell cultivation on collagen scaffolds were in good agreement with the first hypothesis from the current work. It was hypothesized that cells on nanofibrous protein scaffolds would have smaller cell areas than on smooth scaffolds. For collagen scaffolds, this hypothesis was confirmed as it was observed that the fibroblast size on collagen fibers was smaller than on smooth collagen. On binary substrates, a dynamic reduction of cell area was observed when cells migrated from smooth collagen to collagen nanofibers. These results confirmed the hypothesis that topographic changes while maintaining the same biochemistry and mechanics induced changes in fibroblast morphogenesis.

The second hypothesis that cell proliferation would be reduced on nanofibrous protein scaffolds due to the higher surface area and lower cell-to-cell contact compared to smooth substrates was confirmed by the WST-1 assay. In contrast to this finding, the results of the LIVE/DEAD staining showed good general fibroblast viability independent of the underlying topography. For a better insight into cell proliferation on collagen scaffolds with different topography, further studies with alternative methods to assess cell viability, such as LDH assays, would be necessary.

The third hypothesis, which states that the migration speed of cells on nanofibrous collagen would be increased compared to smooth scaffolds, was also confirmed by the experimental data of this study.

4.2 Fibrinogen

To investigate basic biophysical principles, not only differences in topography but also biochemical stimuli should be studied. For future applications in tissue engineering and, for example, for wound dressings, it would, therefore, be very advantageous to transfer this new structuring method to other fibrillar proteins, which can be processed into nanofibrous scaffolds with the aid of a self-assembly routine. Due to its key role in wound healing and its ability to induce fibrillogenesis by salt-induced self-assembly (Stapelfeldt *et al.* 2019a; Stapelfeldt *et al.* 2019b), the blood plasma protein fibrinogen was selected as the second candidate for the production of topographically structured protein scaffolds. The self-assembly method established in this study was modified to produce nanofibrous fibrinogen scaffolds and to use them for subsequent cell culture studies.

4.2.1 Fibrinogen scaffolds

The diameter of the fibrinogen nanofibers was about 230 nm for dry fibers (see Table 8) and increased to 340 nm after rehydration (see Table 8). These findings are in good

agreement with diameters measured for electrospun fibrinogen nanofibers, where diameters of approximately 250 nm have been reported (Mirzaei-Parsa *et al.* 2018). The measured fiber diameters are also in good agreement with the diameters measured for fibrin fibers prepared *in vitro*, which had fiber diameters between 20 nm and 400 nm depending on the preparation method (Li *et al.* 2016). Moreover, Li *et al.* stated that the fiber diameter of fibrin strongly influenced the mechanical properties of fibrin fibers and fiber networks. It would be interesting for a follow-up study to investigate, whether this dependence also applies to the fibrinogen nanofibers analyzed in this work. For this purpose, fiber diameters would have to be varied, for example by adjusting the drying step.

The scaffold thickness determined by means of cross-section SEM was between $2.8 \pm 0.4 \mu\text{m}$ for fibrinogen nanofibers and $1.7 \pm 0.4 \mu\text{m}$ for smooth fibrinogen (see Fig. 63). Since Stapelfeldt *et al.* were the first to produce fibrinogen scaffolds using their self-assembly method, the fibrinogen fibers had never before been used as a cell culture substrate. Electrospun fibrinogen scaffolds prepared with much higher protein concentrations reached scaffold thicknesses of about 0.7 mm (Wnek *et al.* 2003; McManus *et al.* 2006). With regard to a future application in 3D cell culture, it will be interesting to increase the thickness of self-assembled fibrinogen scaffolds, e.g. by adjusting the protein concentration or other parameters in the self-assembly process.

AFM analyses of surface roughness showed that dried fibers had surface roughness values of about 120 nm (see Table 7). In contrast, the surface roughness of dried planar fibrinogen scaffolds was about 7 nm. Rehydrated fibers showed surface roughness values of about 120 nm (see Table 7). In comparison, the surface roughness of planar fibrinogen scaffolds during rehydration was about 9 nm. In a previous study, planar fibrinogen was adsorbed on silica surfaces with a roughness of 10 to 15 nm (Lord *et al.* 2014). Overall, the surface roughness of fibrinogen scaffolds did not increase significantly during rehydration.

Previous studies have shown that crosslinking with formaldehyde vapor preserves the fiber morphology of fibrinogen nanofibers in aqueous environments (Stapelfeldt *et al.* 2019a). With this crosslinking method, the fiber morphology remained stable in dry fibers and after rehydration in cell culture medium (see Fig. 63). Furthermore, the conservation of planar 2D scaffolds was successful. In contrast to the scaffold thickness of 3 to 5 μm made of non-crosslinked fibrinogen presented by Stapelfeldt *et al.*, fibrinogen scaffolds

prepared for cell culture applications and crosslinked with FA steam had a reduced thickness of only 1.7 to 2.75 μm . This could be due to the washing steps following the crosslinking process, which may have led to the removal of the salt from the fibrinogen scaffolds.

Using AFM analyses, it was determined in the present study that nanofibrous and planar fibrinogen scaffolds have unlimited stiffness regardless of the respective topography (see Fig. 65). Thus, they provide the cells with mechanical properties comparable to glass. Sell *et al.* reported a stiffening of electrospun fibrinogen fibers during crosslinking (Sell *et al.* 2008b). This suggests that the mechanics of the presented nanofibrous and planar fibrinogen scaffolds could probably also be mainly influenced by the crosslinking process. To determine the real elastic modulus of the respective substrates, the elastic moduli of the scaffolds would have to be measured with stiffer cantilevers (Suriano *et al.* 2014).

The successful transfer of the new patterning process to fibrinogen now allowed another protein scaffold type (see Fig. 66 and 67). So far, little research has been done to control the formation of fibrinogen nanofibers on surfaces (Reichert *et al.* 2009). Different studies patterned fibrinogen in different ways. In an earlier study, thin fibrillary fibrinogen fibers were aligned on patterned carrier substrates (Reichert *et al.* 2009). Particle lithography was used to pattern fibrinogen in a PEG-silane matrix (Englade-Franklin *et al.* 2013). Microcontact printing was used to directly stamp patterns of fibrinogen for studies of platelet adhesion and activation (Corum and Hlady 2012). In contrast to the results in the present work, all these earlier studies often either assemble fibers on an underlying topography or use smooth protein films. To the knowledge of the author, the combination of two different fibrinogen topographies in a single scaffold was not reported up to now. The results presented here could be a further step towards the development of effective biological scaffold materials for tissue engineering and regenerative applications in medicine. These depend on the ability to provide specific cell populations with precise cues from the environment to direct their position and function (Alsberg *et al.* 2006).

4.2.1 Cell interaction with fibrinogen scaffolds

In this study, the interaction of cells with fibrinogen scaffolds produced by salt-induced self-assembly was investigated for the first time, using NIH 3T3 fibroblasts as a model system. The results on cell viability and cell morphology on substrates with a single topography followed by cell morphology and cell motility on topographically patterned fibrinogen scaffolds are discussed below.

Cell interaction on single topographies:

The WST-1 assay showed a good proliferation rate for fibroblasts over a growth time of 72 h, which was independent of the underlying substrate and fibrinogen topography (see Fig. 68). The WST-1 assay yielded higher extinction values with increasing cultivation time, which confirmed that the cells proliferated on all substrates (Berridge *et al.* 2005). These results are in good agreement with previous studies on fibrinogen fibers. McManus and co-workers performed a WST-1 assay and have shown that electrospun fibrinogen fibers supported the proliferation of cardiac fibroblasts from neonatal rats (McManus *et al.* 2007a). In a different study, human umbilical vein endothelial cells (HUVECs) were cultured on electrospun fibrinogen nanofibers for up to 7 days (Gugutkov *et al.* 2013). Based on the adhesion, morphology, and motility data in their study electrospun fibrinogen nanofibers were considered to be bioactive, although no viability assays were conducted (Gugutkov *et al.* 2013).

To analyze the relative viability the proliferation rates were plotted relative to the glass control. Overall, NIH 3T3 fibroblasts exhibited higher proliferation rates on planar fibrinogen and APTES than on glass (see Fig. 69), which explains viability higher than 100% since the viability of glass was used as the 100% reference value. That is in good agreement with previous studies where it has been reported, that functionalization with APTES increases the number of amino groups and thus enhances cell spreading and proliferation (Kuddannaya *et al.* 2013). Interestingly, the relative viability of NIH 3T3 fibroblasts grown on fibrinogen nanofibers displayed a different trend. The measured metabolic activity decreased after 48 h growth time to a value of approximately 70 %, which is still considered biocompatible (EN ISO 10993-5:2009), and increased to approximately 100 % of the glass control after 72 h. This trend on fibrinogen nanofibers could presumably have been induced by the topography. The higher specific surface area caused by the surface roughness initially led to fewer cell-cell contacts compared to planar fibrinogen (Nelson and Chen 2002). Only after 48h at higher cell density more contacts were established, which in turn accelerated proliferation. Moreover, it was stated before that fibroblasts decrease proliferation rates with increasing surface roughness which is consistent with the finding from this thesis (Kunzler *et al.* 2007). Since fibroblasts normally start depositing ECM between 48 h and 72 h *in vitro*, the increase of fibroblast viability on nanofibrous fibrinogen after 48 h could also be correlated with ECM deposition (Franco-Barraza *et al.* 2016; Kubow *et al.* 2009).

Overall, not many *in vitro* studies of cells on fibrinogen nanofibers have been presented to date, which could provide reference data for cell viability on fibrinogen nanofibers. The results of 3T3 fibroblasts on self-assembled fibrinogen nanofibers in the study are in good agreement with the few available comparative studies. Further investigation of cell viability between 24 h and 48 h could provide better insight into these observed trends. More repetitions of WST-assays could give higher statistical relevance. In future studies, an LDH-assay could also give further insight into cell viability on this novel scaffolds type.

To evaluate the cell morphology, fibroblasts were stained with phalloidin and DAPI and imaged with fluorescence microscopy. The imaging with optical fluorescence microscopy was challenging since cells were difficult to recognize due to the strong autofluorescence of the underlying fibrinogen nanofibers. It has been shown previously, that several crosslinking methods including FA vapor induced autofluorescence (Smith *et al.* 2015). Sodium borohydride and glycine can reduce the fluorescing aldehydes by reducing the aldehyde and ketone active groups to alcohols (Baschong *et al.* 2016). Overall, fibroblasts on nanofibers appeared to be smaller than on planar fibrinogen with fewer stress fibers being visible on nanofibers than on planar scaffolds (see Fig. 70). However, cells on planar fibrinogen showed well spread actin cytoskeletons with distinct stress fibers and few short filopodia. To further study this morphological trend in more detail SEM and confocal microscopy analysis were conducted (see Fig. 71).

In confocal microscopy images, fibroblasts on nanofibrous fibrinogen did not show many stress fibers, while fibroblasts on planar fibrinogen showed pronounced stress fibers (mostly dorsal and ventral stress fibers). Dorsal and ventral stress fibers are associated with focal adhesions, indicating good cell adhesion on planar fibrinogen substrates (Burrige and Wittchen 2013). This trend intensified with increasing growth time and was in good agreement with previous fluorescence microscopic data. Previously, this trend was observed in fibroblasts grown on polybromostyrene and polystyrene with different topographies (Dalby *et al.* 2002b). Fibroblasts grown on rough surfaces showed smaller cell areas and expressed less actin than cells on the smooth controls (Dalby *et al.* 2002b). Analyses on the nanoscale confirmed the trends observed in fluorescence microscopy. SEM images confirmed that cells grown on fibrinogen nanofibers were smaller than cells grown on planar fibrinogen.

To further analyze whether fibroblasts on fibrinogen nanofibers protrude into the 3D scaffolds, confocal microscopic z-stack images were obtained. Cells on fibrinogen nanofibers showed partly few but long filopodia. The cells protruded slightly with their

filopodia into the cavities of the nanofibrous fibrinogen scaffolds. This result indicates a close interaction between fibroblasts and fibrinogen scaffolds, as they are responsible for cell perception and the formation of focal adhesions (Jacquemet *et al.* 2015), which are desirable for applications in the biomedical context (see Figure 72) (Dalby *et al.* 2003). In future studies, the staining of integrins and focal adhesion proteins such as vinculin and paxillin could provide further insights into cell-material interaction. The porosity of protein scaffolds is crucial for the possible migration of cells in three-dimensional scaffolds (Harley *et al.* 2008). Therefore, the porosity of fibrinogen scaffolds would be of interest in future studies.

Cell interaction on binary topographies:

To investigate the dynamic influence of binary patterned surfaces on the cell morphology, fibroblasts were fixed after 36 h cultivation time and examined by SEM. Cells cultivated on the border between nanofibrous and planar regions dynamically adapted their morphology. In cells on the border, the part grown on the planar area showed pronounced stress fibers. The cytoskeleton on the nanofibrous area showed a reduced cell area and stress fibers were not visible or less pronounced than on the planar area (see Fig. 73). These observations are in good agreement with earlier studies showing that different surface roughness dynamically influenced Vascular smooth muscle cell morphology (Kiang *et al.* 2013). Dynamic morphology changes have also been reported for 3T3 fibroblasts (Pholpabu *et al.* 2015).

After establishing the patterning and tracking procedures as well as the analysis procedures for collagen scaffolds, the experimental procedures were applied to fibrinogen scaffolds. The migration rates of fibroblasts on nanofibrous fibrinogen scaffolds were $80 \pm 8 \text{ nm min}^{-1}$. On planar fibrinogen scaffolds, fibroblasts migrated at a rate of $56 \pm 6 \text{ nm min}^{-1}$, while the cell migration rate on glass was $91 \pm 8 \text{ nm min}^{-1}$. The average speeds on nanofibrous fibrinogen scaffolds were higher than on planar scaffolds, which is in good agreement with the observations in confocal microscopy images where cells on planar fibrinogen scaffolds showed pronounced dorsal stress fibers. These are attached to focal adhesions and indicate stationary cells (Pellegrin and Mellor 2007). This suggests that fibroblasts were better attached to planar fibrinogen. Furthermore, fibroblasts on planar fibrinogen showed higher proliferation rates than cells on fibrinogen nanofibers. These two factors may explain the lower migration rates compared to cells grown on fibrinogen fibers. For fibroblasts on fibrin, speeds of about 167 nm min^{-1} have already been reported, which is significantly faster than the speeds reported in the present study

(Hakkinen *et al.* 2011). Proliferation studies in the present work showed high proliferation rates for fibroblasts on both fibrinogen topographies. High cell densities can lead to many cell-cell contacts and consequently to cell clusters (Matsiaka *et al.* 2019). Previously it was observed that the cell migration behavior in cell clusters was different from that of single cells (Painter *et al.* 2010). This could be a possible explanation for the comparatively low migration velocities on fibrinogen scaffolds in the present study.

The results of migration rates on binary substrates must be interpreted with caution since the number of tracks on these scaffolds was lower than on scaffolds with only one topography. The cells migrated much slower on binary substrates than on substrates with only one topography. On nanofibrous regions, the cells migrated at speeds of $42 \pm 5 \text{ nm min}^{-1}$ and on planar regions more slowly at $33 \pm 4 \text{ nm min}^{-1}$ (see Fig. 74). This confirmed the trend observed in samples with only one topography, where the cells migrated faster on fibers than on planar surfaces. Furthermore, the nanofiber areas had to be crosslinked twice due to the structuring process. Attempts were made to prevent the influence on the areas that were already assembled. However, there is no guarantee that a second crosslinking step could also influence the already assembled areas of the binary scaffolds. Thus, more aldehyde residues could be present on the scaffolds and possibly impede cell migration. To prove this hypothesis, it would be useful to carry out control experiments with double crosslinked substrates - possibly also with regard to their mechanics. It has been reported that the crosslinking of fibrinogen leads to a stiffening of such substrates (Sell *et al.* 2008b). Various studies have observed increased migration rates on and towards stiffer substrates such as for tumor cells or for fibroblasts (Pathak and Kumar 2012; Lange and Fabry 2013; Kai *et al.* 2016). According to this, a possible double crosslinking of the fibrous areas could have additionally increased the migration speed. In future studies, imaging routines should be made more comparable to samples with only one topography so that the same area and consequently a comparable number of cells can be examined. This would give the data on binary substrates a higher statistical relevance (Tanaka 1987). Furthermore, proliferation and viability studies on binary substrates should be carried out in the future to, among other things, better classify the migration data.

Concluding the experimental section on fibrinogen scaffolds it can be summarized, that the first working hypothesis in this work was confirmed. Fibroblasts grown on nanofibrous fibrinogen appeared to be smaller than cells grown on planar fibrinogen, where cells were well spread and large. It was reported that various cell types display thick stress fibers on

rigid and flat substrates (Tojkander *et al.* 2012). For cells grown in a three-dimensional environment, a lack of stress fibers was reported (Tojkander *et al.* 2012). Yet, aspects of stress fibers and their connection to focal adhesion remain unclear or are often not in agreement with experimental results (Livne and Geiger 2016). Thus, the platform presented in this work could help to gain further insight into the dependence of topography and stress fiber expression, as the same cell can be observed on two topographies simultaneously. Moreover, it would be interesting to stain focal adhesion proteins, for instance, vinculin, to further elucidate cell-substrate interactions on binary protein scaffolds.

The second hypothesis that fibroblasts grown on nanofibrous scaffolds would reduce their proliferation due to higher surface area and less cell-cell contacts was confirmed. The viability did not differ significantly between nanofibrous and planar fibrinogen scaffolds. Yet, a trend towards lower viability on nanofibers fibrinogen was visible. Fibroblast viability on nanofibrous fibrinogen was always lowest compared to planar fibrinogen and glass over all time points.

Finally, the experimental analysis of migration velocities on different fibrinogen topographies confirmed the hypothesis that cells on nanofibrous scaffolds would migrate faster than on planar fibrinogen scaffolds.

4.3 Collagen vs Fibrinogen

The novel combination of protein self-assembly and polymer patterning enabled us to prepare a new type of protein scaffolds, which combine nanofibrous and planar topographies in the same scaffold. Using the ECM protein collagen as a proof-of-concept, the patterning approach was later transferred to the blood plasma protein fibrinogen, where the novel method of salt-induced self-assembly was used to prepare the nanofibrous scaffold regions. Both scaffold types showed to be very stiff. To estimate the correct Young's moduli of the respective substrates additional measurements with stiffer cantilevers would be needed.

4.3.1 Scaffold characteristics

In principle, both proteins presented in this thesis can built up binary topographies in a scaffold on different substrate materials, which will be advantageous for future applications on different biomaterial surfaces. The scaffold roughness of dried nanofibrous collagen scaffolds was about 40 nm for collagen scaffolds prepared with 0.5 mg ml⁻¹ and about 46 nm for collagen scaffolds prepared with 2.5 mg ml⁻¹. Dried nanofibrous fibrinogen

scaffolds had a higher surface roughness of about 118 nm and thus had a much higher specific surface area than collagen nanofibers. Dried smooth collagen prepared with 0.5 mg ml^{-1} collagen showed a surface roughness of about 9 nm, which was comparable to the surface roughness of about 7 nm measured for dried planar fibrinogen.

Nanofibrous collagen scaffolds prepared with 2.5 mg ml^{-1} protein showed a surface roughness of about 114 nm upon rehydration, which was in a comparable range to the surface roughness of rehydrated nanofibrous fibrinogen scaffolds with a surface roughness of about 120 nm. On the other hand, nanofibrous collagen scaffolds prepared with 0.5 mg ml^{-1} showed a lower surface roughness of about 43 nm during rehydration. Smooth collagen scaffolds showed surface roughness in the range of 20 to 30 nm after rehydration, whereas the roughness of rehydrated planar fibrinogen was much lower with a value of about 9 nm. Overall, for both fibrinogen topographies, no influence of rehydration on roughness was found, which was different from collagen scaffolds, which showed swelling effects leading to higher roughness values during rehydration.

With AFM analysis of dried collagen and fibrinogen nanofibers, fiber diameters in the range of 230 nm were found. Collagen nanofibers had diameters of approximately 400 nm upon rehydration. Fibrinogen fibers had smaller fiber diameters of approximately 340 nm upon rehydration. These results show that fibrinogen fibers swell less than collagen nanofibers. Rehydrated collagen fibers were in the range of electrospun collagen nanofibers rehydrated in PBS (Luo *et al.* 2018). For collagen nanofibers produced by wet spinning and cross-linked with glutaraldehyde solution a significant decrease of swelling ability was reported (Siriwardane *et al.* 2014). For electrospun non-cross-linked fibrinogen, it was previously reported, that fibers did not swell upon rehydration with PBS or water, which is in good agreement with the results obtained in this present study (Kim *et al.* 2011a). Fibrinogen fiber diameters found in the present study are in good agreement with earlier studies where fibrinogen fiber diameter has been found to be between 10 nm and $10 \mu\text{m}$ depending on spinning conditions (Kim *et al.* 2011a).

With the proteins, collagen and fibrinogen the assembly of smooth/planar and nanofibrous areas into a binary scaffold topography could be realized for the first time. With this topography combination in a single protein scaffold, a biophysical model system was established, which offers versatile possibilities for future *in vitro* cell culture studies. In recent studies, both proteins were combined in hydrogels or matrices (Schneider-Barthold *et al.* 2016; NedreLOW *et al.* 2018).

4.3.2 Comparison of fibroblast interaction with collagen and fibrinogen scaffolds

The viability of 3T3 fibroblasts differed between cells on fibrinogen and collagen. While the WST-1 analysis showed a decrease in the viability of fibroblasts on collagen scaffolds after 24 h, the viability of cells on fibrinogen remained high throughout the growth period of 72 h. It should be noted that the fibroblasts used on collagen and fibrinogen scaffolds were the same cell line but from different suppliers. Furthermore, cells on collagen scaffolds were cultivated with 10% FBS and cells on fibrinogen with only 5% FBS - according to the recommendations of the respective suppliers. Therefore the results from both parts can only be discussed very carefully. As the serum contains hormones, growth factors, vitamins, amino acids and several other vital components (van der Valk *et al.* 2010), the difference in FBS content may have had an impact on the cell proliferation and migration observed in this study. Thus, higher concentrations would lead to higher proliferation rates. The opposite was observed in this study. The cells cultivated on collagen with a higher concentration of FBS had lower proliferation rates. In addition, the collagen and fibrinogen scaffolds were cross-linked by different methods and different aldehydes, respectively. Collagen was crosslinked with liquid glutaraldehyde, in contrast to the formaldehyde vapor crosslinking method used for fibrinogen scaffolds. Cell viability was higher in fibrinogen than on collagen. Since it has been reported earlier that FA crosslinking is a gentler treatment than GA crosslinking, this difference may possibly explain the higher proliferation rates on fibrinogen scaffolds (Kiernan 2000). Crosslinking of proteins with FA vapor is less hard than crosslinking with liquid glutaraldehyde, which leads to fewer free aldehyde groups (Peng *et al.* 2017). Zhu *et al.* cultivated human stem cells of the placenta decidua parietalis on GA vapor cross-linked electrospun collagen fibers. They reported cell viabilities of about 100% after 24-hour cultivation (Zhu *et al.* 2017). Vapor crosslinking of the collagen nanofibers presented here could possibly increase cell viability. Although the fiber diameters of collagen and fibrinogen nanofibers were in a comparable range, the overall topography was different, which was confirmed by the different roughness values. The different topographies could additionally influence cell viability. The difference in viability between collagen and fibrinogen could be mainly influenced by the different substrate roughness, the different crosslinking, and the different cultivation medium as well as by the synergy effects. For future comparative studies of collagen and fibrinogen scaffolds, it would be important to use the same cultivation conditions, i.e. cells of the same origin and the same crosslinking methods, to be able to directly compare the results obtained for different protein scaffolds.

For both proteins, fibroblasts reacted with altered morphology depending on the roughness on which they were cultivated. Interestingly, cells on collagen substrates showed spindle-like morphologies and the most pronounced differences in filopodia expression. In contrast, fibroblasts expressed a spread morphology with the most pronounced differences in stress fiber formation when grown on fibrinogen scaffolds. On both proteins, fibroblasts showed a reduced cell area when grown on fibrous surfaces, which is in good agreement with earlier studies (Sales *et al.* 2019). Cells on nanofibrous collagen expressed few but long filopodia, while fibroblasts on smooth collagen showed more but short filopodia. In contrast to these observations, fibroblasts on both fibrinogen topographies expressed fewer filopodia and lamellipodia than on collagen. Nevertheless, a direct comparison would only be possible under the same cultivation conditions. In contrast to the trend on collagen, cells on fibrinogen had a higher tendency to express longer filopodia and lamellipodia on planar fibrinogen scaffolds. These different reactions of 3T3 fibroblasts on collagen and fibrinogen scaffolds might be a reaction to the different topography and roughness of the different protein scaffolds at the same cell densities. Furthermore, the different cellular reactions could be induced by the biochemical signals of the different proteins. SEM images showed that collagen nanofibers were randomly organized, while the fibrinogen scaffolds had randomly organized fibers with islands. The main difference between the two proteins was roughness. Furthermore, the different proliferation behavior could also influence the morphogenesis of the fibroblasts. 3T3 fibroblasts grown on fibrinogen proliferated more than on collagen, regardless of the topography.

It may be possible that cells on collagen express more filopodia and lamellipodia because the scaffolds cross-linked with GA hinder correct adhesion and thus lead to more pronounced migration. The slower migration rates on fibrinogen compared to collagen scaffolds would be in good agreement with this hypothesis. An increase in the migration rate of fibroblasts on GA cross-linked fibronectin fibers has been reported in the literature (Missirlis *et al.* 2017). They postulated that the increase in migration speed on GA-crosslinked protein fibers might be related to changes in ligand accessibility of the crosslinked protein scaffold. In the present study, the cell migration speed of fibroblasts on fibrinogen scaffolds was about four times slower than on collagen scaffolds. It might be possible that cells with higher proliferation rates migrate less, which might explain the differences in migration rates on the respective substrates. It was previously postulated that there is a compromise between proliferation and migration, in which dividing cells are less mobile and mobile cells are less likely to proliferate (Michod and Roze 2001). Since

the migration rates of fibroblasts on glass slides were lower in the fibrinogen series than on glass slides in the collagen experiments, likely, the difference in migration rate was largely related to differences in FBS content in the cell culture media.

4.4 Combination of biochemical cues and topographical cues

Fibroblasts grown on two different proteins showed different morphological reactions and different migration rates. Cultivation parameters were different, but the different biochemical cues could potentially influence the cell response. To investigate basic biophysical principles, not only topographical differences but also biochemical stimuli should be investigated. For this purpose, the pattern concept was then applied to spatially controlled combinations of collagen and fibrinogen scaffolds. In this way, topographical and biochemical stimuli could be combined or adjusted independently of each other in future studies. The technique of patterned self-assembly established and validated in this dissertation could form the basis for a multiparametric biophysical platform that will enable future studies of cellular recognition processes.

The first scaffold type combining fibrinogen and collagen regions was developed to combine spatially controlled nanofibrous collagen and nanofibrous fibrinogen regions. In SEM analysis, the binary scaffold type 1 (fiber-collagen-fiber-fibrinogen) showed a different fiber morphology for both fibrinogen (see Fig. 76B) and collagen (see Fig. 76C) scaffolds. Instead of a direct boundary between the two fiber types, a smooth boundary area was observed between the two fibrous regions (see Fig. 76A). For future applications, the handling of the polymer mask needs to be improved to increase the precision of the topographic patterning. It was not clear which protein was present in the smooth boundary region. To prove the presence of each protein a immunostaining of both proteins could be performed (Maity *et al.* 2013). Nevertheless, defined biochemistry and topography are essential to study the cell response to these cues. Other scaffolds that combine collagen and fibrinogen lack spatial control of these biochemical cues and are therefore limited in their ability to decouple topographic and biochemical cues (Shepherd *et al.* 2017). Therefore, the technique needs to be improved to ensure a reproducible border between the two nanofibrous protein regions.

For binary scaffold type 2, the combination of planar fibrinogen with nanofibrous collagen is shown in Fig. 77. The binary scaffolds type 2 showed very planar fibrinogen regions (see Fig. 77B); while the assembly of the collagen fibers was not successful (see Fig. 77C). No collagen fibers could be found on either triplicate. The cause remains unclear.

The same solutions were used to prepare the sample for sample type 1, in which the fiber assembly was successful. This assembly should be repeated to exclude possible handling errors. It was found that the boundary between the different topographies is visible (see Fig. 77A). However, the collagen layer (see Fig. 77A, right) was detached and partially removed from the carrier substrate with the PDMS mask. PDMS may not be an optimal choice for protein solutions because proteins often adsorb non-specifically on PDMS surfaces due to hydrophobic interactions (Gökaltun *et al.* 2019). This effect might have led to the difficulties in removing the PDMS mask after the drying step in the present study. Increasing the hydrophilicity of PDMS masks by surface modification could reduce the unspecific protein binding in future studies. Other studies reported high-precision structuring using nanoimprint lithography (van Truskett and Watts 2006). Recent advances in the precise preparation of nano- and microstructured biomaterials have already made it possible to control a wide range of cell functions, e.g. by electron beam lithography, microcontact printing or nanoimprint lithography (Ermis *et al.* 2018; Petreaca and Martins-Green 2014). These nano- and microfabrication techniques are mainly used to produce two-dimensional topographies, often using synthetic substrate materials (Ermis *et al.* 2018; Petreaca and Martins-Green 2014). In contrast to the methods listed above, the method presented here still lacks precision in spatial control. Nevertheless, it has the potential to produce three-dimensional scaffolds with spatially controlled topographic and biochemical signals. This would be a significant advantage over the above methods for studying cell-substrate interactions.

Sample type 3 combined smooth collagen with nanofibrous fibrinogen (see Fig. 80). With this set-up as well as with sample Type 2 the nanofibrous scaffold attached to the PDMS mask and parts of the scaffold at the boundary were detached (see Fig. 80A). The assembly itself of both smooth collagen and fibrous fibrinogen was successful (see Fig. 80B). The fibrinogen fibers were well defined (see Fig. 80C). Stapelfeldt *et al.* introduced a novel self-assembly method to produce fibrinogen nanofibers (Stapelfeldt *et al.* 2019a). In the present study, this method was successfully transferred and combined with the novel patterning method combining two topographies and two proteins.

Overall, the novel patterning method to prepare protein scaffolds with nanofibrous and smooth/planar topographies in selected regions could be partially transferred to scaffolds, which combine different proteins. This shows, that if the technical problems have been overcome, that the platform could give the freedom to tailor biochemical as well as topographical cues. Yet, further improvement in sample preparation needs to be done.

The combination of fibrinogen or fibrin and collagen or gelatin in a scaffold was previously studied by different groups. Composites of collagen and fibrinogen were mainly prepared in the form of gels. The group around Dainik for example presented gelatin-fibrinogen cryogels for wound repair (Dainiak *et al.* 2010). They produced macroporous sponge-like scaffolds and cross-linked with GA. Lorusso and co-workers presented a fibrinogen coated collagen patch (Lorusso *et al.* 2011). The mixture of collagen and fibrinogen solution for a gel-formation is also a method, which was used by different groups (Cummings *et al.* 2004; Rowe and Stegemann 2006). Shepherd *et al.* presented collagen and fibrinogen in a porous scaffold using lyophilization (Shepherd *et al.* 2017). All these methods lack the spatial control of the proteins and the topography of each protein. They either present a layered film or sponge-like scaffolds. In contrast to these previous studies, which blended the respective protein components without spatial control, the patterning approach presented in this study allows to spatially control the deposition of different proteins with varying topography. Yet, the combination of varying topographies from different proteins in a single scaffold still needs to be improved further to achieve reproducible patterns.

While nanotopographies have a major effect on cell adhesion and differentiation (Biggs *et al.* 2010; McNamara *et al.* 2010; Dalby *et al.* 2014; Kim *et al.* 2012), microtopographies are known to affect the cell morphology and can for instance influence macrophage morphology, thus modulating the immune response to biomaterials (Nguyen *et al.* 2016; Sridharan *et al.* 2015; McWhorter *et al.* 2015). Previously, the combination of nano- and microtopographies was found to steer the behavior of neuronal cells (López-Fagundo *et al.* 2013; Bruder *et al.* 2006). Therefore, in future studies it will be highly interesting to selectively integrate nanotopographies into micropatterned protein scaffolds using the combination of self-assembly and polymer patterning. It will be interesting to study whether such a combination of nano- and microtopographical cues can modulate the behavior of various cell types in tissue on different length scales (Sridharan *et al.* 2015; López-Fagundo *et al.* 2013; Metavarayuth *et al.* 2016; Patel *et al.* 2018). The method presented in this study has the potential to be further developed and help to individually study topographical, biochemical, and mechanical cues.

The control over the mechanical properties of the here presented scaffolds would be desirable for future studies. Varying the degree of crosslinking with regard to the development of a multiparametric platform could be a possible strategy for future studies. Crosslinking techniques such as EDC, methanol, and riboflavin UV crosslinking have

already shown to maintain the topography of collagen nanofibers in cell culture studies (Hakkinen *et al.* 2011) and may also be suitable to adjust the stiffness of collagen scaffolds in future studies. To further optimize the binary patterns for future cell culture studies, it will be advantageous to reduce the scaffold stiffness and thus more closely mimic the mechanical indications of the native ECM (Balestrini *et al.* 2012; Gilbert *et al.* 2010; Lovett *et al.* 2013). Previously, it was shown that the reaction of different cell types depends crucially on the substrate stiffness. For example, neurons prefer soft surfaces, while fibroblasts grow better on rigid surfaces (Vogel and Sheetz 2006). Therefore, in addition to topographical variations, the control of mechanical signals of the collagen scaffolds presented in this study will be an important tool to control cell response.

5. Conclusion and Outlook

The ECM-cell interaction is mainly influenced by the three factors biochemistry, biomechanics, and topography of the ECM. The complex cross-talk of cells and the ECM in a tissue is not fully understood to date. In this interplay, topographical cues have a large impact on cellular growth and are known to influence proliferation, cell spreading, and migration. To study the particular role of topographical cues of protein scaffolds on cell growth this study aimed to establish a biophysical platform, which combines smooth/planar and nanofibrous topographies in a single scaffold. Therefore, a new scaffold design was established, which allowed disentangling biochemical and mechanical cues from topographical variations in the protein scaffold.

Using collagen as a model system, a new process of structured self-assembly was established to prepare protein scaffolds with spatially controlled variations in topography. In this new synthetic ECM platform, the surface topography was varied between nanofibrous and smooth regions while biochemical and mechanical characteristics remained unchanged. Using collagen scaffolds with combined topographies, topography-induced changes in cell morphology from spindle-shaped fibroblasts on nanofibers to flat spread fibroblasts on smooth regions were observed. Fibroblasts showed different morphologies when grown on the border of two topographies, showing that the cells adapted dynamically to changes in their underlying substrates. In the future, this novel topographical platform could allow tracking of topography-dependent cell recognition processes on a single scaffold in real-time.

After the patterning method was established with the model system collagen, the production method was successfully transferred to fibrinogen. Cell culture studies on nanofibrous and planar scaffolds showed an overall positive cell response to fibrinogen. Fibroblasts on fibrinogen substrates showed good proliferation rates. Fibroblasts on planar fibrinogen expressed significantly more stress fibers than on nanofibrous scaffolds. Similar trends could be observed for single cells on binary substrates growing directly on the topographic boundary and showed that fibroblasts dynamically adapt their morphology even on fibrinogen.

Cell culture experiments revealed that the different biochemical cues possibly induced different cell responses in fibroblasts. The two protein scaffolds had different surface roughness and fiber diameter. For a better insight into these mechanisms, future studies with comparable cultivation conditions are required.

To investigate a basic understanding of the influence of the three parameters of biochemical, biomechanical, and topographical cues on cellular interactions independently, this study could form the basis for a future multiparametric synthetic ECM platform. As a first step into this direction, after the targeted variation of the topography, the different biochemical compositions were explored by using different proteins in the same scaffold. Towards three-dimensional scaffolds, the thickness of the here presented scaffolds needs to be increased in future studies. The combination of different fibrillary proteins in the same 2D/3D scaffolds would be beneficial towards future applications in tissue engineering and to address different cell types via integrin-specific adhesion in combination with varying topographical cues. Such a scaffold design could serve as a co-culture system to optimally control the growth of different cell types in future tissue engineering scaffolds.

The results of this Ph.D. thesis have provided fundamental insight into how fibroblast cells respond to different topographies in the same protein scaffold. A novel method to combine smooth and fibrous topographies was introduced. Overall, this study has the potential to provide a model system that allows further explorations of the interaction between cells and their extracellular environmental cues such as topography, biochemistry, and mechanics individually. If nanotopographies can be selectively integrated into microstructured protein scaffolds through the combination of self-organization and polymer structuring presented here, it might also be possible to modulate the behavior of different cell types in tissue on different length scales.

In future studies, cell experiments should be performed under comparable conditions to achieve comparable results for collagen and fibrinogen scaffolds. As it is currently not possible to differentiate whether the observed differences are due to different biochemical signals or roughness or whether they are due to different cultivation conditions. To compare the migration data of cells on binary substrates with only one topography, the evaluation routines for these two sample types should be improved and made comparable. In the course of this, further viability studies on binary substrates would be important in future studies to analyze whether the new binary substrates influence the proliferation of cells. Also, the methodology for combining these two protein systems should be further improved, as this offers the possibility to study the same cell population in real-time on these different proteins and topographies. To study the third important aspect of extracellular properties with the model presented here, it would be important in the future to control the substrate mechanics e.g. by other crosslinking methods and to be

able to adjust them independently of biochemical and topographic cues. Different cell types respond differently to topography, biomechanics, and biochemistry. Therefore, other cell types such as osteoblasts should be included in future studies. By co-cultivating different cell types, one could, for example, investigate whether the platform presented here offers the possibility to grow cell types spatially controlled on the same scaffold.

Publication bibliography

- AAMODT, JOSEPH M.; GRAINGER, DAVID W. (2016): Extracellular matrix-based biomaterial scaffolds and the host response. In *Biomaterials* 86, pp. 68–82. DOI: 10.1016/j.biomaterials.2016.02.003.
- ALAM, NAVED; GOEL, HIRA LAL; ZARIF, MATTHEW J.; BUTTERFIELD, JULIE E.; PERKINS, HILLARY M.; SANSOUCY, BRIAN G. *et al.* (2007): The integrin—growth factor receptor duet. In *J. Cell. Physiol.* 213 (3), pp. 649–653. DOI: 10.1002/jcp.21278.
- ALBERTS, BRUCE; JOHNSON, ALEXANDER; LEWIS, JULIAN; RAFF, MARTIN; ROBERTS, KEITH; WALTER, PETER (2002): *Fibroblasts and Their Transformations. The Connective-Tissue Cell Family*: Garland Science.
- ALBUSCHIES, JÖRG; VOGEL, VIOLA (2013): The role of filopodia in the recognition of nanotopographies. In *Scientific reports* 3, p. 1658. DOI: 10.1038/srep01658.
- ALSBERG, EBEN; FEINSTEIN, EFRAIM; JOY, M. P.; PRENTISS, MARA; INGBER, DONALD E. (2006): Magnetically-Guided Self-Assembly of Fibrin Matrices with Ordered Nano-Scale Structure for Tissue Engineering. In *Tissue engineering* 12 (11), pp. 3247–3256. DOI: 10.1089/ten.2006.12.3247.
- ANISHKIN, ANDRIY; LOUKIN, STEPHEN H.; TENG, JINFENG; KUNG, CHING (2014): Feeling the hidden mechanical forces in lipid bilayer is an original sense. In *Proceedings of the National Academy of Sciences of the United States of America* 111 (22), pp. 7898–7905. DOI: 10.1073/pnas.1313364111.
- ARNADÓTTIR, JÓHANNA; CHALFIE, MARTIN (2010): Eukaryotic mechanosensitive channels. In *Annual review of biophysics* 39, pp. 111–137. DOI: 10.1146/annurev.biophys.37.032807.125836.
- ARNOLD, MARCO; CAVALCANTI-ADAM, ELISABETTA ADA; GLASS, ROMAN; BLÜMMEL, JACQUES; ECK, WOLFGANG; KANTLEHNER, MARTIN *et al.* (2004): Activation of integrin function by nanopatterned adhesive interfaces. In *Chemphyschem : a European journal of chemical physics and physical chemistry* 5 (3), pp. 383–388. DOI: 10.1002/cphc.200301014.
- ASSOIAN, RICHARD K.; SCHWARTZ, MARTIN A. (2001): Coordinate signaling by integrins and receptor tyrosine kinases in the regulation of G1 phase cell-cycle progression. In *Current Opinion in Genetics & Development* 11 (1), pp. 48–53. DOI: 10.1016/S0959-437X(00)00155-6.

- ATALA, ANTHONY (2004): Tissue engineering and regenerative medicine. Concepts for clinical application. In *Rejuvenation research* 7 (1), pp. 15–31. DOI: 10.1089/154916804323105053.
- BADYLAK, STEPHEN F.; FREYTES, O.; GILBERT, THOMAS W. (2009): Extracellular matrix as a biological scaffold material. Structure and function. In *Acta biomaterialia* 5 (1), pp. 1–13. DOI: 10.1016/j.actbio.2008.09.013.
- BAE, HYUN-SU; HAIDER, ADNAN; SELIM, K. M. KAMRUZZAMAN; KANG, DONG-YOON; KIM, EUN-JIN; KANG, INN-KYU (2013): Fabrication of highly porous PMMA electrospun fibers and their application in the removal of phenol and iodine. In *Journal of Polymer Research* 20 (7), p. 158. DOI: 10.1007/s10965-013-0158-9.
- BALESTRINI, JENNA L.; CHAUDHRY, SIDHARTH; SARRAZY, VINCENT; KOEHLER, ANNE; HINZ, BORIS (2012): The mechanical memory of lung myofibroblasts. In *Integrative biology : quantitative biosciences from nano to macro* 4 (4), pp. 410–421. DOI: 10.1039/c2ib00149g.
- BALIAN, G.; CLICK, E. M.; BORNSTEIN, P. (1980): Location of a collagen-binding domain in fibronectin. In *J. Biol. Chem.* 255 (8), pp. 3234–3236. Available online at <http://www.jbc.org/content/255/8/3234.full.pdf>.
- BAO, L.-R.; CHENG, X.; HUANG, X. D.; GUO, L. J.; PANG, S. W.; YEE, A. F. (2002): Nanoimprinting over topography and multilayer three-dimensional printing. In *J. Vac. Sci. Technol. B* 20 (6), p. 2881. DOI: 10.1116/1.1526355.
- BARNES, CATHERINE; SELL, SCOTT A.; BOLAND, EUGENE; SIMPSON, DAVID; BOWLIN, GARY (2007): Nanofiber technology. Designing the next generation of tissue engineering scaffolds. In *Advanced drug delivery reviews* 59 (14), pp. 1413–1433. DOI: 10.1016/j.addr.2007.04.022.
- BASCHONG, WERNER; SUETTERLIN, ROSMARIE; LAENG, R. HUBERT (2016): Control of Autofluorescence of Archival Formaldehyde-fixed, Paraffin-embedded Tissue in Confocal Laser Scanning Microscopy (CLSM). In *J Histochem Cytochem.* 49 (12), pp. 1565–1571. DOI: 10.1177/002215540104901210.
- BEACHAM, DOROTHY A.; AMATANGELO, MICHAEL D.; CUKIERMAN, EDNA (2007): Preparation of extracellular matrices produced by cultured and primary fibroblasts. In *Current protocols in cell biology* Chapter 10, Unit 10.9. DOI: 10.1002/0471143030.cb1009s33.

- BELL, E.; IVARSSON, B.; MERRILL, C. (1979): Production of a tissue-like structure by contraction of collagen lattices by human fibroblasts of different proliferative potential in vitro. In *PNAS* 76 (3), pp. 1274–1278. DOI: 10.1073/pnas.76.3.1274.
- BELLA, J.; EATON, M.; BRODSKY, B.; BERMAN, H. M. (1994): CRYSTAL AND MOLECULAR STRUCTURE OF A COLLAGEN-LIKE PEPTIDE AT 1.9 ANGSTROM RESOLUTION.
- BENTLEY, D.; TOROIAN-RAYMOND, A. (1986): Disoriented pathfinding by pioneer neurone growth cones deprived of filopodia by cytochalasin treatment. In *Nature* 323 (6090), pp. 712–715. DOI: 10.1038/323712a0.
- BERNARD, A.; RENAULT, J. P.; MICHEL, B.; BOSSHARD, H. R.; DELAMARCHE, E. (2000): Microcontact Printing of Proteins. In *Adv. Mater.* 12 (14), pp. 1067–1070. DOI: 10.1002/1521-4095(200007)12:14<1067::AID-ADMA1067>3.0.CO;2-M.
- BERRIDGE, MICHAEL V.; HERST, PATRIES M.; TAN, AN S. (2005): Tetrazolium dyes as tools in cell biology. New insights into their cellular reduction. In M. Raafat El-Gewely (Ed.): *Biotechnology annual review*. vol. 11, vol. 11. Amsterdam, New York: Elsevier (Biotechnology Annual Review), pp. 127–152.
- BERRIER, ALLISON L.; YAMADA, KENNETH M. (2007): Cell-matrix adhesion. In *Journal of cellular physiology* 213 (3), pp. 565–573. DOI: 10.1002/jcp.21237.
- BETTINGER, CHRISTOPHER J.; LANGER, ROBERT; BORENSTEIN, JEFFREY T. (2009): Engineering substrate topography at the micro- and nanoscale to control cell function. In *Angewandte Chemie (International ed. in English)* 48 (30), pp. 5406–5415. DOI: 10.1002/anie.200805179.
- BHANA, BASHIR; IYER, ROHIN K.; CHEN, WEN LI KELLY; ZHAO, RUOGANG; SIDER, KRISTA L.; LIKHITPANICHKUL, MORAKOT *et al.* (2010): Influence of substrate stiffness on the phenotype of heart cells. In *Biotechnol. Bioeng.* 25, n/a-n/a. DOI: 10.1002/bit.22647.
- BIANCHERA, A., CATANZANO, O., BOATENG, J., & ELVIRI, L. 2020: The Place of Biomaterials in Wound Healing. In: *Therapeutic Dressings and Wound Healing Applications*, pp. 337–366. Available online at <https://onlinelibrary.wiley.com/doi/pdf/10.1002/9781119433316.ch15>, checked on 3/3/2020.
- BIGGS, MANUS JONATHAN PAUL; RICHARDS, R. GEOFF; DALBY, MATTHEW J. (2010): Nanotopographical modification. A regulator of cellular function through focal

- adhesions. In *Nanomedicine : nanotechnology, biology, and medicine* 6 (5), pp. 619–633. DOI: 10.1016/j.nano.2010.01.009.
- BIGI, A.; COJAZZI, G.; PANZAVOLTA, S.; RUBINI, K.; ROVERI, N. (2001): Mechanical and thermal properties of gelatin films at different degrees of glutaraldehyde crosslinking. In *Biomaterials* 22 (8), pp. 763–768. DOI: 10.1016/S0142-9612(00)00236-2.
- EN ISO 10993-5:2009, 2009-10: Biologische Beurteilung von Medizinprodukten - Teil 5: Prüfungen auf In-vitro-Zytotoxizität (ISO 10993-5:2009). Available online at <https://www.beuth.de/de/norm/din-en-iso-10993-5/113571989>, checked on 28.12.19.
- BIRK, D. E.; ZYCBAND, E. I.; WINKELMANN, D. A.; TRELSTAD, R. L. (1989): Collagen fibrillogenesis in situ. Fibril segments are intermediates in matrix assembly. In *Proceedings of the National Academy of Sciences of the United States of America* 86 (12), pp. 4549–4553. DOI: 10.1073/pnas.86.12.4549.
- BLANCO, ANTONIO; BLANCO, GUSTAVO (2017): Hemostasis. In Antonio Blanco, Gustavo Blanco (Eds.): *Medical Biochemistry*. Saint Louis: Academic Press, pp. 781–789.
- BOLAND, EUGENE D.; MATTHEWS, JAMIL A.; PAWLOWSKI, KRISTIN J.; SIMPSON, DAVID G.; WNEK, GARY E.; BOWLIN, GARY L. (2004): Electrospinning collagen and elastin. Preliminary vascular tissue engineering. In *Frontiers in bioscience : a journal and virtual library* 9, pp. 1422–1432. DOI: 10.2741/1313.
- BONNANS, CAROLINE; CHOU, JONATHAN; WERB, ZENA (2014): Remodelling the extracellular matrix in development and disease. In *Nature reviews. Molecular cell biology* 15 (12), pp. 786–801. DOI: 10.1038/nrm3904.
- BRATOSIN, DANIELA; MITROFAN, LAURA; PALII, CARMEN; ESTAQUIER, JÉRÔME; MONTREUIL, JEAN (2005): Novel fluorescence assay using calcein-AM for the determination of human erythrocyte viability and aging. In *Cytometry. Part A : the journal of the International Society for Analytical Cytology* 66 (1), pp. 78–84. DOI: 10.1002/cyto.a.20152.
- BRUDER, JAN M.; MONU, NICHOLAS C.; HARRISON, MICHAEL W.; HOFFMAN-KIM, DIANE (2006): Fabrication of polymeric replicas of cell surfaces with nanoscale resolution. In *Langmuir : the ACS journal of surfaces and colloids* 22 (20), pp. 8266–8270. DOI: 10.1021/la0608563.
- BRYANT, STEPHANIE J.; CHOWDHURY, TINA T.; LEE, DAVID A.; BADER, DAN L.; ANSETH, KRISTI S. (2004): Crosslinking Density Influences Chondrocyte Metabolism in

- Dynamically Loaded Photocrosslinked Poly(ethylene glycol) Hydrogels. In *Annals of biomedical engineering* 32 (3), pp. 407–417. DOI: 10.1023/B:ABME.0000017535.00602.ca.
- BUDYANTO, L.; GOH, Y. Q.; OOI, C. P. (2009): Fabrication of porous poly(L-lactide) (PLLA) scaffolds for tissue engineering using liquid–liquid phase separation and freeze extraction. In *Journal of Materials Science: Materials in Medicine* 20 (1), pp. 105–111. DOI: 10.1007/s10856-008-3545-8.
- BUEHLER, MARKUS J. (2006): Nature designs tough collagen: Explaining the nanostructure of collagen fibrils. In *PNAS* 103 (33), pp. 12285–12290. DOI: 10.1073/pnas.0603216103.
- BURRIDGE, K.; CHRZANOWSKA-WODNICKA, M. (1996): Focal adhesions, contractility, and signaling. In *Annual review of cell and developmental biology* 12, pp. 463–518. DOI: 10.1146/annurev.cellbio.12.1.463.
- BURRIDGE, KEITH; WITTCHEM, ERIKA S. (2013): The tension mounts. Stress fibers as force-generating mechanotransducers. In *The Journal of cell biology* 200 (1), pp. 9–19. DOI: 10.1083/jcb.201210090.
- BUSBY, GRAHAME A.; GRANT, M. HELEN; MACKAY, SIMON P.; RICHES, PHILIP E. (2013): Confined compression of collagen hydrogels. In *Journal of biomechanics* 46 (4), pp. 837–840. DOI: 10.1016/j.jbiomech.2012.11.048.
- BUTRUK-RASZEJA, BEATA A.; DRESLER, MAGDALENA S.; KUŹMIŃSKA, ALEKSANDRA; CIACH, TOMASZ (2016): Endothelialization of polyurethanes. Surface silanization and immobilization of REDV peptide. In *Colloids and surfaces. B, Biointerfaces* 144, pp. 335–343. DOI: 10.1016/j.colsurfb.2016.04.017.
- BUXBOIM, AMNON; RAJAGOPAL, KARTHIKAN; BROWN, ANDRE' E. X.; DISCHER, DENNIS E. (2010): How deeply cells feel. Methods for thin gels. In *J. Phys.: Condens. Matter* 22 (19), p. 194116. DOI: 10.1088/0953-8984/22/19/194116.
- CACCIAFFESTA, PAOLA; HUMPHRIS, ANDREW D. L.; JANDT, KLAUS D.; MILES, MERVYN J. (2000): Human Plasma Fibrinogen Adsorption on Ultraflat Titanium Oxide Surfaces Studied with Atomic Force Microscopy. In *Langmuir : the ACS journal of surfaces and colloids* 16 (21), pp. 8167–8175. DOI: 10.1021/la000362k.
- CANTY, ELIZABETH G.; LU, YINHUI; MEADOWS, ROGER S.; SHAW, MICHAEL K.; HOLMES, DAVID F.; KADLER, KARL E. (2004): Coalignment of plasma membrane channels and

- protrusions (fibripositors) specifies the parallelism of tendon. In *The Journal of cell biology* 165 (4), pp. 553–563. DOI: 10.1083/jcb.200312071.
- CARLISLE, CHRISTINE R.; COULAIS, CORENTIN; NAMBOOTHIRY, MANOJ; CARROLL, DAVID L.; HANTGAN, ROY R.; GUTHOLD, MARTIN (2009): The mechanical properties of individual, electrospun fibrinogen fibers. In *Biomaterials* 30 (6), pp. 1205–1213. DOI: 10.1016/j.biomaterials.2008.11.006.
- CARY, L. A.; CHANG, J. F.; GUAN, J. L. (1996): Stimulation of cell migration by overexpression of focal adhesion kinase and its association with Src and Fyn. In *Journal of cell science* 109 (Pt 7), pp. 1787–1794.
- CARY, L. A.; GUAN, J. L. (1999): Focal adhesion kinase in integrin-mediated signaling. In *Frontiers in bioscience : a journal and virtual library* 4, D102-13. DOI: 10.2741/cary.
- CASPER, CHERYL L.; YANG, WEIDONG; FARACH-CARSON, MARY C.; RABOLT, JOHN F. (2007): Coating electrospun collagen and gelatin fibers with perlecan domain I for increased growth factor binding. In *Biomacromolecules* 8 (4), pp. 1116–1123. DOI: 10.1021/bm061003s.
- CASTELLA, LYSIANNE FOLLONIER; BUSCEMI, LARA; GODBOUT, CHARLES; MEISTER, JEAN-JACQUES; HINZ, BORIS (2010): A new lock-step mechanism of matrix remodelling based on subcellular contractile events. In *Journal of cell science* 123 (Pt 10), pp. 1751–1760. DOI: 10.1242/jcs.066795.
- CATLEDGE, SHANE A.; VOHRA, YOGESH K.; BELLIS, SUSAN L.; SAWYER, AMBER A. (2004): Mesenchymal stem cell adhesion and spreading on nanostructured biomaterials. In *J. Nanosci. Nanotech.* 4 (8), pp. 986–989. DOI: 10.1166/jnn.2004.137.
- CERRAI, P.; GUERRA, G. D.; TRICOLI, M.; KRAJEWSKI, A.; RAVAGLIOLI, A.; MARTINETTI, R. *et al.* (1999): Periodontal membranes from composites of hydroxyapatite and bioresorbable block copolymers. In *Journal of materials science. Materials in medicine* 10 (10/11), pp. 677–682. DOI: 10.1023/a:1008904229292.
- CHEN, C. S.; MRKSICH, M.; HUANG, S.; WHITESIDES, G. M.; INGBER, D. E. (1997): Geometric control of cell life and death. In *Science (New York, N.Y.)* 276 (5317), pp. 1425–1428. DOI: 10.1126/science.276.5317.1425.
- CHEN, GUOJUN; NI, NANTING; WANG, BINGHE; XU, BINGQIAN (2010): Fibrinogen nanofibril growth and self-assembly on Au (1,1,1) surface in the absence of thrombin. In

- Chemphyschem* : a European journal of chemical physics and physical chemistry 11 (3), pp. 565–568. DOI: 10.1002/cphc.200900916.
- CHEN, NATHAN H.; DJOKO, KARRERA Y.; VEYRIER, FRÉDÉRIC J.; MCEWAN, ALASTAIR G. (2016): Formaldehyde Stress Responses in Bacterial Pathogens. In *Frontiers in microbiology* 7, p. 257. DOI: 10.3389/fmicb.2016.00257.
- CHEN, SHIXUAN; LIU, BING; CARLSON, MARK A.; GOMBART, ADRIAN F.; REILLY, DEBRA A.; XIE, JINGWEI (2017): Recent advances in electrospun nanofibers for wound healing. In *Nanomedicine (London, England)* 12 (11), pp. 1335–1352. DOI: 10.2217/nnm-2017-0017.
- CHEN, WEIQIANG; VILLA-DIAZ, LUIS G.; SUN, YUBING; WENG, SHINUO; KIM, JIN KOO; LAM, RAYMOND H. W. *et al.* (2012): Nanotopography influences adhesion, spreading, and self-renewal of human embryonic stem cells. In *ACS nano* 6 (5), pp. 4094–4103. DOI: 10.1021/nn3004923.
- COHEN, JACOB (2013): *Statistical Power Analysis for the Behavioral Sciences*. 2nd ed. Hoboken: Taylor and Francis. Available online at <http://gbv.ebib.com/patron/FullRecord.aspx?p=1192162>.
- CORUM, LINDSEY E.; HLADY, VLADIMIR (2012): The effect of upstream platelet-fibrinogen interactions on downstream adhesion and activation. In *Biomaterials* 33 (5), pp. 1255–1260. DOI: 10.1016/j.biomaterials.2011.10.074.
- COSTA, ALESSANDRA; NARANJO, JUAN DIEGO; LONDONO, RICARDO; BADYLAK, STEPHEN F. (2017): Biologic Scaffolds. In *Cold Spring Harb Perspect Med* 7 (9), a025676. DOI: 10.1101/cshperspect.a025676.
- CÔTÉ, MARIE-FRANCE; DOILLON, CHARLES J. (1992): Wettability of cross-linked collagenous biomaterials. In vitro study. In *Biomaterials* 13 (9), pp. 612–616. DOI: 10.1016/0142-9612(92)90029-N.
- CROCINI, CLAUDIA; WALKER, CIERRA J.; ANSETH, KRISTI S.; LEINWAND, LESLIE A. (2019): Three-dimensional encapsulation of adult mouse cardiomyocytes in hydrogels with tunable stiffness. In *Progress in biophysics and molecular biology*. DOI: 10.1016/j.pbiomolbio.2019.04.008.
- CROUCH, ADAM S.; MILLER, D.; LUEBKE, KEVIN J.; HU, W. (2009): Correlation of anisotropic cell behaviors with topographic aspect ratio. In *Biomaterials* 30 (8), pp. 1560–1567. DOI: 10.1016/j.biomaterials.2008.11.041.

- CSADEROVA, LUCIA; MARTINES, ELENA; SEUNARINE, KRISHNA; GADEGAARD, NIKOLAJ; WILKINSON, CHRIS D. W.; RIEHLE, MATHIS O. (2010): A biodegradable and biocompatible regular nanopattern for large-scale selective cell growth. In *Small (Weinheim an der Bergstrasse, Germany)* 6 (23), pp. 2755–2761. DOI: 10.1002/smll.201000193.
- CUKIERMAN, EDNA; PANKOV, ROUMEN; YAMADA, KENNETH M. (2002): Cell interactions with three-dimensional matrices. In *Current opinion in cell biology* 14 (5), pp. 633–640. DOI: 10.1016/S0955-0674(02)00364-2.
- CUMMINGS, CHRISTOPHER L.; GAWLITTA, DEBBY; NEREM, ROBERT M.; STEGEMANN, JAN P. (2004): Properties of engineered vascular constructs made from collagen, fibrin, and collagen-fibrin mixtures. In *Biomaterials* 25 (17), pp. 3699–3706. DOI: 10.1016/j.biomaterials.2003.10.073.
- CURTIS, A.; RIEHLE, M. (2001): Tissue engineering. The biophysical background. In *Physics in medicine and biology* 46 (4), R47-65. DOI: 10.1088/0031-9155/46/4/201.
- CURTIS, ADAM; WILKINSON, CHRIS (2001): Nantotechniques and approaches in biotechnology. In *Trends in biotechnology* 19 (3), pp. 97–101. DOI: 10.1016/S0167-7799(00)01536-5.
- CUSTOMER SERVICE THERMO SCIENTIFIC: Crosslinking Technical Handbook. easy molecular bonding cross linking technology. Reactivity chemistries, applications and structure references. Edited by Thermo Scientific. Available online at <https://tools.thermofisher.com/content/sfs/brochures/1602163-Crosslinking-Reagents-Handbook.pdf>, checked on 04.12.19.
- DAINIAK, MARIA B.; ALLAN, IAIN U.; SAVINA, IRINA N.; CORNELIO, LISA; JAMES, ELIZABETH S.; JAMES, STUART L. *et al.* (2010): Gelatin-fibrinogen cryogel dermal matrices for wound repair. Preparation, optimisation and in vitro study. In *Biomaterials* 31 (1), pp. 67–76. DOI: 10.1016/j.biomaterials.2009.09.029.
- DALBY, M. J.; CHILDS, S.; RIEHLE, M. O.; JOHNSTONE, H.J.H.; AFFROSSMAN, S.; CURTIS, A.S.G. (2003): Fibroblast reaction to island topography. Changes in cytoskeleton and morphology with time. In *Biomaterials* 24 (6), pp. 927–935. DOI: 10.1016/S0142-9612(02)00427-1.
- DALBY, M. J.; RIEHLE, M. O.; JOHNSTONE, H.; AFFROSSMAN, S.; CURTIS, A.S.G. (2002a): In vitro reaction of endothelial cells to polymer demixed nanotopography. In *Biomaterials* 23 (14), pp. 2945–2954. DOI: 10.1016/S0142-9612(01)00424-0.

- DALBY, M. J.; RIEHLE, M. O.; JOHNSTONE, H.J.H.; AFFROSSMAN, S.; CURTIS, A.S.G. (2002b): Polymer-Demixed Nanotopography. Control of Fibroblast Spreading and Proliferation. In *Tissue engineering* 8 (6), pp. 1099–1108. DOI: 10.1089/107632702320934191.
- DALBY, MATTHEW J.; GADEGAARD, NIKOLAJ; OREFFO, RICHARD O. C. (2014): Harnessing nanotopography and integrin-matrix interactions to influence stem cell fate. In *Nature materials* 13 (6), pp. 558–569. DOI: 10.1038/NMAT3980.
- DALBY, MATTHEW J.; GADEGAARD, NIKOLAJ; RIEHLE, MATHIS O.; WILKINSON, CHRIS D. W.; CURTIS, ADAM S. G. (2004): Investigating filopodia sensing using arrays of defined nano-pits down to 35 nm diameter in size. In *The international Journal of Biochemistry & Cell Biology* 36 (10), pp. 2005–2015. DOI: 10.1016/j.biocel.2004.03.001.
- DALBY, MATTHEW J.; MARSHALL, GEORGE E.; JOHNSTONE, HEATHER J. H.; AFFROSSMAN, STANLEY; RIEHLE, MATHIS O. (2002c): Interactions of human blood and tissue cell types with 95-nm-high nanotopography. In *IEEE transactions on nanobioscience* 1 (1), pp. 18–23. DOI: 10.1109/tnb.2002.806933.
- DALBY, MATTHEW J.; YARWOOD, STEPHEN J.; RIEHLE, MATHIS O.; JOHNSTONE, HEATHER J. H.; AFFROSSMAN, STANLEY; CURTIS, ADAM S. G. (2002d): Increasing fibroblast response to materials using nanotopography. Morphological and genetic measurements of cell response to 13-nm-high polymer demixed islands. In *Experimental cell research* 276 (1), pp. 1–9. DOI: 10.1006/excr.2002.5498.
- DARBY, IAN A.; LAVERDET, BETTY; BONTÉ, FRÉDÉRIC; DESMOULIÈRE, ALEXIS (2014): Fibroblasts and myofibroblasts in wound healing. In *Clinical, cosmetic and investigational dermatology* 7, pp. 301–311. DOI: 10.2147/CCID.S50046.
- DAVIS, A. SALLY; RICHTER, ANKE; BECKER, STEVEN; MOYER, JENNA E.; SANDOUK, ALINE; SKINNER, JEFF; TAUBENBERGER, JEFFERY K. (2014): Characterizing and Diminishing Autofluorescence in Formalin-fixed Paraffin-embedded Human Respiratory Tissue. In *J Histochem Cytochem.* 62 (6), pp. 405–423. DOI: 10.1369/0022155414531549.
- DAVISON, NOEL L.; BARRÈRE-DE GROOT, FLORENCE; GRIJPMA, DIRK W. (2015): Degradation of Biomaterials. In Clemens A. van Blitterswijk, Jan de Boer (Eds.): *Tissue engineering. Second edition.* Amsterdam, Boston, Heidelberg: Elsevier Academic Press, pp. 177–215.
- DECKER, THOMAS; LOHMANN-MATTHES, MARIE-LUISE (1988): A quick and simple method for the quantitation of lactate dehydrogenase release in measurements of cellular

- cytotoxicity and tumor necrosis factor (TNF) activity. In *Journal of Immunological Methods* 115 (1), pp. 61–69. DOI: 10.1016/0022-1759(88)90310-9.
- DENT, ERIK W.; GERTLER, FRANK B. (2003): Cytoskeletal Dynamics and Transport in Growth Cone Motility and Axon Guidance. In *Neuron* 40 (2), pp. 209–227. DOI: 10.1016/S0896-6273(03)00633-0.
- DESAI, RAVI A.; KHAN, MOHAMMED K.; GOPAL, SMITHA B.; CHEN, CHRISTOPHER S. (2011): Subcellular spatial segregation of integrin subtypes by patterned multicomponent surfaces. In *Integrative biology : quantitative biosciences from nano to macro* 3 (5), pp. 560–567. DOI: 10.1039/c0ib00129e.
- DESJARDINS-PARK, HEATHER E.; FOSTER, DESHKA S.; LONGAKER, MICHAEL T. (2018): Fibroblasts and wound healing. An update. In *Regenerative medicine* 13 (5), pp. 491–495. DOI: 10.2217/rme-2018-0073.
- DESMARAIS, VERA; EDDY, ROBERT J.; SHARMA, VED P.; STONE, ORRIN; CONDEELIS, JOHN S. (2019): Optimizing leading edge F-actin labeling using multiple actin probes, fixation methods and imaging modalities. In *BioTechniques* 66 (3), pp. 113–119. DOI: 10.2144/btn-2018-0112.
- DIKOVSKY, DANIEL; BIANCO-PELED, HAVAZELET; SELIKTAR, DROR (2006): The effect of structural alterations of PEG-fibrinogen hydrogel scaffolds on 3-D cellular morphology and cellular migration. In *Biomaterials* 27 (8), pp. 1496–1506. DOI: 10.1016/j.biomaterials.2005.09.038.
- DISCHER, DENNIS E.; MOONEY, DAVID J.; ZANDSTRA, PETER W. (2009): Growth factors, matrices, and forces combine and control stem cells. In *Science (New York, N.Y.)* 324 (5935), pp. 1673–1677. DOI: 10.1126/science.1171643.
- DISTLER, JÖRG H. W.; JÜNGEL, ASTRID; HUBER, LARS C.; SEEMAYER, CHRISTIAN A.; REICH, CHARLES F.; GAY, RENATE E. *et al.* (2005): The induction of matrix metalloproteinase and cytokine expression in synovial fibroblasts stimulated with immune cell microparticles. In *Proceedings of the National Academy of Sciences of the United States of America* 102 (8), pp. 2892–2897. DOI: 10.1073/pnas.0409781102.
- DOOLITTLE, R. F. (1984): Fibrinogen and fibrin. In *Annual review of biochemistry* 53, pp. 195–229. DOI: 10.1146/annurev.bi.53.070184.001211.

- DOWNING, TIMOTHY L.; SOTO, JENNIFER; MOREZ, CONSTANT; HOUSSIN, TIMOTHEE; FRITZ, ASHLEY; YUAN, FALEI *et al.* (2013): Biophysical regulation of epigenetic state and cell reprogramming. In *Nature Mater* 12 (12), pp. 1154–1162. DOI: 10.1038/nmat3777.
- DU, C.; CUI, F. Z.; ZHU, X. D.; GROOT, K. DE (1999): Three-dimensional nano-HAp/collagen matrix loading with osteogenic cells in organ culture. In *Journal of biomedical materials research* 44 (4), pp. 407–415. DOI: 10.1002/(SICI)1097-4636(19990315)44:4<407::AID-JBM6>3.0.CO;2-T.
- DUBROVIN, EVGENIY V.; BARINOV, NIKOLAY A.; SCHÄFFER, TILMAN E.; KLINOV, DMITRY V. (2019): In Situ Single-Molecule AFM Investigation of Surface-Induced Fibrinogen Unfolding on Graphite. In *Langmuir : the ACS journal of surfaces and colloids* 35 (30), pp. 9732–9739. DOI: 10.1021/acs.langmuir.9b01178.
- EHRlich, H. P.; HEMBRY, R. M. (1984): A comparative study of fibroblasts in healing freeze and burn injuries in rats. In *The American journal of pathology* 117 (2), pp. 218–224.
- ELIASON, MARCUS T.; CHAREST, JOSEPH L.; SIMMONS, BLAKE A.; GARCÍA, ANDRÉS J.; KING, WILLIAM P. (2007): Nanoimprint fabrication of polymer cell substrates with combined microscale and nanoscale topography. In *J. Vac. Sci. Technol. B* 25 (4), L31. DOI: 10.1116/1.2748792.
- ELLIOTT, JOHN T.; WOODWARD, JOHN T.; UMARJI, ANITA; MEI, YING; TONA, ALESSANDRO (2007): The effect of surface chemistry on the formation of thin films of native fibrillar collagen. In *Biomaterials* 28 (4), pp. 576–585. DOI: 10.1016/j.biomaterials.2006.09.023.
- ELSDALE, T.; BARD, J. (1972): Collagen substrata for studies on cell behavior. In *The Journal of cell biology* 54 (3), pp. 626–637.
- ENGLADE-FRANKLIN, LAUREN E.; SANER, CHAMARRA K.; GARNO, JAYNE C. (2013): Spatially selective surface platforms for binding fibrinogen prepared by particle lithography with organosilanes. In *Interface focus* 3 (3), p. 20120102. DOI: 10.1098/rsfs.2012.0102.
- ERLER, JANINE T.; WEAVER, VALERIE M. (2009): Three-dimensional context regulation of metastasis. In *Clinical & experimental metastasis* 26 (1), pp. 35–49. DOI: 10.1007/s10585-008-9209-8.
- ERMIS, M., ANTMEN, E., & HASIRCI, V. (2018): Micro and Nanofabrication methods to control cell-substrate interactions and cell behavior: A review from the tissue

- engineering perspective. In *Bioactive materials* (3 (3)), pp. 355–369. Available online at <https://www.sciencedirect.com/science/article/pii/S2452199X1730155X>.
- FANG, MING; GOLDSTEIN, ELIZABETH L.; MATICH, ERYN K.; ORR, BRADFORD G.; HOLL, MARK M. BANASZAK (2013): Type I collagen self-assembly: the roles of substrate and concentration. In *Langmuir : the ACS journal of surfaces and colloids* 29 (7), pp. 2330–2338. DOI: 10.1021/la3048104.
- FEINBERG, ADAM W.; PARKER, KEVIN KIT (2010): Surface-initiated assembly of protein nanofabrics. In *Nano letters* 10 (6), pp. 2184–2191. DOI: 10.1021/nl100998p.
- FENSKY, FLORIAN; REICHERT, JOHANNES C.; TRAUBE, ANDREA; RACKWITZ, LARS; SIEBENLIST, SEBASTIAN; NÖTH, ULRICH (2014): Chondrogenic predifferentiation of human mesenchymal stem cells in collagen type I hydrogels. In *Biomedical Engineering / Biomedizinische Technik* 59 (5). DOI: 10.1515/bmt-2013-0076.
- FERNÁNDEZ, ARIEL; SINANOĞLU, OKTAY (1985): Denaturation of proteins in methanol/water mixtures. In *Biophysical Chemistry* 21 (3-4), pp. 163–166. DOI: 10.1016/0301-4622(85)80002-8.
- FILIPPONI, LUISA; LIVINGSTON, PETER; KAŠPAR, ONDŘEJ; TOKÁROVÁ, VIOLA; NICOLAU, DAN V. (2016): Protein patterning by microcontact printing using pyramidal PDMS stamps. In *Biomedical microdevices* 18. DOI: 10.1007/s10544-016-0036-4.
- FISHMAN, JONATHAN M.; WILES, KATHERINE; WOOD, KATHRYN J. (2015): The Acquired Immune System Response to Biomaterials, Including Both Naturally Occurring and Synthetic Biomaterials. In Stephen F. Badylak (Ed.): Host response to biomaterials. The impact of host response on biomaterial selection. Amsterdam: Academic Press, pp. 151–187.
- FOUCHARD, JONATHAN; BIMBARD, CÉLIAN; BUFI, NATHALIE; DURAND-SMET, PAULINE; PROAG, AMSHA; RICHERT, ALAIN *et al.* (2014): Three-dimensional cell body shape dictates the onset of traction force generation and growth of focal adhesions. In *Proceedings of the National Academy of Sciences of the United States of America* 111 (36), pp. 13075–13080. DOI: 10.1073/pnas.1411785111.
- FRANCIS, MICHAEL P.; MOGHADDAM-WHITE, YAS M.; SACHS, PATRICK C.; BECKMAN, MATTHEW J.; CHEN, STEPHEN M.; BOWLIN, GARY L. *et al.* (2016): Modeling early stage bone regeneration with biomimetic electrospun fibrinogen nanofibers and adipose-derived mesenchymal stem cells. In *Electrospinning* 1 (1), p. 1. DOI: 10.1515/esp-2016-0002.

- FRANCK, CHRISTIAN; MASKARINEC, STACEY A.; TIRRELL, DAVID A.; RAVICHANDRAN, GURUSWAMI (2011): Three-dimensional traction force microscopy. A new tool for quantifying cell-matrix interactions. In *PloS one* 6 (3), e17833. DOI: 10.1371/journal.pone.0017833.
- FRANCO-BARRAZA, JANUSZ; BEACHAM, DOROTHY A.; AMATANGELO, MICHAEL D.; CUKIERMAN, EDNA (2016): Preparation of Extracellular Matrices Produced by Cultured and Primary Fibroblasts. In *Current protocols in cell biology* 71, 10.9.1-10.9.34. DOI: 10.1002/cpcb.2.
- FRANTZ, CHRISTIAN; STEWART, KATHLEEN M.; WEAVER, VALERIE M. (2010): The extracellular matrix at a glance. In *Journal of cell science* 123 (Pt 24), pp. 4195–4200. DOI: 10.1242/jcs.023820.
- FRASER, SARAH A.; TING, YUK-HONG; MALLON, KELLY S.; WENDT, AMY E.; MURPHY, CHRISTOPHER J.; NEALEY, PAUL F. (2008): Sub-micron and nanoscale feature depth modulates alignment of stromal fibroblasts and corneal epithelial cells in serum-rich and serum-free media. In *Journal of biomedical materials research. Part A* 86 (3), pp. 725–735. DOI: 10.1002/jbm.a.31519.
- FRATZL, PETER; MISOF, KLAUS AND ZIZAK, IVO (1998): Fibrillar Structure and Mechanical Properties of Collagen. In *Journal of structural biology* 122 (1-2), pp. 119–122. DOI: 10.1006/jsbi.1998.3966.
- FREY, MARGO T.; TSAI, IRENE Y.; RUSSELL, THOMAS P.; HANKS, STEVEN K.; WANG, YU-LI (2006): Cellular responses to substrate topography. Role of myosin II and focal adhesion kinase. In *Biophysical journal* 90 (10), pp. 3774–3782. DOI: 10.1529/biophysj.105.074526.
- GALBRAITH, CATHERINE G.; YAMADA, KENNETH M.; GALBRAITH, JAMES A. (2007): Polymerizing actin fibers position integrins primed to probe for adhesion sites. In *Science (New York, N.Y.)* 315 (5814), pp. 992–995. DOI: 10.1126/science.1137904.
- GALEOTTI, F.; PISCO, M.; CUSANO, A. (2018): Self-assembly on optical fibers. A powerful nanofabrication tool for next generation “lab-on-fiber” optrodes. In *Nanoscale* 10 (48), pp. 22673–22700. DOI: 10.1039/C8NR06002A.
- GEIGER, BENJAMIN; SPATZ, JOACHIM P.; BERSHADSKY, ALEXANDER D. (2009): Environmental sensing through focal adhesions. In *Nature reviews. Molecular cell biology* 10 (1), pp. 21–33. DOI: 10.1038/nrm2593.

- GERECHT, SHARON; BETTINGER, CHRISTOPHER J.; ZHANG, ZHITONG; BORENSTEIN, JEFFREY T.; VUNJAK-NOVAKOVIC, GORDANA; LANGER, ROBERT (2007): The effect of actin disrupting agents on contact guidance of human embryonic stem cells. In *Biomaterials* 28 (28), pp. 4068–4077. DOI: 10.1016/j.biomaterials.2007.05.027.
- GHALIA, MUSTAFA ABU; DAHMAN, YASER (2016): Advanced nanobiomaterials in tissue engineering. In Alexandru Mihai Grumezescu (Ed.): *Nanobiomaterials in soft tissue engineering. Applications of nanobiomaterials*. Kidlington, Oxford, UK: William Andrew is an imprint of Elsevier (Applications of nanobiomaterials, volume 5), pp. 141–172.
- GHEZZI, CHIARA E.; MUJA, NASER; MARELLI, BENEDETTO; NAZHAT, SHOWAN N. (2011): Real time responses of fibroblasts to plastically compressed fibrillar collagen hydrogels. In *Biomaterials* 32 (21), pp. 4761–4772. DOI: 10.1016/j.biomaterials.2011.03.043.
- GHOSH, KAUSTABH; PAN, ZHI; GUAN, E.; GE, SHOUREN; LIU, YAJIE; NAKAMURA, TOSHIO *et al.* (2007): Cell adaptation to a physiologically relevant ECM mimic with different viscoelastic properties. In *Biomaterials* 28 (4), pp. 671–679. DOI: 10.1016/j.biomaterials.2006.09.038.
- GIANNONE, GRÉGORY; DUBIN-THALER, BENJAMIN J.; DÖBEREINER, HANS-GÜNTHER; KIEFFER, NELLY; BRESNICK, ANNE R.; SHEETZ, MICHAEL P. (2004): Periodic Lamellipodial Contractions Correlate with Rearward Actin Waves. In *Cell* 116 (3), pp. 431–443. DOI: 10.1016/S0092-8674(04)00058-3.
- GILBERT, P. M.; HAVENSTRITE, K. L.; MAGNUSSON, K. E. G.; SACCO, A.; LEONARDI, N. A.; KRAFT, P. *et al.* (2010): Substrate elasticity regulates skeletal muscle stem cell self-renewal in culture. In *Science (New York, N.Y.)* 329 (5995), pp. 1078–1081. DOI: 10.1126/science.1191035.
- GOBEAUX, F.; MOSSER, G.; ANGLO, A.; PANINE, P.; DAVIDSON, P.; GIRAUD-GUILLE, M-M; BELAMIE, E. (2008): Fibrillogenesis in dense collagen solutions: a physicochemical study. In *Journal of molecular biology* 376 (5), pp. 1509–1522. DOI: 10.1016/j.jmb.2007.12.047.
- GÖKALTUN, ASLIHAN; KANG, YOUNG BOK ABRAHAM; YARMUSH, MARTIN L.; USTA, O. BERK; ASATEKIN, AYSE (2019): Simple Surface Modification of Poly(dimethylsiloxane) via Surface Segregating Smart Polymers for Biomicrofluidics. In *Scientific reports* 9 (1), p. 7377. DOI: 10.1038/s41598-019-43625-5.
- GOLD, T. B.; SMITH, S. L.; DIGENIS, G. A. (1996): Studies on the influence of pH and pancreatin on ¹³C-formaldehyde-induced gelatin cross-links using nuclear magnetic

- resonance. In *Pharmaceutical development and technology* 1 (1), pp. 21–26. DOI: 10.3109/10837459609031414.
- GOUGH, JULIE E.; SCOTCHFORD, COLIN A.; DOWNES, SANDRA (2002): Cytotoxicity of glutaraldehyde crosslinked collagen/poly(vinyl alcohol) films is by the mechanism of apoptosis. In *Journal of biomedical materials research* 61 (1), pp. 121–130. DOI: 10.1002/jbm.10145.
- GREENSPAN, DANIEL S. (2005): Biosynthetic Processing of Collagen Molecules. In Jürgen Brinckmann, Hans Peter Bächinger (Eds.): *Collagen. Primer in structure, processing and assembly*, vol. 247. Berlin Heidelberg: Springer (Topics in Current Chemistry, 247), pp. 149–183.
- GRINNELL, FREDERICK; HO, CHIN-HAN; TAMARIZ, ELISA; LEE, DAVID J.; SKUTA, GABRIELLA (2003): Dendritic fibroblasts in three-dimensional collagen matrices. In *Molecular biology of the cell* 14 (2), pp. 384–395. DOI: 10.1091/mbc.e02-08-0493.
- GRUSCHWITZ, RITA; FRIEDRICHS, JENS; VALTINK, MONIKA; FRANZ, CLEMENS M.; MÜLLER, DANIEL J.; FUNK, RICHARD H. W.; ENGELMANN, KATRIN (2010): Alignment and cell-matrix interactions of human corneal endothelial cells on nanostructured collagen type I matrices. In *Investigative ophthalmology & visual science* 51 (12), pp. 6303–6310. DOI: 10.1167/iovs.10-5368.
- GUGUTKOV, D.; GUSTAVSSON, J.; CANTINI, M.; SALMERON-SÁNCHEZ, M.; ALTANKOV, G. (2017): Electrospun fibrinogen-PLA nanofibres for vascular tissue engineering. In *Journal of tissue engineering and regenerative medicine* 11 (10), pp. 2774–2784. DOI: 10.1002/term.2172.
- GUGUTKOV, DENCHO; GUSTAVSSON, JOHAN; GINEBRA, MARIA PAU; ALTANKOV, GEORGE (2013): Fibrinogen nanofibers for guiding endothelial cell behavior. In *Biomater. Sci.* 1 (10), pp. 1065–1073. DOI: 10.1039/C3BM60124B.
- GUPTON, S. L.; GERTLER, F. B. (2007): Filopodia. The Fingers That Do the Walking. In *Science's STKE* 2007 (400), re5-re5. DOI: 10.1126/stke.4002007re5.
- GUZ, NATALIIA; DOKUKIN, MAXIM; KALAPARTHI, VIVEKANAND; SOKOLOV, IGOR (2014): If cell mechanics can be described by elastic modulus. Study of different models and probes used in indentation experiments. In *Biophysical journal* 107 (3), pp. 564–575. DOI: 10.1016/j.bpj.2014.06.033.

- HAIDER, ADNAN; HAIDER, SAJJAD; KANG, INN-KYU (2015): A comprehensive review summarizing the effect of electrospinning parameters and potential applications of nanofibers in biomedical and biotechnology. In *Arabian Journal of Chemistry* 11 (8), pp. 1165–1188. DOI: 10.1016/j.arabjc.2015.11.015.
- HAIDER, SAJJAD; AL-ZEGHAYER, YOUSEF; AHMED ALI, FEKRI A.; HAIDER, ADNAN; MAHMOOD, ASIF; AL-MASRY, WAHEED A. *et al.* (2013): Highly aligned narrow diameter chitosan electrospun nanofibers. In *J Polym Res* 20 (4). DOI: 10.1007/s10965-013-0105-9.
- HAKKINEN, KIRSI M.; HARUNAGA, JILL S.; DOYLE, ANDREW D.; YAMADA, KENNETH M. (2011): Direct comparisons of the morphology, migration, cell adhesions, and actin cytoskeleton of fibroblasts in four different three-dimensional extracellular matrices. In *Tissue engineering. Part A* 17 (5-6), pp. 713–724. DOI: 10.1089/ten.TEA.2010.0273.
- HALLMANN, RUPERT; ZHANG, XUELI; DI RUSSO, JACOPO; LI, LIXIA; SONG, JIAN; HANNOCKS, MELANIE-JANE; SOROKIN, LYDIA (2015): The regulation of immune cell trafficking by the extracellular matrix. In *Current opinion in cell biology* 36, pp. 54–61. DOI: 10.1016/j.ceb.2015.06.006.
- HALPER, JAROSLAVA; KJAER, MICHAEL (2014): Basic components of connective tissues and extracellular matrix. Elastin, fibrillin, fibulins, fibrinogen, fibronectin, laminin, tenascins and thrombospondins. In *Advances in experimental medicine and biology* 802, pp. 31–47. DOI: 10.1007/978-94-007-7893-1_3.
- HÄMISCH, BENJAMIN; BÜNGELER, ANNE; KIELAR, CHARLOTTE; KELLER, ADRIAN; STRUBE, OLIVER; HUBER, KLAUS (2019): Self-Assembly of Fibrinogen in Aqueous, Thrombin-Free Solutions of Variable Ionic Strengths. In *Langmuir : the ACS journal of surfaces and colloids* 35 (37), pp. 12113–12122. DOI: 10.1021/acs.langmuir.9b01515.
- HARLEY, BRENDAN A. C.; KIM, HYUNG-DO; ZAMAN, MUHAMMAD H.; YANNAS, IOANNIS V.; LAUFFENBURGER, DOUGLAS A.; GIBSON, LORNA J. (2008): Microarchitecture of three-dimensional scaffolds influences cell migration behavior via junction interactions. In *Biophysical journal* 95 (8), pp. 4013–4024. DOI: 10.1529/biophysj.107.122598.
- HARRIS, J. ROBIN; REIBER, ANDREAS (2007): Influence of saline and pH on collagen type I fibrillogenesis in vitro: fibril polymorphism and colloidal gold labelling. In *Micron (Oxford, England : 1993)* 38 (5), pp. 513–521. DOI: 10.1016/j.micron.2006.07.026.
- HARRIS, J. ROBIN; SOLIAKOV, ANDREI; LEWIS, RICHARD J. (2013): In vitro fibrillogenesis of collagen type I in varying ionic and pH conditions. In *Micron (Oxford, England : 1993)* 49, pp. 60–68. DOI: 10.1016/j.micron.2013.03.004.

- HE, JING; SU, YAO; HUANG, TAO; JIANG, BO; WU, FANG; GU, ZHONGWEI (2014): Effects of material and surface functional group on collagen self-assembly and subsequent cell adhesion behaviors. In *Colloids and surfaces. B, Biointerfaces* 116, pp. 303–308. DOI: 10.1016/j.colsurfb.2014.01.009.
- HEINO, JYRKI (2007): The collagen family members as cell adhesion proteins. In *BioEssays : news and reviews in molecular, cellular and developmental biology* 29 (10), pp. 1001–1010. DOI: 10.1002/bies.20636.
- HELARY, CHRISTOPHE; BATAILLE, ISABELLE; ABED, AICHA; ILLOUL, CORINNE; ANGLO, ANNIE; LOUEDEC, LILIANE *et al.* (2010): Concentrated collagen hydrogels as dermal substitutes. In *Biomaterials* 31 (3), pp. 481–490. DOI: 10.1016/j.biomaterials.2009.09.073.
- HELBING, CHRISTIAN; STOEßEL, ROBERT; HERING, DOMINIK A.; ARRAS, MATTHIAS M. L.; BOSSERT, JÖRG; JANDT, KLAUS D. (2016): pH-Dependent Ordered Fibrinogen Adsorption on Polyethylene Single Crystals. In *Langmuir : the ACS journal of surfaces and colloids* 32 (45), pp. 11868–11877. DOI: 10.1021/acs.langmuir.6b03110.
- HEMLER, MARTIN E.; LOBB, ROY R. (1995): The leukocyte $\beta 1$ integrins. In *Current Opinion in Hematology* 2 (1), pp. 61–67. DOI: 10.1097/00062752-199502010-00009.
- HERMANSON, GREG T. (2013): Heterobifunctional Crosslinkers. In : *Bioconjugate Techniques*: Elsevier, pp. 299–339.
- HOBRO, ALISON J.; SMITH, NICHOLAS I. (2017): An evaluation of fixation methods. Spatial and compositional cellular changes observed by Raman imaging. In *Vibrational Spectroscopy* 91, pp. 31–45. DOI: 10.1016/j.vibspec.2016.10.012.
- HOGREBE, NATHANIEL J.; GOOCH, KEITH J. (2016): Direct influence of culture dimensionality on human mesenchymal stem cell differentiation at various matrix stiffnesses using a fibrous self-assembling peptide hydrogel. In *Journal of biomedical materials research. Part A* 104 (9), pp. 2356–2368. DOI: 10.1002/jbm.a.35755.
- HU, W.; YIM, E. K. F.; REANO, R. M.; LEONG, K. W.; PANG, S. W. (2005): Effects of nanoimprinted patterns in tissue-culture polystyrene on cell behavior. In *Journal of vacuum science & technology. A, Vacuum, surfaces, and films : an official journal of the American Vacuum Society* 23 (6), pp. 2984–2989. DOI: 10.1116/1.2121729.
- HUANG, L.; APKARIAN, R. P.; CHAIKOF, E. L. (2001a): High-resolution analysis of engineered type I collagen nanofibers by electron microscopy. In *Scanning* 23 (6), pp. 372–375. DOI: 10.1002/sca.4950230603.

- HUANG, L.; NAGAPUDI, K.; APKARIAN, R. P.; CHAIKOF, E. L. (2001b): Engineered collagen-PEO nanofibers and fabrics. In *Journal of biomaterials science. Polymer edition* 12 (9), pp. 979–993. DOI: 10.1163/156856201753252516.
- HUANG, LIHONG; HU, JUN; LE LANG; WANG, XIN; ZHANG, PEIBIAO; JING, XIABIN *et al.* (2007): Synthesis and characterization of electroactive and biodegradable ABA block copolymer of polylactide and aniline pentamer. In *Biomaterials* 28 (10), pp. 1741–1751. DOI: 10.1016/j.biomaterials.2006.12.007.
- HUANG, NGAN F.; LAI, EDWINA S.; RIBEIRO, ALEXANDRE J. S.; PAN, STEPHEN; PRUITT, BETH L.; FULLER, GERALD G.; COOKE, JOHN P. (2013): Spatial patterning of endothelium modulates cell morphology, adhesiveness and transcriptional signature. In *Biomaterials* 34 (12), pp. 2928–2937. DOI: 10.1016/j.biomaterials.2013.01.017.
- HUANG, ZHENG-MING; ZHANG, Y.-Z.; KOTAKI, M.; RAMAKRISHNA, S. (2003): A review on polymer nanofibers by electrospinning and their applications in nanocomposites. In *Composites Science and Technology* 63 (15), pp. 2223–2253. DOI: 10.1016/S0266-3538(03)00178-7.
- HUEBSCH, NATHANIEL; ARANY, PRAVEEN R.; MAO, ANGELO S.; SHVARTSMAN, DMITRY; ALI, OMAR A.; BENCHERIF, SIDI A. *et al.* (2010): Harnessing traction-mediated manipulation of the cell/matrix interface to control stem-cell fate. In *Nature materials* 9 (6), pp. 518–526. DOI: 10.1038/NMAT2732.
- HUMPHRIES, JONATHAN D.; BYRON, ADAM; HUMPHRIES, MARTIN J. (2006): Integrin ligands at a glance. In *Journal of cell science* 119 (Pt 19), pp. 3901–3903. DOI: 10.1242/jcs.03098.
- HUTTER, JEFFREY L.; BECHHOEFER, JOHN (1993): Calibration of atomic-force microscope tips. In *Review of Scientific Instruments* 64 (7), pp. 1868–1873. DOI: 10.1063/1.1143970.
- HUXLEY-JONES, JULIE; ROBERTSON, DAVID L.; BOOT-HANDFORD, RAYMOND P. (2007): On the origins of the extracellular matrix in vertebrates. In *Matrix biology : journal of the International Society for Matrix Biology* 26 (1), pp. 2–11. DOI: 10.1016/j.matbio.2006.09.008.
- HYNES, RICHARD O. (2002): Integrins. Bidirectional, Allosteric Signaling Machines. In *Cell* 110 (6), pp. 673–687. DOI: 10.1016/S0092-8674(02)00971-6.

- HYNES, RICHARD O. (2009): The extracellular matrix. Not just pretty fibrils. In *Science (New York, N.Y.)* 326 (5957), pp. 1216–1219. DOI: 10.1126/science.1176009.
- HYNES, RICHARD O.; NABA, ALEXANDRA (2012): Overview of the matrisome—an inventory of extracellular matrix constituents and functions. In *Cold Spring Harbor perspectives in biology* 4 (1), a004903. DOI: 10.1101/cshperspect.a004903.
- IAFISCOL, MICHELE; QUIRICI, NADIA; FOLTRAN, ISMAELA; RIMONDINI, LIA (2013): Electrospun collagen mimicking the reconstituted extracellular matrix improves osteoblastic differentiation onto titanium surfaces. In *J. Nanosci. Nanotech.* 13 (7), pp. 4720–4726. DOI: 10.1166/jnn.2013.7195.
- IKADA, YOSHITO (2006): Challenges in tissue engineering. In *J. R. Soc. Interface* 3 (10), pp. 589–601. DOI: 10.1098/rsif.2006.0124.
- IOZZO, RENATO V.; SANDERSON, RALPH D. (2011): Proteoglycans in cancer biology, tumour microenvironment and angiogenesis. In *Journal of cellular and molecular medicine* 15 (5), pp. 1013–1031. DOI: 10.1111/j.1582-4934.2010.01236.x.
- IOZZO, RENATO V.; SCHAEFER, LILIANA (2015): Proteoglycan form and function. A comprehensive nomenclature of proteoglycans. In *Matrix biology : journal of the International Society for Matrix Biology* 42, pp. 11–55. DOI: 10.1016/j.matbio.2015.02.003.
- JABŁOŃSKA-TRYPUĆ, AGATA; MATEJCZYK, MARZENA; ROSOCHACKI, STANISŁAW (2016): Matrix metalloproteinases (MMPs), the main extracellular matrix (ECM) enzymes in collagen degradation, as a target for anticancer drugs. In *Journal of enzyme inhibition and medicinal chemistry* 31 (sup1), pp. 177–183. DOI: 10.3109/14756366.2016.1161620.
- JACOBS, CHRISTOPHER R.; HUANG, HAYDEN; KWON, RONALD Y. (2013): Introduction to cell mechanics and mechanobiology. New York, NY: Garland.
- JACQUEMET, GUILLAUME; HAMIDI, HELLYEH; IVASKA, JOHANNA (2015): Filopodia in cell adhesion, 3D migration and cancer cell invasion. In *Current opinion in cell biology* 36, pp. 23–31. DOI: 10.1016/j.ceb.2015.06.007.
- JÄRVELÄINEN, HANNU; SAINIO, ANNELE; KOULU, MARKKU; WIGHT, THOMAS N.; PENTTINEN, RISTO (2009): Extracellular matrix molecules. Potential targets in pharmacotherapy. In *Pharmacological reviews* 61 (2), pp. 198–223. DOI: 10.1124/pr.109.001289.

- JENSEN, KRISTIAN H. R.; BERG, RUNE W. (2016): CLARITY-compatible lipophilic dyes for electrode marking and neuronal tracing. In *Scientific reports* 6, p. 32674. DOI: 10.1038/srep32674.
- JIANG, HONGMEI; GRINNELL, FREDERICK (2005): Cell-matrix entanglement and mechanical anchorage of fibroblasts in three-dimensional collagen matrices. In *Molecular biology of the cell* 16 (11), pp. 5070–5076. DOI: 10.1091/mbc.E05-01-0007.
- JIANG, YING; WANG, HAIBO; DENG, MINGXIA; WANG, ZHONGWEN; ZHANG, JUNTAO; WANG, HAIYIN; ZHANG, HANJUN (2016): Effect of ultrasonication on the fibril-formation and gel properties of collagen from grass carp skin. In *Materials science & engineering. C, Materials for biological applications* 59, pp. 1038–1046. DOI: 10.1016/j.msec.2015.11.007.
- JOHANES, IECUN; MIHELIC, ELAINE; SIVASANKAR, MAHALAKSHMI; IVANISEVIC, ALBENA (2011): Morphological Properties of Collagen Fibers in Porcine Lamina Propria. In *Journal of Voice* 25 (2), pp. 254–257. DOI: 10.1016/j.jvoice.2009.09.006.
- JOO, JAE YEON; AMIN, MD. LUTFUL; RAJANGAM, THANAVEL; AN, SEONG SOO A. (2015): Fibrinogen as a promising material for various biomedical applications. In *Molecular & Cellular Toxicology* 11 (1), pp. 1–9. DOI: 10.1007/s13273-015-0001-y.
- JULIANO, R. L.; HASKILL, S. (1993): Signal transduction from the extracellular matrix. In *The Journal of cell biology* 120 (3), pp. 577–585. DOI: 10.1083/jcb.120.3.577.
- KADLER, K. E.; HOLMES, D. F.; TROTTER, J. A.; CHAPMAN, J. A. (1996): Collagen fibril formation. In *Biochemical Journal* 316 (Pt 1), pp. 1–11.
- KADLER, KARL E.; BALDOCK, CLAIR; BELLA, JORDI; BOOT-HANDFORD, RAYMOND P. (2007): Collagens at a glance. In *Journal of cell science* 120 (Pt 12), pp. 1955–1958. DOI: 10.1242/jcs.03453.
- KAI, FUIBOON; LAKLAI, HANANE; WEAVER, VALERIE M. (2016): Force Matters. Biomechanical Regulation of Cell Invasion and Migration in Disease. In *Trends in Cell Biology* 26 (7), pp. 486–497. DOI: 10.1016/j.tcb.2016.03.007.
- KALSON, NICHOLAS S.; STARBORG, TOBIAS; LU, YINHUI; MIRONOV, ALEKSANDR; HUMPHRIES, SALLY M.; HOLMES, DAVID F.; KADLER, KARL E. (2013): Nonmuscle myosin II powered transport of newly formed collagen fibrils at the plasma membrane. In *Proceedings of the National Academy of Sciences of the United States of America* 110 (49), E4743-52. DOI: 10.1073/pnas.1314348110.

- KHADEMHOSEINI, ALI; LANGER, ROBERT (2016): A decade of progress in tissue engineering. In *Nat Protoc* 11 (10), pp. 1775–1781. DOI: 10.1038/nprot.2016.123.
- KIANG, JENNIFER D.; WEN, JESSICA H.; DEL ÁLAMO, JUAN C.; ENGLER, ADAM J. (2013): Dynamic and reversible surface topography influences cell morphology. In *Journal of biomedical materials research. Part A* 101 (8), pp. 2313–2321. DOI: 10.1002/jbm.a.34543.
- KIERNAN, JOHN A. (2000): Formaldehyde, Formalin, Paraformaldehyde And Glutaraldehyde. What They Are And What They Do. In *Microsc. Today* 8 (1), pp. 8–13. DOI: 10.1017/S1551929500057060.
- KIERSZENBAUM, ABRAHAM L.; TRES, LAURA L. (2012): Histology and cell biology. An introduction to pathology. 3. ed. Philadelphia, PA: Elsevier Saunders.
- KIM, DEOK-HO; PROVENZANO, PAOLO P.; SMITH, CHRIS L.; LEVCHENKO, ANDRE (2012): Matrix nanotopography as a regulator of cell function. In *The Journal of cell biology* 197 (3), pp. 351–360. DOI: 10.1083/jcb.201108062.
- KIM, DEOK-HO; SEO, CHANG-HO; HAN, KARAM; KWON, KEON WOO; LEVCHENKO, ANDRE; SUH, KAHP-YANG (2009): Guided Cell Migration on Microtextured Substrates with Variable Local Density and Anisotropy. In *Adv. Funct. Mater.* 19 (10), pp. 1579–1586. DOI: 10.1002/adfm.200801174.
- KIM, H.-S.; LEE, D.-Y.; PARK, J.-H.; KIM, J.-H.; HWANG, J.-H.; JUNG, H.-I. (2007): Optimization Of Electrohydrodynamic Writing Technique To Print Collagen. In *Exp Techniques* 31 (4), pp. 15–19. DOI: 10.1111/j.1747-1567.2007.00154.x.
- KIM, JEONGYONG; SONG, HUGEUN; PARK, INHO; CARLISLE, CHRISTINE R.; BONIN, KEITH; GUTHOLD, MARTIN (2011a): Denaturing of single electrospun fibrinogen fibers studied by deep ultraviolet fluorescence microscopy. In *Microscopy research and technique* 74 (3), pp. 219–224. DOI: 10.1002/jemt.20896.
- KIM, SOO-HYUN; TURNBULL, JEREMY; GUIMOND, SCOTT (2011b): Extracellular matrix and cell signalling. The dynamic cooperation of integrin, proteoglycan and growth factor receptor. In *Journal of Endocrinology* 209 (2), pp. 139–151. DOI: 10.1530/JOE-10-0377.
- KOO, JASEUNG; GALANAKIS, DENNIS; LIU, YING; RAMEK, ALEXANDER; FIELDS, ADAM; BA, XIAOLAN *et al.* (2012): Control of anti-thrombogenic properties: surface-induced self-

- assembly of fibrinogen fibers. In *Biomacromolecules* 13 (5), pp. 1259–1268. DOI: 10.1021/bm2015976.
- KORZENIEWSKI, CAROL; CALLEWAERT, DENIS M. (1983): An enzyme-release assay for natural cytotoxicity. In *Journal of Immunological Methods* 64 (3), pp. 313–320. DOI: 10.1016/0022-1759(83)90438-6.
- KUBOW, KRISTOPHER E.; KLOTZSCH, ENRICO; SMITH, MICHAEL L.; GOURDON, DELPHINE; LITTLE, WILLIAM C.; VOGEL, VIOLA (2009): Crosslinking of cell-derived 3D scaffolds up-regulates the stretching and unfolding of new extracellular matrix assembled by reseeded cells. In *Integrative biology : quantitative biosciences from nano to macro* 1 (11-12), pp. 635–648. DOI: 10.1039/b914996a.
- KUCHLING, HORST (2011): Taschenbuch der Physik. Mit Tabellen. 20., aktualisierte Aufl. München: Fachbuchverl. Leipzig im Carl Hanser Verl.
- KUDDANNAYA, SHREYAS; CHUAH, YON JIN; LEE, MIN HUI ADELINE; MENON, NISHANTH V.; KANG, YUEJUN; ZHANG, YILEI (2013): Surface chemical modification of poly(dimethylsiloxane) for the enhanced adhesion and proliferation of mesenchymal stem cells. In *ACS applied materials & interfaces* 5 (19), pp. 9777–9784. DOI: 10.1021/am402903e.
- KUMMROW, A.; FRANKOWSKI, M.; BOCK, N.; WERNER, C.; DZIEKAN, T.; NEUKAMMER, J. (2013): Quantitative assessment of cell viability based on flow cytometry and microscopy. In *Cytometry. Part A : the journal of the International Society for Analytical Cytology* 83 (2), pp. 197–204. DOI: 10.1002/cyto.a.22213.
- KUNZLER, TOBIAS P.; DROBEK, TANJA; SCHULER, MARTIN; SPENCER, NICHOLAS D. (2007): Systematic study of osteoblast and fibroblast response to roughness by means of surface-morphology gradients. In *Biomaterials* 28 (13), pp. 2175–2182. DOI: 10.1016/j.biomaterials.2007.01.019.
- KWAK, EUN-A; AHN, SUJI; JAWORSKI, JUSTYN (2015): Microfabrication of Custom Collagen Structures Capable of Guiding Cell Morphology and Alignment. In *Biomacromolecules* 16 (6), pp. 1761–1770. DOI: 10.1021/acs.biomac.5b00295.
- LAI, EDWINA S.; ANDERSON, CLAIRE M.; FULLER, GERALD G. (2011): Designing a tubular matrix of oriented collagen fibrils for tissue engineering. In *Acta biomaterialia* 7 (6), pp. 2448–2456. DOI: 10.1016/j.actbio.2011.03.012.

- LAI, EDWINA S.; HUANG, NGAN F.; COOKE, JOHN P.; FULLER, GERALD G. (2012a): Aligned nanofibrillar collagen regulates endothelial organization and migration. In *Regenerative medicine* 7 (5), pp. 649–661. DOI: 10.2217/rme.12.48.
- LAI, EDWINA S.; HUANG, NGAN F.; COOKE, JOHN P.; FULLER, GERALD G. (2012b): Aligned nanofibrillar collagen regulates endothelial organization and migration. In *Regenerative medicine* 7 (5), pp. 649–661. DOI: 10.2217/rme.12.48.
- LAI, JUI-YANG; LUO, LI-JYUAN; MA, DAVID HUI-KANG (2018): Effect of Cross-Linking Density on the Structures and Properties of Carbodiimide-Treated Gelatin Matrices as Limbal Stem Cell Niches. In *International journal of molecular sciences* 19 (11). DOI: 10.3390/ijms19113294.
- LANGE, JANINA R.; FABRY, BEN (2013): Cell and tissue mechanics in cell migration. In *Experimental cell research* 319 (16), pp. 2418–2423. DOI: 10.1016/j.yexcr.2013.04.023.
- LANGER, R. (2000): Biomaterials in drug delivery and tissue engineering. One laboratory's experience. In *Accounts of chemical research* 33 (2), pp. 94–101. DOI: 10.1021/ar9800993.
- LAURENS, N.; KOOLWIJK, P.; MAAT, M. P. M. DE (2006): Fibrin structure and wound healing. In *Journal of thrombosis and haemostasis : JTH* 4 (5), pp. 932–939. DOI: 10.1111/j.1538-7836.2006.01861.x.
- LECKBAND, D. E.; ROOIJ, J. DE (2014): Cadherin adhesion and mechanotransduction. In *Annual review of cell and developmental biology* 30, pp. 291–315. DOI: 10.1146/annurev-cellbio-100913-013212.
- LEE, JUNMIN; ABDEEN, AMR A.; KILIAN, KRISTOPHER A. (2014): Rewiring mesenchymal stem cell lineage specification by switching the biophysical microenvironment. In *Scientific reports* 4, p. 5188. DOI: 10.1038/srep05188.
- LEE, KWAHUN; CHOI, SUNGMOON; YANG, CHUN; WU, HAI-CHEN; YU, JUNHUA (2013): Autofluorescence generation and elimination. A lesson from glutaraldehyde. In *Chemical communications (Cambridge, England)* 49 (29), pp. 3028–3030. DOI: 10.1039/c3cc40799c.
- LEGATE, KYLE R.; WICKSTRÖM, SARA A.; FÄSSLER, REINHARD (2009): Genetic and cell biological analysis of integrin outside-in signaling. In *Genes & development* 23 (4), pp. 397–418. DOI: 10.1101/gad.1758709.

- LENGSFELD, A. M.; LÖW, I.; WIELAND, T.; DANCKER, P.; HASSELBACH, W. (1974): Interaction of phalloidin with actin. In *Proceedings of the National Academy of Sciences of the United States of America* 71 (7), pp. 2803–2807. DOI: 10.1073/pnas.71.7.2803.
- LEVY, R. J.; SCHOEN, F. J.; SHERMAN, F. S.; NICHOLS, J.; HAWLEY, M. A.; LUND, S. A. (1986): Calcification of subcutaneously implanted type I collagen sponges. Effects of formaldehyde and glutaraldehyde pretreatments. In *The American journal of pathology* 122 (1), pp. 71–82.
- LI, CHEN XI; TALELE, NILESH P.; BOO, STELLAR; KOEHLER, ANNE; KNEE-WALDEN, ERICKA; BALESTRINI, JENNA L. *et al.* (2017): MicroRNA-21 preserves the fibrotic mechanical memory of mesenchymal stem cells. In *Nature materials* 16 (3), pp. 379–389. DOI: 10.1038/nmat4780.
- LI, WEI; SIGLEY, JUSTIN; PIETERS, MARLIEN; HELMS, CHRISTINE CARLISLE; NAGASWAMI, CHANDRASEKARAN; WEISEL, JOHN W.; GUTHOLD, MARTIN (2016): Fibrin Fiber Stiffness Is Strongly Affected by Fiber Diameter, but Not by Fibrinogen Glycation. In *Biophysical journal* 110 (6), pp. 1400–1410. DOI: 10.1016/j.bpj.2016.02.021.
- LI, YAWEN; BOU-AKL, THERESE (2016): Electrospinning in Tissue Engineering. In Sajjad Haider, Adnan Haider (Eds.): *Electrospinning - Material, Techniques, and Biomedical Applications*: InTech.
- LI, YUPING; ASADI, AMRAN; MONROE, MARGO R.; DOUGLAS, ELLIOT P. (2009): pH effects on collagen fibrillogenesis in vitro. Electrostatic interactions and phosphate binding. In *Materials Science and Engineering: C* 29 (5), pp. 1643–1649. DOI: 10.1016/j.msec.2009.01.001.
- LIA, MENGYAN; MONDRINOSA, MARK J. MILIND; GANDHIA, R.; KOB, FRANK K. (2005): Electrospun protein fibers as matrices for tissue engineering. In *Biomaterials* 26 (30), pp. 5999–6008. DOI: 10.1016/j.biomaterials.2005.03.030.
- LIM, JUNG YUL; HANSEN, JOSHUA C.; SIEDLECKI, CHRISTOPHER A.; HENGSTEBECK, ROBERT W.; CHENG, JUAN; WINOGRAD, NICHOLAS; DONAHUE, HENRY J. (2005a): Osteoblast adhesion on poly(L-lactic acid)/polystyrene demixed thin film blends. Effect of nanotopography, surface chemistry, and wettability. In *Biomacromolecules* 6 (6), pp. 3319–3327. DOI: 10.1021/bm0503423.
- LIM, JUNG YUL; HANSEN, JOSHUA C.; SIEDLECKI, CHRISTOPHER A.; RUNT, JAMES; DONAHUE, HENRY J. (2005b): Human foetal osteoblastic cell response to polymer-demixed

- nanotopographic interfaces. In *Journal of the Royal Society, Interface* 2 (2), pp. 97–108. DOI: 10.1098/rsif.2004.0019.
- LIN, KAILI; ZHANG, DAWEI; MACEDO, MARIA HELENA; CUI, WENGUO; SARMENTO, BRUNO; SHEN, GUOFANG (2019): Advanced Collagen-Based Biomaterials for Regenerative Biomedicine. In *Adv. Funct. Mater.* 29 (3), p. 1804943. DOI: 10.1002/adfm.201804943.
- LIU, TING; HOULE, JOHN D.; XU, JINYE; CHAN, BARBARA P.; CHEW, SING YIAN (2012): Nanofibrous collagen nerve conduits for spinal cord repair. In *Tissue engineering. Part A* 18 (9-10), pp. 1057–1066. DOI: 10.1089/ten.TEA.2011.0430.
- LIU, XIAOHUA; MA, PETER X. (2004): Polymeric scaffolds for bone tissue engineering. In *Annals of biomedical engineering* 32 (3), pp. 477–486. DOI: 10.1023/b:abme.0000017544.36001.8e.
- LIVNE, ARIEL; GEIGER, BENJAMIN (2016): The inner workings of stress fibers - from contractile machinery to focal adhesions and back. In *Journal of cell science* 129 (7), pp. 1293–1304. DOI: 10.1242/jcs.180927.
- LONG, JOSEPH; KIM, HYEJIN; KIM, DAJEONG; LEE, JONG BUM; KIM, DEOK-HO (2017): A biomaterial approach to cell reprogramming and differentiation. In *Journal of materials chemistry. B* 5 (13), pp. 2375–2379. DOI: 10.1039/C6TB03130G.
- LÓPEZ-FAGUNDO, CRISTINA; MITCHEL, JENNIFER A.; RAMCHAL, TALISHA D.; DINGLE, YU-TING L.; HOFFMAN-KIM, DIANE (2013): Navigating neurites utilize cellular topography of Schwann cell somas and processes for optimal guidance. In *Acta biomaterialia* 9 (7), pp. 7158–7168. DOI: 10.1016/j.actbio.2013.03.032.
- LORD, MEGAN S.; WHITELOCK, JOHN M.; SIMMONS, ANNE; WILLIAMS, RACHEL L.; MILTHORPE, BRUCE K. (2014): Fibrinogen adsorption and platelet adhesion to silica surfaces with stochastic nanotopography. In *Biointerphases* 9 (4), p. 41002. DOI: 10.1116/1.4900993.
- LORUSSO, ROBERTO; CICCIO, GIUSEPPE DE; VIZZARDI, ENRICO; GELSOMINO, SANDRO (2011): Human fibrinogen/thrombin-coated collagen patch to control intraoperative severe pulmonary hemorrhage and air leakage after correction of a ruptured thoracic aortic aneurysm. In *The Annals of thoracic surgery* 91 (3), pp. 917–919. DOI: 10.1016/j.athoracsur.2010.08.015.

- LOVETT, DAVID B.; SHEKHAR, NANDINI; NICKERSON, JEFFREY A.; ROUX, KYLE J.; LELE, TANMAY P. (2013): Modulation of Nuclear Shape by Substrate Rigidity. In *Cellular and Molecular Bioengineering* 6 (2), pp. 230–238. DOI: 10.1007/s12195-013-0270-2.
- LUKASHEV, M. (1998): ECM signalling. Orchestrating cell behaviour and misbehaviour. In *Trends in Cell Biology* 8 (11), pp. 437–441. DOI: 10.1016/S0962-8924(98)01362-2.
- LUO, XUESHI; GUO, ZHENZHAO; HE, PING; CHEN, TIAN; LI, LIHUA; DING, SHAN; LI, HONG (2018): Study on structure, mechanical property and cell cytocompatibility of electrospun collagen nanofibers crosslinked by common agents. In *International journal of biological macromolecules* 113, pp. 476–486. DOI: 10.1016/j.ijbiomac.2018.01.179.
- LUTOLF, M. P.; HUBBELL, J. A. (2005): Synthetic biomaterials as instructive extracellular microenvironments for morphogenesis in tissue engineering. In *Nat Biotechnol* 23 (1), pp. 47–55. DOI: 10.1038/nbt1055.
- MA, PETER X. (2004): Scaffolds for tissue fabrication. In *Materials Today* 7 (5), pp. 30–40. DOI: 10.1016/S1369-7021(04)00233-0.
- MA, PETER X. (2008): Biomimetic materials for tissue engineering. In *Advanced drug delivery reviews* 60 (2), pp. 184–198. DOI: 10.1016/j.addr.2007.08.041.
- MA, PETER X.; ZHANG, RUIYUN (1999): Synthetic nano-scale fibrous extracellular matrix. In *Journal of biomedical materials research* 46 (1), pp. 60–72. DOI: 10.1002/(SICI)1097-4636(199907)46:1<60::AID-JBM7>3.0.CO;2-H.
- MA, ZUWEI; KOTAKI, MASAYA; INAI, RYUJI; RAMAKRISHNA, SEERAM (2005): Potential of nanofiber matrix as tissue-engineering scaffolds. In *Tissue engineering* 11 (1-2), pp. 101–109. DOI: 10.1089/ten.2005.11.101.
- MAAS, MICHAEL; GUO, PENG; KEENEY, MICHAEL; YANG, FAN; HSU, TAMMY M.; FULLER, GERALD G. *et al.* (2011): Preparation of mineralized nanofibers: collagen fibrils containing calcium phosphate. In *Nano letters* 11 (3), pp. 1383–1388. DOI: 10.1021/nl200116d.
- MACHACEK, M.; DANUSER, G. (2006): Morphodynamic profiling of protrusion phenotypes. In *Biophysical journal* 90 (4), pp. 1439–1452. DOI: 10.1529/biophysj.105.070383.
- MACKENNA, D. (2000): Role of mechanical factors in modulating cardiac fibroblast function and extracellular matrix synthesis. In *Cardiovascular Research* 46 (2), pp. 257–263. DOI: 10.1016/S0008-6363(00)00030-4.

- MAITY, BISWANATH; SHEFF, DAVID; FISHER, RORY A. (2013): Immunostaining. In P. Michael Conn (Ed.): *Laboratory methods in cell biology. Imaging*, vol. 113. 1st ed. Amsterdam, Netherlands, Boston, Mass: Elsevier/Academic Press (Methods in Cell Biology, v. 113), pp. 81–105.
- MAKOGONENKO, EVGENY; TSURUPA, GALINA; INGHAM, KENNETH; MEDVED, LEONID (2002): Interaction of fibrin(ogen) with fibronectin. Further characterization and localization of the fibronectin-binding site. In *Biochemistry* 41 (25), pp. 7907–7913. DOI: 10.1021/bi025770x.
- MALONEY, JOHN M.; WALTON, EMILY B.; BRUCE, CHRISTOPHER M.; VAN VLIET, KRISTYN J. (2008): Influence of finite thickness and stiffness on cellular adhesion-induced deformation of compliant substrata. In *Physical review. E, Statistical, nonlinear, and soft matter physics* 78 (4 Pt 1), p. 41923. DOI: 10.1103/PhysRevE.78.041923.
- MARCHIN, KATHERINE L.; BERRIE, CINDY L. (2003): Conformational Changes in the Plasma Protein Fibrinogen upon Adsorption to Graphite and Mica Investigated by Atomic Force Microscopy. In *Langmuir : the ACS journal of surfaces and colloids* 19 (23), pp. 9883–9888. DOI: 10.1021/la035127r.
- MATSIKA, OLEKSII M.; BAKER, RUTH E.; SHAH, ESHA T.; SIMPSON, MATTHEW J. (2019): Mechanistic and experimental models of cell migration reveal the importance of cell-to-cell pushing in cell invasion. In *Biomed. Phys. Eng. Express* 5 (4), p. 45009. DOI: 10.1088/2057-1976/ab1b01.
- MATTHEWS, JAMIL A.; WNEK, GARY E.; SIMPSON, DAVID G.; BOWLIN, GARY L. (2002): Electrospinning of Collagen Nanofibers. In *Biomacromolecules* 3 (2), pp. 232–238. DOI: 10.1021/bm015533u.
- MATTILA, PIETA K.; LAPPALAINEN, PEKKA (2008): Filopodia. Molecular architecture and cellular functions. In *Nature reviews. Molecular cell biology* 9 (6), pp. 446–454. DOI: 10.1038/nrm2406.
- MAZZOTTA, COSIMO; CAPOROSSI, TOMASO; DENARO, ROSARIO; BOVONE, CRISTINA; SPARANO, CATERINA; PARADISO, ANNA *et al.* (2012): Morphological and functional correlations in riboflavin UV A corneal collagen cross-linking for keratoconus. In *Acta ophthalmologica* 90 (3), pp. 259–265. DOI: 10.1111/j.1755-3768.2010.01890.x.
- MCBEATH, ROWENA; PIRONE, DANA M.; NELSON, CELESTE M.; BHADRIRAJU, KIRAN; CHEN, CHRISTOPHER S. (2004): Cell Shape, Cytoskeletal Tension, and RhoA Regulate Stem

- Cell Lineage Commitment. In *Developmental Cell* 6 (4), pp. 483–495. DOI: 10.1016/S1534-5807(04)00075-9.
- MCINTOSH, J. M. (2018): Organic Chemistry. Fundamentals and Concepts: De Gruyter. Available online at <https://books.google.de/books?id=YwNPDwAAQBAJ>.
- MCMANUS, MICHAEL; BOLAND, EUGENE; SELL, SCOTT; BOWEN, WHITNEY; KOO, HARRY; SIMPSON, DAVID; BOWLIN, GARY (2007a): Electrospun nanofibre fibrinogen for urinary tract tissue reconstruction. In *Biomedical materials (Bristol, England)* 2 (4), pp. 257–262. DOI: 10.1088/1748-6041/2/4/008.
- MCMANUS, MICHAEL C.; BOLAND, EUGENE D.; KOO, HARRY P.; BARNES, CATHERINE P.; PAWLOWSKI, KRISTIN J.; WNEK, GARY E. *et al.* (2006): Mechanical properties of electrospun fibrinogen structures. In *Acta biomaterialia* 2 (1), pp. 19–28. DOI: 10.1016/j.actbio.2005.09.008.
- MCMANUS, MICHAEL C.; BOLAND, EUGENE D.; SIMPSON, DAVID G.; BARNES, CATHERINE P.; BOWLIN, GARY L. (2007b): Electrospun fibrinogen: feasibility as a tissue engineering scaffold in a rat cell culture model. In *Journal of biomedical materials research. Part A* 81 (2), pp. 299–309. DOI: 10.1002/jbm.a.30989.
- MCMANARA, LAURA E.; MCMURRAY, REBECCA J.; BIGGS, MANUS J. P.; KANTAWONG, FAHSAI; OREFFO, RICHARD O. C.; DALBY, MATTHEW J. (2010): Nanotopographical control of stem cell differentiation. In *Journal of tissue engineering* 2010, p. 120623. DOI: 10.4061/2010/120623.
- MCWHORTER, FRANCES Y.; DAVIS, CHASE T.; LIU, WENDY F. (2015): Physical and mechanical regulation of macrophage phenotype and function. In *Cellular and molecular life sciences : CMLS* 72 (7), pp. 1303–1316. DOI: 10.1007/s00018-014-1796-8.
- MEINEL, LORENZ; FAJARDO, ROBERT; HOFMANN, SANDRA; LANGER, ROBERT; CHEN, JAKE; SNYDER, BRIAN *et al.* (2005): Silk implants for the healing of critical size bone defects. In *Bone* 37 (5), pp. 688–698. DOI: 10.1016/j.bone.2005.06.010.
- MERKEL, R.; KIRCHGEßNER, N.; CESA, C. C.; HOFFMANN, B. (2007): Cell Force Microscopy on Elastic Layers of Finite Thickness. In *Biophysical journal* 93 (9), pp. 3314–3323. DOI: 10.1529/biophysj.107.111328.
- METAVARAYUTH, KAMOLRAT; SITASUWAN, PONGKWAN; ZHAO, XIA; LIN, YUAN; WANG, QIAN (2016): Influence of Surface Topographical Cues on the Differentiation of Mesenchymal

- Stem Cells in Vitro. In *ACS Biomater. Sci. Eng.* 2 (2), pp. 142–151. DOI: 10.1021/acsbiomaterials.5b00377.
- METZ, BERNARD; KERSTEN, GIDEON F. A.; HOOGERHOUT, PETER; BRUGGHE, HUMPHREY F.; TIMMERMANS, HANS A. M.; JONG, AD DE *et al.* (2004): Identification of formaldehyde-induced modifications in proteins. Reactions with model peptides. In *The Journal of biological chemistry* 279 (8), pp. 6235–6243. DOI: 10.1074/jbc.M310752200.
- MICHOD, R. E.; ROZE, D. (2001): Cooperation and conflict in the evolution of multicellularity. In *Heredity* 86 (Pt 1), pp. 1–7. DOI: 10.1046/j.1365-2540.2001.00808.x.
- MIGUEL, SÓNIA P.; FIGUEIRA, DANIELA R.; SIMÕES, DÉBORAH; RIBEIRO, MAXIMIANO P.; COUTINHO, PAULA; FERREIRA, PAULA; CORREIA, ILÍDIO J. (2018): Electrospun polymeric nanofibres as wound dressings. A review. In *Colloids and surfaces. B, Biointerfaces* 169, pp. 60–71. DOI: 10.1016/j.colsurfb.2018.05.011.
- MILLARD, THOMAS H.; MARTIN, PAUL (2008): Dynamic analysis of filopodial interactions during the zipper phase of *Drosophila* dorsal closure. In *Development (Cambridge, England)* 135 (4), pp. 621–626. DOI: 10.1242/dev.014001.
- MIRZAEI-PARSA, MOHAMAD JAVAD; GHANIZADEH, AMIN; EBADI, MALIHE T. K.; FARIDI-MAJIDI, REZA (2018): An alternative solvent for electrospinning of fibrinogen nanofibers. In *Bio-medical materials and engineering* 29 (3), pp. 279–287. DOI: 10.3233/BME-181736.
- MISSIRLIS, DIMITRIS; HARASZTI, TAMÁS; KESSLER, HORST; SPATZ, JOACHIM P. (2017): Fibronectin promotes directional persistence in fibroblast migration through interactions with both its cell-binding and heparin-binding domains. In *Scientific reports* 7 (1), p. 3711. DOI: 10.1038/s41598-017-03701-0.
- MITRA, SATYAJIT K.; HANSON, DANIEL A.; SCHLAEPFER, DAVID D. (2005): Focal adhesion kinase. In command and control of cell motility. In *Nat Rev Mol Cell Biol* 6 (1), pp. 56–68. DOI: 10.1038/nrm1549.
- MOE, AUNG AUNG KYWE; SURYANA, MONA; MARCY, GUILLAUME; LIM, SANDY KEAT; ANKAM, SONEELA; GOH, JEROME ZHI WEN *et al.* (2012): Microarray with micro- and nanotopographies enables identification of the optimal topography for directing the differentiation of primary murine neural progenitor cells. In *Small (Weinheim an der Bergstrasse, Germany)* 8 (19), pp. 3050–3061. DOI: 10.1002/smll.201200490.
- MOLNAR, J.; FONG, K.S.K.; HE, Q. P.; HAYASHI, K.; KIM, Y.; FONG, S.F.T. *et al.* (2003): Structural and functional diversity of lysyl oxidase and the LOX-like proteins. In

- Biochimica et Biophysica Acta (BBA) - Proteins and Proteomics* 1647 (1-2), pp. 220–224. DOI: 10.1016/S1570-9639(03)00053-0.
- MONROE, MARGO R.; LI, YUPING; AJINKYA, SHAUN B.; GOWER, LAURIE B.; DOUGLAS, ELLIOT P. (2009): Directed collagen patterning on gold-coated silicon substrates via micro-contact printing. In *Materials Science and Engineering: C* 29 (8), pp. 2365–2369. DOI: 10.1016/j.msec.2009.06.007.
- MOSESSON, M. W. (2005): Fibrinogen and fibrin structure and functions. In *Journal of thrombosis and haemostasis : JTH* 3 (8), pp. 1894–1904. DOI: 10.1111/j.1538-7836.2005.01365.x.
- MOUW, JANNA K.; OU, GUANQING; WEAVER, VALERIE M. (2014): Extracellular matrix assembly. A multiscale deconstruction. In *Nature reviews. Molecular cell biology* 15 (12), pp. 771–785. DOI: 10.1038/nrm3902.
- MUNIR, N.; CALLANAN, A. (2018): Novel phase separated polycaprolactone/collagen scaffolds for cartilage tissue engineering. In *Biomedical materials (Bristol, England)* 13 (5), p. 51001. DOI: 10.1088/1748-605X/aac91f.
- MURRAY, LYNNE A.; KNIGHT, DARRYL A.; LAURENT, GEOFFREY J. (2009): FIBROBLASTS. In Peter J. Barnes (Ed.): *Asthma and COPD. Basic mechanisms and clinical management*. 2. ed. Amsterdam, Boston: Elsevier/Academic Press, pp. 193–200.
- MUSSA FARKHANI, SAMAD; VALIZADEH, ALIREZA (2014): Electrospinning and electrospun nanofibres. In *IET Nanobiotechnology* 8 (2), pp. 83–92. DOI: 10.1049/iet-nbt.2012.0040.
- MUTHUSUBRAMANIAM, LALITHA; PENG, LILY; ZAITSEVA, TATIANA; PAUKSHTO, MICHAEL; MARTIN, GEORGE R.; DESAI, TEJAL A. (2012): Collagen fibril diameter and alignment promote the quiescent keratocyte phenotype. In *Journal of biomedical materials research. Part A* 100 (3), pp. 613–621. DOI: 10.1002/jbm.a.33284.
- MYLLYHARJU, JOHANNA; KIVIRIKKO, KARI I. (2004): Collagens, modifying enzymes and their mutations in humans, flies and worms. In *Trends in genetics : TIG* 20 (1), pp. 33–43. DOI: 10.1016/j.tig.2003.11.004.
- NAAHIDI, SHEVA; JAFARI, MOUSA; LOGAN, MEGAN; WANG, YUJIE; YUAN, YONGFANG; BAE, HOJAE *et al.* (2017): Biocompatibility of hydrogel-based scaffolds for tissue engineering applications. In *Biotechnology advances* 35 (5), pp. 530–544. DOI: 10.1016/j.biotechadv.2017.05.006.

- NEDRELOW, DAVID S.; BANKWALA, DANESH; HYYPIO, JEFFREY D.; LAI, VICTOR K.; BAROCAS, VICTOR H. (2018): Mechanics of a two-fiber model with one nested fiber network, as applied to the collagen-fibrin system. In *Acta biomaterialia* 72, pp. 306–315. DOI: 10.1016/j.actbio.2018.03.053.
- NELSON, CELESTE M.; CHEN, CHRISTOPHER S. (2002): Cell-cell signaling by direct contact increases cell proliferation via a PI3K-dependent signal. In *FEBS Letters* 514 (2-3), pp. 238–242. DOI: 10.1016/s0014-5793(02)02370-0.
- NGUYEN, ANH TUAN; SATHE, SHARVARI R.; YIM, EVELYN K. F. (2016): From nano to micro. Topographical scale and its impact on cell adhesion, morphology and contact guidance. In *Journal of physics. Condensed matter : an Institute of Physics journal* 28 (18), p. 183001. DOI: 10.1088/0953-8984/28/18/183001.
- NIKOLOVA, MARIA P.; CHAVALI, MURTHY S. (2019): Recent advances in biomaterials for 3D scaffolds. A review. In *Bioactive materials* 4, pp. 271–292. DOI: 10.1016/j.bioactmat.2019.10.005.
- O'BRIEN, FERGAL J. (2011): Biomaterials & scaffolds for tissue engineering. In *Materials Today* 14 (3), pp. 88–95. DOI: 10.1016/S1369-7021(11)70058-X.
- O'CONNOR, T. P.; DUERR, J. S.; BENTLEY, D. (1990): Pioneer growth cone steering decisions mediated by single filopodial contacts in situ. In *J. Neurosci.* 10 (12), pp. 3935–3946. DOI: 10.1523/JNEUROSCI.10-12-03935.1990.
- OKADA, MASAHIRO; YASUDA, SHOJI; KIMURA, TSUYOSHI; IWASAKI, MITSUNOBU; ITO, SEISHIRO; KISHIDA, AKIO; FURUZONO, TSUTOMU (2006): Optimization of amino group density on surfaces of titanium dioxide nanoparticles covalently bonded to a silicone substrate for antibacterial and cell adhesion activities. In *Journal of biomedical materials research. Part A* 76A (1), pp. 95–101. DOI: 10.1002/jbm.a.30513.
- ORIA, ROGER; WIEGAND, TINA; ESCRIBANO, JORGE; ELOSEGUI-ARTOLA, ALBERTO; URIARTE, JUAN JOSE; MORENO-PULIDO, CRISTIAN *et al.* (2017): Force loading explains spatial sensing of ligands by cells. In *Nature* 552 (7684), pp. 219–224. DOI: 10.1038/nature24662.
- PAINTER, KEVIN J.; ARMSTRONG, NICOLA J.; SHERRATT, JONATHAN A. (2010): The impact of adhesion on cellular invasion processes in cancer and development. In *Journal of Theoretical Biology* 264 (3), pp. 1057–1067. DOI: 10.1016/j.jtbi.2010.03.033.

- PALCHESKO, RACHELLE N.; SUN, YAN; ZHANG, LING; SZYMANSKI, JOHN M.; JALLERAT, QUENTIN; FEINBERG, ADAM W. (2013a): Nanofiber Biomaterials. In Robert Vajtai (Ed.): Springer Handbook of Nanomaterials. Berlin, Heidelberg: Springer Berlin Heidelberg, pp. 977–1010.
- PALCHESKO, RACHELLE N.; SUN, YAN; ZHANG, LING; SZYMANSKI, JOHN M.; JALLERAT, QUENTIN; FEINBERG, ADAM W. (2013b): Nanofiber Biomaterials. In Robert Vajtai (Ed.): Springer Handbook of Nanomaterials. Berlin, Heidelberg, s.l.: Springer Berlin Heidelberg, pp. 977–1010.
- PARENTEAU-BAREIL, RÉMI; GAUVIN, ROBERT; BERTHOD, FRANÇOIS (2010): Collagen-Based Biomaterials for Tissue Engineering Applications. In *Materials* 3 (3), pp. 1863–1887. DOI: 10.3390/ma3031863.
- PARK, KYUNG MIN; SHIN, YOUNG MIN; KIM, KYOBUM; SHIN, HEUNGSOO (2018): Tissue Engineering and Regenerative Medicine 2017. A Year in Review. In *Tissue engineering. Part B, Reviews* 24 (5), pp. 327–344. DOI: 10.1089/ten.TEB.2018.0027.
- PARTRIDGE, MICHAEL A.; MARCANTONIO, EUGENE E. (2006): Initiation of attachment and generation of mature focal adhesions by integrin-containing filopodia in cell spreading. In *Molecular biology of the cell* 17 (10), pp. 4237–4248. DOI: 10.1091/mbc.e06-06-0496.
- PASAPERA, ANA M.; SCHNEIDER, IAN C.; RERICHA, ERIN; SCHLAEPFER, DAVID D.; WATERMAN, CLARE M. (2010): Myosin II activity regulates vinculin recruitment to focal adhesions through FAK-mediated paxillin phosphorylation. In *The Journal of cell biology* 188 (6), pp. 877–890. DOI: 10.1083/jcb.200906012.
- PATEL, BIJAL; XU, ZHENGFAN; PINNOCK, CAMERON B.; KABBANI, LOAY S.; LAM, MAI T. (2018): Self-assembled Collagen-Fibrin Hydrogel Reinforces Tissue Engineered Adventitia Vessels Seeded with Human Fibroblasts. In *Scientific reports* 8 (1), p. 3294. DOI: 10.1038/s41598-018-21681-7.
- PATHAK, A.; KUMAR, S. (2012): Independent regulation of tumor cell migration by matrix stiffness and confinement. In *PNAS* 109 (26), pp. 10334–10339. DOI: 10.1073/pnas.1118073109.
- PELLEGRIN, STÉPHANIE; MELLOR, HARRY (2007): Actin stress fibres. In *Journal of cell science* 120 (Pt 20), pp. 3491–3499. DOI: 10.1242/jcs.018473.

- PENG, YONG Y.; GLATTAUER, VERONICA; RAMSHAW, JOHN A. M. (2017): Stabilisation of Collagen Sponges by Glutaraldehyde Vapour Crosslinking. In *International journal of biomaterials* 2017, p. 8947823. DOI: 10.1155/2017/8947823.
- PEREIRA, MARIAN; RYBARCZYK, BRAIN J.; ODRLJIN, TATJANA M.; HOCKING, DENISE C.; SOTTILE, JANE; SIMPSON-HAIDARIS, PATRICIA J. (2002): The incorporation of fibrinogen into extracellular matrix is dependent on active assembly of a fibronectin matrix. In *Journal of cell science* 115 (Pt 3), pp. 609–617.
- PETREACA, M.; MARTINS-GREEN, M. (2014): The Dynamics of Cell-ECM Interactions, with Implications for Tissue Engineering. In Robert P. Lanza, Robert S. Langer, Joseph Vacanti (Eds.): *Principles of tissue engineering*. 4. ed. Amsterdam: Elsevier Acad. Press, pp. 161–187.
- PHOLPABU, PITIRAT; KUSTRA, STEPHEN; WU, HAOSHENG; BALASUBRAMANIAN, ADITYA; BETTINGER, CHRISTOPHER J. (2015): Lithography-free fabrication of reconfigurable substrate topography for contact guidance. In *Biomaterials* 39, pp. 164–172. DOI: 10.1016/j.biomaterials.2014.10.078.
- PLACE, ELSIE S.; EVANS, NICHOLAS D.; STEVENS, MOLLY M. (2009): Complexity in biomaterials for tissue engineering. In *Nature materials* 8 (6), pp. 457–470. DOI: 10.1038/nmat2441.
- POGODA, KATARZYNA; JACZEWSKA, JUSTYNA; WILTOWSKA-ZUBER, JOANNA; KLYMENKO, OLESYA; ZUBER, KAZIMIERZ; FORMAL, MARIA; LEKKA, MAŁGORZATA (2012): Depth-sensing analysis of cytoskeleton organization based on AFM data. In *European biophysics journal : EBJ* 41 (1), pp. 79–87. DOI: 10.1007/s00249-011-0761-9.
- POWELL, HEATHER M.; BOYCE, STEVEN T. (2006): EDC cross-linking improves skin substitute strength and stability. In *Biomaterials* 27 (34), pp. 5821–5827. DOI: 10.1016/j.biomaterials.2006.07.030.
- POWELL, HEATHER M.; SUPP, DOROTHY M.; BOYCE, STEVEN T. (2008): Influence of electrospun collagen on wound contraction of engineered skin substitutes. In *Biomaterials* 29 (7), pp. 834–843. DOI: 10.1016/j.biomaterials.2007.10.036.
- QUARANTA, V. (2000): Cell migration through extracellular matrix. Membrane-type metalloproteinases make the way. In *The Journal of cell biology* 149 (6), pp. 1167–1170. DOI: 10.1083/jcb.149.6.1167.

- RAJANGAM, THANAVEL; AN, SEONG SOO A. (2013): Fibrinogen and fibrin based micro and nano scaffolds incorporated with drugs, proteins, cells and genes for therapeutic biomedical applications. In *International Journal of Nanomedicine* 8, pp. 3641–3662. DOI: 10.2147/IJN.S43945.
- RAMÍREZ-RODRÍGUEZ, GLORIA BELÉN; IAFISCO, MICHELE; TAMPIERI, ANNA; GÓMEZ-MORALES, JAIME; DELGADO-LÓPEZ, JOSÉ MANUEL (2014): pH-responsive collagen fibrillogenesis in confined droplets induced by vapour diffusion. In *Journal of Materials Science: Materials in Medicine* 25 (10), pp. 2305–2312. DOI: 10.1007/s10856-014-5189-1.
- RAOUFI, MOHAMMAD; ASLANKOOHI, NEDA; MOLLENHAUER, CHRISTINE; BOEHM, HEIKE; SPATZ, JOACHIM P.; BRUGGEMANN, DOROTHEA (2016): Template-assisted extrusion of biopolymer nanofibers under physiological conditions. In *Integrative biology : quantitative biosciences from nano to macro* 8 (10), pp. 1059–1066. DOI: 10.1039/c6ib00045b.
- RAOUFI, MOHAMMAD; DAS, TAMAL; SCHOEN, INGMAR; VOGEL, VIOLA; BRUGGEMANN, DOROTHEA; SPATZ, JOACHIM P. (2015): Nanopore Diameters Tune Strain in Extruded Fibronectin Fibers. In *Nano letters* 15 (10), pp. 6357–6364. DOI: 10.1021/acs.nanolett.5b01356.
- RAZAFIARISON, TOJO; SILVÁN, UNAI; MEIER, DANIELA; SNEDEKER, JESS G. (2016): Surface-Driven Collagen Self-Assembly Affects Early Osteogenic Stem Cell Signaling. In *Advanced healthcare materials* 5 (12), pp. 1481–1492. DOI: 10.1002/adhm.201600128.
- REDDY, NARENDRA; REDDY, ROOPA; JIANG, QIURAN (2015): Crosslinking biopolymers for biomedical applications. In *Trends in biotechnology* 33 (6), pp. 362–369. DOI: 10.1016/j.tibtech.2015.03.008.
- REICHERT, JÖRG; WEI, GANG; JANDT, KLAUS D. (2009): Formation and Topotactical Orientation of Fibrinogen Nanofibrils on Graphite Nanostructures. In *Adv. Eng. Mater.* 11 (11), B177-B181. DOI: 10.1002/adem.200900084.
- RHO, KYONG SU; JEONG, LIM; LEE, GENE; SEO, BYOUNG-MOO; PARK, YOON JEONG; HONG, SEONG-DOO *et al.* (2006): Electrospinning of collagen nanofibers: effects on the behavior of normal human keratinocytes and early-stage wound healing. In *Biomaterials* 27 (8), pp. 1452–1461. DOI: 10.1016/j.biomaterials.2005.08.004.

- RIANNA, C.; RADMACHER, M. (2017): Influence of microenvironment topography and stiffness on the mechanics and motility of normal and cancer renal cells. In *Nanoscale* 9 (31), pp. 11222–11230. DOI: 10.1039/c7nr02940c.
- RIANNA, CARMELA; RADMACHER, MANFRED (2016): Cell mechanics as a marker for diseases. Biomedical applications of AFM. In. PHYSICS OF CANCER: INTERDISCIPLINARY PROBLEMS AND CLINICAL APPLICATIONS (PC'16): Proceedings of the International Conference on Physics of Cancer: Interdisciplinary Problems and Clinical Applications 2016. Tomsk, Russia, 22–25 March 2016: Author(s) (AIP Conference Proceedings), p. 20057.
- RICARD-BLUM, SYLVIE (2011): The collagen family. In *Cold Spring Harbor perspectives in biology* 3 (1), a004978. DOI: 10.1101/cshperspect.a004978.
- RICARD-BLUM, SYLVIE; RUGGIERO, FLORENCE (2005): The collagen superfamily. From the extracellular matrix to the cell membrane. In *Pathologie-biologie* 53 (7), pp. 430–442. DOI: 10.1016/j.patbio.2004.12.024.
- RICE, MARK A.; DODSON, BRENNAN T.; ARTHUR, JEFFREY A.; ANSETH, KRISTI S. (2005): Cell-based therapies and tissue engineering. In *Otolaryngologic clinics of North America* 38 (2), 199-214, v. DOI: 10.1016/j.otc.2004.10.010.
- RISS, TERRY; NILES, ANDREW; MORAVEC, RICH; KARASSINA, NATASHIA; VIDUGIRIENE, JOLANTA (2019): Cytotoxicity Assays. In *Vitro Methods to Measure Dead Cells*: Eli Lilly & Company and the National Center for Advancing Translational Sciences.
- ROTTNER, KLEMENS; FAIX, JAN; BOGDAN, SVEN; LINDER, STEFAN; KERKHOFF, EUGEN (2017): Actin assembly mechanisms at a glance. In *Journal of cell science* 130 (20), pp. 3427–3435. DOI: 10.1242/jcs.206433.
- ROWE, SHANEEN L.; STEGEMANN, JAN P. (2006): Interpenetrating collagen-fibrin composite matrices with varying protein contents and ratios. In *Biomacromolecules* 7 (11), pp. 2942–2948. DOI: 10.1021/bm0602233.
- RUEDEN, CURTIS T.; SCHINDELIN, JOHANNES; HINER, MARK C.; DEZONIA, BARRY E.; WALTER, ALISON E.; ARENA, ELLEN T.; ELICEIRI, KEVIN W. (2017): ImageJ2. ImageJ for the next generation of scientific image data. In *BMC bioinformatics* 18 (1), p. 529. DOI: 10.1186/s12859-017-1934-z.
- RUOSLAHTI, E. (1988): Fibronectin and its receptors. In *Annual review of biochemistry* 57, pp. 375–413. DOI: 10.1146/annurev.bi.57.070188.002111.

- SAHNI, A.; FRANCIS, C. W. (2000): Vascular endothelial growth factor binds to fibrinogen and fibrin and stimulates endothelial cell proliferation. In *Blood* 96 (12), pp. 3772–3778.
- SAHNI, A.; ODR LJIN, T.; FRANCIS, C. W. (1998): Binding of basic fibroblast growth factor to fibrinogen and fibrin. In *The Journal of biological chemistry* 273 (13), pp. 7554–7559. DOI: 10.1074/jbc.273.13.7554.
- SALASZNYK, ROMAN M.; KLEES, ROBERT F.; WILLIAMS, WILLIAM A.; BOSKEY, ADELE; PLOPPER, GEORGE E. (2007): Focal adhesion kinase signaling pathways regulate the osteogenic differentiation of human mesenchymal stem cells. In *Experimental cell research* 313 (1), pp. 22–37. DOI: 10.1016/j.yexcr.2006.09.013.
- SALES, ADRIA; ENDE, KAREN; DIEMER, JENNIFER; KYVIK, ADRIANA R.; VECIANA, JAUME; RATERA, IMMA *et al.* (2019): Cell Type-Dependent Integrin Distribution in Adhesion and Migration Responses on Protein-Coated Microgrooved Substrates. In *ACS omega* 4 (1), pp. 1791–1800. DOI: 10.1021/acsomega.8b03608.
- SCHÄFER, CLAUDIA; FAUST, UTA; KIRCHGESSNER, NORBERT; MERKEL, RUDOLF; HOFFMANN, BERND (2011): The filopodium. A stable structure with highly regulated repetitive cycles of elongation and persistence depending on the actin cross-linker fascin. In *Cell adhesion & migration* 5 (5), pp. 431–438. DOI: 10.4161/cam.5.5.17400.
- SCHNEIDER-BARTHOLD, CAROLINE; BAGANZ, SABRINA; WILHELMI, MATHIAS; SCHEPER, THOMAS; PEPELANOVA, ILIYANA (2016): Hydrogels based on collagen and fibrin – frontiers and applications. In *BioNanoMaterials* 17 (1-2), p. 3307. DOI: 10.1515/bnm-2015-0025.
- SCHNELLER, M. (1997): alpha vbeta 3 integrin associates with activated insulin and PDGFbeta receptors and potentiates the biological activity of PDGF. In *The EMBO journal* 16 (18), pp. 5600–5607. DOI: 10.1093/emboj/16.18.5600.
- SCHÖNHERR, ELKE; HAUSSER, HEINZ-JÜRGEN (2000): Extracellular Matrix and Cytokines. A Functional Unit. In *Developmental Immunology* 7 (2-4), pp. 89–101. DOI: 10.1155/2000/31748.
- SCHWARZ, U. D.; HAEFKE, H.; REINMANN, P.; GÜNTHERODT, H.-J. (1994): Tip artefacts in scanning force microscopy. In *Journal of Microscopy* 173 (3), pp. 183–197. DOI: 10.1111/j.1365-2818.1994.tb03441.x.

- SCHWARZBAUER, JEAN E.; DESIMONE, DOUGLAS W. (2011): Fibronectins, their fibrillogenesis, and in vivo functions. In *Cold Spring Harbor perspectives in biology* 3 (7). DOI: 10.1101/cshperspect.a005041.
- SEED, B. (2001): Silanizing glassware. In *Current protocols in cell biology* Appendix 3, Appendix 3E. DOI: 10.1002/0471143030.cba03es08.
- SELL, SCOTT; BARNES, CATHERINE; SIMPSON, DAVID; BOWLIN, GARY (2008a): Scaffold permeability as a means to determine fiber diameter and pore size of electrospun fibrinogen. In *Journal of biomedical materials research. Part A* 85 (1), pp. 115–126. DOI: 10.1002/jbm.a.31556.
- SELL, SCOTT A.; FRANCIS, MICHAEL P.; GARG, KOYAL; MCCLURE, MICHAEL J.; SIMPSON, DAVID G.; BOWLIN, GARY L. (2008b): Cross-linking methods of electrospun fibrinogen scaffolds for tissue engineering applications. In *Biomedical materials (Bristol, England)* 3 (4), p. 45001. DOI: 10.1088/1748-6041/3/4/045001.
- SHAW, TANYA J.; MARTIN, PAUL (2009): Wound repair at a glance. In *Journal of cell science* 122 (Pt 18), pp. 3209–3213. DOI: 10.1242/jcs.031187.
- SHEEHY, E. J.; CUNNIFFE, G. M.; O'BRIEN, F. J. (2018): Collagen-based biomaterials for tissue regeneration and repair. In Mário A. Barbosa, M. Cristina L. Martins (Eds.): *Peptides and proteins as biomaterials for tissue regeneration and repair*. Duxford, Cambridge, MA, Kidlington: Woodhead publishing an imprint of Elsevier (Woodhead publishing series in biomaterials), pp. 127–150.
- SHEN, KEYUE; QI, JIE; KAM, LANCE C. (2008): Microcontact Printing of Proteins for Cell Biology. In *JoVE* (22). DOI: 10.3791/1065.
- SHEPHERD, JENNIFER; BAX, DANIEL; BEST, SERENA; CAMERON, RUTH (2017): Collagen-Fibrinogen Lyophilised Scaffolds for Soft Tissue Regeneration. In *Materials* 10 (6). DOI: 10.3390/ma10060568.
- SHIH, YU-RU V.; CHEN, CHUNG-NAN; TSAI, SHIAO-WEN; WANG, YNG JIIN; LEE, OSCAR K. (2006): Growth of mesenchymal stem cells on electrospun type I collagen nanofibers. In *STEM CELLS* 24 (11), pp. 2391–2397. DOI: 10.1634/stemcells.2006-0253.
- SHIN, Y. M.; HOHMAN, M. M.; BRENNER, M. P.; RUTLEDGE, G. C. (2001): Experimental characterization of electrospinning. The electrically forced jet and instabilities. In *Polymer* 42 (25), pp. 9955–9967. DOI: 10.1016/S0032-3861(01)00540-7.

- SHOULDERS, MATTHEW D.; RAINES, RONALD T. (2009): Collagen structure and stability. In *Annual review of biochemistry* 78, pp. 929–958. DOI: 10.1146/annurev.biochem.77.032207.120833.
- SIEBENLIST, KEVIN R.; MOSESSON, MICHAEL W.; HERNANDEZ, IRENE; BUSH, LESLIE A.; DI CERA, ENRICO; SHAINOFF, JOHN R. *et al.* (2005): Studies on the basis for the properties of fibrin produced from fibrinogen-containing γ' chains. In *Blood* 106 (8), pp. 2730–2736. DOI: 10.1182/blood-2005-01-0240.
- SIRIWARDANE, MEVAN L.; DEROSA, KATHLEEN; COLLINS, GEORGE; PFISTER, BRYAN J. (2014): Controlled formation of cross-linked collagen fibers for neural tissue engineering applications. In *Biofabrication* 6 (1), p. 15012. DOI: 10.1088/1758-5082/6/1/015012.
- SMALL, J.VICTOR; ROTTNER, K.; KAVERINA, I.; ANDERSON, K. I. (1998): Assembling an actin cytoskeleton for cell attachment and movement. In *Biochimica et Biophysica Acta (BBA) - Molecular Cell Research* 1404 (3), pp. 271–281. DOI: 10.1016/S0167-4889(98)00080-9.
- SMITH, SARAH E.; WHITE, RICHARD A.; GRANT, DAVID A.; GRANT, SHEILA A. (2015): Fluorescence imaging preparation methods for tissue scaffolds implanted into a green fluorescent protein porcine model. In *Transgenic research* 24 (5), pp. 911–919. DOI: 10.1007/s11248-015-9891-7.
- SPURLIN, TIGHE A.; BHADRIRAJU, KIRAN; CHUNG, KOO-HYUN; TONA, ALESSANDRO; PLANT, ANNE L. (2009): The treatment of collagen fibrils by tissue transglutaminase to promote vascular smooth muscle cell contractile signaling. In *Biomaterials* 30 (29), pp. 5486–5496. DOI: 10.1016/j.biomaterials.2009.07.014.
- SPURLIN, TIGHE A.; FORRY, SAMUEL P.; COOKSEY, GREGORY A.; PLANT, ANNE L. (2010): Characterization of collagen fibrils films formed on polydimethylsiloxane surfaces for microfluidic applications. In *Langmuir : the ACS journal of surfaces and colloids* 26 (17), pp. 14111–14117. DOI: 10.1021/la102150s.
- SRIDHARAN, RUKMANI; CAMERON, ANDREW R.; KELLY, DANIEL J.; KEARNEY, CATHAL J.; O'BRIEN, FERGAL J. (2015): Biomaterial based modulation of macrophage polarization. A review and suggested design principles. In *Materials Today* 18 (6), pp. 313–325. DOI: 10.1016/j.mattod.2015.01.019.
- STAPELFELDT, KARSTEN; STAMBOROSKI, STEPHANI; MEDNIKOVA, POLINA; BRÜGGEMANN, DOROTHEA (2019a): Fabrication of 3D-nanofibrous fibrinogen scaffolds using salt-

- induced self assembly. In *Biofabrication* 11 (2), p. 25010. DOI: 10.1088/1758-5090/ab0681.
- STAPELFELDT, KARSTEN; STAMBOROSKI, STEPHANI; WALTER, IRINA; SUTER, NAIANA; KOWALIK, THOMAS; MICHAELIS, MONIKA; BRÜGGEMANN, DOROTHEA (2019b): Controlling the Multiscale Structure of Nanofibrous Fibrinogen Scaffolds for Wound Healing. In *Nano letters* 19 (9), pp. 6554–6563. DOI: 10.1021/acs.nanolett.9b02798.
- STARBORG, TOBIAS; KALSON, NICHOLAS S.; LU, YINHUI; MIRONOV, ALEKSANDR; COOTES, TIMOTHY F.; HOLMES, DAVID F.; KADLER, KARL E. (2013): Using transmission electron microscopy and 3View to determine collagen fibril size and three-dimensional organization. In *Nature protocols* 8 (7), pp. 1433–1448. DOI: 10.1038/nprot.2013.086.
- STAROS, JAMES V.; WRIGHT, RICK W.; SWINGLE, DEBORAH M. (1986): Enhancement by N-hydroxysulfosuccinimide of water-soluble carbodiimide-mediated coupling reactions. In *Analytical Biochemistry* 156 (1), pp. 220–222. DOI: 10.1016/0003-2697(86)90176-4.
- STEBEL, SOPHIE (2018): Cellular Interaction with Collagen Nanofiber Scaffolds. University of Applied Sciences Bonn-Rhein-Sieg. Department of Natural Sciences.
- STEKETEE, MICHAEL B.; TOSNEY, KATHRYN W. (2002): Three Functionally Distinct Adhesions in Filopodia. Shaft Adhesions Control Lamellar Extension. In *J. Neurosci.* 22 (18), pp. 8071–8083. DOI: 10.1523/JNEUROSCI.22-18-08071.2002.
- STORM, CORNELIS; PASTORE, JENNIFER J.; MACKINTOSH, F. C.; LUBENSKY, T. C.; JANMEY, PAUL A. (2005): Nonlinear elasticity in biological gels. In *Nature* 435 (7039), pp. 191–194. DOI: 10.1038/nature03521.
- STYLIANOU, ANDREAS; YOVA, DIDO; ALEXANDRATOU, ELENI (2013): Nanotopography of collagen thin films in correlation with fibroblast response. In *J. Nanophoton* 7 (1), p. 73590. DOI: 10.1117/1.JNP.7.073590.
- SURIANO, RAFFAELLA; CREDI, CATERINA; LEVI, MARINELLA; TURRI, STEFANO (2014): AFM nanoscale indentation in air of polymeric and hybrid materials with highly different stiffness. In *Applied Surface Science* 311, pp. 558–566. DOI: 10.1016/j.apsusc.2014.05.108.
- TAGLIETTI, ANGELO; ARCIOLA, CARLA RENATA; D'AGOSTINO, AGNESE; DACARRO, GIACOMO; MONTANARO, LUCIO; CAMPOCCIA, DAVIDE *et al.* (2014): Antibiofilm activity of a monolayer of silver nanoparticles anchored to an amino-silanized glass surface. In *Biomaterials* 35 (6), pp. 1779–1788. DOI: 10.1016/j.biomaterials.2013.11.047.

- TAN, KENNETH K. B.; TANN, JASON Y.; SATHE, SHARVARI R.; GOH, SEOK HONG; MA, DONGLIANG; GOH, EYLEEN L. K.; YIM, EVELYN K. F. (2015): Enhanced differentiation of neural progenitor cells into neurons of the mesencephalic dopaminergic subtype on topographical patterns. In *Biomaterials* 43, pp. 32–43. DOI: 10.1016/j.biomaterials.2014.11.036.
- TANAKA, J. S. (1987): "How Big Is Big Enough? ": Sample Size and Goodness of Fit in Structural Equation Models with Latent Variables. In *Child Development* 58 (1), p. 134. DOI: 10.2307/1130296.
- TANDARA, ANDREA A.; MUSTOE, THOMAS A. (2011): MMP- and TIMP-secretion by human cutaneous keratinocytes and fibroblasts – impact of coculture and hydration. In *Journal of Plastic, Reconstructive & Aesthetic Surgery* 64 (1), pp. 108–116. DOI: 10.1016/j.bjps.2010.03.051.
- TAWFICK, SAMEH; VOLDER, MICHAEL DE; COPIC, DAVOR; PARK, SEI JIN; OLIVER, C. RYAN; POLSEN, ERIK S. *et al.* (2012): Engineering of micro- and nanostructured surfaces with anisotropic geometries and properties. In *Advanced materials (Deerfield Beach, Fla.)* 24 (13), pp. 1628–1674. DOI: 10.1002/adma.201103796.
- TENNENT, GLENYS A.; BRENNAN, STEPHEN O.; STANGOU, ARIE J.; O'GRADY, JOHN; HAWKINS, PHILIP N.; PEPYS, MARK B. (2007): Human plasma fibrinogen is synthesized in the liver. In *Blood* 109 (5), pp. 1971–1974. DOI: 10.1182/blood-2006-08-040956.
- THEOCHARIS, ACHILLEAS D.; SKANDALIS, SPYRIDON S.; TZANAKAKIS, GEORGE N.; KARAMANOS, NIKOS K. (2010): Proteoglycans in health and disease. Novel roles for proteoglycans in malignancy and their pharmacological targeting. In *The FEBS journal* 277 (19), pp. 3904–3923. DOI: 10.1111/j.1742-4658.2010.07800.x.
- THEOCHARIS, ACHILLEAS D.; SKANDALIS, SPYROS S.; GIALELI, CHRYSOSTOMI; KARAMANOS, NIKOS K. (2016): Extracellular matrix structure. In *Advanced drug delivery reviews* 97, pp. 4–27. DOI: 10.1016/j.addr.2015.11.001.
- TIAN, ZHENHUA; LI, CONGHU; DUAN, LIAN; LI, GUOYING (2014): Physicochemical properties of collagen solutions cross-linked by glutaraldehyde. In *Connective tissue research* 55 (3), pp. 239–247. DOI: 10.3109/03008207.2014.898066.
- TIAN, ZHENHUA; LIU, WENTAO; LI, GUOYING (2016): The microstructure and stability of collagen hydrogel cross-linked by glutaraldehyde. In *Polymer Degradation and Stability* 130, pp. 264–270. DOI: 10.1016/j.polymdegradstab.2016.06.015.

- TIRELLA, A.; LIBERTO, T.; AHLUWALIA, A. (2012): Riboflavin and collagen. New crosslinking methods to tailor the stiffness of hydrogels. In *Materials Letters* 74, pp. 58–61. DOI: 10.1016/j.matlet.2012.01.036.
- TOJKANDER, SARI; GATEVA, GERGANNA; LAPPALAINEN, PEKKA (2012): Actin stress fibers-- assembly, dynamics and biological roles. In *Journal of cell science* 125 (Pt 8), pp. 1855–1864. DOI: 10.1242/jcs.098087.
- TONNIGES, JEFFREY R.; ALBERT, BENJAMIN; CALOMENI, EDWARD P.; ROY, SHUVRO; LEE, JOAN; MO, XIAOKUI *et al.* (2016): Collagen Fibril Ultrastructure in Mice Lacking Discoidin Domain Receptor 1. In *Microscopy and microanalysis : the official journal of Microscopy Society of America, Microbeam Analysis Society, Microscopical Society of Canada* 22 (3), pp. 599–611. DOI: 10.1017/S1431927616000787.
- TORRES-GINER, SERGIO; GIMENO-ALCAÑIZ, JOSE V.; OCIO, MARIA J.; LAGARON, JOSE M. (2009): Comparative performance of electrospun collagen nanofibers cross-linked by means of different methods. In *ACS applied materials & interfaces* 1 (1), pp. 218–223. DOI: 10.1021/am800063x.
- TRAPPMANN, BRITTA; GAUTROT, JULIEN E.; CONNELLY, JOHN T.; STRANGE, DANIEL G. T.; LI, YUAN; OYEN, MICHELLE L. *et al.* (2012): Extracellular-matrix tethering regulates stem-cell fate. In *Nature materials* 11 (7), pp. 642–649. DOI: 10.1038/nmat3339.
- UTTAYARAT, PIMPON; TOWORFE, GEORGE K.; DIETRICH, FRANZISKA; LELKES, PETER I.; COMPOSTO, RUSSELL J. (2005): Topographic guidance of endothelial cells on silicone surfaces with micro- to nanogrooves. Orientation of actin filaments and focal adhesions. In *Journal of biomedical materials research. Part A* 75 (3), pp. 668–680. DOI: 10.1002/jbm.a.30478.
- VAN DER VALK, J.; BRUNNER, D.; SMET, K. DE; FEX SVENNINGSSEN, A.; HONEGGER, P.; KNUDSEN, L. E. *et al.* (2010): Optimization of chemically defined cell culture media-- replacing fetal bovine serum in mammalian in vitro methods. In *Toxicology in vitro : an international journal published in association with BIBRA* 24 (4), pp. 1053–1063. DOI: 10.1016/j.tiv.2010.03.016.
- VAN TRUSKETT, N.; WATTS, MICHAEL P. C. (2006): Trends in imprint lithography for biological applications. In *Trends in biotechnology* 24 (7), pp. 312–317. DOI: 10.1016/j.tibtech.2006.05.005.

- VARIOLA, FABIO (2015): Atomic force microscopy in biomaterials surface science. In *Physical chemistry chemical physics : PCCP* 17 (5), pp. 2950–2959. DOI: 10.1039/C4CP04427D.
- VASCONCELOS, DANIEL M.; GONÇALVES, RAQUEL M.; ALMEIDA, CATARINA R.; PEREIRA, INÊS O.; OLIVEIRA, MARTA I.; NEVES, NUNO *et al.* (2016): Fibrinogen scaffolds with immunomodulatory properties promote in vivo bone regeneration. In *Biomaterials* 111, pp. 163–178. DOI: 10.1016/j.biomaterials.2016.10.004.
- VASIOUKHIN, VALERI; BAUER, CHRISTOPH; YIN, MEI; FUCHS, ELAINE (2000): Directed Actin Polymerization Is the Driving Force for Epithelial Cell–Cell Adhesion. In *Cell* 100 (2), pp. 209–219. DOI: 10.1016/S0092-8674(00)81559-7.
- VELNAR, TOMAZ; BAILEY, T.; SMRKOLJ, V. (2009): The wound healing process. An overview of the cellular and molecular mechanisms. In *The Journal of international medical research* 37 (5), pp. 1528–1542. DOI: 10.1177/147323000903700531.
- VENTRE, MAURIZIO; NETTI, PAOLO A. (2016): Engineering Cell Instructive Materials To Control Cell Fate and Functions through Material Cues and Surface Patterning. In *ACS applied materials & interfaces* 8 (24), pp. 14896–14908. DOI: 10.1021/acsami.5b08658.
- VICIDOMINI, GIUSEPPE; BIANCHINI, PAOLO; DIASPRO, ALBERTO (2018): STED super-resolved microscopy. In *Nat Methods* 15 (3), pp. 173–182. DOI: 10.1038/nmeth.4593.
- VOGEL, VIOLA (2018): Unraveling the Mechanobiology of Extracellular Matrix. In *Annual review of physiology* 80, pp. 353–387. DOI: 10.1146/annurev-physiol-021317-121312.
- VOGEL, VIOLA; SHEETZ, MICHAEL (2006): Local force and geometry sensing regulate cell functions. In *Nature reviews. Molecular cell biology* 7 (4), pp. 265–275. DOI: 10.1038/nrm1890.
- VUORI, K. (1998): Integrin signaling. Tyrosine phosphorylation events in focal adhesions. In *The Journal of membrane biology* 165 (3), pp. 191–199. DOI: 10.1007/s002329900433.
- WALKER, CAMERON; MOJARES, ELIJAH; DEL RÍO HERNÁNDEZ, ARMANDO (2018): Role of Extracellular Matrix in Development and Cancer Progression. In *International journal of molecular sciences* 19 (10). DOI: 10.3390/ijms19103028.

- WALTERS, B. D.; STEGEMANN, J. P. (2014): Strategies for directing the structure and function of three-dimensional collagen biomaterials across length scales. In *Acta biomaterialia* 10 (4), pp. 1488–1501. DOI: 10.1016/j.actbio.2013.08.038.
- WANG, H. B.; DEMBO, M.; HANKS, S. K.; WANG, Y. (2001): Focal adhesion kinase is involved in mechanosensing during fibroblast migration. In *Proceedings of the National Academy of Sciences of the United States of America* 98 (20), pp. 11295–11300. DOI: 10.1073/pnas.201201198.
- WANG, JINHUI; WANG, HAIXIA; WANG, YIZHU; LI, JINGFENG; SU, ZHIQIANG; WEI, GANG (2014): Alternate layer-by-layer assembly of graphene oxide nanosheets and fibrinogen nanofibers on a silicon substrate for a biomimetic three-dimensional hydroxyapatite scaffold. In *J. Mater. Chem. B* 2 (42), pp. 7360–7368. DOI: 10.1039/C4TB01324G.
- WANG, KAI; BRUCE, ALLISON; MEZAN, RYAN; KADIYALA, ANAND; WANG, LIYING; DAWSON, JEREMY *et al.* (2016): Nanotopographical Modulation of Cell Function through Nuclear Deformation. In *ACS applied materials & interfaces* 8 (8), pp. 5082–5092. DOI: 10.1021/acsami.5b10531.
- WASILEWSKA, MONIKA; ADAMCZYK, ZBIGNIEW (2011): Fibrinogen adsorption on mica studied by AFM and in situ streaming potential measurements. In *Langmuir : the ACS journal of surfaces and colloids* 27 (2), pp. 686–696. DOI: 10.1021/la102931a.
- WEI, GANG; REICHERT, JÖRG; BOSSERT, JÖRG; JANDT, KLAUS D. (2008a): Novel biopolymeric template for the nucleation and growth of hydroxyapatite crystals based on self-assembled fibrinogen fibrils. In *Biomacromolecules* 9 (11), pp. 3258–3267. DOI: 10.1021/bm800824r.
- WEI, GANG; REICHERT, JÖRG; JANDT, KLAUS D. (2008b): Controlled self-assembly and templated metallization of fibrinogen nanofibrils. In *Chem. Commun.* (33), pp. 3903–3905. DOI: 10.1039/B806316H.
- WIGREN, ROGER; ELWING, HANS; ERLANDSSON, RAGNAR; WELIN, STEFAN; LUNDSTRÖM, INGEMAR (1991): Structure of adsorbed fibrinogen obtained by scanning force microscopy. In *FEBS Letters* 280 (2), pp. 225–228. DOI: 10.1016/0014-5793(91)80298-H.
- WILSON, W. D.; TANIOUS, F. A.; BARTON, H. J.; JONES, R. L.; FOX, K.; WYDRA, R. L.; STREKOWSKI, L. (1990): DNA sequence dependent binding modes of 4',6-diamidino-2-phenylindole (DAPI). In *Biochemistry* 29 (36), pp. 8452–8461. DOI: 10.1021/bi00488a036.

- WNEK, GARY E.; CARR, MARCUS E.; SIMPSON, DAVID G.; BOWLIN, GARY L. (2003): Electrospinning of Nanofiber Fibrinogen Structures. In *Nano Lett.* 3 (2), pp. 213–216. DOI: 10.1021/nl025866c.
- WOLF, KATARINA; FRIEDL, PETER (2011): Extracellular matrix determinants of proteolytic and non-proteolytic cell migration. In *Trends in Cell Biology* 21 (12), pp. 736–744. DOI: 10.1016/j.tcb.2011.09.006.
- XU, BAIYAO; SONG, GUANBIN; JU, YANG; LI, XIAN; SONG, YUANHUI; WATANABE, SACHI (2012): RhoA/ROCK, cytoskeletal dynamics, and focal adhesion kinase are required for mechanical stretch-induced tenogenic differentiation of human mesenchymal stem cells. In *Journal of cellular physiology* 227 (6), pp. 2722–2729. DOI: 10.1002/jcp.23016.
- YAMAMOTO, MASAYA; TAKAHASHI, YOSHITAKE; TABATA, YASUHIKO (2003): Controlled release by biodegradable hydrogels enhances the ectopic bone formation of bone morphogenetic protein. In *Biomaterials* 24 (24), pp. 4375–4383. DOI: 10.1016/S0142-9612(03)00337-5.
- YAMANUSHI, T. T.; BOYETT, M. R.; YAMAMOTO, Y.; OHSAKI, H.; HIRAKAWA, E.; DOBRZYNSKI, H. (2015): Comparison of formaldehyde and methanol fixatives used in the detection of ion channel proteins in isolated rat ventricular myocytes by immunofluorescence labelling and confocal microscopy. In *Folia morphologica* 74 (2), pp. 258–261. DOI: 10.5603/FM.2015.0041.
- YANG, CHUN; TIBBITT, MARK W.; BASTA, LENA; ANSETH, KRISTI S. (2014a): Mechanical memory and dosing influence stem cell fate. In *Nature Mater* 13 (6), pp. 645–652. DOI: 10.1038/nmat3889.
- YANG, KISUK; JUNG, HYUNJUNG; LEE, HAK-RAE; LEE, JONG SEUNG; KIM, SU RAN; SONG, KI YEONG *et al.* (2014b): Multiscale, hierarchically patterned topography for directing human neural stem cells into functional neurons. In *ACS nano* 8 (8), pp. 7809–7822. DOI: 10.1021/nn501182f.
- YANG, LANTI; FITIE, CAREL F. C.; VAN DER WERF, KEES O; BENNINK, MARTIN L.; DIJKSTRA, PIETER J.; FEIJEN, JAN (2008): Mechanical properties of single electrospun collagen type I fibers. In *Biomaterials* 29 (8), pp. 955–962. DOI: 10.1016/j.biomaterials.2007.10.058.
- YANG, YONG; WANG, KAI; GU, XIAOSONG; LEONG, KAM W. (2017): Biophysical Regulation of Cell Behavior-Cross Talk between Substrate Stiffness and Nanotopography. In *Engineering (Beijing, China)* 3 (1), pp. 36–54. DOI: 10.1016/J.ENG.2017.01.014.

- YANG, CHUNRONG (2012): Enhanced physicochemical properties of collagen by using EDC/NHS-crosslinking. In *Bull Mater Sci* 35 (5), pp. 913–918. DOI: 10.1007/s12034-012-0376-5.
- YEUNG, TONY; GEORGES, PENELOPE C.; FLANAGAN, LISA A.; MARG, BEATRICE; ORTIZ, MIGUELINA; FUNAKI, MAKOTO *et al.* (2005): Effects of substrate stiffness on cell morphology, cytoskeletal structure, and adhesion. In *Cell motility and the cytoskeleton* 60 (1), pp. 24–34. DOI: 10.1002/cm.20041.
- YIM, EVELYN K. F.; PANG, STELLA W.; LEONG, KAM W. (2007): Synthetic nanostructures inducing differentiation of human mesenchymal stem cells into neuronal lineage. In *Experimental cell research* 313 (9), pp. 1820–1829. DOI: 10.1016/j.yexcr.2007.02.031.
- ZAIDEL-BAR, R.; COHEN, M.; ADDADI, L.; GEIGER, B. (2004): Hierarchical assembly of cell-matrix adhesion complexes. In *Biochemical Society transactions* 32 (Pt3), pp. 416–420. DOI: 10.1042/BST0320416.
- ZEUGOLIS, DIMITRIOS I.; KHEW, SHIH T.; YEW, ELIJAH S. Y.; EKAPUTRA, ANDREW K.; TONG, YEN W.; YUNG, LIN-YUE L. *et al.* (2008): Electro-spinning of pure collagen nano-fibres - just an expensive way to make gelatin? In *Biomaterials* 29 (15), pp. 2293–2305. DOI: 10.1016/j.biomaterials.2008.02.009.
- ZHANG, LIUDI; CASEY, BRENDAN; GALANAKIS, D. K.; MARMORAT, CLEMENT; SKOOG, SHELBY; VORVOLAKOS, KATHERINE *et al.* (2017): The influence of surface chemistry on adsorbed fibrinogen conformation, orientation, fiber formation and platelet adhesion. In *Acta biomaterialia* 54, pp. 164–174. DOI: 10.1016/j.actbio.2017.03.002.
- ZHAO, LINGZHOU; MEI, SHENGLIN; CHU, PAUL K.; ZHANG, YUMEI; WU, ZHIFEN (2010): The influence of hierarchical hybrid micro/nano-textured titanium surface with titania nanotubes on osteoblast functions. In *Biomaterials* 31 (19), pp. 5072–5082. DOI: 10.1016/j.biomaterials.2010.03.014.
- ZHAO, NAN; ZHU, DONGHUI (2014): Collagen self-assembly on orthopedic magnesium biomaterials surface and subsequent bone cell attachment. In *PloS one* 9 (10), e110420. DOI: 10.1371/journal.pone.0110420.
- ZHONG, SHAOPING; TEO, WEE EONG; ZHU, XIAO; BEUERMAN, ROGER W.; RAMAKRISHNA, SEERAM; YUNG, LIN YUE LANRY (2006): An aligned nanofibrous collagen scaffold by electrospinning and its effects on in vitro fibroblast culture. In *Journal of biomedical materials research. Part A* 79 (3), pp. 456–463. DOI: 10.1002/jbm.a.30870.

- ZHU, BOFAN; LI, WEN; CHI, NAIWEI; LEWIS, RANDOLPH V.; OSAMOR, JUDE; WANG, RONG (2017): Optimization of Glutaraldehyde Vapor Treatment for Electrospun Collagen/Silk Tissue Engineering Scaffolds. In *ACS omega* 2 (6), pp. 2439–2450. DOI: 10.1021/acsomega.7b00290.
- ZHU, SHICHEN; YUAN, QIJUAN; YIN, TAO; YOU, JUAN; GU, ZHIPENG; XIONG, SHANBAI; HU, YANG (2018): Self-assembly of collagen-based biomaterials. Preparation, characterizations and biomedical applications. In *J. Mater. Chem. B* 6 (18), pp. 2650–2676. DOI: 10.1039/C7TB02999C.
- ZHU, YANXIA; DONG, ZHUXIN; WEJINYA, UCHECHUKWU C.; JIN, SHA; YE, KAIMING (2011): Determination of mechanical properties of soft tissue scaffolds by atomic force microscopy nanoindentation. In *Journal of biomechanics* 44 (13), pp. 2356–2361. DOI: 10.1016/j.jbiomech.2011.07.010.
- ZOU, YUAN; ZHANG, LIN; YANG, LEI; ZHU, FANG; DING, MINGMING; LIN, FEI *et al.* (2018): "Click" chemistry in polymeric scaffolds. Bioactive materials for tissue engineering. In *Journal of controlled release : official journal of the Controlled Release Society* 273, pp. 160–179. DOI: 10.1016/j.jconrel.2018.01.023.
- ZUO, WEIWEI; ZHU, MEIFANG; YANG, WEN; YU, HAO; CHEN, YANMO; ZHANG, YU (2005): Experimental study on relationship between jet instability and formation of beaded fibers during electrospinning. In *Polym. Eng. Sci.* 45 (5), pp. 704–709. DOI: 10.1002/pen.20304.

Internet Refereces:

- URL 1 <https://www.thermofisher.com/order/catalog/product/A35391#/A35391> (04.06.20)
- URL 2 <https://www.takarabio.com/learning-centers/cell-biology/technical-notes/cell-viability-and-proliferation-measurement> (04.06.20)
- URL 3 <https://www.thermofisher.com/order/catalog/product/R37112#/R37112> (04.06.20)
- URL 4 <https://www.sigmaaldrich.com/catalog/product/aldrich/468495?lang=de®ion=DE> (04.06.20)

Appendix

Materials

Table 9. Materials

Material	Product description	Supplier
12-well plates	Culture Treated polystyrene, Nunc [™] Delta Surface Treatment	Nunc Brand Products, Thermo Fisher Scientific, Germany
Anodized aluminum oxide (AAO) membranes		Whatman, Sigma-Aldrich, Taufkirchen, Germany
Cantilevers	Silicon nitride cantilevers	MLCT Bio, Bruker, Wissembourg, France
Cellulose membranes		Sigma, Steinheim, Germany
Cell culture flasks	25 cm ²	VWR, Darmstadt, Germany
Glass Coverslips	diameter: 15 mm	VWR International, Germany
Object slides	REF: 631-1550	VWR, Germany
Serological pipettes	6133E und 7296K	VWR, Darmstadt, Germany
Petri dishes	7022611	Sarstedt, Nümbrecht, Germany
Petri dishes cell culture treated	7023811	Sarstedt, Nümbrecht, Germany
Petri dishes	60 mm	Sarstedt, Nümbrecht, Germany
Polydimethylsiloxane (PDMS)	-	Distrelec, Bremen, Germany
Sample containers	2427239	Licefa, Salzuflen, Germany
Cuvettes photometer	Cat-No. 7590 15	Brand, Wertheim, Germany

Table 10. Devices

Devices	Product description	Supplier
Atomic Force Microscope	MFP3D	Asylum Research, Santa Barbara, USA
Confocal Laser Microscope	LSM880 system	Carl Zeiss, Oberkochen, Germany
Fluorescence Microscope	Eclipse Ti Inverted Microscope	Nikon, Amsterdam, Netherland
Incubator	Hera Cell 240	Thermo Electron Corporation, Waltham, Massachusetts, USA
MilliQ water filtration device	TKA Wasseraufbereitungssystem	Thermo Fisher Scientific, Schwerte, Germany
Photometer	Ce 1021	Cecil, Cambridge, UK
Pipettes	0.5-10 μ L, 10-100 μ L, 20-200 μ L, 100-1000 μ L, 500-5000 μ L	Eppendorf AG, Hamburg, Germany
Scanning Electron Microscopy	Zeiss Auriga	Zeiss, Oberkochen, Germany
Sputter System	Bal-Tec SCD 005	Leica Microsystems GmbH, Wetzlar, Germany
Thermomixer	Thermomixer C	Eppendorf AG, Hamburg, Germany
Ultrasonication bath	Branson Ultrasonic Cleaner	Branson, Wessling, Germany

Table 11. Chemicals

Chemicals	Product Descriptions	Supplier
Acetic Acid Glacial ACS	CAS: 64-19-7	VWR International, Pennsylvania, USA
ActinRed 555 ReadyProbes reagent	REF: R37112	Life Technologies, Invitrogen, Thermo Fisher Scientific, Schwerte, Germany
Ammoniumbicarbonate (Ammonium Hydrogen Carbonate)	CAS: 1066-33-7	Carl Roth GmbH, Karlsruhe, Germany
APTES	SHBJ 6515	Sigma-Aldrich, Steinheim, Germany
CaCl₂	A247872042	Merck, Darmstadt, Germany
Calcein AM Viability Dye (UltraPure Grade)	REF: 65-0853-39 Stock: 2 mM in dimethylsulfoxide (DMSO)	eBioscience – affimetrix, Thermo Fisher Scientific, Dreieich, Germany
Collagen, from calf skin	CAS: 9007-345 Lot#SLBH0446V	Sigma-Aldrich, Steinheim, Germany
α-D-Glucose		Janssen Chimica, Beerse, Belgium
Dimethylsulfoxide 99.5% for analytical applications	REF: 102811000	FA Grüssing, Filsum, Germany
Disodiumhydrogenphosphate		Merck, Darmstadt, Germany
Dulbecco's Modified Eagle Medium (DMEM)	REF: FG0435-500ml	Merck, Sigma-Aldrich, Steinheim, Germany
D-Glucose	71185/1	Janssen Chimica, Beerse, Belgium
Ethanol absolute AnalaR NORMAPUR ACS	CAS: 64-17-5	VWR International, Pennsylvania, USA
Ethidium homodimer-1	CAS: 61926-22-5 Stock: 4 mM in DMSO	PromoCell GmbH, Promokine, Heidelberg, Germany

Continuation Table 11. Chemicals

Chemicals	Product Descriptions	Supplier
FBS	CAS: 1066-33-7	Merck, Sigma-Aldrich, Steinheim, Germany
Fibrinogen	3011333 und 2896727	Merck, Darmstadt, Germany
Fixogum		Marabu GmbH + Co. KG, Germany
Formaldehyde 37%	8N000092	AppliChem, Darmstadt, Germany
Glutaraldehyde solution 50%	REF: A3166,0100- 100ml	Sigma-Aldrich, Steinheim, Germany
HEPES	A0233527	Roth, Karlsruhe, Germany
KCl	502194907	Sigma, Steinheim, Germany
MgCl₂	S36734305	Merck, Darmstadt, Germany
Na₂HPO₄	K32176680333	Merck, Darmstadt, Germany
NaCl	3E010249	AppliChem, Darmstadt, Germany
NaOH	17L214125	VWR, Darmstadt, Germany
Hydrogen peroxide solution	CAS: 7722-84-1	Sigma-Aldrich, Steinheim, Germany
Nitrogen (aerially)	CAS: 7727-37-9	AIR LIQUIDE, Paris, France
Nuclear Blue Live	REF: R37605	Life Technologies, Invitrogen, Thermo Fisher Scientific, Dreieich, Germany
PBS Tablets	REF: 18912-014	Gibco, Life Technologies, Invitrogen, Thermo Fisher Scientific, Dreieich, Germany
Penicillin/Streptomycin	REF: A2212-50ml	Merck, Sigma-Aldrich, Steinheim, Germany
Potassium chloride		Sigma, Steinheim, Germany
ProLong Gold antifade reagent	CAS: 56-81-5	Life Technologies, Invitrogen, Thermo Fisher Scientific, Dreieich, Germany
Sulfuric acid 95%	CAS: 7664-93-9	VWR, Darmstadt, Germany
Sodium chloride		AppliChem, Darmstadt, Germany

Continuation Table 121. Chemicals

Chemicals	Product Descriptions	Supplier
Sodium hydroxide		VWR, Darmstadt, Germany
Triton	17676525	Roth, Karlsruhe, Germany
Trypsin/EDTA (0,05%/0.02%)	0222G	Biochrom, Berlin, Germany
Hydrogen peroxide 30%	CAS: 7722-84-1	Sigma-Aldrich, Steinheim, Germany
(4-[3-(4-Iodophenyl)-2-(4-nitrophenyl)-2H-5-tetrazolio]-1,3-benzene disulfonate) WST-1	32508400	Sigma, Mannheim, Germany

Table 13. Solutions

Solution	Components
<p align="center">Cell culture medium for NIH 3T3 mouse fibroblasts (CLS Cell Lines Service GmbH, Eppelheim, Germany)</p>	<p>94% DMEM cell culture medium (Biochrom GmbH, Germany) 5% FBS (Sigma-Aldrich Chemie GmbH, Germany) 1% P/S pH 7.4 adjusted with 5% CO₂</p>
<p align="center">Cell culture medium for old NIH 3T3 mouse fibroblasts (ATCC CRL1658, a kind gift from Louis Lim, Institute of Molecular and Cell Biology ASTAR Singapore)</p>	<p>88% DMEM cell culture medium (Biochrom GmbH, Germany) 10% FBS (Sigma-Aldrich Chemie GmbH, Germany) 2% P/S pH 7.4 adjusted with 5% CO₂</p>
<p align="center">Incubation buffer for WST-1 assay</p>	<p>1.8 mM CaCl₂ 1 mM MgCl₂ 5.4 mM KCl 145 mM NaCl 0.8 mM Na₂HPO₄ 20 mM HEPES 20 mM D-Glucose 1 M NaOH pH=7.4 (measured at 37 C)</p>
<p align="center">Piranha acid</p>	<p>2 parts 95% sulfuric acid 1 part 30% hydrogen peroxide</p>
<p align="center">Phosphate buffered saline (PBS)</p>	<p>10 mM Potassium phosphate 150 mM Sodium chloride pH 7.3 – 7.5</p>

Atomic force microscopy

Figure 81 shows the mechanical analysis of a collagen scaffold. The slope of the force curve was approximately 1. Thus, the software defined the scaffold mechanic infinitely stiff.

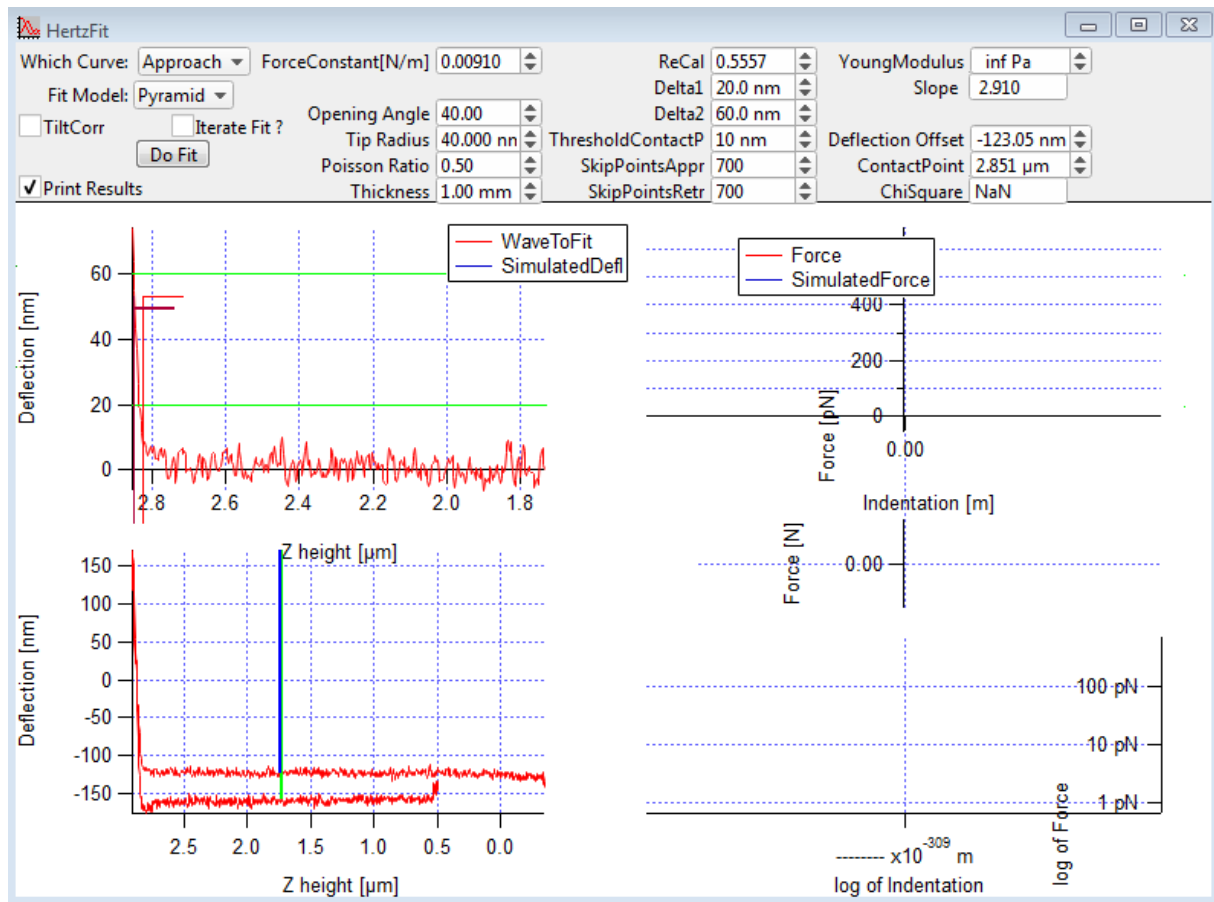


Figure 82. Screenshot of approach and retract curves on nanofibrous collagen scaffold prepared with 2.5 mg ml⁻¹ collagen. The Cantilevers were too soft to measure the stiff collagen substrates. The HertzFit window shows the Young's Modulus as infinitely stiff.

Live Cell tracking

All histograms of all samples for live-cell tracking are shown in this section. For each sample type, all histograms for each independent experiment (n=1 to n=4) are shown in a different color. The triplicates are shown in the same color for each n. The lowest black histogram always represents the pooled migration velocities for all experiments for each respective sample type.

Velocity analysis of fibroblasts on collagen

Histograms for migration velocities on collagen scaffolds prepared with 0.5 mg ml⁻¹:

Collagen Nanofibers (0.5 mg ml⁻¹)

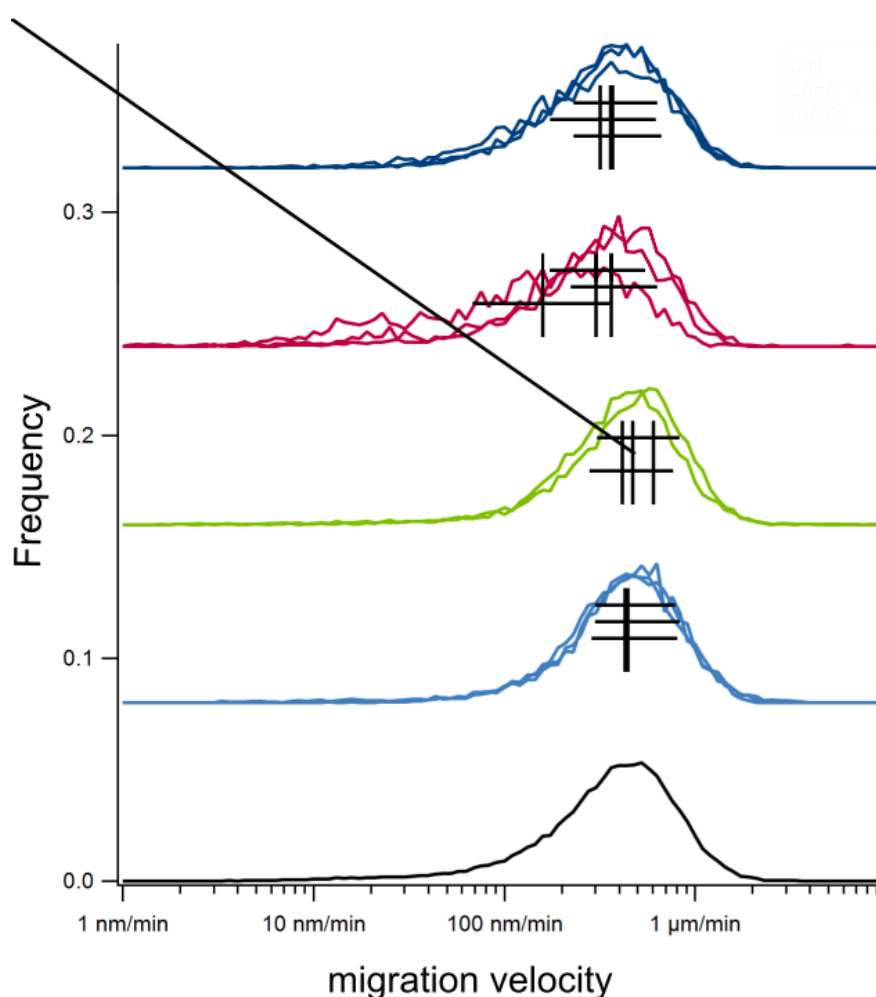


Figure 83. Normalized pooled histograms of migration velocities of 3T3 fibroblasts on nanofibrous collagen prepared with 0.5 mg ml⁻¹ collagen. This graph displays the median velocities. The velocities are plotted on a logarithmic axis. Median velocities of cells on the same dependent triplicates are shown in the same color. Different independent experiments are shown in different colors n=1 (light blue), n=2 (green), n=3 (purple) and n=4 (dark blue). Vertical black lines in the histograms represent the median velocity. Horizontal black lines in the histograms represent the standard deviation. The black histogram represents the pooled median migration velocity of cells on glass (all experiments pooled). Overall, all histograms are very similar indicating reproducible results for independent experiments.

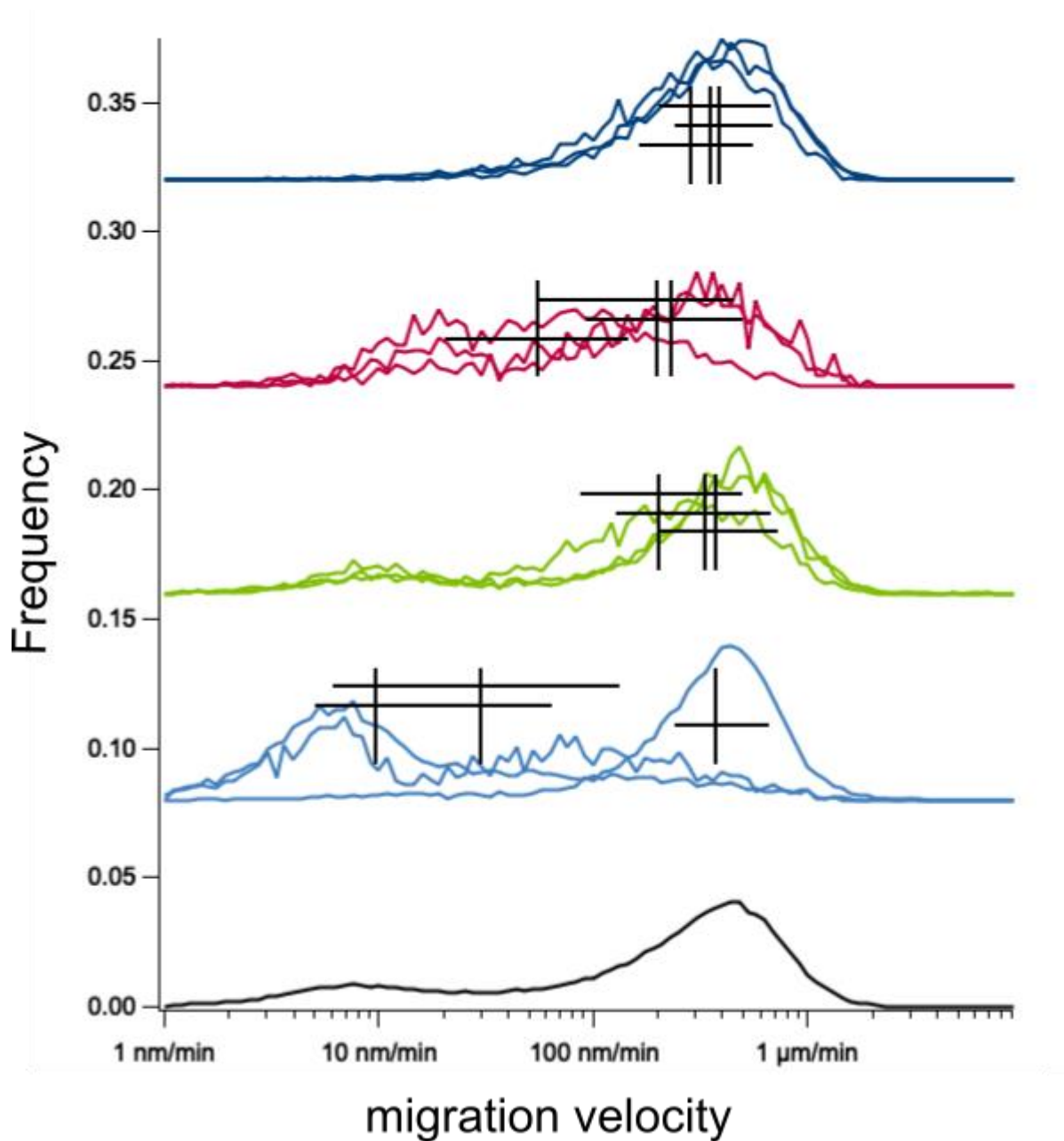
0.5 mg ml⁻¹ smooth collagen (0.5 mg ml⁻¹)

Figure 84. Normalized pooled histograms of migration velocities of 3T3 fibroblasts on smooth collagen prepared with 0.5 mg ml⁻¹ collagen. This graph displays the median velocities. The velocities are plotted on a logarithmic axis. Median velocities of cells on the same dependent triplicates are shown in the same color. Different independent experiments are shown in different colors n=1 (light blue), n=2 (green), n=3 (purple) and n=4 (dark blue). Vertical black lines in the histograms represent the median velocity. Horizontal black lines in the histograms represent the standard deviation. The black histogram represents the pooled median migration velocity of cells on glass (all experiments pooled).

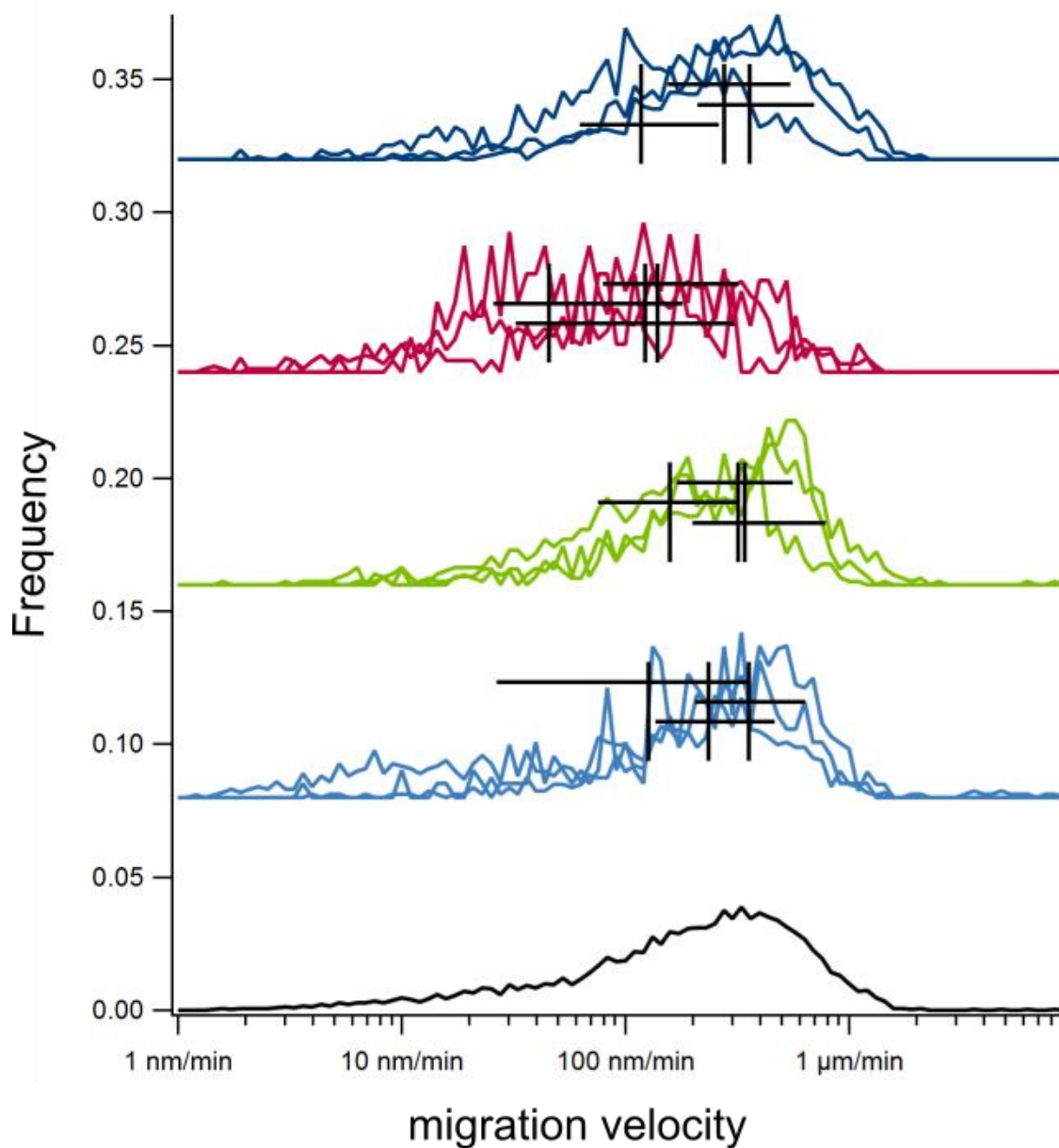
Collagen nanofibrous are of binary scaffolds (0.5 mg ml^{-1})

Figure 85. Normalized pooled histograms of migration velocities of 3T3 fibroblasts on nanofibrous areas of binary patterned collagen prepared with 0.5 mg ml^{-1} collagen. This graph displays the median velocities. The velocities are plotted on a logarithmic axis. Median velocities of cells on the same dependent triplicates are shown in the same color. Different independent experiments are shown in different colors $n=1$ (light blue), $n=2$ (green), $n=3$ (purple) and $n=4$ (dark blue). Vertical black lines in the histograms represent the median velocity. Horizontal black lines in the histograms represent the standard deviation. The black histogram represents the pooled median migration velocity of cells on glass (all experiments pooled). Overall, all histograms are very similar indicating reproducible results for independent experiments.

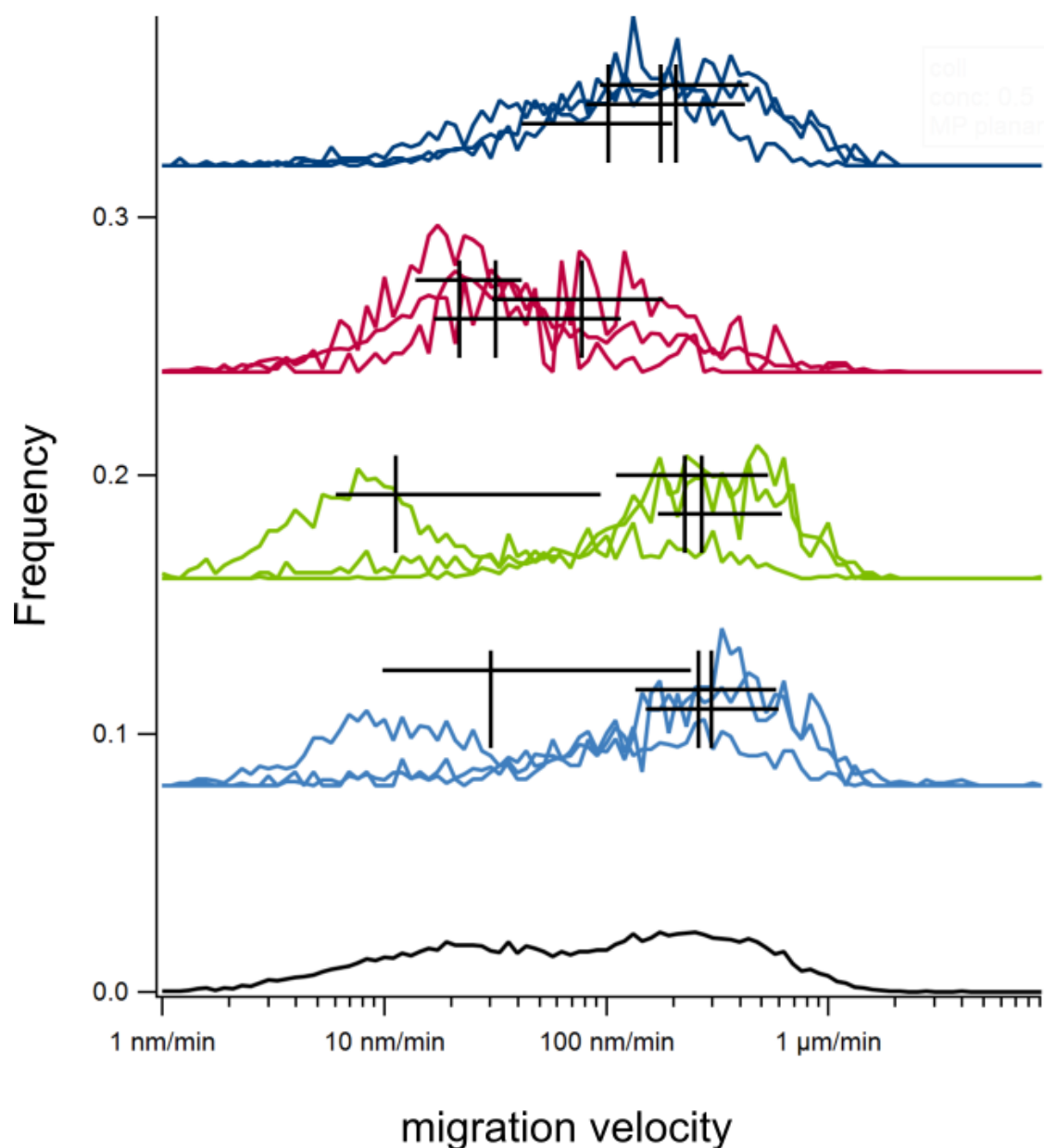
Smooth area of binary scaffolds (0.5 mg ml^{-1})

Figure 86. Normalized pooled histograms of migration velocities of 3T3 fibroblasts on smooth areas of binary patterned collagen prepared with 0.5 mg ml^{-1} collagen. This graph displays the median velocities. The velocities are plotted on a logarithmic axis. Median velocities of cells on the same dependent triplicates are shown in the same color. Different independent experiments are shown in different colors $n=1$ (light blue), $n=2$ (green), $n=3$ (purple) and $n=4$ (dark blue). Vertical black lines in the histograms represent the median velocity. Horizontal black lines in the histograms represent the standard deviation. The black histogram represents the pooled median migration velocity of cells on glass (all experiments pooled). Overall all histograms are very similar indicating reproducible results for independent experiments. The distribution is very broad and two peaks are visible.

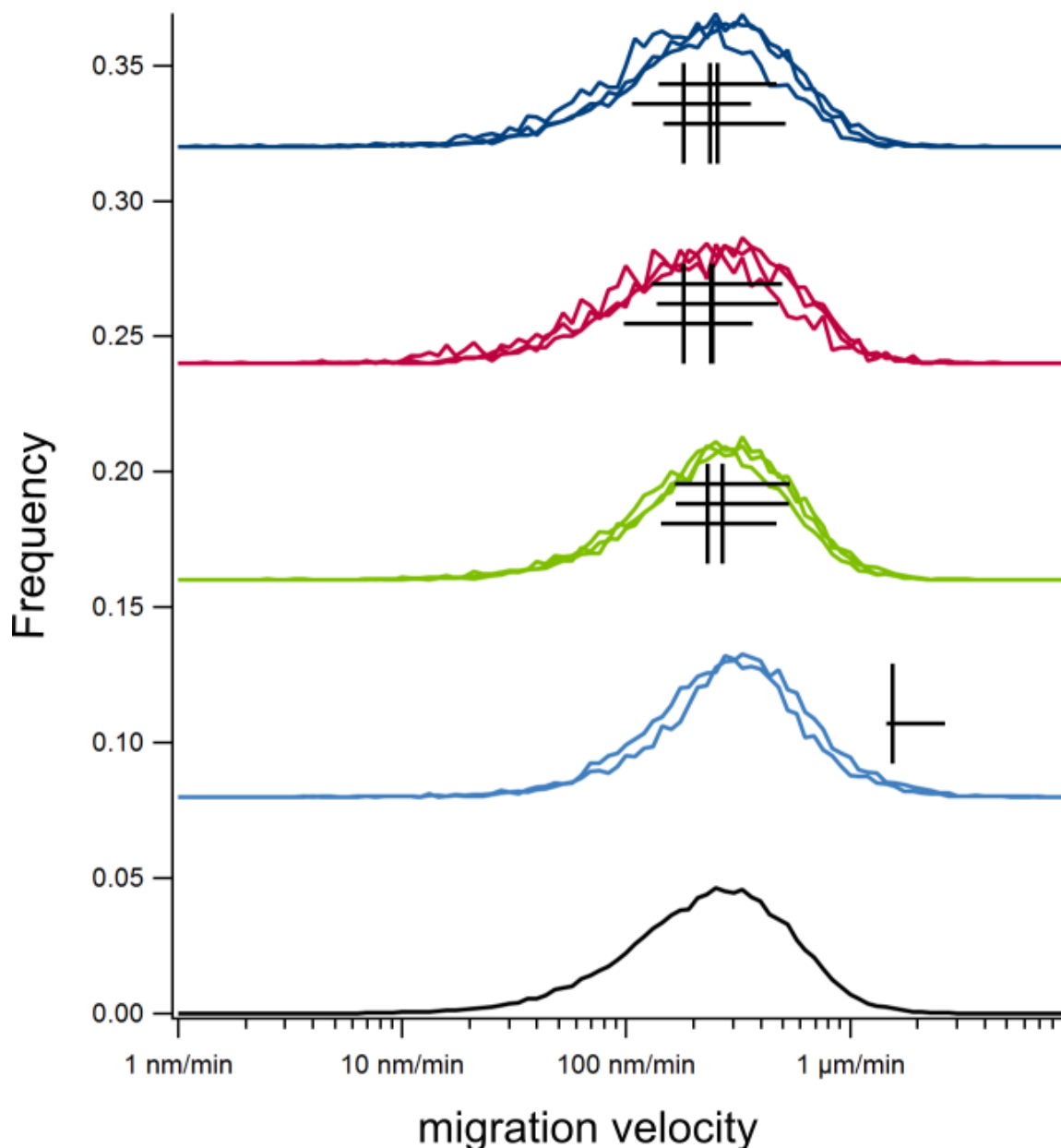
Glass (0.5 mg ml^{-1})

Figure 87. Normalized pooled histograms of migration velocities of 3T3 fibroblasts on glass, which was used as a reference in the collagen experiments with 0.5 mg ml^{-1} collagen. This graph displays the median velocities. The velocities are plotted on a logarithmic axis. Median velocities of cells on the same dependent triplicates are shown in the same color. Different independent experiments are shown in different colors n=1 (light blue), n=2 (green), n=3 (purple) and n=4 (dark blue). Vertical black lines in the histograms represent the median velocity. Horizontal black lines in the histograms represent the standard deviation. The black histogram represents the pooled median migration velocity of cells on glass (all experiments pooled). Overall all histograms are very similar, indicating reproducible results for independent experiments.

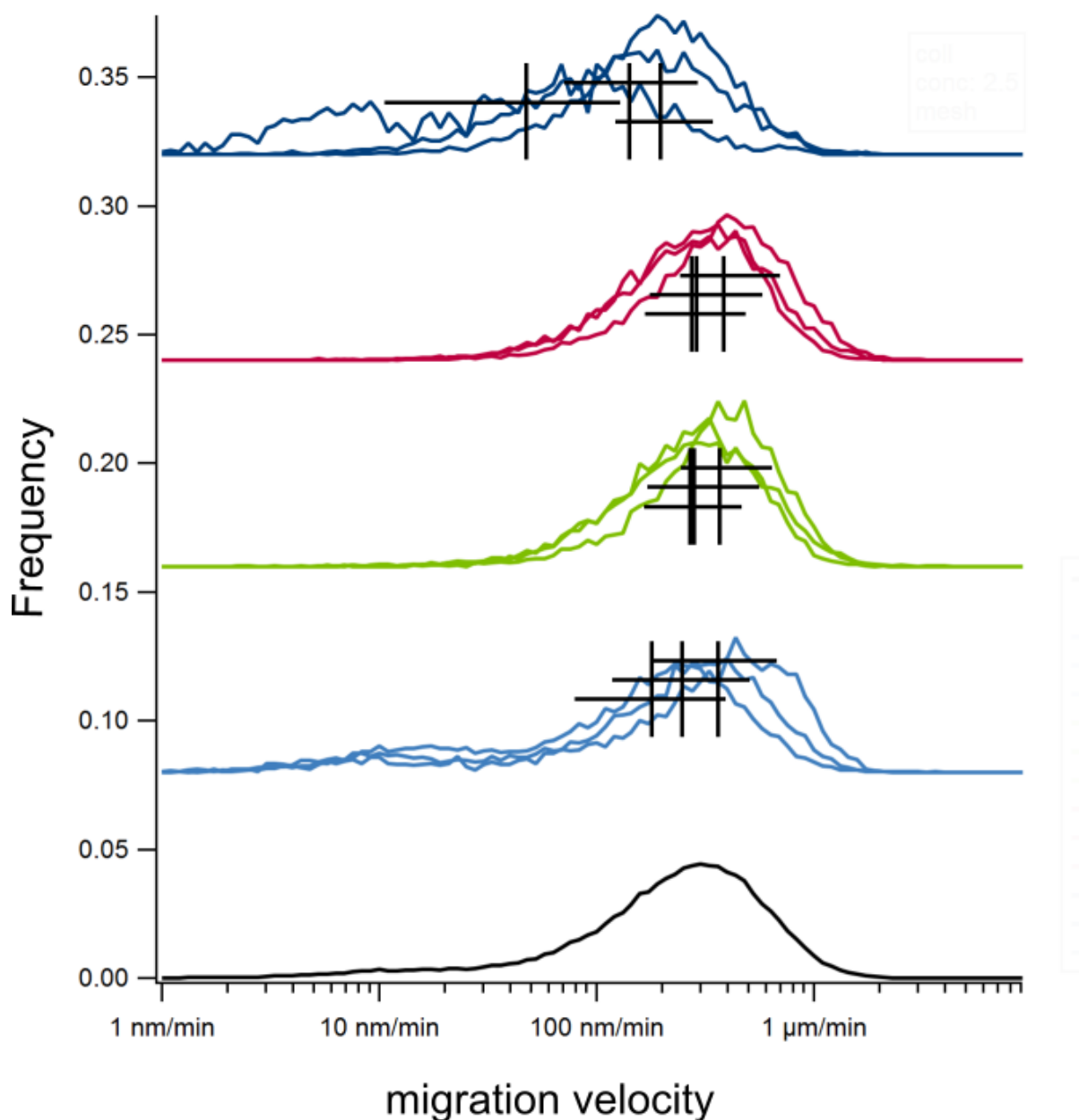
Histograms for migration velocities on collagen scaffolds prepared with 2.5 mg ml⁻¹:**Collagen Nanofibers (2.5 mg ml⁻¹)**

Figure 88. Normalized pooled histograms of migration velocities of 3T3 fibroblasts on nanofibrous collagen prepared with 2.5 mg ml⁻¹ collagen. This graph displays the median velocities. The velocities are plotted on a logarithmic axis. Median velocities of cells on the same dependent triplicates are shown in the same color. Different independent experiments are shown in different colors n=1 (light blue), n=2 (green), n=3 (purple) and n=4 (dark blue). Vertical black lines in the histograms represent the median velocity. Horizontal black lines in the histograms represent the standard deviation. The black histogram represents the pooled median migration velocity of cells on glass (all experiments pooled). Overall all histograms are very similar indicating reproducible results for independent experiments.

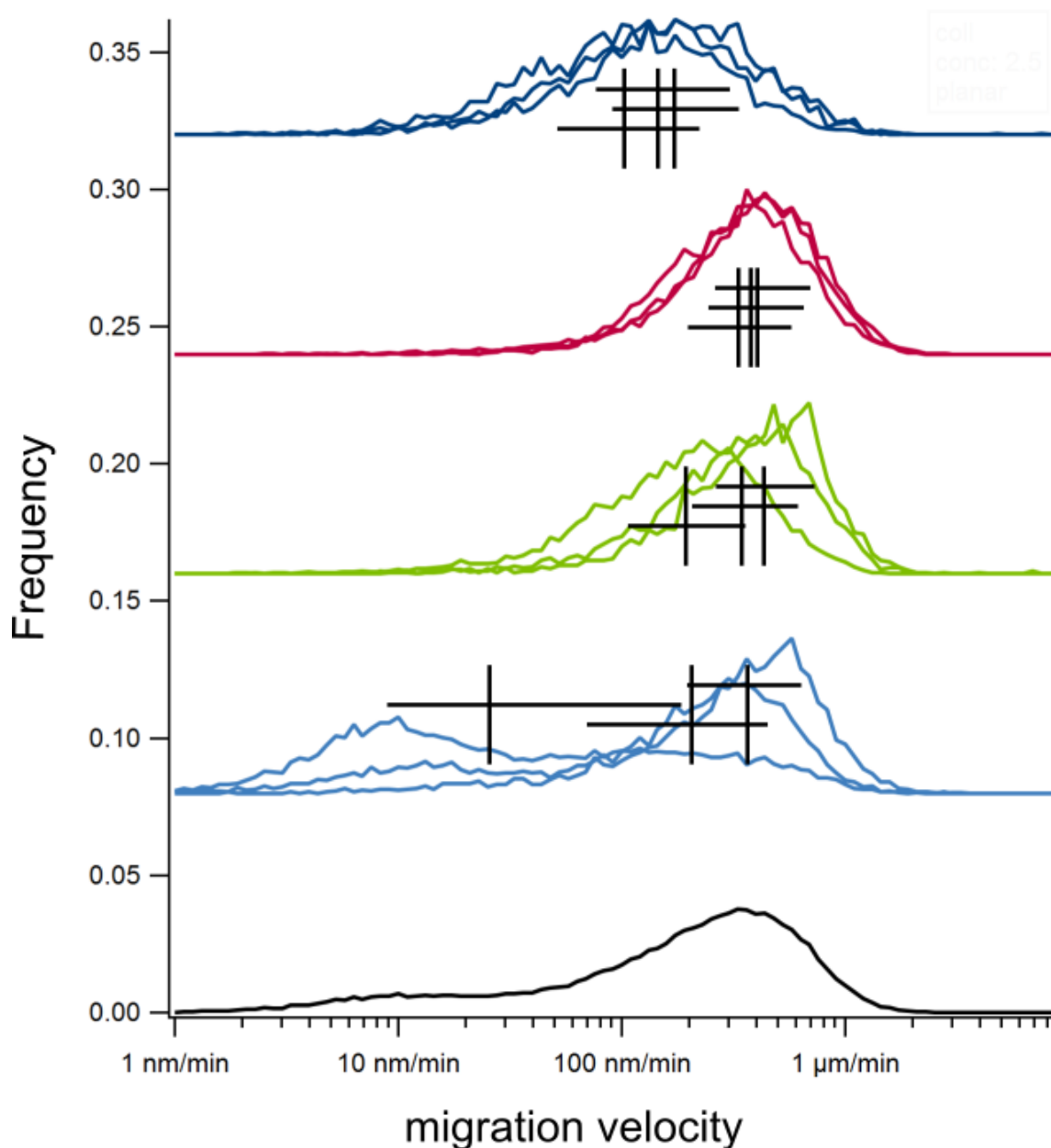
Smooth Collagen (2.5 mg ml^{-1})

Figure 89. Normalized pooled histograms of migration velocities of 3T3 fibroblasts on smooth collagen prepared with 2.5 mg ml^{-1} collagen. This graph displays the median velocities. The velocities are plotted on a logarithmic axis. Median velocities of cells on the same dependent triplicates are shown in the same color. Different independent experiments are shown in different colors $n=1$ (light blue), $n=2$ (green), $n=3$ (purple) and $n=4$ (dark blue). Vertical black lines in the histograms represent the median velocity. Horizontal black lines in the histograms represent the standard deviation. The black histogram represents the pooled median migration velocity of cells on glass (all experiments pooled). Overall all histograms are very similar indicating reproducible results for independent experiments.

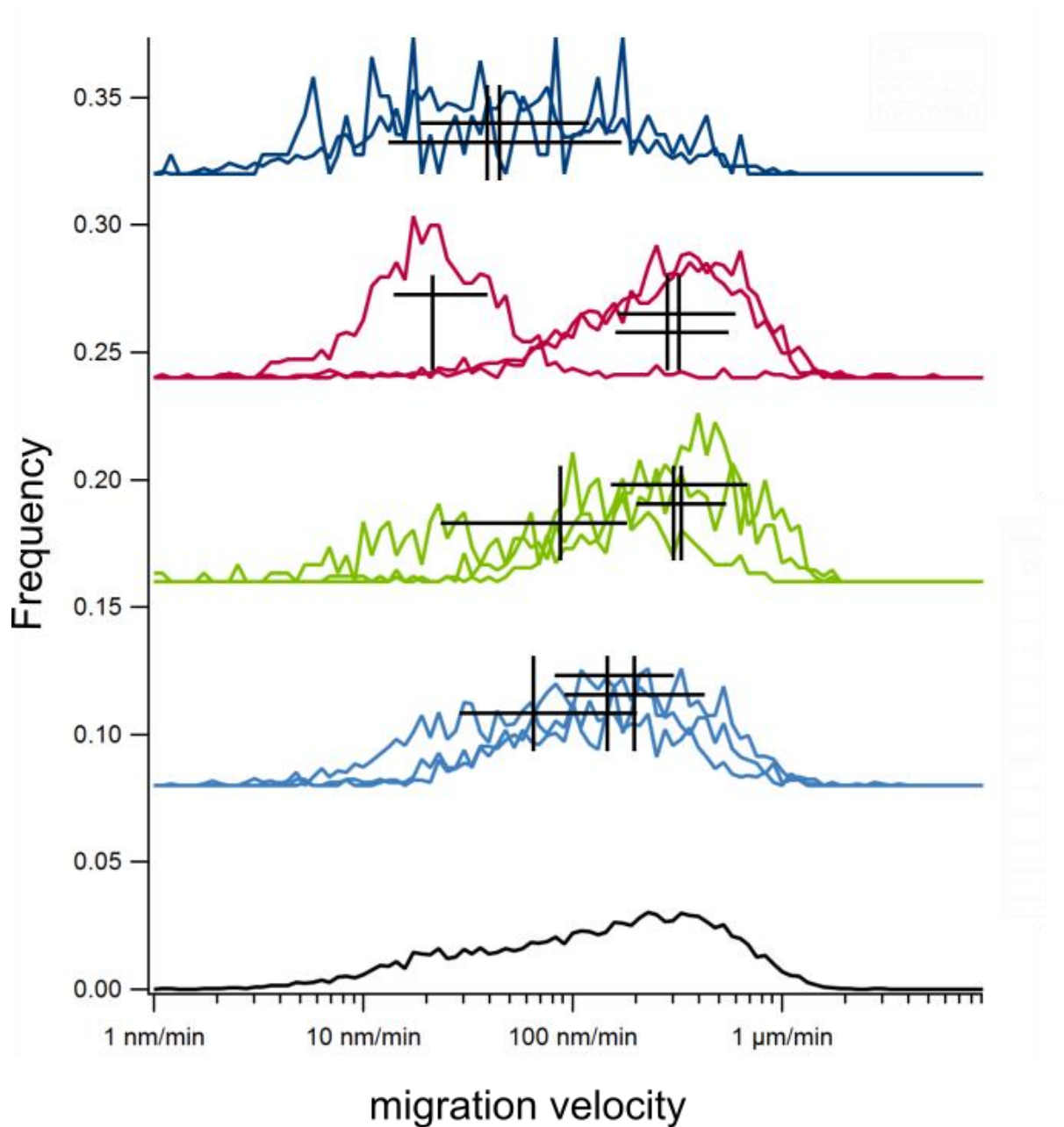
Nanofibrous are of binary Scaffolds (2.5 mg ml^{-1})

Figure 90. Normalized pooled histograms of migration velocities of 3T3 fibroblasts on nanofibrous areas of binary patterned collagen prepared with 2.5 mg ml^{-1} collagen. This graph displays the median velocities. The velocities are plotted on a logarithmic axis. Median velocities of cells on the same dependent triplicates are shown in the same color. Different independent experiments are shown in different colors n=1 (light blue), n=2 (green), n=3 (purple) and n=4 (dark blue). Vertical black lines in the histograms represent the median velocity. Horizontal black lines in the histograms represent the standard deviation. The black histogram represents the pooled median migration velocity of cells on glass (all experiments pooled).

Smooth area of binary scaffolds (2.5 mg ml^{-1})

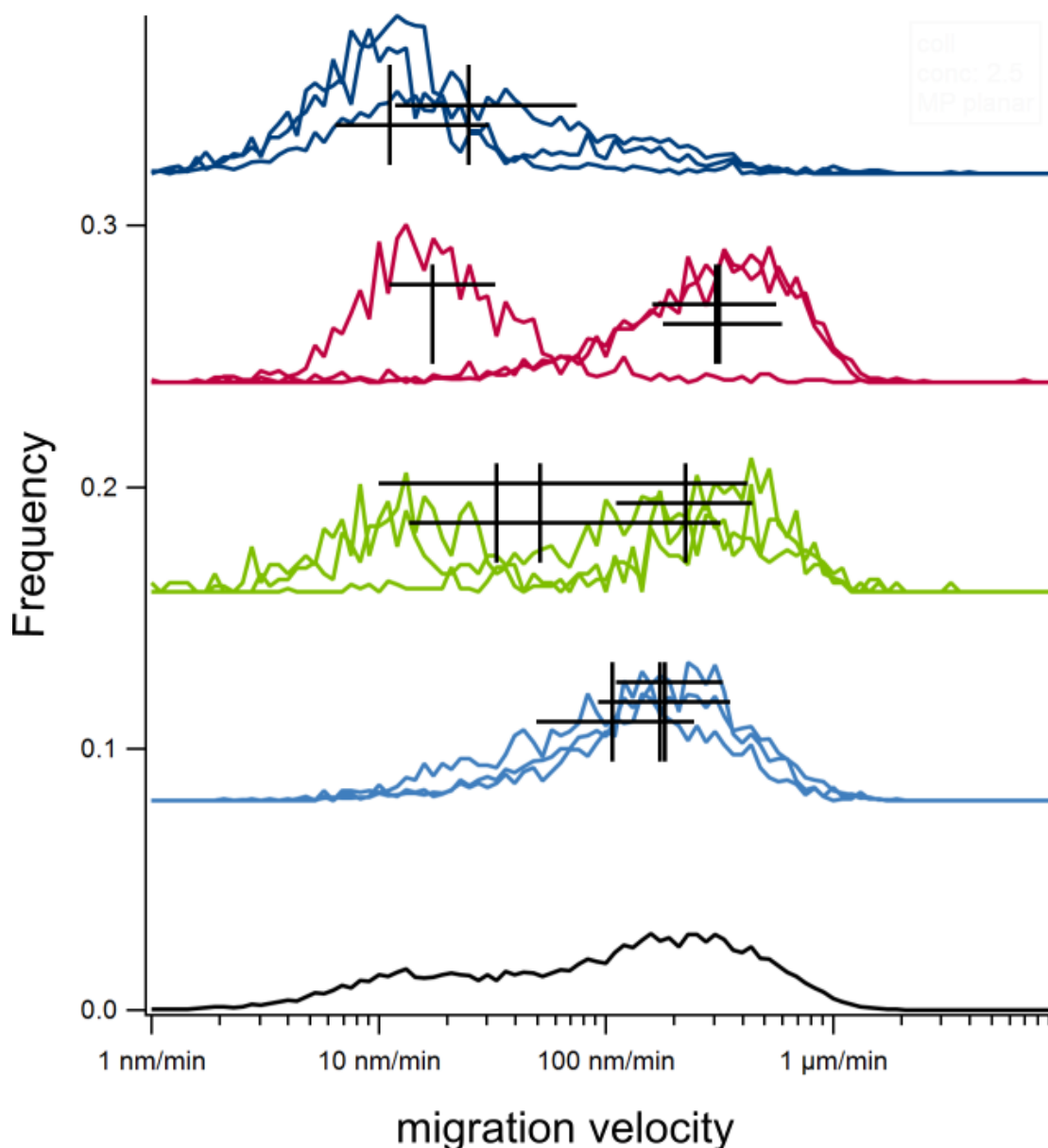


Figure 91. Normalized pooled histograms of migration velocities of 3T3 fibroblasts on smooth areas of binary patterned collagen prepared with 2.5 mg ml^{-1} collagen. This graph displays the median velocities. The velocities are plotted on a logarithmic axis. Median velocities of cells on the same dependent triplicates are shown in the same color. Different independent experiments are shown in different colors $n=1$ (light blue), $n=2$ (green), $n=3$ (purple) and $n=4$ (dark blue). Vertical black lines in the histograms represent the median velocity. Horizontal black lines in the histograms represent the standard deviation. The black histogram represents the pooled median migration velocity of cells on glass (all experiments pooled). The distribution is very broad and two peaks are visible.

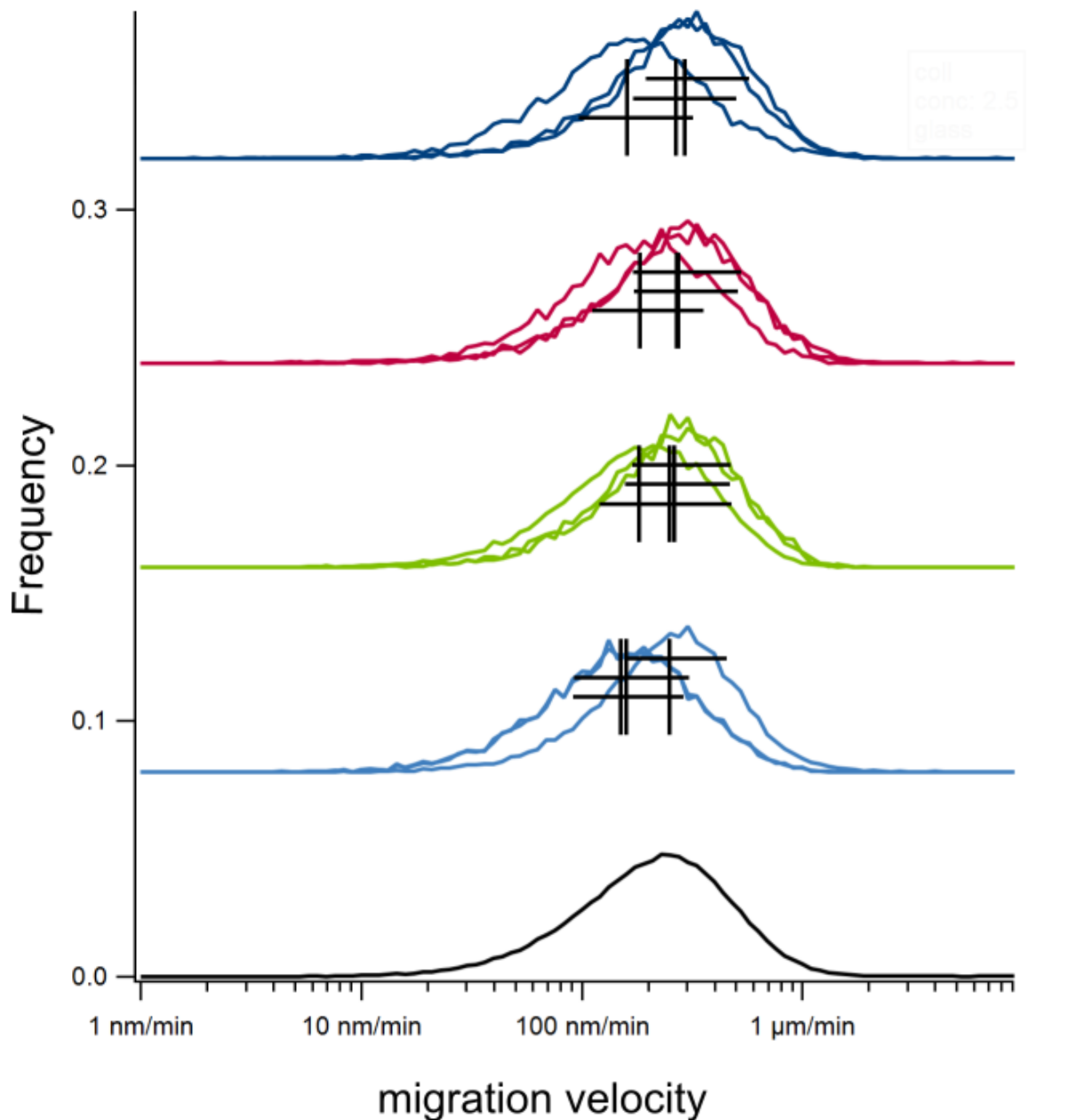
Glass (2.5 mg ml^{-1})

Figure 92. Normalized pooled histograms of migration velocities of 3T3 fibroblasts on glass, which was used as a reference substrate in the collagen series with 2.5 mg ml^{-1} . This graph displays the median velocities. The velocities are plotted on a logarithmic axis. Median velocities of cells on the same dependent triplicates are shown in the same color. Different independent experiments are shown in different colors n=1 (light blue), n=2 (green), n=3 (purple) and n=4 (dark blue). Vertical black lines in the histograms represent the median velocity. Horizontal black lines represent the standard deviation. The black histogram represents the pooled median migration velocity of cells on glass (all experiments pooled). Overall all histograms are very similar, indicating reproducible results for independent experiments.

Table 14. Overview cell velocities (nm min⁻¹) with standard deviation and Cohens's d of 3T3 fibroblasts on collagen scaffolds prepared with 0.5 mg ml⁻¹ collagen.

	N 1	N2	Sample type 1	Sample type 2	avg1	stdv1	avg2	stdv2	Cohen's d
Without fit	65509	44152	Glass	Smooth	239.8832919	-13.5450717	122.4616199	-13.4987714	0.5195
With fit					267.3006409	-19.5727671	341.9794425	-28.4489239	-0.212
Without fit	65509	58777	Glass	Fibers	239.8832919	-13.5450717	349.945167	-20.5544001	-0.4355
With fit					267.3006409	-19.5727671	429.5364268	-27.6597982	-0.4592
Without fit	65509	8213	Glass	Binary-Smooth	239.8832919	-13.5450717	79.43282347	-7.90076901	1.132
With fit					267.3006409	-19.5727671	180.7174126	-20.8348979	0.3246
Without fit	65509	7423	Glass	Binary-Fibers	239.8832919	-13.5450717	180.3017741	-14.5973856	0.3141
With fit					267.3006409	-19.5727671	273.5268726	-24.2685811	-0.02046
Without fit	44152	58777	Smooth	Fibers	122.4616199	-13.4987714	349.945167	-20.5544001	-0.7933
With fit					341.9794425	-28.4489239	429.5364268	-27.6597982	-0.2114
Without fit	44152	8213	Smooth	Binary-Smooth	122.4616199	-13.4987714	79.43282347	-7.90076901	0.2487
With fit					341.9794425	-28.4489239	180.7174126	-20.8348979	0.4753
Without fit	44152	7423	Smooth	Binary-Fibers	122.4616199	-13.4987714	180.3017741	-14.5973856	-0.2295
With fit					341.9794425	-28.4489239	273.5268726	-24.2685811	0.178
Without fit	58777	8213	Fibers	Binary-Smooth	349.945167	-20.5544001	79.43282347	-7.90076901	1.488
With fit					429.5364268	-27.6597982	180.7174126	-20.8348979	0.7983
Without fit	58777	7423	Fibers	Binary-Fibers	349.945167	-20.5544001	180.3017741	-14.5973856	0.7173
With fit					429.5364268	-27.6597982	273.5268726	-24.2685811	0.4531
Without fit	8213	7423	Binary- lanar	Binary-Fibers	79.43282347	-7.90076901	180.3017741	-14.5973856	-0.5605
With fit					180.7174126	-20.8348979	273.5268726	-24.2685811	-0.2598

Table 15. Overview cell velocities (nm min⁻¹) with standard deviation and Cohens's d of 3T3 fibroblasts on collagen scaffolds prepared with 2.5 mg ml⁻¹ collagen.

	N 1	N2	Sample type 1	Sample type 2	avg1	stdv1	avg2	stdv2	Cohen's d
Without fit	109425	69995	Glass	Smooth	199.5262315	-10.7803725	157.3982864	-14.2683409	0.2155
With fit					222.3309891	-15.8502312	285.1018268	-23.9799168	-0.2141
Without fit	109425	73242	Glass	Fibers	199.5262315	-10.7803725	220.8004733	-15.1568113	-0.1083
With fit					222.3309891	-15.8502312	286.417797	-21.112533	-0.2318
Without fit	109425	11049	Glass	Binary-Smooth	199.5262315	-10.7803725	64.71426157	-6.39851122	1.203
With fit					222.3309891	-15.8502312	188.7991349	-20.533731	0.141
Without fit	109425	8681	Glass	Binary-Fibers	199.5262315	-10.7803725	122.7439231	-10.5391758	0.5507
With fit					222.3309891	-15.8502312	199.5262315	-22.8948906	0.09336
Without fit	69995	73242	Smooth	Fibers	157.3982864	-14.2683409	220.8004733	-15.1568113	-0.271
With fit					285.1018268	-23.9799168	286.417797	-21.112533	-0.004756
Without fit	69995	11049	Smooth	Binary-Smooth	157.3982864	-14.2683409	64.71426157	-6.39851122	0.6125
With fit					285.1018268	-23.9799168	188.7991349	-20.533731	0.3098
Without fit	69995	8681	Smooth	Binary-Fibers	157.3982864	-14.2683409	122.7439231	-10.5391758	0.1765
With fit					285.1018268	-23.9799168	199.5262315	-22.8948906	0.268
Without fit	73242	11049	Fibers	Binary-Smooth	220.8004733	-15.1568113	64.71426157	-6.39851122	1.07
With fit					286.417797	-21.112533	188.7991349	-20.533731	0.3481
Without fit	73242	8681	Fibers	Binary-Fibers	220.8004733	-15.1568113	122.7439231	-10.5391758	0.5388
With fit					286.417797	-21.112533	199.5262315	-22.8948906	0.3028
Without fit	11049	8681	Binary-smooth	Binary-Fibers	64.71426157	-6.39851122	122.7439231	-10.5391758	-0.4196
With fit					188.7991349	-20.533731	199.5262315	-22.8948906	-0.03223

Velocity analysis of fibroblasts on fibrinogen

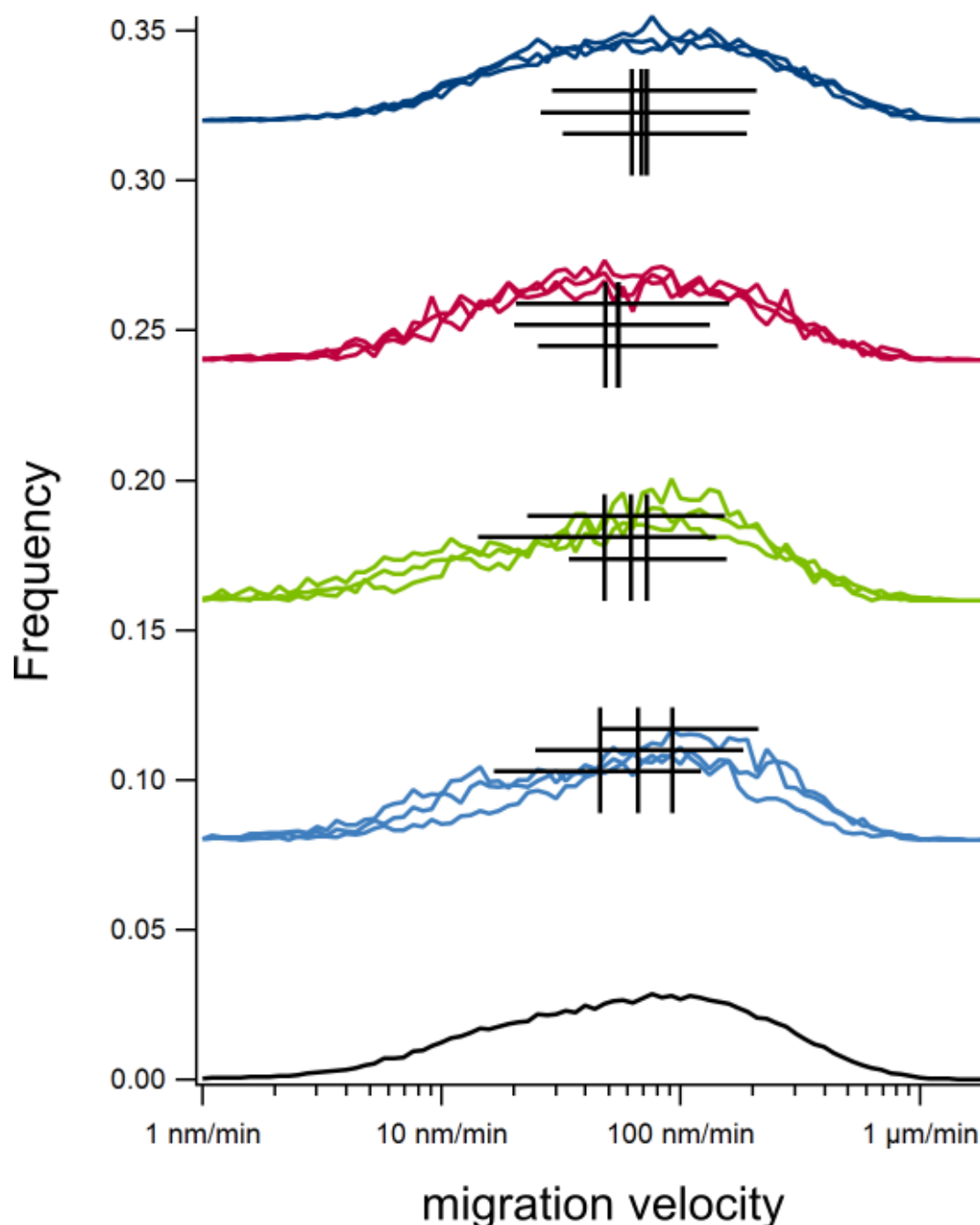
Fibrinogen Nanofibers

Figure 93. Normalized pooled histograms of migration velocities of 3T3 fibroblasts on nanofibrous fibrinogen prepared with 5 mg ml⁻¹ fibrinogen. This graph displays the median velocities. The velocities are plotted on a logarithmic axis. Median velocities of cells on the same dependent triplicates are shown in the same color. Different independent experiments are shown in different colors n=1 (light blue), n=2 (green), n=3 (purple) and n=4 (dark blue). Vertical black lines in the histograms represent the median velocity. Horizontal black lines in the histograms represent the standard deviation. The black histogram represents the pooled median migration velocity of cells on glass (all experiments pooled). Overall, the histograms are very similar indicating reproducible results for independent experiments.

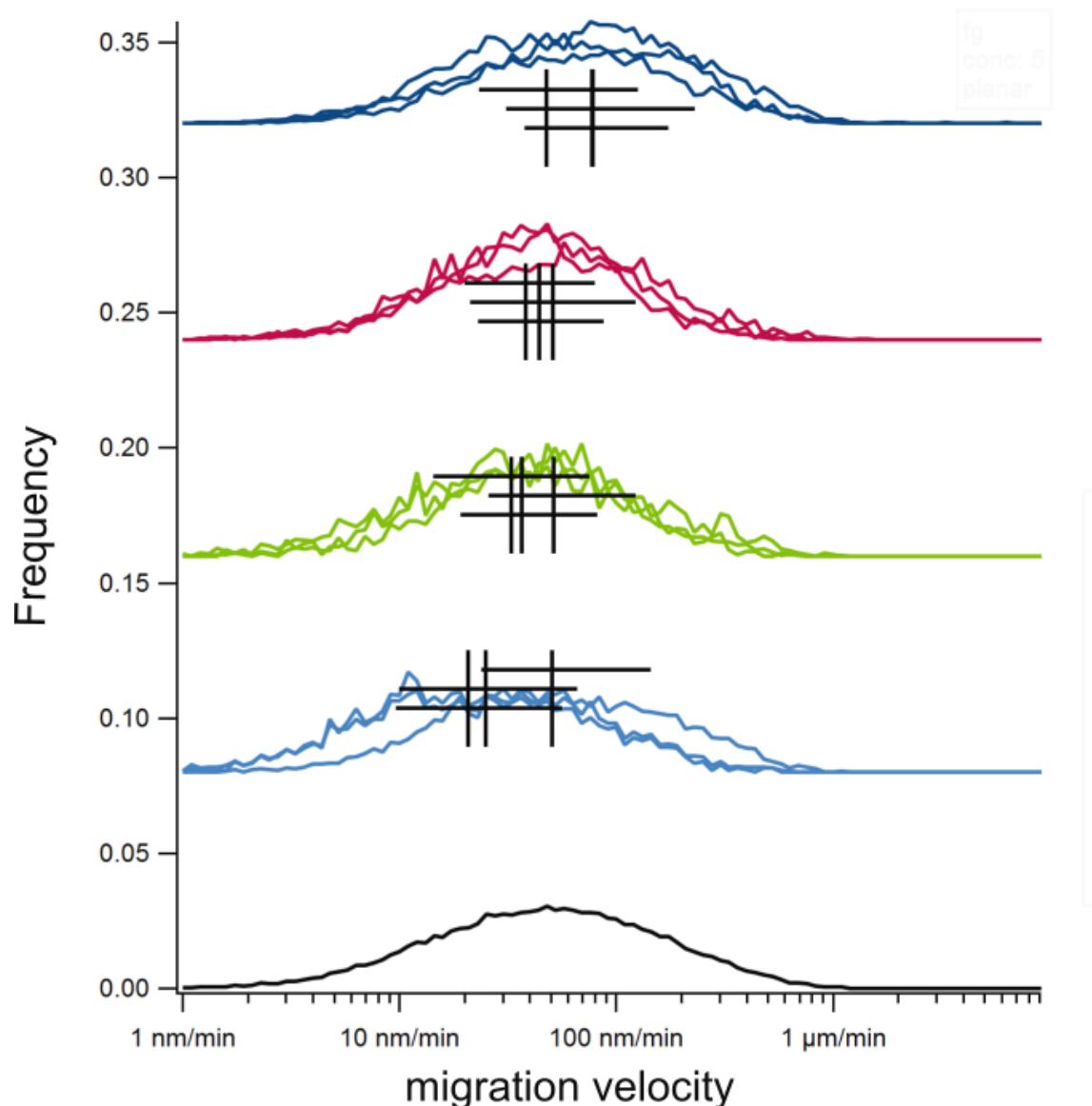
Planar Fibrinogen

Figure 94. Normalized pooled histograms of migration velocities of 3T3 fibroblasts on planar fibrinogen prepared with 5 mg ml⁻¹ fibrinogen. This graph displays the median velocities. The velocities are plotted on a logarithmic axis. Median velocities of cells on the same dependent triplicates are shown in the same color. Different independent experiments are shown in different colors n=1 (light blue), n=2 (green), n=3 (purple) and n=4 (dark blue). Vertical black lines in the histograms represent the median velocity. Horizontal black lines in the histograms represent the standard deviation. The black histogram represents the pooled median migration velocity of cells on glass (all experiments pooled). Overall, all histograms are very similar indicating reproducible results for independent experiments.

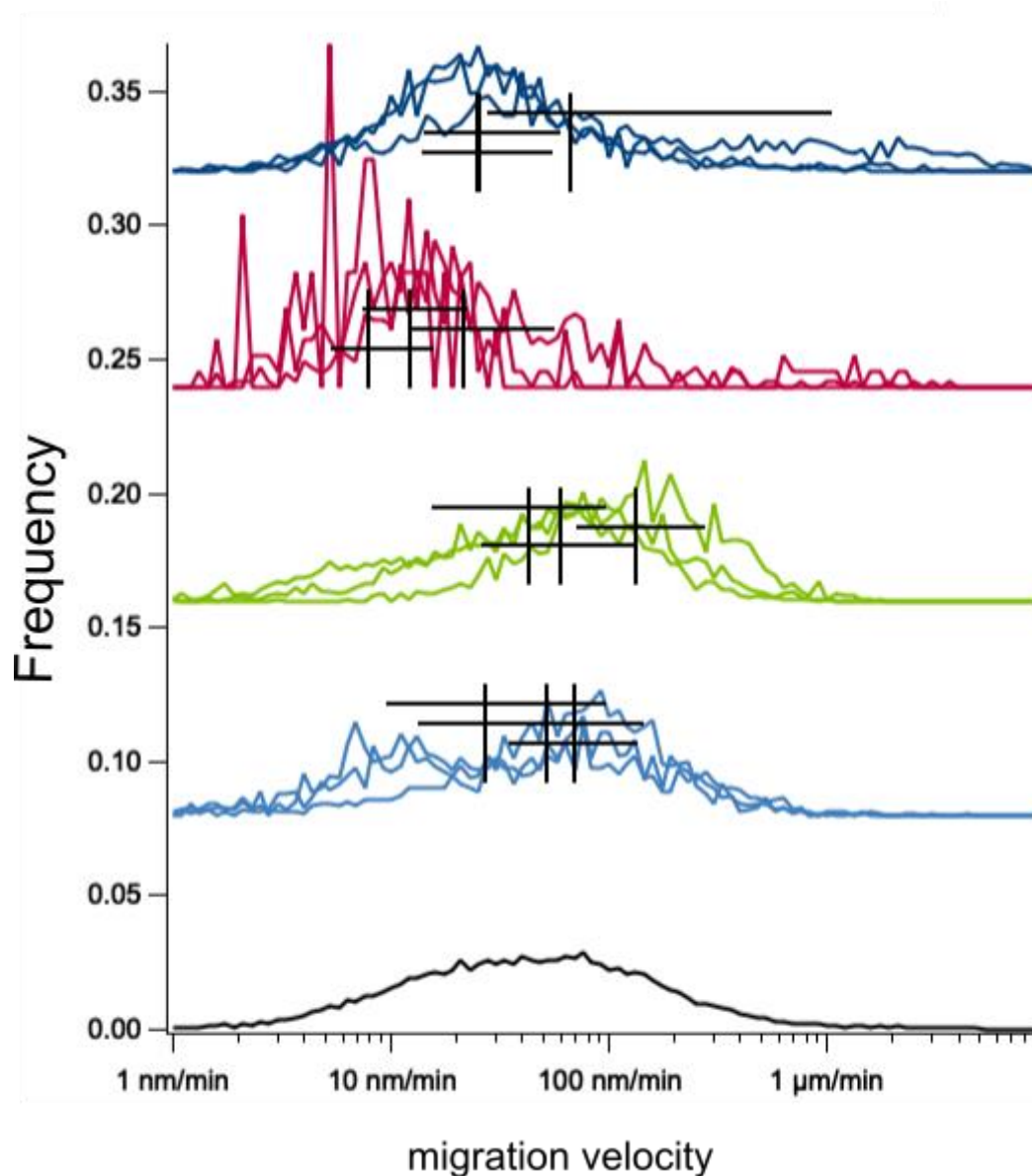
Nanofibrous area of binary fibrinogen scaffolds

Figure 95. Normalized pooled histograms of migration velocities of 3T3 fibroblasts on the nanofibrous area of binary patterned fibrinogen prepared with 5 mg ml^{-1} fibrinogen. This graph displays the median velocities. The velocities are plotted on a logarithmic axis. Median velocities of cells on the same dependent triplicates are shown in the same color. Different independent experiments are shown in different colors $n=1$ (light blue), $n=2$ (green), $n=3$ (purple) and $n=4$ (dark blue). Vertical black lines in the histograms represent the median velocity. Horizontal black lines in the histograms represent the standard deviation. The black histogram represents the pooled median migration velocity of cells on glass (all experiments pooled).

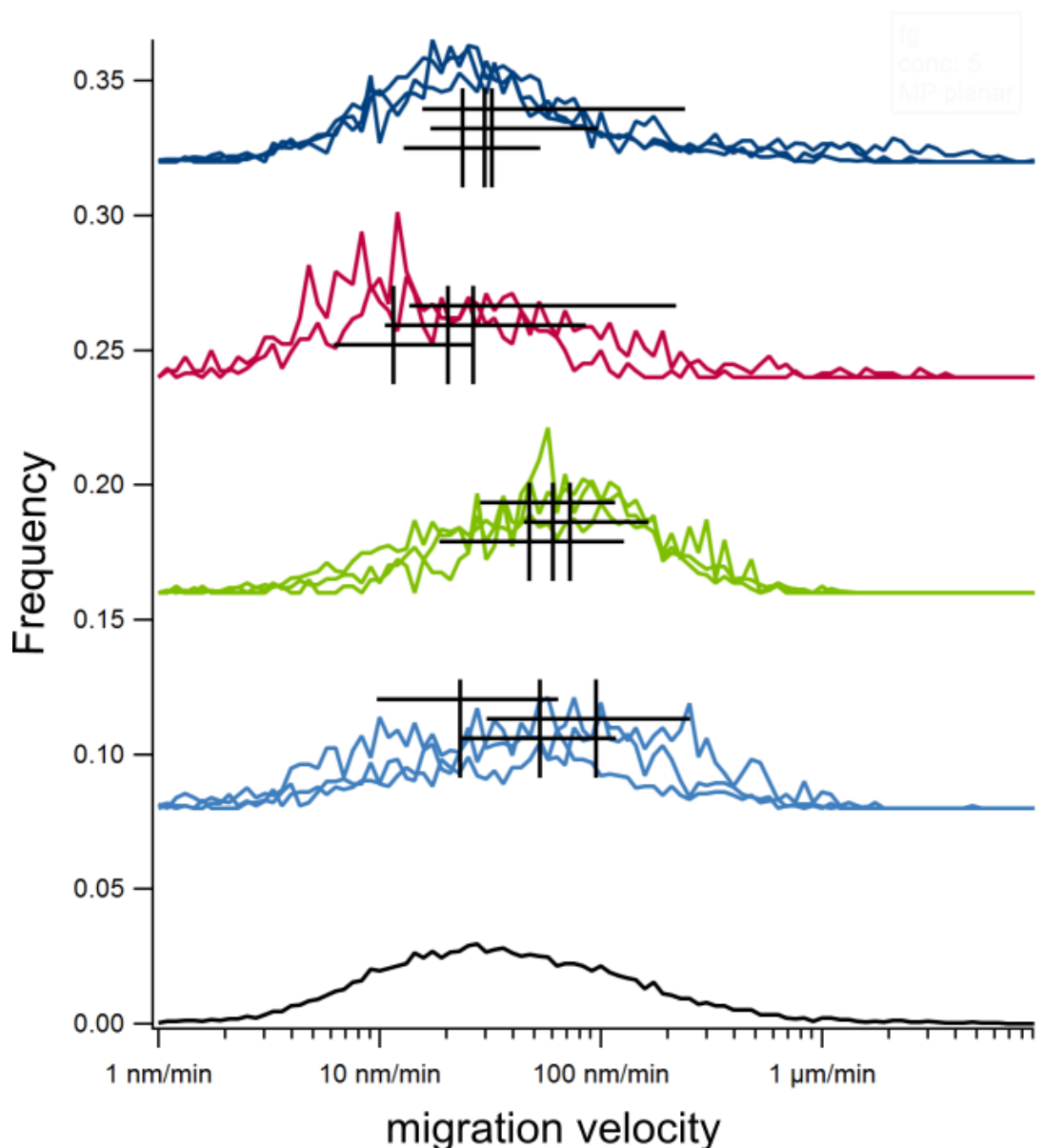
Planar area of binary fibrinogen scaffolds

Figure 96. Normalized pooled histograms of migration velocities of 3T3 fibroblasts on the planar area of binary patterned fibrinogen prepared with 5 mg ml⁻¹ fibrinogen. This graph displays the median velocities. The velocities are plotted on a logarithmic axis. Median velocities of cells on the same dependent triplicates are shown in the same color. Different independent experiments are shown in different colors n=1 (light blue), n=2 (green), n=3 (purple) and n=4 (dark blue). Vertical black lines in the histograms represent the median velocity. Horizontal black lines in the histograms represent the standard deviation. The black histogram represents the pooled median migration velocity of cells on glass (all experiments pooled).

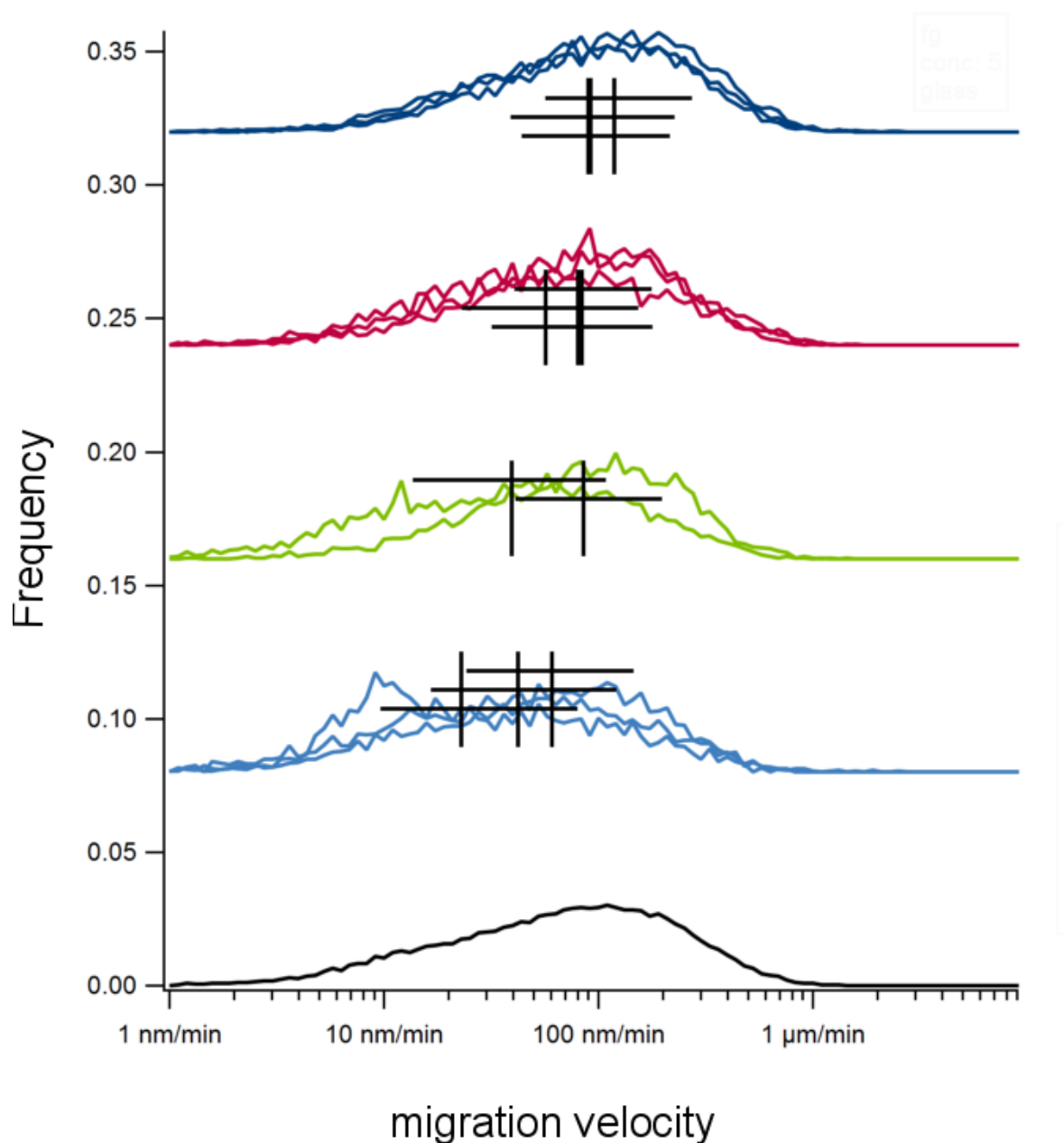
Glass

Figure 97. Normalized pooled histograms of migration velocities of 3T3 fibroblasts on glass, which was used as a reference in the cell tracking experiments on different fibrinogen scaffolds. This graph displays the median velocities. The velocities are plotted on a logarithmic axis. Median velocities of cells on the same dependent triplicates are shown in the same color. Different independent experiments are shown in different colors n=1 (light blue), n=2 (green), n=3 (purple) and n=4 (dark blue). Vertical black lines in the histograms represent the median velocity. Horizontal black lines in the histograms represent the standard deviation. The black histogram represents the pooled median migration velocity of cells on glass (all experiments pooled). Overall, all histograms are very similar, indicating reproducible results for independent experiments.

Table 16. Overview cell velocities (nm min⁻¹) with standard deviation and Cohens's d of 3T3 fibroblasts on fibrinogen scaffolds prepared with 5 mg ml⁻¹ fibrinogen.

	N 1	N2	Sample type 1	Sample type 2	avg1	stdv1	avg2	stdv2	Cohen's d
Without fit	50588	50220	Glass	Planar	62.08690342	-4.75623413	49.20395357	-3.63104709	0.1859
With fit					90.78205302	-8.40526819	55.84701947	-5.75101873	0.3009
Without fit	50588	61024	Glass	Fibers	62.08690342	-4.75623413	56.88529308	-4.34668023	0.0697
With fit					90.78205302	-8.40526819	79.9834255	-7.82365704	0.08166
Without fit	50588	14929	Glass	Binary-Planar	62.08690342	-4.75623413	36.39150361	-2.82659105	0.4164
With fit					90.78205302	-8.40526819	33.34264128	-3.80695638	0.6188
Without fit	50588	13133	Glass	Binary-Fibers	62.08690342	-4.75623413	41.59106105	-3.46094428	0.3089
With fit					90.78205302	-8.40526819	42.26686143	-4.7133225	0.4806
Without fit	50220	61024	Planar	Fibers	49.20395357	-3.63104709	56.88529308	-4.34668023	-0.1149
With fit					55.84701947	-5.75101873	79.9834255	-7.82365704	-0.2168
Without fit	50220	14929	Planar	Binary-Planar	49.20395357	-3.63104709	36.39150361	-2.82659105	0.2388
With fit					55.84701947	-5.75101873	33.34264128	-3.80695638	0.2901
Without fit	50220	13133	Planar	Binary-Fibers	49.20395357	-3.63104709	41.59106105	-3.46094428	0.1318
With fit					55.84701947	-5.75101873	42.26686143	-4.7133225	0.1586
Without fit	61024	14929	Fibers	Binary-Planar	56.88529308	-4.34668023	36.39150361	-2.82659105	0.3471
With fit					79.9834255	-7.82365704	33.34264128	-3.80695638	0.5216
Without fit	61024	13133	Fibers	Binary-Fibers	56.88529308	-4.34668023	41.59106105	-3.46094428	0.241
With fit					79.9834255	-7.82365704	42.26686143	-4.7133225	0.3852
Without fit	14929	13133	Binary- Planar	Binary-Fibers	36.39150361	-2.82659105	41.59106105	-3.46094428	-0.09694
With fit					33.34264128	-3.80695638	42.26686143	-4.7133225	-0.1229

